A Voltage Drop Study in a Megawatt Level Quasi-Steady Magnetoplasma Dynamic Thruster Via Probe Diagnostics

by

Mohanjit Singh Jolly

Submitted to the Department of Aeronautics and Astronautics
in partial fulfillment of the requirements for the degree of

Master of Science in Aeronautics and Astronautics

at the

MASSACHUSETTS INSTITUTE OF TECHNOLOGY

June 1993

—

Author . . . . . _ . . . . . . ╒.┅╤╗┉ ╦. . . . .┳ . . . . ╒╦╗ . . . .
Department of Aeronautics and Astronautics
May 7, 1993

Certified by . . . . ╱. .⁻. . . : . . . . .ν. . . . .⁻. . . . . .
Manuel Martinez-Sanchez
Associate Professor
Thesis Supervisor

Accepted by . . . . .⁻. . . . . ⁻. . . .⨎. . . . .
Prof. Harold Y. Wachman
Chairman, Departmental Graduate Committee

Aero

A Voltage Drop Study in a Megawatt Level Quasi-Steady Magnetoplasma Dynamic Thruster Via Probe Diagnostics

by

Mohanjit Singh Jolly

Abstract

A 1.625 in. long and 3.0 in. diameter cylindrical quasi-steady magnetoplasma-dynamic (MPD) thruster was used to conduct a voltage drop study. Several probe diagnostic techniques were used to determine radial and axial plasma parameter profiles throughout the MPD near the anode starvation regime. The experiments were conducted to determine axial and radial variations in plasma characteristics such as anode fall, electron temperature, electron density, magnetic field and current density. System response was acquired with Argon as the working gas flowing at .5 grams per second.

A floating probe was inserted into the MPD thruster 1 mm. from the anode surface to determine the anode voltage drop as a function of increasing thruster current. Thruster current was varied from 2.2 kA to 5.34 kA and the corresponding voltage drop varied from 16 volts to 33 volts. A jump in the anode fall was noticed at two 4.8 and 5.11 kA current levels. The 4.8 kA level was used as the point of operation for all probe experiments.

A near anode axial traverse was conducted using a Langmuir triple probe to determine the electron temperature and density profiles. The electron temperature as a function of thruster current varied between .2 eV and 6 eV with the electron density varying between $2 \times 10^{19} m^{-3}$ and $7 \times 10^{19} m^{-3}$. The triple probe was also used to determine the radial temperature and density profiles at .23 in., .98 in. and 1.47 in. from the thruster exit plane. The electron temperature varied throuout the thruster between 1 eV and 4 eV, being highest near the cathode and dropping radially. The temperature and density increased near the cathode root and the anode lip due to high current concentration measured at those locations. The electron density varied from $3.5 \times 10^{19} m^{-3}$ near the anode to $2.6 \times 10^{20} m^{-3}$ near the cathode.

Radial traverses were also conducted with a floating probe to determine plasma potential profiles. Voltage drop near (.125 in. from either electrode) the two electrodes accounted for approximately 60% of the total thruster voltage. Near the anode, the voltage drop varied from 6.2 V at the backplate to 35.2 V at the exit. The cathode drop was found to be much larger being approximately 36 V near the backplate and

43 V at the mid-thruster level.

A planar current map was obtained at 4.4 and 4.8 kA current levels using a magnetic induction probe. Ampere's law was used to deduce the current density from the measured magnetic field strengths near both electrodes. Current density near the anode varied from $99 A/cm^2$ near the backplate to $180 A/cm^2$ near the exit plane. Cathode current density measurements varied from $250 A/cm^2$ near the backplate to $50 A/cm^2$ near the exit plane.

The anode starvation regime preceeded the unstable "onset" regime that is usually marked by severe voltage fluctuation and electrode ablation. The MPD onset regime was experimentally determined to be at thruster current level of 5.6 kA for .5 grams per second. Voltage-current characteristics were also determined at mass flow rates of 1 and 1.5 grams per second. The corresponding onset current levels for the two mass flows were 6.2 and 6.5 kA, respectively.

Thesis Supervisor: Manuel Martinez-Sanchez
Title: Associate Professor

Acknowledgements

There are altogether too many people who made this project a success and I am going to mention all of them.

I would like to thank first and foremost Prof. Martinez-Sanchez, the god of MPD physics, for his support and advice during the last two years. I want to thank him for giving me the opportunity to learn about the electric propulsion field and get lots of hands-on experience at the same time.

I would also like to thank the crowd at the EP Lab at Edwards Air Force Base for providing the facilities and the entertainment needed to get all the experiments done in the desert: Ron S., Ron R., Keith, Matt, Darron, Chris, Alan, Gary. Thanks especially to Dennis and Sal for their technical support during the experiments especially when it seemed like everything I touched broke down. Also thanks to the Desert Villa posse on base, Paul, Jason, Knof and Scott for keeping me somewhat sane on main base. Thanks also to Chris Berman and the ESPN crowd for providing most of the entertainment during the winter of 1992.

How can I forget the SPPL crowd: Chris, Jim, John, Ray, Pam, Dave, Renee, Scott, Eli, and Eric for the moral support and the friday social hours. I still think that you should try Kappy's.

Thanks to all the guys from the Phi Kap house for providing me food and shelter on those late nights of heavy tooling and thesisizing.

Thanks to my good friend and roommate for two years, Ski, for keeping me off continuous microwaveable meals and more importantly, introducing me to Sega Hockey.

Finally, I want to thank my parents who stood by me through my academic and personal turmoils and to whom I could turn for moral and more importantly financial support.

Thanks guys.

Contents

List of Figures

10

List of Tables

Chapter 1

Introduction

1.1 Background

With the mindset of the National space program leaning towards interplanetary missions, increasingly more emphasis is being placed on high efficiency, low cost methods of space propulsion. Propulsion systems having high exhaust velocity ($Ue > 10$ km/sec) are desirable for interplanetary space missions. A review of the rocket equation shows that to give a mass M a desired change in velocity ΔV, the initial mass M_o of the propulsion system must be:

$$M_o = M exp(\Delta V / U_e) \tag{1.1}$$

where U_e is the rocket exhaust velocity. The initial mass that must be placed in orbit increases exponentially with ΔV required by subsequent missions. Such missions may involve raising equipment and personnel from Low Earth Orbit to synchronous orbit, repeated small velocity corrections δV or significant changes in orbital characteristics (e.g. orbit plane change). Clearly, therefore, higher exhaust velocities relative to ΔV allow lower values of M_o and a resulting reduction in launch costs. For a specified ΔV, however, it can be shown that the maximum ratio of payload mass to initial mass M_o is achieved with a characteristic velocity:

$$V_{ch} = \sqrt{\frac{2\eta}{\alpha} t} \qquad\qquad (1.2)$$

where V_{ch} is the characteristic velocity needed for the mission, t is the mission duration, η is the thruster efficiency and α is the specific power for the system. To be highly fuel efficient, the exhaust velocity of a propulsion system should be on the order of this characteristic velocity. Another term often used to describe fuel efficiency is the so-called Specific Impulse (Isp) which is the propulsion system exhaust velocity divided by the the gravitational constant ($Isp = \frac{U_e}{g}$).

Previous studies have concluded that for even the modest space missions, a ΔV of a few tens of kilometers per second is necessary [52, 25, 3, 24]. Chemical rockets which rely on the intrinsic energy available from the chemical reactions of the constituent propellants, are inherently limited to exhaust velocities of 5 km/sec, a value far short of those desired for planetary missions. Another term often used to describe fuel efficiency of propulsion systems is the so-called Specific Impulse (Isp) which is the system exhaust velocity divided by the gravitational constant. Isp available through chemical rockets, therefore, is less than 500 sec.

To remove the limitation placed on performance by chemical systems, a scheme has been developed whereby propellant is heated via passage through an active nuclear reactor. By heating the propellant independently of chemical reactions, the limitation of energy available for conversion into gas enthalpy from the chemical energy of the propellant has been removed and the performance of the engine is dictated instead by the thermal and structural limitations of engine components. Solid core nuclear thermal rockets are capable of providing exhaust velocities in excess of 8 km/sec with hydrogen propellant [6]. Low pressure solid core nuclear rockets as well as rather exotic systems such as particle bed reactor rockets have shown theoretical exhaust velocities as high as 60 km/sec [25, 46, 15]. The feasibility of these systems has yet to be demonstrated, however.

To achieve the needed exhaust velocities, a propulsive system must do so without relying on chemical reactions or heat transfer from a solid heating element. One

approach that has been researched extensively is the application of electrical energy to a gas stream in the form of ohmic heating and/or electrical and magnetic body forces. This type of propulsion system is commonly described as electric propulsion.

Electric propulsion can be divided into three general categories [33]:

- Electrothermal Propulsion: electrical energy in the form of a constricted arc is used to heat the flowing gas propellant which is subsequently expanded through a conventional nozzle. This kind of electric propulsion device is usually described as an arcjet.

- Electrostatic Propulsion: ionized propellant is accelerated through the application of strong electric field between two grids. The device in this case is commonly referred to as an ion thruster.

- Electromagnetic Propulsion: ionized propellant is accelerated by the interaction of an electric current, driven through the propellant, with magnetic fields that are induced by the current and/or supplied externally via solenoids. The former is referred to as a "self-field" Magnetoplasma Dynamic (MPD) thruster and the latter as an "applied-field" MPD.

Several systems studies conducted for space propulsion applications have shown electric propulsion devices to be a viable option due to high Isp ($\sim 1000 - 4000sec$) and the resulting overall weight reduction [6, 36, 35].

Electrothermal systems that rely on resistive heating elements suffer from the same thermal and structural limitations as the solid core nuclear rockets mentioned earlier, and are therefore limited to exhaust velocities below 10 km/sec [6, 33]. Electrothermal devices which use arcs to heat the working gas, although alleviating part of the structural heating problem by removing the resistive heating elements, are still constrained by heat transfer to the nozzle wall and frozen flow losses. As such, arcjets are limited to exhaust velocities of 15 km/sec with hydrogen and thrust efficiencies of .5 [54, 55, 10, 14].

Thrust efficiency (η_{th}) is defined as the fraction of total input power that is converted to directed thrust power:
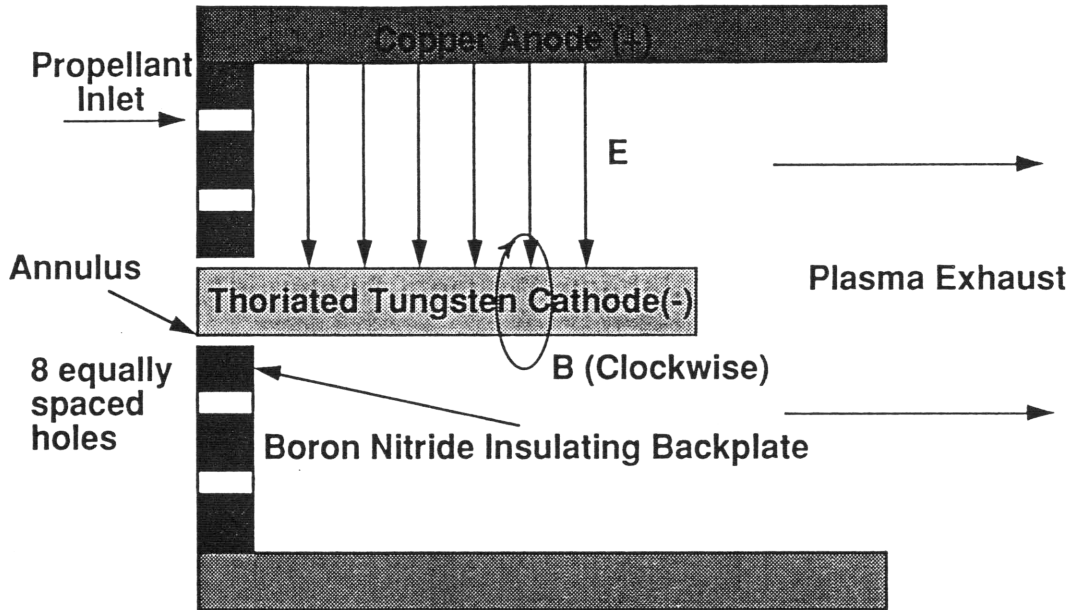
Figure 1-1: MPD Thruster Schematic

$$\eta_{th} = \frac{\dot{m}U_e{}^2}{2P_t} \qquad (1.3)$$

where $\dot{m}$ is the propellant mass flow rate, U_e is the propellant exhaust velocity and P_t is the total input power.

Electrostatic engines (ion thrusters), which can achieve large exhaust velocities ($U_e > 50$ km/sec) at high thrust efficiencies ($> .7$), have demonstrated efficient performance only at power levels below 30 kW [33, 32, 2, 5]. Studies have shown that an electrically propelled unmanned cargo vessel for lunar or mars basing requires a propulsion system capable of producing at least one Megawatt of thrust power at thrust in excess of 50 N [3, 26, 28]. Even though attempts to develop 100 kW ion engines that use mercury as propellant have met with limited success [47], still higher individual thruster power is necessary to maintain a manageable level of propulsion system complexity.

By virtue of the fact that MPD thrusters do not rely on body forces which entail macroscopic space charge to accelerate particles and, therefore, are not "space charge" limited in propellant throughput, this class of engines offers large exhaust velocities (5-100 km/sec) at thrust densities up to 10^5 N/m^2 [38, 58]. A typical MPD thruster schematic is shown in Fig. 1-1.

19

The MPD thruster uses two axisymmetric electrodes, the outer cylindrical anode and a central rod cathode, to drive current through a flowing propellant. The heat from the current in the form of collisions leads to a high degree of propellant ionization. The propellant plasma is accelerated through the interaction of the current with the magnetic field (J x B Lorentz force), which may be induced by the current (self-field) or supplied externally (applied-field), as mentioned before. The conversion of the propellant enthalpy into directed kinetic energy adds to the thrust from the MPD. The electromagnetic portion of the MPD thrust is given by the following equation:

$$T = \frac{\mu_o}{4\pi} I^2 ln(\frac{r_a}{r_c})$$

(1.4)

where μ_o is the permittivity of free space, I is the thruster current r_a is the cylindrical anode inner radius and r_c is the cathode radius.

In addition to self-field and applied-field divisions, MPDs can be further categorized into steady-state and quasi-steady operation modes. There are some logistical problems with high power level ($> 1MW$) MPD thruster experimental research. To test a steady multi-megawatt MPD thruster in a sufficiently low background pressure (.5 mTorr), would require a pumping capacity that is not viable (several hundred 2.5 ft. diameter diffusion pumps)[38]. Low pressures are required during the MPD operation to minimize the influence of ambient gas in the vacuum chamber on MPD performance. In addition, lack of usable multi-megawatt power supplies in a laboratory makes steady state MPD operation at that power level impossible. Steady state studies performed with MPD's, with few exceptions, have been limited to a maximum level of tens of kilowatts[55, 63].

With the available vacuum technology, the MPD thrusters can be run in a so-called quasi-steady mode. In this mode, the thruster operates in pulses of sufficient length ($\sim 1msec$) such that over most of the pulse, a steady thruster operation is achieved at constant thruster current and terminal voltage. The benefits of operation an MPD thruster in quasi-steady mode are threefold: 1. the vacuum requirement for a test facility is reduced drastically; 2. the thruster components are subjected to

lower thermal loads which results in longer testing operation and 3. this allows the use of intrusive techniques such as probe diagnostics for plasma parameter studies. Steady state operation may, however, prove beneficial for spectroscopic studies by eliminating the need to electronically gate a firing to determine the steady state parameters. Although quasi-steady operation is much different from its steady-state counterpart, the drawbacks mentioned earlier require multi-megawatt firings to be limited to quasi-steady mode.

MPD thrusters have been operated at a variety of power levels ranging from one kilowatt (steady state) to multi-megawatt (quasi-steady). Although these devices offer high exhaust velocities as are needed for interplanetary missions, they lack the high efficiency of an ion thruster or an arcjet [6]. The highest reported thrust efficiency obtained with non- liquid metal propellants is .45 with hydrogen [63]. For manned planetary missions, studies have shown that utilization of MPD thrusters with thrust efficiencies in excess of .5 can reduce the initial spacecraft mass to levels significantly below those that are chemically propelled [28].

1.2   Motivation For The Study

Due to the aforementioned advantages of MPDs, they have been the subject of numerous theoretical and experimental investigation within the past twenty years. Significant advances are being made by theoretical investigations such as those by Professor Martinez-Sanchez of the Massachusetts Institute of Technology [45], Dr. Kuriki of the Japan Institute of Space and Astronautical Science [39], and Dr. King, formerly of the Jet Propulsion Laboratory [38]. In order to test the validity of these models and to guide their future development, accurate measurement of plasma parameters such as electron temperature, electron density and anode voltage drop are crucial. Despite the intensive research over the past two and a half decades on the MPD, many important aspects of the plasma physics remain poorly understood due to both lack of data and unreliable theory. To prove the advantages of an MPD propulsion system over a conventional one, higher efficiency must be achieved. Two major loss

mechanisms prevent that from happening, however: frozen flow losses, which are dominant above the 1 megawatt power level, and anode losses [22]. Previous studies have shown that at below one megawatt level, most of the thruster input power is deposited into the anode [22]. Although the fraction of the thruster power that gets deposited into the anode decreases with increasing power, the heat flux to the anode poses a major thermal loading problem and in turn, could reduce the anode lifetime, which for many space missions under consideration should exceed several thousand hours [26].

As mentioned earlier, much remains to be understood about the electrical devices under investigation. Since the invention of these devices (circa 1964 [33]), a great many studies have been conducted to understand the anode phenomena. Due to the efficiency loss resulting from power deposition to the anode, it was known from the beginning that the physical processes occuring in the region had to be fully understood if MPD technology was to be proven viable. Although considerable progress has been made in the numerical simulation of MPDs, complexity of all physical processes involved have limited the modelling of anode phenomena. Careful experimentation, therefore, has to provide some of the answers to aid the ongoing theoretical efforts in the field.

Early research in the field focused primarily on characterizing the modes of anode energy transfer in sub 50 kilowatt steady state devices[60, 7, 61]. Since these propulsion systems were water cooled, anode power fraction could be easily detected through water calorimetry techniques. The studies concluded that as much as 80% of the total thruster power was being deposited at the anode, and that this fraction decreased with increasing thruster power. The anode power fraction can be written as [19]

$$\eta_a = \frac{P_a}{VI} = \frac{1}{VI} \int_S \dot{q}_a dS \qquad (1.5)$$

where P_a is the total power absorbed at the anode, V is the total thruster voltage, I is the discharge current, and $\dot{q}_a$ is the local anode heat flux. The integration in the
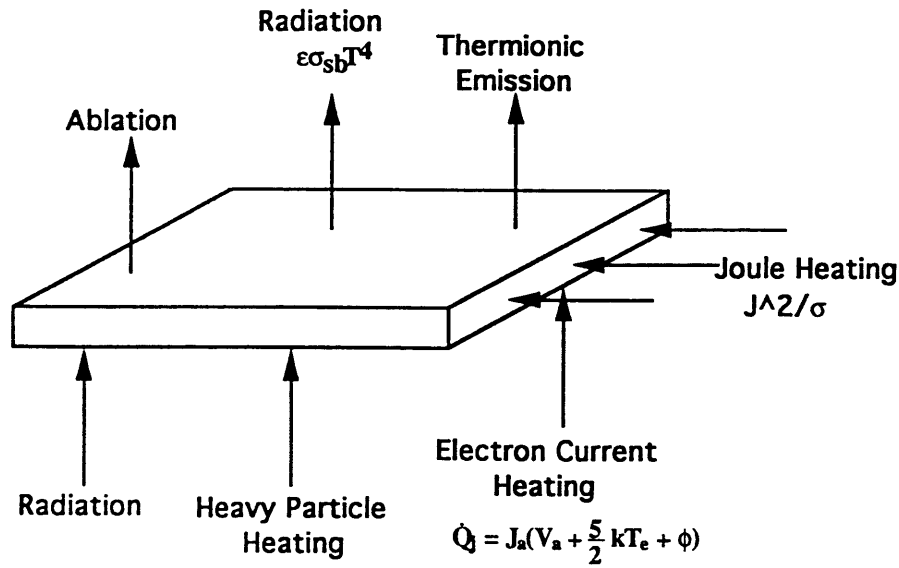
Figure 1-2: Anode Power Balance

above equation is performed over the entire current conducting surface of the anode. The integrand of the above equation is defined as

$$\dot{q}_a = j_a\left(V_a + \frac{5kT_e}{2e} + \phi\right) + \dot{q}_c + \dot{q}_r \tag{1.6}$$

where j_a is the local anode current density; terms within the parentheses represent the contribution to anode heating from the kinetic energy imparted onto the electron due to the potential difference between the anode and the local plasma, known as the anode fall (V_a), the random electron thermal energy $(\frac{kT_e}{e})$ and the heat liberated due to the work function of the anode material (ϕ). $\dot{q}_c$ and $\dot{q}_r$ represent the heating due to plasma convection and radiation, respectively. At equilibrium, neglecting regenerative or liquid cooling of the thruster, the power deposited to the anode is balanced by cooling mechanisms, such as heat conduction to a thermal reservoir, radiation, ablation and thermionic emission, as shown in Fig. 1-2.

1.3 Review of Earlier MPD Research

Before outlining the approach of this study towards examining the anode loss phenomenon, it is imperative to put the research in this field into perspective by mentioning prior work. Many anode phenomena studies before 1971 were conducted with

low power ($< 50kW$) water cooled steady-state devices. Experiments with a 20 kW thruster showed that the anode heat flux and consequently the anode power fraction decreased with increased chamber pressure and propellant mass flow rate [60]. Anode power was also shown to increase linearly with discharge current.

In reference [7], the results of anode heat transfer experiments with a 3 kW thruster with azimuthally sectioned anode is presented. In addition to measuring anode heat flux and anode via calorimetry, the researchers used a small Langmuir probe between two adjacent anode segments to determine electron temperature and plasma potential near the anode surface. Reference [61] describes experiments on the azimuthally segmented anode thruster where 70% to 80% of the total anode power was deposited by current carrying electrons. In addition, below a certain mass flow rate, current attachment to the anode was found to change from a diffuse to a spot mode. This phenomenon, which is now referred to as "onset" is known to cause considerable electrode ablation and voltage fluctuations in the MPD thruster and has been the subject of many recent investigations [34, 42, 45, 56].

Much of the earlier work, although useful in the characterization of anode heat transfer, was conducted with thruster powers two or three orders of magnitude lower than those required for most space missions. By the early 1970's, however, experiments were being conducted on multi-megawatt quasi-steady devices with maximum anode heat flux in excess of ten kilowatts per square centimeter [50]. For low power devices of the 60s, convection and radiation could accont for as much as 50% of the total anode heat flux. In the multi-megawatt devices of the 70s, the two processes accounted for 10% of the total heating rate [50, 67]. For typical operating conditions, the anode heating contribution from the anode fall, which can exceed 20 volts, is much greater than that due to electron random thermal energy ($\frac{kT_e}{e} = 2eV$), or the work function ($\sim 4eV$). Therefore, understanding the underlying physics of the anode fall is essential for reduction of anode losses and consequent increase in efficiency.

Researchers have used probe diagnostics to study anode phenomena with considerable success. Oberth [50] used Langmuir probes to measure difference in potential between the anode and the plasma at 1 mm. from the anode surface. Designated

24

the anode fall, this quantity was found, in limited operating conditions, to decrease with increasing current density. In addition, when the thruster was operated at high current levels and low mass flow rates, the anode fall and thruster terminal voltage increased rapidly with increasing current. This condition, which has been mentioned previously as "onset" results in extensive voltage oscillations and electrode ablation. It was theorized that when the mass flow rate is too low for a given current (i.e. the electrode is "starved"), the flux of electrons from the adjacent plasma due to their thermal motion is inadequate to maintain the prescribed current density. In this situation, according to Oberth, large electric fields (i.e. anode falls) form near the anode to enhance current conduction by both increasing the number of available current carriers through joule heating induced ionization, and by increasing the effective anode surface area. This effect which is commonly referred to as "Anode Starvation", has been described by several other researchers as well [66, 31].

Vainberg et al., in their experiments clearly demonstrated the effects of anode starvation on thruster operation [66]. Langmuir probes were used to measure ion and electron densities along with electron temperatures a few millimeters from the anode of a 20 kW MPD thruster. For a given mass flow rate, they found that, at sufficiently low currents the anode fall assumed negative values. As the current was increased, the anode fall changed signs became increasingly large, reaching 10 V at a thruster voltage of 25 V. Simultaneously, the electron number density decreased and the temperature increased. Further increase in the thruster current led to severe anode ablation. Anode starvation was invoked by the authors to explain their results. They argued that as the current is increased, the magnetic field and electron temperature near the anode also increase causing the current to flow parallel to the anode surface. These axial currents, in turn, lead to radial components of the Lorentz force (the pumping force). This pumping force reduces the ion and electron density near the anode by pushing the particles radially towards the thruster axis. If prolonged, this effect could result in anode surface material ablation and subsequent ionization to create new charge carriers to replace those displaced by the pumping force.

Dyuzhev et al. [16, 17] observed identical trends in both high pressure stationary

arcs and MPD thrusters. They observed that current conduction at the anode transitions from a diffuse mode with electron repelling falls, to a destructive spot mode with large positive anode falls when the local anode current density equals or exceeds that supplied by the thermal motion of the electrons. This transition from diffuse to spot mode conduction leads to ablation of the anode surface material as noted by Vainberg[66].

Similar results were obtained by Hugel with water cooled, 250 kW MPD thruster where again the anode fall was seen to increase from small negative values (-2 V) to large positive values (30 V) with increasing current at constant propellant flow rate [31].

Attempts to model anode processes have evolved from the need to predict the thruster conditions at which the mode of operation transitions from a stable to an unstable one accompanied by terminal voltage oscillations and electrode ablation. Baksht et al.[4] have developed an expression for the "limiting" current as a function of thruster geometry, propellant mass flow rate, propellant species mass and electron temperature.

Shubin [62] has developed an expression for the limiting current similar to Baksht's differing only by a numerical constant of roughly two. He performed his analysis based on plasma microturbulence from wave-particle interactions. He defines the critical current as the point at which electrostatic oscillations in the plasma near the anode are driven unstable. He argues that this condition exists when the electron drift velocity exceeds a certain threshold and cites possible instabilities which he felt could be excited near the anode. Excitation of these instabilities is expected to cause anomalously high resitivity in the local plasma; a mechanism that may explain the existence of large electric fields found near the anode.

The fact that two completely independent studies using two different techniques to study anode starvation produce similar results must imply that the plasma conditions necessary to cause classical anode starvation effects (Lorentz pumping force) and anomalous resistivities from plasma microturbulence are the same. Gallimore [23] shows that the commonality between the two is the large electron Hall parameter.

26

He also describes the Hall parameter as a major scaling parameter for the anode fall.

The Hall parameter (Ω), defined as the ratio of the electron gyrofrequency (ω_e) to the electron collision frequency (ν_e), is a measure of the tendency of the current to flow perpendicular to both the electric and magnetic fields, or subsequently parallel to the electrode surface. When the Hall parameter is less than one, the current flows generally parallel with the electric field. Large axial currents correspond to a Hall parameter much greater than one. Niewood [49] has developed a two-dimensional two fluid non-equilibrium MPD code including viscosity, heat conduction, and variable electrical conductivity which predicts large voltage drops at the anode of an axisymmetric multi-megawatt MPD thruster as a result of anode starvation. He numerically predicts large Hall parameters near the anode that cause highly skewed current lines parallel to the anode surface.

Choueiri et al. have shown a strong correlation between anomalous resistivity due to plasma turbulence, and the electron Hall parameter[13, 9]. They predict electrical conductivities that are thirty times lower than classical values for Hall parameter of twelve. The anode fall (ΔV_a) predicted is insufficient for the Hall parameter value, however.

Another mechanism which has been presented as an explanation for large voltage drops near the anode is the presence of a sheath [21]. In the presence of a solid body such as a wall or a probe surface within a plasma, the potential drop between the ambient plasma and the wall surface is confined primarily to a narrow region a few Debye lengths thick. The plasma outside of this region usually cannot feel the presence of the wall surface. In general, quasi-neutrality is not maintained throughout the sheath, leading to large electric fields. Sheaths may form near the anode to maintain current continuity by enhancing electron current collection or by creating new charge carriers through field enhanced electron impact ionization.

Now that the problem has been identified and outlined, it is important to outline the objectives and the approach of this study.

1.4 Thesis Approach

Although MPD devices have been a subject of considerable research for the last three decades, they are still inefficient due in part to the high anode losses. A clearer understanding of the anode phenomena is therefore needed if MPDs are to be proven a viable option for interplanetary missions. This need is the motivation for the experimental study undertaken here.

The approach of the study is as follows:

- Determine the voltage-current characteristics of the MPD thruster at various mass flow rates to determine a stable regime of operation.

- Measure anode voltage drop as a function of increasing thruster current.

- Determine radial plasma potential profiles at three axial thruster locations corresponding to near exit, middle and back of the thruster.

- Determine radial profiles for electron density and temperature at three axial locations corresponding to near exit, middle and back of the thruster. In addition, measure the near anode electron density and temperature at various axial locations.

- Measure the magnetic field profiles throughout the thruster and determine the enclosed current profiles along with near electrode current densities.

As mentioned earlier, the physics of these electric propulsion devices is not well understood. One of the most important loss mechanisms in these devices is the anode fall. One has to understand or at least know how the various plasma parameters are changing throughout the thruster in the high anode fall regime. The thesis was, therefore, an attempt to measure the axial and radial profiles of the important plasma parameters.

The remainder of the thesis is outlined below:

- Chapter 2 describes some of the plasma diagnostic techniques that can be used to measure the plasma parameters of interest.

- Chapter 3 illustrates the experimental facilities and probe diagnostics used in the study.

- Chapter 4 details the floating probe experimental results, both near anode axial traverses and radial traverses at the three axial locations.

- Chapter 5 describes and discusses the Langmuir triple probe results.

- Chapter 6 expounds upon the Magnetic Induction probe results.

- Chapter 7 draws conclusions and makes suggestions for future work.

Appendix A describes the theory related to the three probes used in these experiments. Appendix B includes raw data from various triple probe measurements.

Chapter 2

Plasma Diagnostic Techniques

Plasma physics is a field that relies heavily on a variety of diagnostic techniques for determination of various plasma parameters. Plasma diagnostic techniques can be divided into three main categories:

- Electrostatic, Magnetic, and Langmuir probes.

- Spectroscopy: Emission, Absorption, Scattering etc.

- Microwave diagnostics.

Before describing the probe techniques used in the experiments for this study, other methods should be mentioned. Typical values of the MPD plasma properties should be kept in mind when reviewing the following diagnostic techniques. Electron densities are approximately $10^{20} m^{-3}$ and Electron temperatures vary between 1 eV and 4 eV. The techniques described below can be used for measurements of electron density and temperature.

2.1 Density Measurements

A number of optical or spectroscopic techniques exist for the measurement of electron density[43, 20]. Spectroscopy is the arch rival of probe diagnostics with arguments in favor of and against both methodologies. Although, spectroscopic diagnostics such

as the ones described below tend to be more accurate than probes, they tend to be both tedious and expensive requiring careful set-up, optical alignment, extensive post-experimental analysis along with costly spectrometers, gratings and other data acquisition and optical equipment. Both spatial and temporal resolution issues become vital. In addition, spectroscopic techniques cannot be used to study parameters withing the thruster without considerable physical modifications such as using slits to allow optical access to the MPD chamber.

Emission spectroscopy can be used to measure a number of plasma parameters. One such commonly used technique is referred to as Stark broadening. Stark broadening technique has been used successfully in plasma physics and in electric propulsion diagnostics [18, 69, 37]. This particular spectroscopic technique is based on the fact that when each atom interacts with its neighbors, there occurs a shift in the energy level from which a transition may occur. Long range interactions with charged particles cause a change in the energy level of the emitter resulting in the so-called Stark broadening of the line. The perturbed potential due to the electric field caused by a neighboring particle causes the shift in higher energy states. This Stark effect is dependent mainly on electron density as shown by the following expression:

$$\Delta\lambda_{1/2} = 2.50x10^{-9}\alpha_{1/2}N_e^{2/3} \tag{2.1}$$

where α is the theoretical (half) half-width at full-maximum (FWHM) of the line which have been tabulated [30]. The line most commonly used with the Stark broadening technique is the Hydrogen-β line ($6562\mathring{A}$). In MPD thruster investigations, therefore, the working gas (usually Argon), is seeded with Hydrogen to take advantage of the Stark effect which is much more profound for Hydrogen than for Argon. Care must be taken, however, to make sure that the seeded Hydrogen is only a few percent (by volume) of the gas entering the thruster to not change the voltage-current characteristics of the thruster [37].

Absolute line intensity measurements can be used to determine relative upper-level number densities for both neutrals and ions [68, 57]. The emitted intensity of

an atomic or ionic spectral line is proportional to the population in the upper level of the transition.

$$\epsilon_{ul} = \frac{1}{4\pi} A_{ul} n_{i,u} h \nu_{ul} \qquad (2.2)$$

where h is Planck's constant, $n_{i,u}$ is the population density of the chemical species i, in the excited state u, ν_{ul} is the frequency corresponding to the transition from level u to level l, A is the transition probability between the two energy levels and ϵ_{ul} is the volumetric emission coefficient of the line given by:

$$\epsilon_{ul} = \int_{\Delta\lambda} \epsilon_\lambda d\lambda \qquad (2.3)$$

One drawback to this technique is the necessity for an absolute intensity calibration. Additionally, spectral line wings extending into the continuum frequency domain can introduce considerable errors into the measured intensities. An absolute measurement of the total intensity of a spectral line emitted from optically thin layers primarily yields the density of the atoms or ions in the upper state of the line integrated along the line of sight.

The refractivity of the plasma is yet another parameter that can be used for electron density deduction. The refractivity of a plasma is nearly a linear function of the various charged species densities present within it. The deviation from unity of the refractive index can be related to these densities[43]. The difference in the refractivities measured on two sides of a line is proportional to the density in the appropriate lower state and can be calculated from:

$$(n-1)_{line} = \frac{r_o f_{ul} \lambda_{ul}^2}{4\pi\Delta\lambda} \left(N_l - \frac{g_l}{g_u} N_m \right) \qquad (2.4)$$

Such measurements require observations with spectrometer and interferometer in series. Extracting a specific species density from the measurement, however, can be difficult. For low densities, the actual deviation can be quite small and difficult to measure. Currently microwave diagnostics are used to determine the index of refraction. The main drawback of the technique is that only one data point can

be acquired per shot. This technique is mainly used for measuring parameters for a laboratory plasma created through a pin cathode discharge or a hollow cathode discharge technique.

Thompson scattering offers yet another mechanism for electron density and electron temperature measurements. Electrons are capable of scattering photons that are directed at them. The intensity of the scattered light as a function of the scattering angle is a function of electron density and electron temperature and can therefore be used as a diagnostic tool. Michels and Sigman at NASA Lewis in 1971 made such a measurement on nitrogen fed applied field MPD thruster. In 1972, Michels presented additional data for both self field and applied field thrusters. Thompson scattering, unlike most other optical techniques, does not require a local thermal equilibrium (LTE) assumption. LTE is an assumption that the species are in collisional equilibrium with respect to the electrons at each energy level. As with refractivity measurements, however, Thompson scattering only allows one data point per shot. To fully characterize the plasma which is one of the goals of the study, a great many time consuming shots would need to be taken. In addition, only MPD thruster plume analysis could be done using this technique without making significant changes to the thruster itself.

An optical technique that can be used for the neutral atomic density determination relies not on emission but absorption spectroscopy. Radiation corresponding to resonant condition in the plasma is used to excite the ground state particles and then the spontaneous radiative decay is recorded. This technique is also referred to as Laser Induced Fluorescence (LIF). The intensity of the radiation can be directly related to the population in the ground state. For Argon, however, the resonant frequencies correspond to a very hard ultra-violet regime which has major drawbacks. The first excited Argon atomic level is at 11.6 eV corresponding to a high UV frequency. There are no available sources of hard UV that can be used as excitation devices. Additionally, non-visible range of energies represent problems for the available spectrometers.

The optical techniques described above have been used by several researchers to

study electric propulsion devices [69, 18].

2.2 Temperature Measurements

The most straightforward spectroscopic measure of electron temperature is the relative line intensity method. Assuming that the atomic or ionic upper level densities are in equilibrium (that is, governed by a Boltzmann distribution) wherein the free electron collisions govern the transition rates, then the ratio of the two line intensities is only a function of atomic constants (degeneracies and transition probabilities) and electron temperature.

$$\frac{\epsilon_1}{\epsilon_2} = \frac{A_1 \nu_1 g_1}{A_2 \nu_2 g_2} exp[-(E_1 - E_2)/kT_e] \tag{2.5}$$

where ϵ is the emission coefficient, A is the transition probability, ν is the frequency of the respective line and E is the energy associated with each of the two lines. Atomic transition probabilities and degeneracies of the different argon levels are well known. The main concern, however, is the tenuous assumption of equilibrium. For improved accuracy, a number of lines are measured and a Boltzmann line fit is used to deduce the temperature.

As mentioned earlier, Thompson scattering provides yet another way to measure electron temperature but the aforementioned drawbacks to the method still hold.

A third spectroscopic technique, based on the second order Stark effect is also available. While the primary effect of Stark broadening is a dispersion of emissions, a secondary effect is a small shift in the line center. Depending on the particular line and temperature, the shift can be an extremely sensitive measure of electron density and can directly yield electron temperature. Unfortunately, typical shift to width ratios are on the order or .1, hence requiring a high wavelength resolution. Burgess and Cooper describe the method and an experimental procedure to perform it. Accurate temperature determinations require detailed theoretical calculations of the shift to width ratios. Unlike the Hydrogen Balmer lines in Stark broadening where such calculations exist, second-order Stark effect theory is much more complex and

34

therefore needs further development.

Other optical techniques for electron temperature measurement include line-to-continuum intensity measurements, X-ray absorption measurements and line intensity variation in time. The spectroscopic and microwave techniques mentioned above are described in detail in references [29, 30].

Besides spectroscopic and microwave techniques, electrostatic and Langmuir probes can be used to determine plasma properties in MPD devices. Probes have been used to study plasma parameters in electric propulsion systems as long as there have been electric thrusters. Although probes have the decided disadvantage of disturbing the plasma by generating shocks and impurities, they do provide one with a reasonably accurate description of the plasma by measuring the electron temperature to within 20% and electron density to within 80%. Probes have two distinct advantages over spectroscopic techniques: they are inexpensive and require relatively little post-experimental analysis when used with digitizing oscilloscopes.

As mentioned above, probes can be used in plasma experiments to determine the details of electron and ion parameters. One type of diagnostic known as the Langmuir probe has been used to serve a full range of roles over a variety of plasma densities. The Langmuir probe theory is provided in Appendix A. A typical Langmuir probe comprises of a single electrode with a ramping bias voltage. By ramping the voltage with the probe inserted in a plasma device, a hollow cathode discharge for example, a voltage-current characteristic can be derived. There exist two distinct limiting regimes of the probe characteristic, namely the electron saturation and ion saturation, along with the regime with no saturations. The former occurs as the probe is made increasingly positive until very little increase in current occurs with large increase in bias voltage. The ion saturation corresponds then to the current level where making the bias voltage negative does not attract any more ions. The slope of the probe V-I curve can be used to determine the temperature (see Appendix A). The magnitudes of either the ion saturation or electron saturation current can be used subsequently to determine the electron or ion density.

Since a typical Langmuir probe requires the probe voltage to be ramped, it is

not suited for quasi-steady MPD thrusters such as the one used in this study. A new Langmuir probe technique has been developed by Chen and Sekiguchi[12] that eliminates the need for a voltage ramp making it possible to acquire temperature and density values in a pulsed firing. Such a probe is referred to as a Langmuir triple probe. A triple probe consists of three electrodes, one of which is floating with respect to the plasma and the other two are biased with respect to each other. Using Kirchoff's current law at each electrode and assuming a thin sheath next to the probe, the measured voltage between the floating and the positively biased electrodes can be used to directly yield the electron temperature. The current flowing between the two biased electrodes can be used to deduce the electron density. A detailed triple probe theory is provided in Appendix A.

Besides electron temperature and densities, probes are the simplest means of measuring floating plasma potentials and magnetic field strengths. A floating probe can be used to measure the former. This particular probe consists of a floating electrode (i.e. there is no net charge exchange between the plasma and the probe) referenced with respect to one of the electrodes. This technique can, therefore, be used to yield radial and axial floating potential profiles. To get plasma potential profiles, however, the floating potential has to be corrected with a factor proportional to the electron temperature.

Magnetic field strengths can be measured via a so-called induction probe. This particular probe consists of a cylindrical coil of wire inserted into a shield (usually quartz) which is then sealed at one end to protect the coil from being damaged by the plasma. The probe is based on the fact that a magnetic field varying with time induces a proportional voltage in a coil of wire. The voltage output can be electronically integrated to yield a profile proportional to the magnetic field itself. A calibration can be perfomed to convert the measured probe signal to the actual magnetic field by comparing a known magnetic field to the probe signal. With electrostatic and Langmuir probes there always exists an error due to contamination. With an MPD thruster firing, for example, contaminants such as tungsten and boron are bound to be present in the exhaust. As a result, the probes need to be cleaned with either an

electron or an ion-bombardment process to assure reasonably accurate results. This is no longer needed in an induction probe since it is physically shielded from the plasma.

2.3 Selected Techniques

This particular investigation focused on measurements of electron density, electron temperature, current distribution and anode fall voltage in an MPD thruster. Due to their relatively straightforward evaluation of the parameters under study and simple fabrication process, probes were used as the diagnostic tool for the MPD experiments. The only drawback of using probes in plasma experiments such as those conducted for this study is the perturbation introduced by inserting a probe in a plasma, especially in the vicinity of the probe. On the other hand, most other techniques described in the earlier chapter reduce the domain of the experimentation to the plume. Comparison of data acquired through probes and spectroscopic techniques in the plume region shows agreement in the measurement of electron temperature and density [64].

The first set of probe experiments conducted measured the near anode voltage drop. The anode fall voltage was determined using an electrostatic floating probe. The probe was placed about 1 mm. from the anode surface to determine the floating potential drop. To determine the actual voltage drop near the anode, the measured potential (i.e. the floating potential) needs to be converted to the plasma potential through an electron temperature correction term. This converted voltage drop could then be plotted as a fraction of the terminal voltage to determine thruster conditions at which that fraction reached 30%. The thruster current level corresponding to the 30% voltage fraction was used as the operating condition for the triple probe and magnetic probe experiments that followed. The floating probe was also used for determination of the radial plasma potential profiles.

Electron temperature and density was determined using a so-called Triple Langmuir probe, which allows the aforementioned measurements without using a voltage ramp like the one needed for conventional single Langmuir probes [64, 12]. By

mounting the probe on a translation stage, a radial and axial profile of the electron temperature and density can be determined.

Finally a current map was obtained within the thruster at the 4.4 and 4.8 kiloamp levels using a magnetic induction probe. Ampere's law was then used to deduce the enclosed current and near electrode current densities from the measured magnetic field strengths in the thruster.

A theoretical basis for the techniques mentioned above is given in Appendix A. The fabrication of the probes and the experimental set-up for all the necessary experiments is described in the next chapter.

Chapter 3

Experimental Apparatus and Diagnostics

3.1 Introduction

The pulsed multi-megawatt facility used for this study is located at the Phillips Electric Propulsion Laboratory, Edwards Air Force Base, California. The thruster design, facility description and diagnostics used in this work are described in some detail in the sections to follow.

The apparatus used to make the necessary measurements can be divided into four sub-systems: the quasi-steady MPD thruster, the plasma generation system and the plasma diagnostics and data acquisition system.

3.2 The Quasi-Steady MPD Thruster Design

The particular MPD device used in this study was designed at the Phillips Laboratory and manufactured at the Jet Propulsion Laboratory in Pasadena, California. The thruster used in this study was a self-field MPD. A detailed MPD schematic is shown in Fig. 3-1 below.

The MPD consists of a .5 inch thick pure Copper cylindrical anode with a 3.0 in. (7.62 cm) inner diameter. The thruster chamber length from the backplate to the
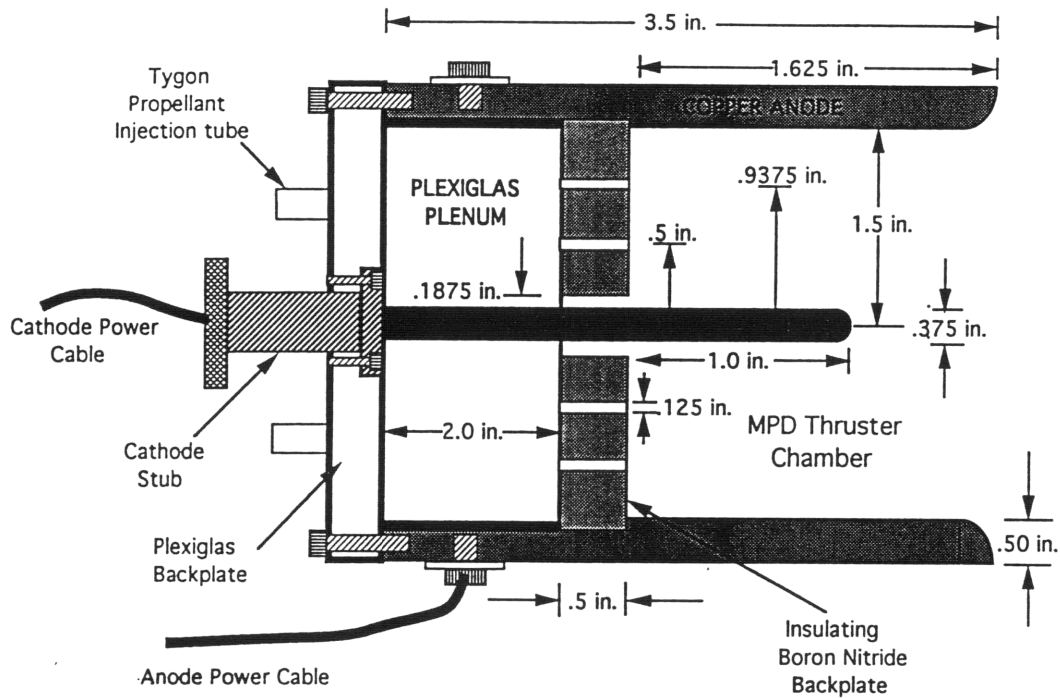
Figure 3-1: The MPD Thruster Schematic

exit plane is 1.625 in. (4.1275 cm.). The cathode is 1.0 in. long, .375 in. diameter thoriated tungsten rod which is recessed .625 in. from the thruster exit plane. The outside of the thruster is insulated with plexiglass. The electrode power coaxial cables are insulated with fusion wrap and insulating tape. Argon propellant is injected into the thruster through a Boron-nitride backplate via 16 .125 in. diameter holes at a radius of .5 in. and .9375 in., and through a .1875 in. annulus at the base of the cathode. Mass flow is distributed to the holes via a high precision orifice from where the gas enters the thruster through two .25 inch plastic tubes. Since the propellant flow through the orifice is choked, the mass flow rate is proportional to the pressure in the spherical steel plenum that was placed outside the chamber. Details of the mass flow calibration are presented in a later section. The uncertainty in the mass flow rates is estimated to be 8%.

A schematic of entire MPD thruster assembly is shown in Fig. 3-2.

The boron nitride insulating backplate fits snuggly against a lip in the anode. The boron nitride plate is glued to a cylindrical plexiglass plenum, which in turn fits into a

40

Tungsten Cathode

Coppper Anode

Boron Nitride
Propellant Feed Plate

Plexiglas Plenum

Copper Cathode Stub

Plexiglas Backplate

Copper Cathode
Power Attachment
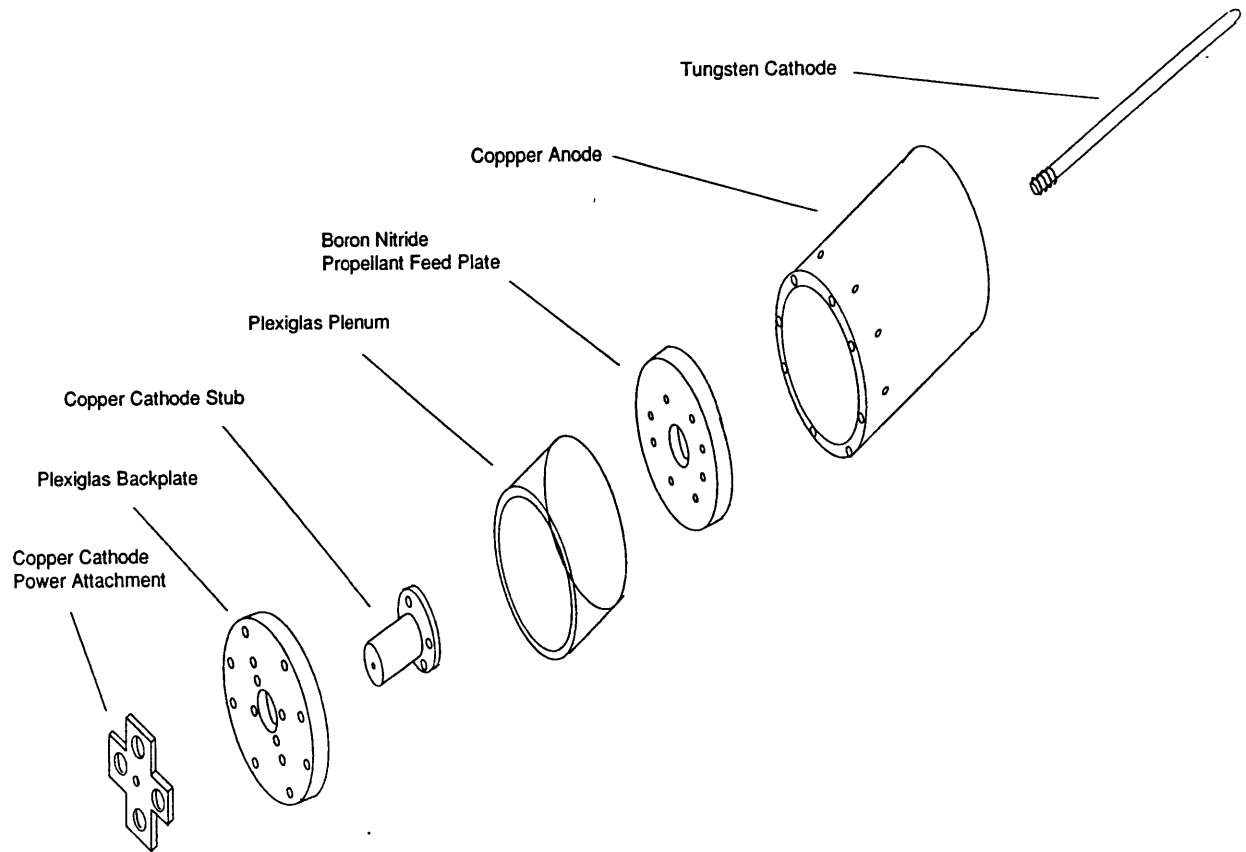
Figure 3-2: A Magnetoplasma-dynamic (MPD) Thruster Assembly Drawing

circular groove in the plexiglass backplate. The plexiglass backplate holds the entire assembly together through eight screws. The cathode is press fitted into a copper cathode stub which is attached to the plexiglass backplate with four hex screws. The coaxial Copper power cables from the Pulse Forming Network (PFN) are attached to the cathode via a copper cross which attaches to the cathode stub with a screw. The PFN power to the anode is connected via a screw and washer assembly at four azimuthal locations on the anode. The main copper wire connection from the PFN is split into four sets of wires, each of which is then wrapped around a screw and under a washer. The washer acts as a plate pressing down on the wires as the screw is tightened to assure a good connection.

3.3   Plasma Generation System

The plasma generation systems consists of three different subsystems: the MPD vacuum system, the propellant feed system and the electrical system.
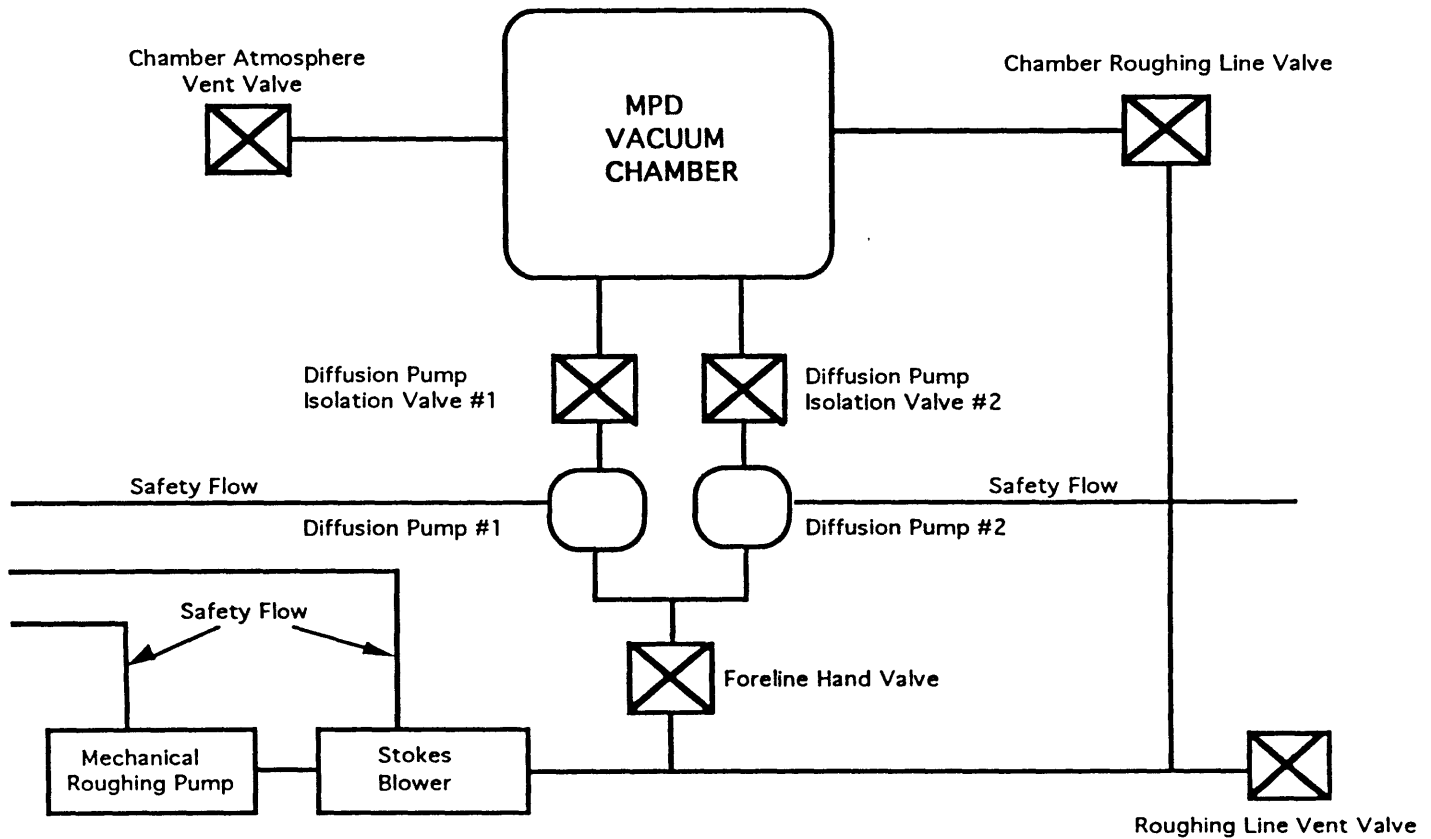
Figure 3-3: The MPD Vacuum System

3.3.1 MPD Vacuum System

The vacuum facility consisted of a stainless steel cylinder which was 8 feet (2.438 m) in diameter and 12 feet (3.658 m) long. The total interior volume of the chamber is roughly 602 ft^3 ($17.1m^3$). The chamber had 3 plexiglass and 1 quartz portal for optical access either directly or through a mirror used to reflect the image (towards a camera, for example). A Stokes 412H-10 mechanical pump, a Roots 615 RGS blower and two Varian 0185 10 inch (.254 m) oil diffusion pumps were use to bring the chamber pressure to 3 x 10^{-4} Torr range before firing the thruster. After each pulsed

firing, the chamber can be brought down to the required pressure in five minutes. Chamber vacuum pressure is measured with a Varian 843 cold cathode gage. The gauge is expected to be accurate to within .025 millitorr. The vacuum system set-up used for this study is shown in Fig. 3-3.

3.3.2 MPD Propellant System

The propellant system is a choked flow pulsed gas system which consists of a standard 326 ft^3 (9.232 m^3) Argon T-bottle and regulator supply. A .25 inch propellant line feeds from a T-bottle into a .836 ft^3 (.02367 m^3) spherical plenum (nominal 15 in. diameter) located outside the vacuum chamber. An Omega pressure gauge measures absolute plenum pressure, and a thermocouple attached to the plenum tank measures the propellant temperature. A schematic of the propellant system is shown in Fig. 3-4.

From the plenum, a propellant line feeds through the vacuum chamber to a Valcor solenoid valve. The valve is located as close as possible to the MPD thruster to reduce delay times in the gas pulse to the thruster. Immediately following the valve is a 2 millimeter diameter Fox precision orifice, which serves as the choke point for the propellant flow. A Kistler piezoelectric pressure transducer is attached downstream of the orifice. The transducer output reflects the gas pulse profile required to determine the time delay before starting the thruster. The propellant line feeds into .25 inch Tygon tubing which leads to the thruster plenum.

During thruster operation, a fast acting solenoid valve opens to release a 60 millisecond gas pulse, which typically achieves steady state flow in about 15 milliseconds. The thruster was fired 20 milliseconds after the initiation of a gas pulse. A typical gas pulse profile is shown in Fig. 3-5.

It is during the steady flow portion of the pulse that the thruster is fired. It is important to fire as close to the start of the steady state pulse region as possible. If the thruster is fired several tens of milliseconds after the start of the gas pulse, gas can get entrained in the thruster, thereby increasing the background pressure and resulting in highly inaccurate probe measurements. A Stanford Research Systems
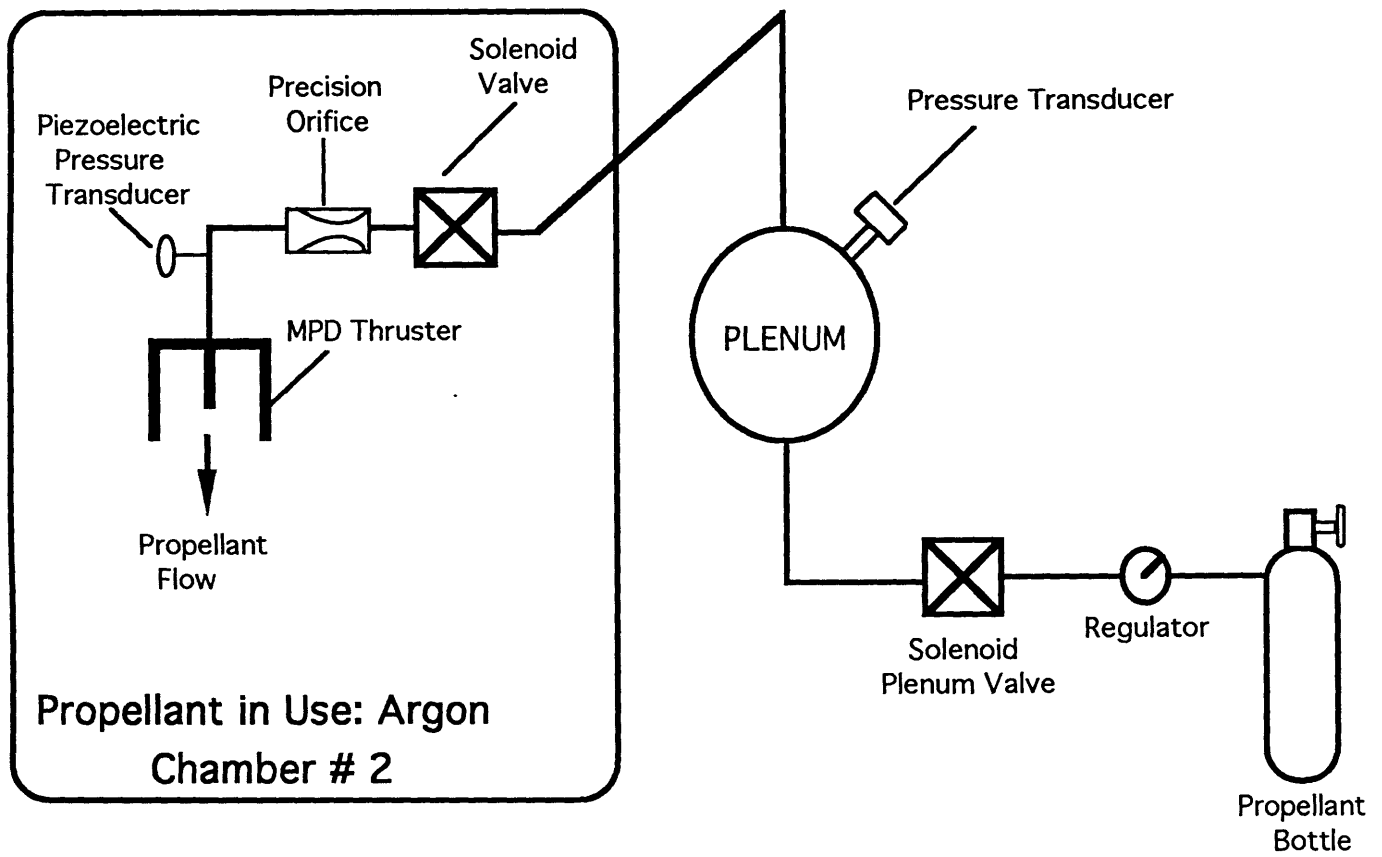
Figure 3-4: MPD Propellant System

1V

200mV
/div
EA

Inotl
trig'd

-1V
-9.8ms   10ms/div   90.2ms
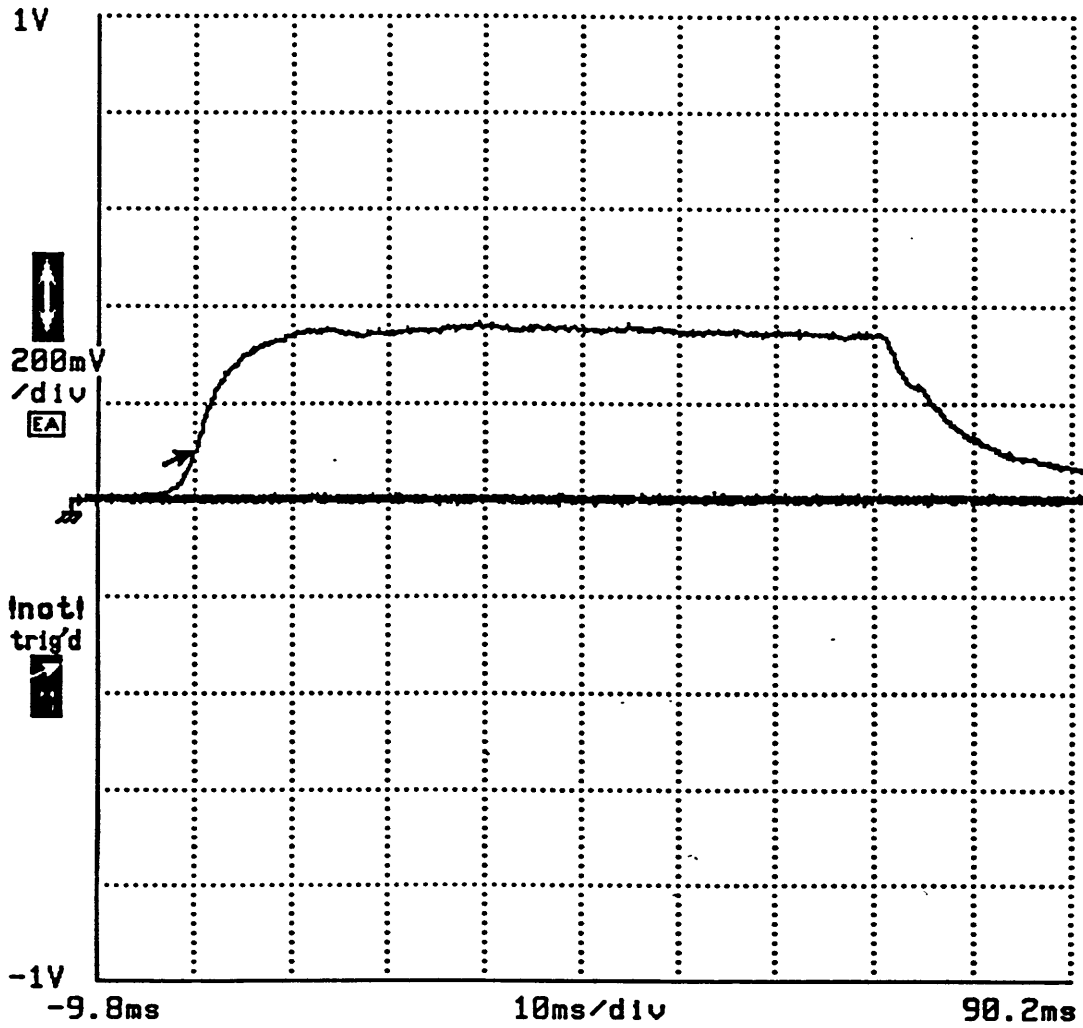
Figure 3-5: MPD Gas Pulse
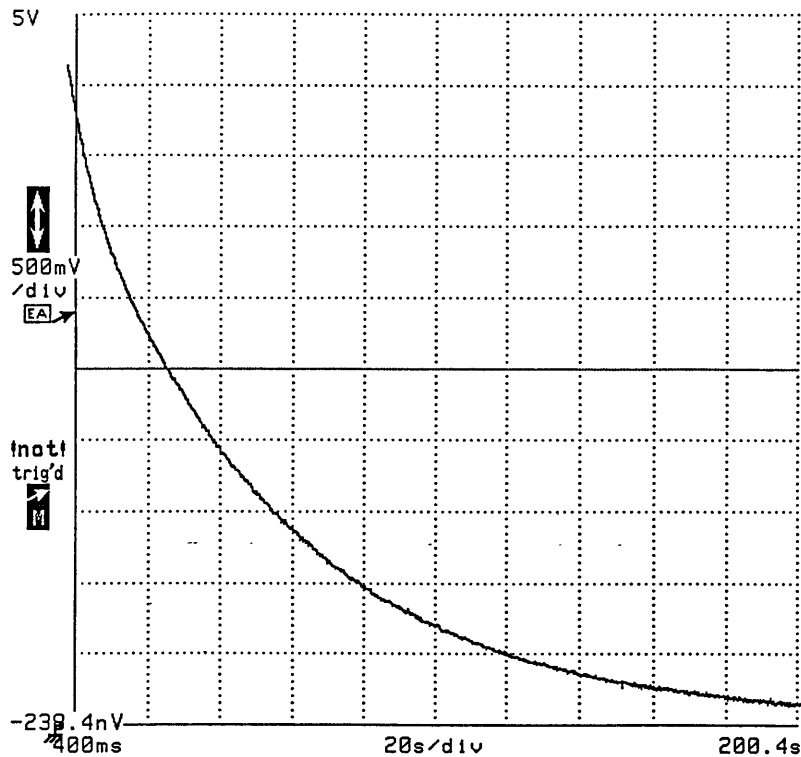
Figure 3-6: Plenum Pressure Drop For Mass Flow Calibration

DG635 signal generator is used to regulate the timing between gas pulse initiation and thruster start.

MPD thruster firing requires accurate mass flow measurement and calibration. For calibration, propellant fills the plenum to maximum system pressure, and then is discharge through the thruster into the vacuum tank. The calibration theory is based on the ideal gas law, PV=nRT, which is accurate for low pressure, low density argon used in the tests. Mass flow which is proportional to the plenum pressure for choked flow, is related to the rate of change of pressure by the following expression:

$$\frac{dm}{dt} = -\frac{MV}{RT}\frac{dP}{dT} = cP \tag{3.1}$$

where M is the molecular weight, V is the plenum volume, R is the universal gas constant, T is the plenum gas temperature, P is the plenum gas pressure and c is the proportionality constant. Fig. 3-6 shows the measured pressure drop in the plenum.

Equation 3.1 is based on the assumption that the process is isothermal. This

46

assumption was verified experimentally using a thermocouple to measure the plenum gas temperature. The solution to the equation is an exponential function of pressure versus time. A Tektronix DSA601 digital signal analyzer was used to record plenum pressure versus time. The pressure history is then fit to an exponential function to yield the constant of proportionality between mass flow and plenum pressure. In the tests performed, a plenum pressure of 10.7 psi corresponded to a mass flow of .5 gram/sec ($\pm 8\%$).

3.3.3 MPD Electrical System

A schematic of the electrical system for the thruster is shown in Fig. 3-7.

The power source for the quasi-steady MPD thruster is a pulse forming network (PFN). The PFN is a ten section LC network with a nominal .01 ohm output impedance. Each section consists of three 2000 microfarad, 800 volt Maxwell electrolytic Castor oil capacitors connected in parallel and a 5 turn, .53 microhenry inductor. Together they release a one to two millisecond current pulse at up to 40 kAmps and 400 volts, assuming a matched load [11]. The PFN stores approximately 25 kilojoules of electric energy, which corresponds to a maximum thruster power on the order of 10 Megawatts. A Del Electronics Corp HPS-1-8000-3 power supply provides up to to 8 kWe of power to the PFN. PFN charging voltage varied from 100 V to 200 V corresponding to thruster currents between 2.2 kA and 5.34 kA with Argon flowing at .5 grams per second. All experiments conducted in this study utilized a 1 millisecond pulse.

Thruster firing sequence is shown in Fig. 3-8. The firing sequence begins with the charging of the PFN until a desired voltage is reached, at which time the PFN is disconnected from the charging power supply. The PFN voltage is applied directly to the MPD without a ballast resistor in series with it. There was no need for a ballast in this particular set up since the thruster and the PFN had similar impedances. The researcher ensures that the chamber pressure has dropped to 3 x $10^{-4}Torr$ before going on to the actual firing.

All the controls for the PFN and the timing devices were mounted on a console
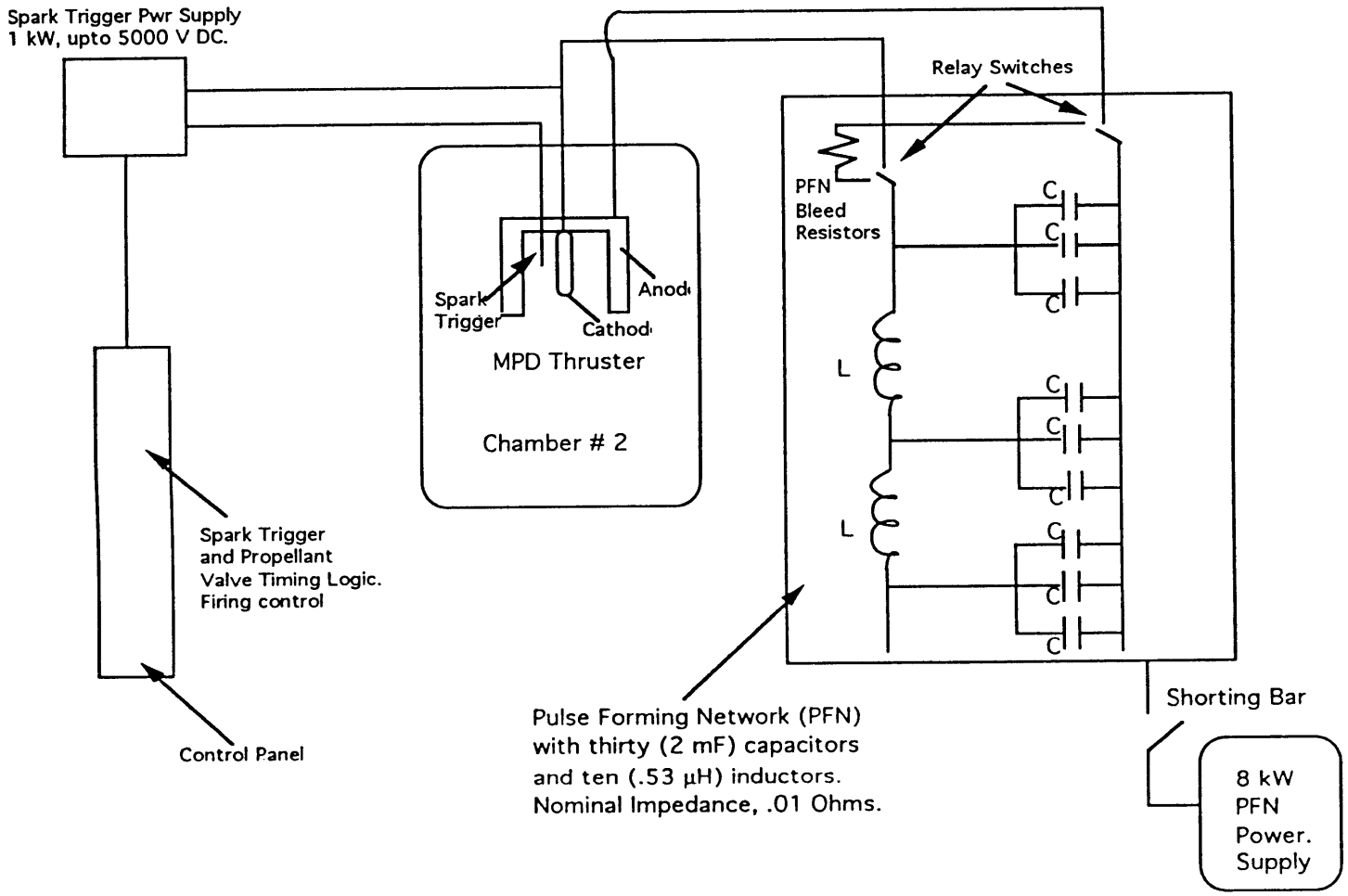
Figure 3-7: MPD Electrical System
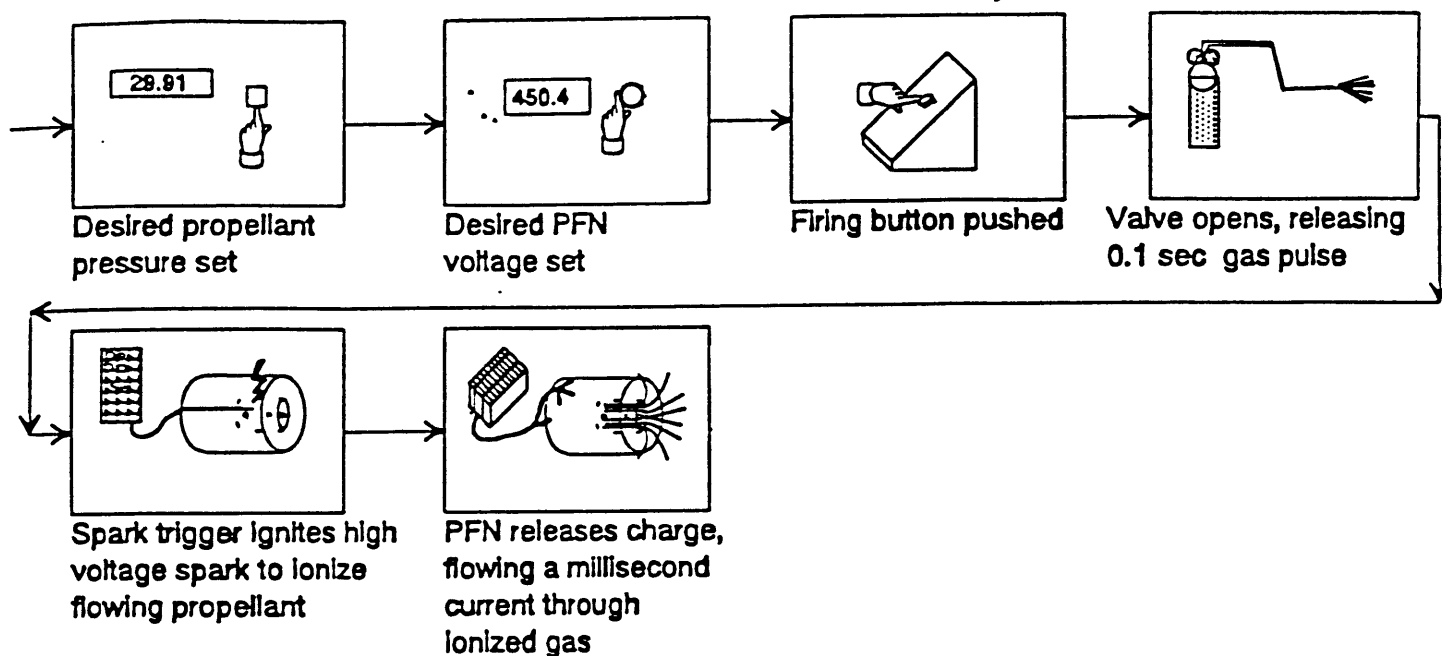
Figure 3-8: Thruster Firing Sequence

```
                                        ⌐DefWfm¬
    100V ┬ ⋯ ⋯ ⋯ ⋯ ⋯ ⋯ ⋯ ⋯ ⋯
         │
         │
     20V │
    ∕div │
         │
         │
    !not!│
   trig'd│
     [M] │
         │
   -100V ┴
     -490µs            500µs∕div            4.51ms
```
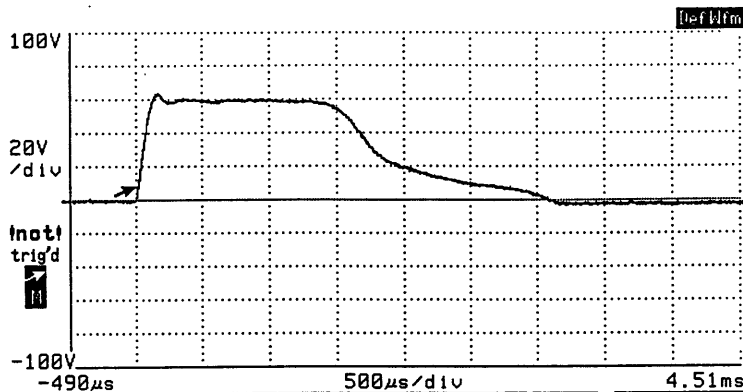
Figure 3-9: A Typical MPD Current Profile

next to the chamber. Once the "fire" button is pushed, a TTL logic pulse acts as a trigger for the signal generator which sends out two square pulses, namely the gas pulse and the spark pulse. The gas pulse is an 80 msec pulse that opens the solenoid valve. 20 milliseconds later, the spark pulse is initiated. The spark occurs once the gas pulse has reached steady state. This spark initially ionizes the gas to create a current path for the PFN discharge. The spark trigger is a .01 inch diameter tungsten wire fed through a thruster propellant injection hole. This spark trigger wire is used to provide an initial high voltage spark that ionizes the propellant and initiates thruster operation. The spark trigger circuit is essentially a 70 microfarad, 2.5 kilovolt Maxwell capacitor charged by a Del Electronics Corp 5 kilovolt, 200 milliamp power supply, operated between 700 and 1000 volts. A high voltage relay is used to transfer the capacitor high voltage to the spark trigger. Thruster current is measured by a Pearson Electronics current pulse transformer which saturates at 20 kAmps for a one millisecond pulse. Current responses were relatively noise-free with an initial overshoot of no more than 10 per cent. The current pulse had an exponential rise and decay with an extremely flat steady state portion, especially at low power levels. A typical current profile is shown in Fig. 3-9.

Voltage across the thruster is measured using two Tektronix 1000:1 high voltage
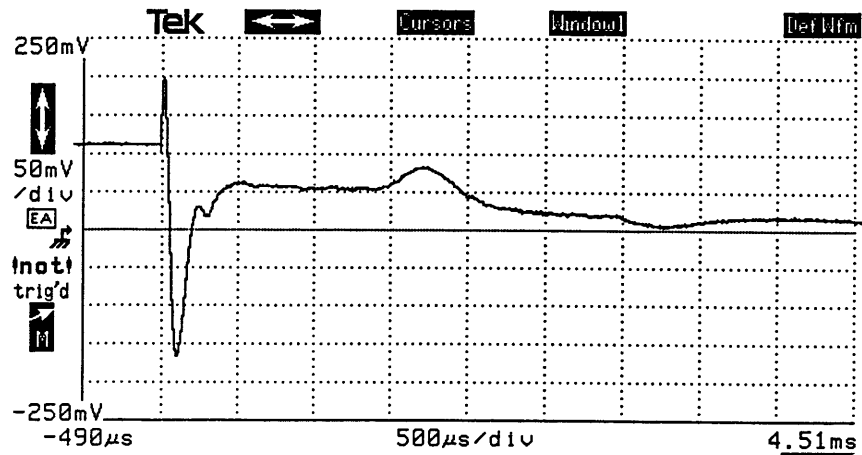
Figure 3-10: A Typical MPD Voltage Profile

probes attached to the thruster power feed-throughs outside the chamber. Fluctuations in the terminal voltage are readily apparent with the use of the Tektronix probes because they are high frequency response devices. This is quite useful when detecting "onset" in the MPD, a phenomenon which is signified by large voltage oscillations. The voltage drop in the power cables from the voltage probes attachment sight to the thruster is estimated to be 1 V. A typical MPD stable voltage profile is shown in the Fig. 3-10.

The voltage trace was characterized by a large noise spike at the trigger time, followed by a steady state region of $\sim$ 1 msec. Very little noise for observed in the voltage signal at low power levels. Higher power levels led to observable voltage fluctuations, however. A Tektronix DSA 601 digital signal analyzer is used to record the thruster current and voltage profiles. Signal conditioning for the various experiments is aided by the use of Tektronix AM501 operational amplifiers. The terminal voltage and current measurements are accurate to within 5%.
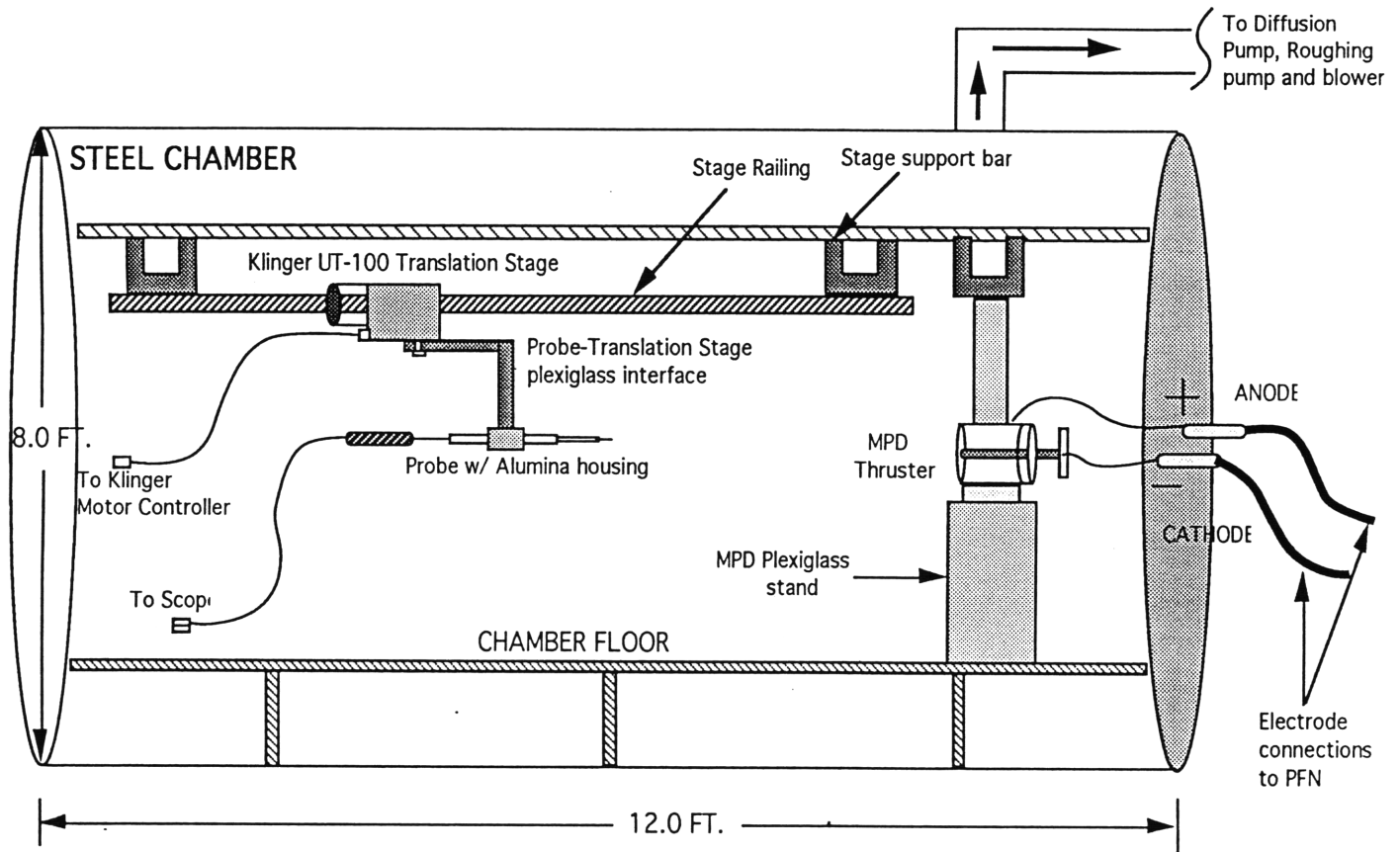
Figure 3-11: Experimental Probe Mounting Setup

3.4   MPD Diagnostics

The MPD diagnostic set-up consists of two categories: the probe mounting set-up
inside the thruster and the probe diagnostics.

3.4.1   Translation Stage System and Probe Mounting

The plexiglass mounting system and permanent motor translation stage were used to
position the several probes used in this particular study. The schematic of the entire
translation stage and mounting system inside the vacuum chamber is given below in
Fig. 3-11.

The cylindrical plexiglass mounting bracket was attached to a Klinger UT100
permanent magnet translation stage. The stage motion was controlled by a Klinger

MC-4 motion controller. Since only one degree of freedom was available with the one translation stage, the entire set-up had to be rotated manually by 90 degrees when switching from the initial floating probe axial experiments to the triple probe and floating probe radial experiments. During the induction probe experiments, magnetic field map had to be acquired in the entire meridional plane of the thruster. In that case, the translation stage was set up to allow radial traverses. After a radial translation was completed at one axial location, the probe was moved by hand to the next desired axial location and so on. Extreme precaution was taken in assuring the alignment of the probe with the thruster axis. The error associated with the axial location is estimated to $\pm.015$ in. Same procedure was followed for the floating probe and triple probe experiments. In those cases, however, only three radial traverses were conducted at three different axial locations, instead of an entire planar map.

The following four sets of experiments were conducted:

- An axial traverse of the thruster with a floating probe to determine the voltage drop near the anode.

- Radial floating probe traverses at three axial locations.

- Radial triple probe traverses at the same three axial locations.

- A current mapping of the entire thruster at the condition of interest (i.e. the thruster current level corresponding to a sharp rise in the voltage drop) using an induction probe.

Although the MC-4 stage motion controller could be used to move the stage, it could not, however, be used to monitor the distance. A secondary visual technique was employed to aid with determining the actual position of the probe. For the axial traverses, a masking tape was placed on the side of the plexiglass mounting bracket and twelve marks were made on it at a spacing of .125 inch. A motor controllable camera was used to monitor the firings. The camera was focused on the masking tape with the marks. Another masking tape was placed across the video monitor outside the chamber with only one mark on it. The probe position could be known to within

53

.015 in. by lining up the mark on translation stage tape with that on the screen. To assure a certain amount of reliability, a square was marked on the floor 3 feet from the video monitor. The author stood in the square when the stage was being traversed axially to a new location. Since the probe positioning had to accomplished visually rather than through automatic control as would be desirable, the technique described above was utilized. For the near anode floating probe tests needed to determine the anode fall, it was crucial that the probe position be 1 mm from the anode surface. This was accomplished by placing the probe 1 mm from the anode and then scanning axially from the exit plane to the backplate, measuring the probe-anode distance at various axial locations to verify that the distance from the anode surface did not vary.

During the radial traverses, a slightly different position technique was used. The entire translation stage set up was rotated by 90 degrees. A dark line was placed throughout the length of the plexiglass cylindrical shaft to which the probe holder was attached. Due to the physical circumstances, the camera could not be positioned in such a way as to look straigth at the thruster. A mirror was, therefore, used to get a head-on view of the thruster. The camera was focused, instead on the line that had been drawn on the plexiglass piece. A masking tape with eight equally spaced markings on it was placed on the video monitor. The first and eighth markings corresponded to the near anode and near cathode probe positions, respectively. The alignment of the mark on the probe holding piece inside the vacuum chamber with the desired mark on the video monitor was used as the radial probe positioning technique. Again, the error introduced by this technique in the radial location is estimated to be ±.015 in.

3.5   Plasma Diagnostic Techniques

Three probe techniques were used to obtain the necessary measurements. A floating probe was used to determine the anode fall and radial plasma potential profiles; a triple Langmuir was used to determine the near anode axial electron temperature and density profiles in addition to radial profiles of the same parameters and finally a

54

magnetic induction probe was used to determine magnetic field strengths throughout the thruster. In each case, the probe was level with the thruster axis. The description of the three probes is given in the following subsections. The theoretical basis for the probes is described in Appendix A.

3.5.1 Floating Probe

Floating probes are the easiest means of determining plasma potentials. Floating probe is essentially a floating electrode (i.e. there is no net current exchange between the probe and the plasma). The number of ions and electrons being absorbed by the probe must then equal the ions and electrons leaving the probe. The value for the floating potential as a function of the electron and ion current is derived in Appendix A.

The construction of the probe is a rather straightforward process. The probe consists of a Tungsten electrode .0625 mm. in radius having an exposed length of approximately 4 mm, inserted into an insulating alumina tube of .125 mm. inner radius and .5 mm outer radius. EPOTEK high temperature epoxy is used to attach the wires to the alumina tube. This thin alumina tube is, in turn, inserted into a four hole alumina holder with 1.5 mm diameter holes and 6.0 mm outer diameter and sealed with Ceramabond 671 ceramic paste. The alumina holder provides the needed structural integrity. The tungsten electrode is connected to a coaxial cable for electrostatic shielding and to allow the use of BNC connectors for transporting signals from the probe inside the MPD to the scope. The floating probe schematic is shown below in Fig. 3-12.

The floating probe is referenced with respect to the anode. As the name suggests, the potential measured by the floating probe is the near-anode floating potential drop in the thruster, not the anode fall. A Tektronix differential comparator is used to determine the floating potential drop. This floating potential has to be corrected by subtracting the factor proportional to the electron temperature and masses of the plasma species, given by the equation below to determine the actual anode voltage drop. A detailed description of the Langmuir and triple probe theories is given in
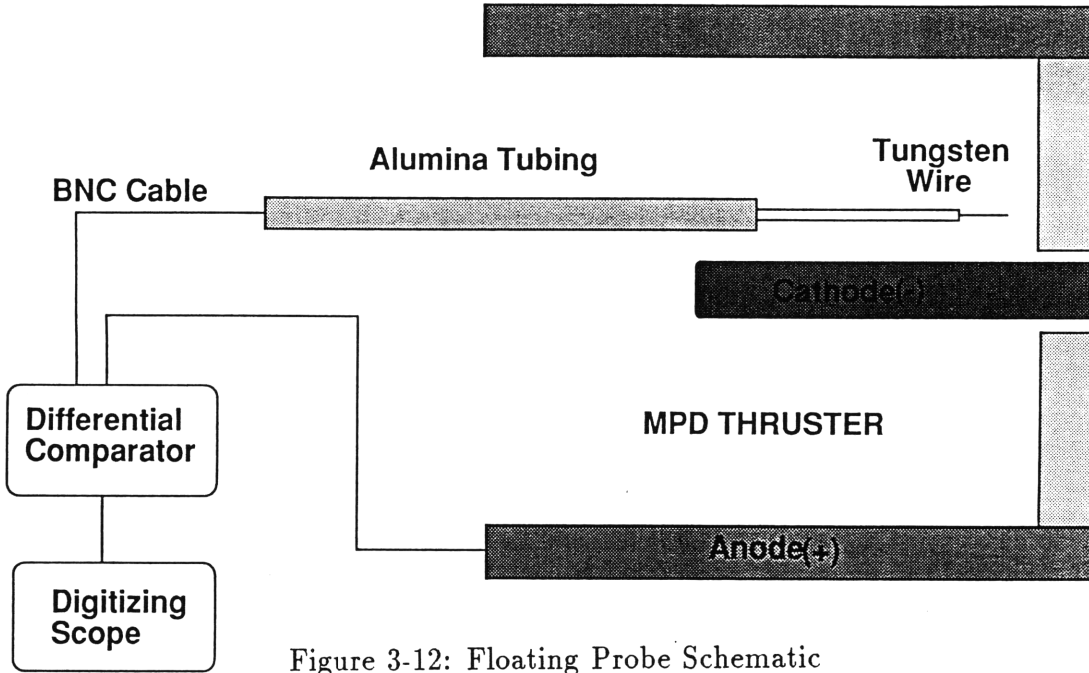
Figure 3-12: Floating Probe Schematic

Appendix A.

$$V_p = V_f - \frac{kT_e}{2e}(ln(\frac{m_e}{m_i})) \qquad (3.2)$$

The above factor is approximately $5.3kT_e(eV)$. Based on the accuracy of the electron temperature measurements, plasma potentials obtained from floating probe measurements are accurate to within $\pm 9\%$.

3.5.2 Triple Probe

The construction process for the triple is quite similar with that for the floating probe. In this case, three tungsten electrodes, .0625 mm in radius and 5.2 mm in length are used, supported by three parallel thin alumina tubes spaced approximately 2 mm from each other. The thin alumina tubes are in turn inserted into a four hole alumina holder with 6 mm outer diameter for structural integrity. High temperature EPOTEK epoxy is used to seal the end of the thin alumina tubes containing the electrodes and Ceramabond 671 ceramic paste is used to seal the thinner alumina tubes to the bigger holder. For electrostatic shielding purposes, the electrodes are attached to coaxial cables that attach to the BNC feedthroughs inside the vacuum
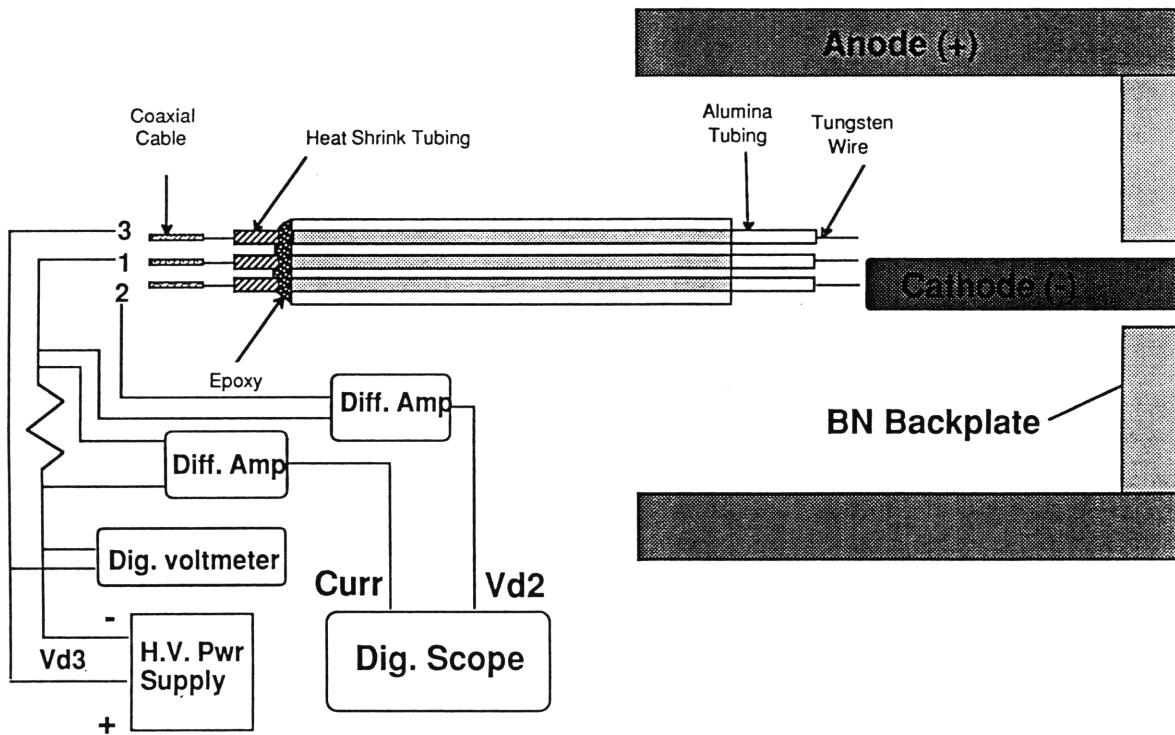
Figure 3-13: Triple Probe Electronics

chamber. Another set of three BNC cables are connected from the outside of the chamber to their respective electronics. A triple probe structural schematic along with the necessary electronics is shown below in Fig. 3-13.

One of the electrodes is floating while the other two are biased with respect to each other. The simultaneous measurements of the current flowing between electrodes 1 and 3 and the voltage difference between electrodes 1 and 2, values for the electron density and temperature, respectively, can be obtained.

3.5.3 Probe Cleaning Set-Up

During pulsed MPD firing, at the startup transient stage, the inserted probes are expected to be coated with MPD by-products such as tungsten and boron nitride. It is imperative, therefore, to clean the probe periodically in order to obtain reasonably accurate results. Both floating and triple probes were cleaned after every ten shots in the near anode axial traverses and the radial traverses.

57

TRIPLE PROBE   **BNC CABLES**

1. Flow Argon at 6 psi through the thruster
2. Dial voltage on the HV power supply to 1100 V.
3. The above two steps should lead to a glow discharge cleaning of the probes. The probes discharge to the anode which is at 0 V.

5KΩ RESISTOR

Set at 1100 V

GLASSMAN H.V. POWER SUPPLY
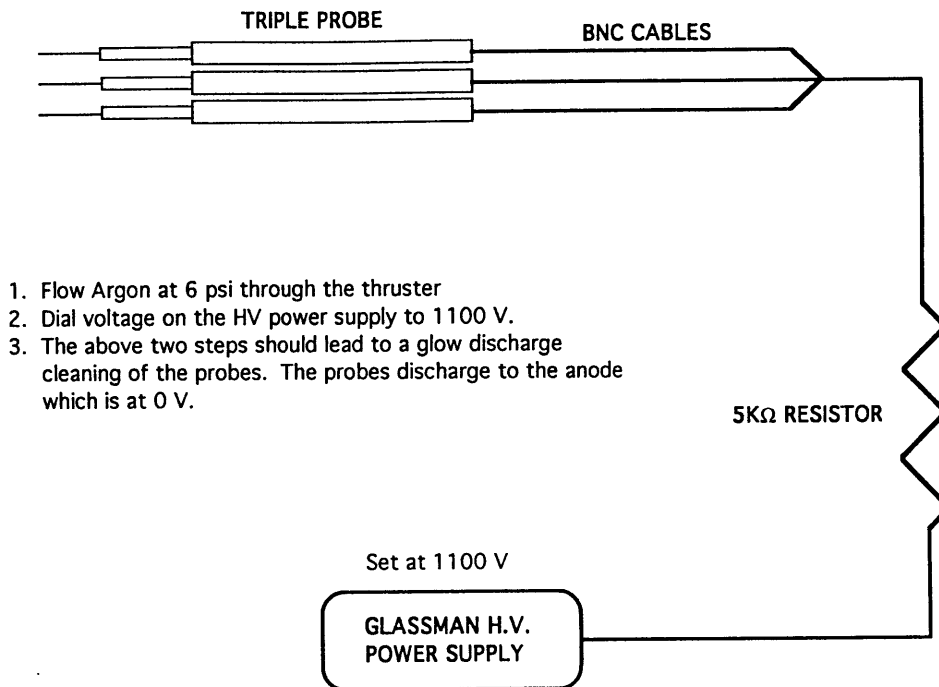
Figure 3-14: Probe Cleaning Set-up

A glow discharge technique was used to clean the probe. The probe was connected to a 5 kilo-ohm resitor in series with a Glassman high voltage (5 kV) power supply. The probe cleaning set-up is shown below in Fig. 3-14.

Approximately 1000 V were applied to the electrodes and the resulting electron bombardment was used to get rid of contaminants. A blue glow discharge could be clearly seen inside the thruster during this cleaning process. Especially near the cathode, due to high temperatures and tungsten ablation, contaminants can cover the electrodes after only a few shots. To get more accurate probe measurements in the near cathode region, the probes should be cleaned after every shot. Time constraints, however, prevented the probe cleaning procedure to be performed more often than every ten shots.

3.5.4 Magnetic Induction Probe

To measure enclosed currents and current densities throughout the MPD thruster, a magnetic induction probe is used. The probe construction is relatively simple. The probe consists of a 1.6 mm (.0625 in) diameter 75 turn cylindrical copper wire coil inserted into a 3 mm. diameter quartz tube was used to measure magnetic field strengths throughout the thruster. Enclosed current contours and current density

58
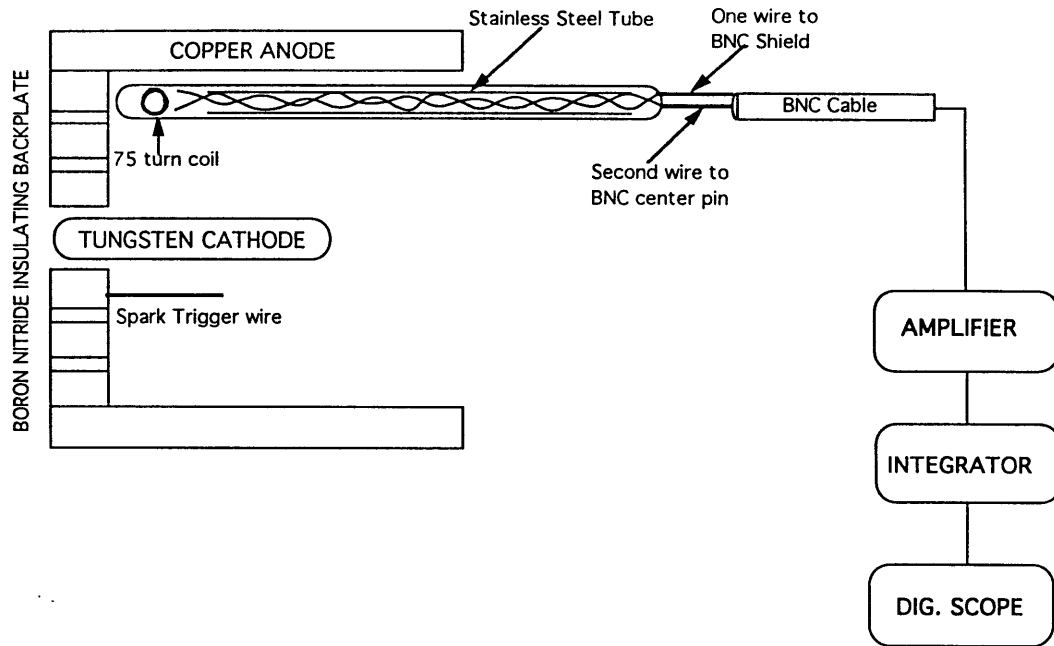
Figure 3-15: Induction Probe Schematic

values can be deduced from the measured magnetic fields, as described in Appendix A. The probe was oriented such that the coil axis was parallel to the magnetic field lines (azimuthal). An induction probe schmematic is shown in Fig. 3-15.

The design used produced high signal to noise ratios with a frequency response on the order of 100s of MHz. Mean field strength in the steady state region of the pulse was used in the calculations. The voltage induced in the probe is proportional not to the magnetic field itself, but the time derivative of the magnetic field. An integrator is used, therefore, to derive the actual magnetic field strength. The effective cutoff frequency of the integrator is 10 MHz. The circuit is therefore limited in response not by the probe but by the operational amplifier.

A calibration had to be performed to determine actual magnetic field strengths from the probe voltage output. To do so, the probe was placed at the the outermost radial location possible and as close to the backplate as possible to assure that the probe would enclose all the current. Ampere's law as given by Equation 3.3 was used to relate the enclosed current to the magnetic field.

$$B_\theta = \frac{\mu_o I_{encl}}{2\pi R} \tag{3.3}$$

where B_θ is the magnetic field in the azimuthal direction, I_{encl} is the measured

59
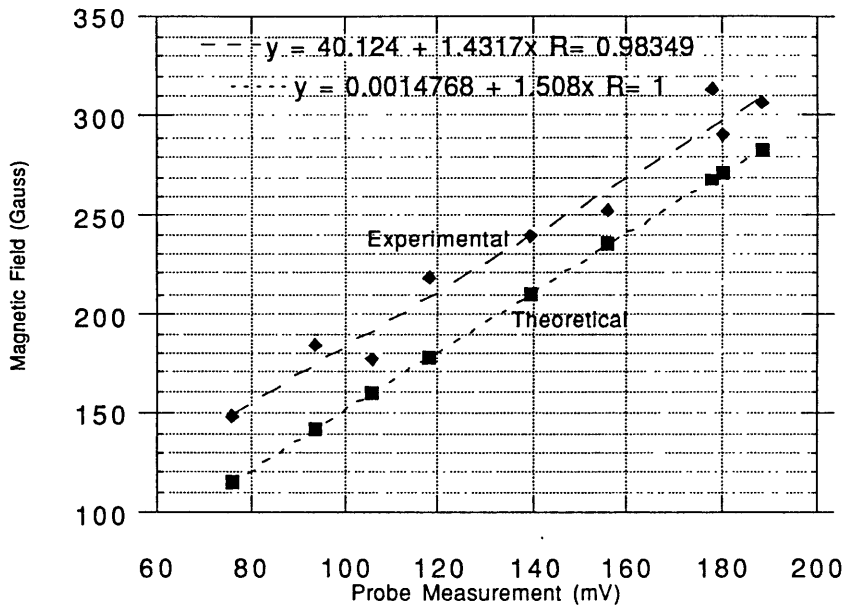
Figure 3-16: B-Probe Output as a Function of Thruster Current

thruster current and R is the radial probe location. The thruster was fired at current levels varying from 2 kA to 6 kA. The probe output was plotted as a function of the thruster current and a least squares curve fit was applied to the data. The resultant calibration curve was determined to be $1.408 mV/Gauss$. A comparison of the measured probe output voltage with the theoretical output ($V_{out} = \pi r^2 n B_z / RC$) for a cylindrical coil as a function of the thruster current is shown below in Fig. 3-16.

Although the probe was placed so as to enclose the entire thruster current, a substantial error was involved with the calibration. The coil itself was embedded approximately .125 in. from the quartz tube end. There is a possibility, therefore, that some of the current was unenclosed leading to a lower voltage output. The error associated with the calibration process is ±10%. The probe was attached to a translation stage and traversed radially. After each radial traverse, the probe was moved manually .25 in. and another radial traverse was performed. The measurements were taken on a spatial grid made up of seven axial and eight radial points. Three measurements were made at each spatial location for each of the two thruster current levels (4.4 kA and 4.8 kA). The average of the three values was taken as the magnetic field for analysis purposes.

60

Chapter 4

Characterization of the MPD Thruster

Before the series of probe tests could begin, the thruster performance was characterized to determine its regime of stable operation. MPD experimentation has shown that at a certain current level for a given mass flow, (more specifically, the parameter $J^2/\dot{m}$) the thruster reaches a point of high plasma instability accompanied by high thruster voltage fluctuations and electrode ablation. These fluctuations signify the so-called "onset" level of MPD operation which results not only in physical damage to the electrodes but severe reduction in thruster efficiency [67, 34]. The thruster was fired with Argon flowing at .5, 1.0, and 1.5 grams per second. Argon was injected into the thruster via two .25 in. press-fitted tygon tubes. A high voltage spark was initiated to intially ionize the propellant. The ionized propellant, in turn, provided a conducting path for the high current discharge supplied by the 10-section LC (Inductor-Capacitor) Pulse Forming Network (PFN). The PFN voltage was varied from 100 to 300 volts corresponding to a thruster current variation from roughly 2.0 kiloamps to 7.0 kiloamps. The determination of onset was based on a 10% fluctuation of the thruster voltage profile [44]. Figs. 4-1, 4-2 and 4-3 show the voltage and current profiles at "onset" for the three mass flow rates.

The hashing of the thruster terminal voltage is clearly visible in Figs. 4-1 through 4-3. The transition from a smooth voltage profile to an unstable one was abrupt.
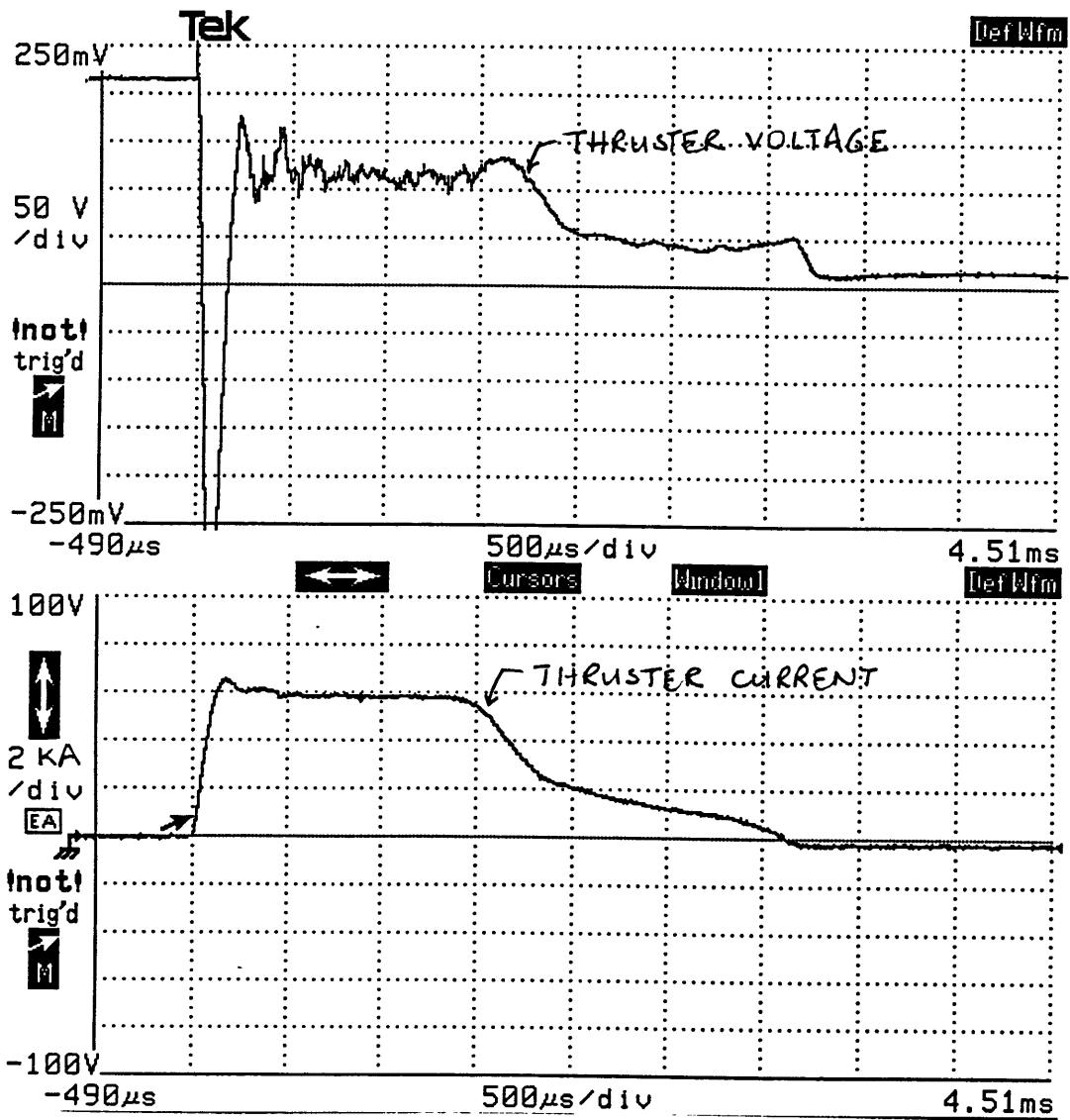
Figure 4-1: Onset Voltage and Current Profiles For .5 g/s (215 V PFN)
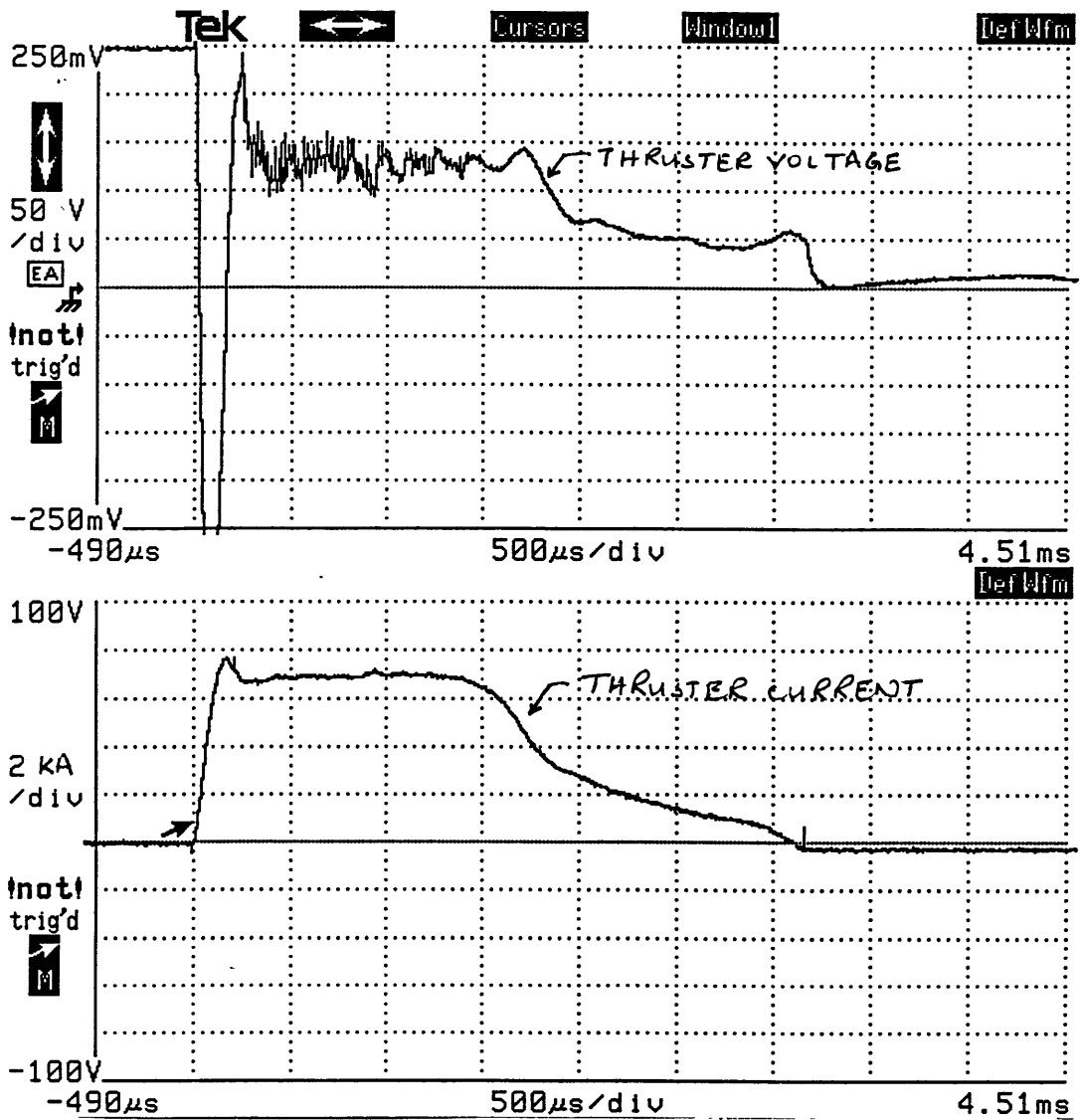
Figure 4-2: Onset Voltage and Current Profiles For 1.0 g/s (250 V PFN)
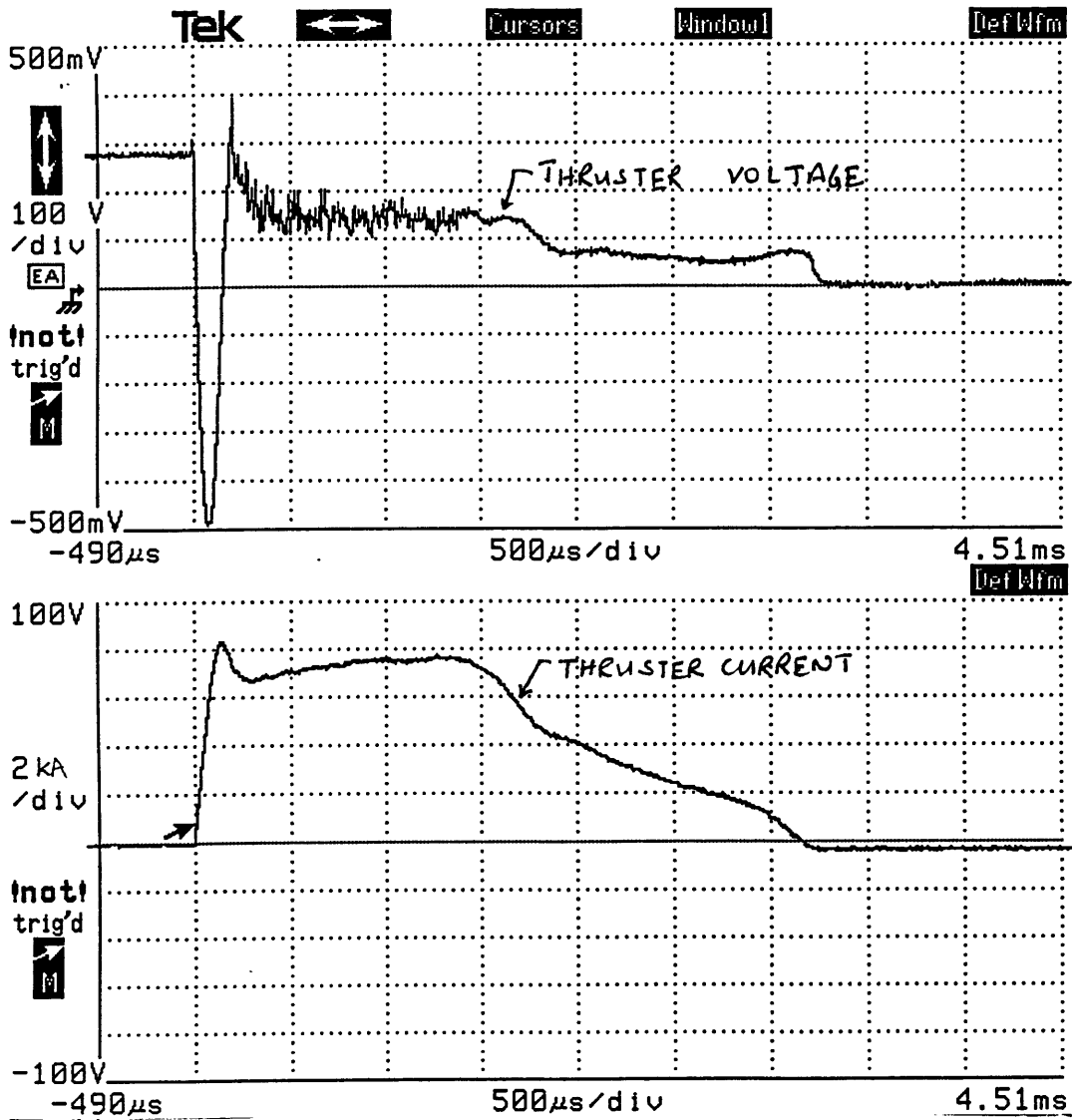
Figure 4-3: Onset Voltage and Current Profiles For 1.5 g/s (280 V PFN)
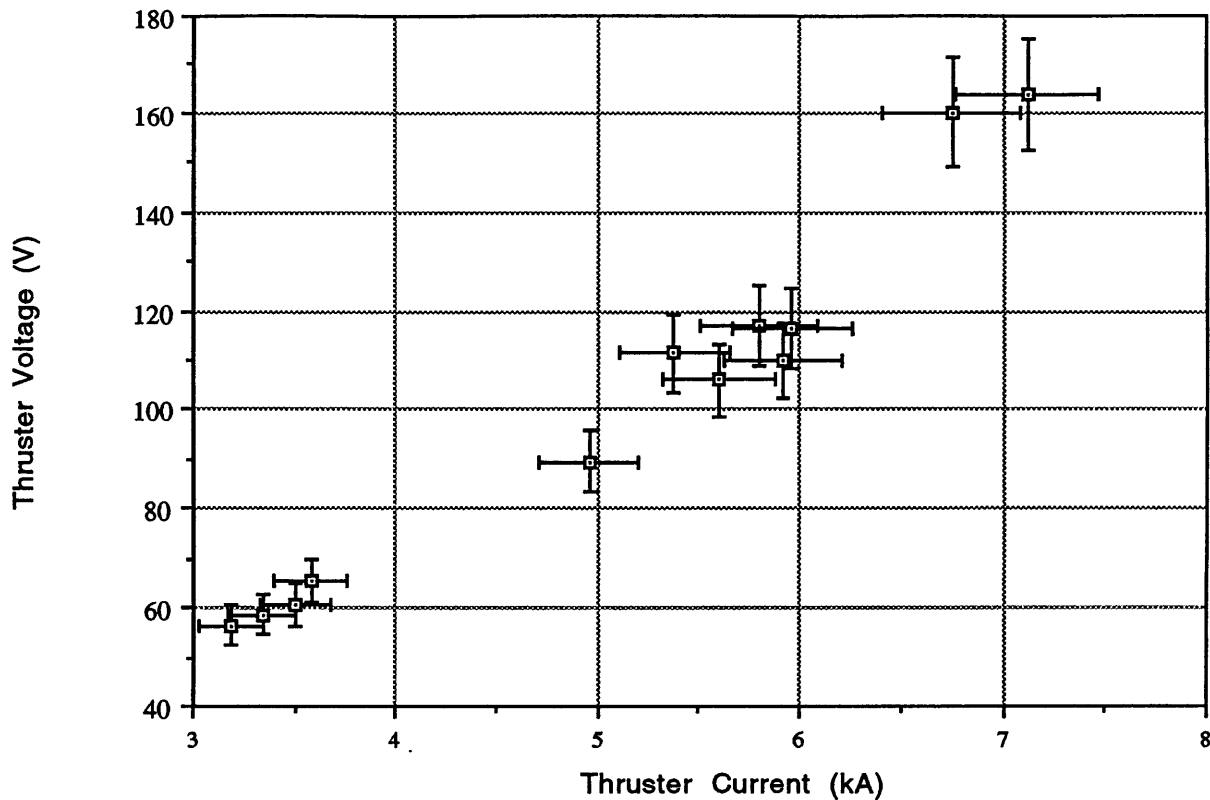
Figure 4-4: Voltage-Current Characteristics For The MPD At .5 grams/sec

For .5 grams per second case, for example, little or no hashing was seen at PFN voltage setting of 205 V, corresponding to 5.45 kA current level. At 215 V PFN (5.6 kA), however, the hashing had exceeded 10% of the total thruster voltage. The onset current levels were found to be 5.6 kiloamps, 6.2 kiloamps and 6.5 kiloamps ($\pm 5\%$) for .5, 1.0 and 1.5 g/sec flow rates, respectively.

The determined voltage-current characteristics for the three mass flow rates are shown in Figs. 4-4, 4-5 and 4-6.

The transition from a linear to a non-linear regime corresonding to a move from stable to unstable thruster operation is very apparent, especially for the 1.0 and 1.5 g/s cases. The thruster voltage and current values are accurate to within 5%. For increased measurement accuracy, the thruster was fired three times at each setting and the average of the three values for both the current and voltage was used for analysis purposes.

Researchers in the field have theorized that when the mass flow rate is too low
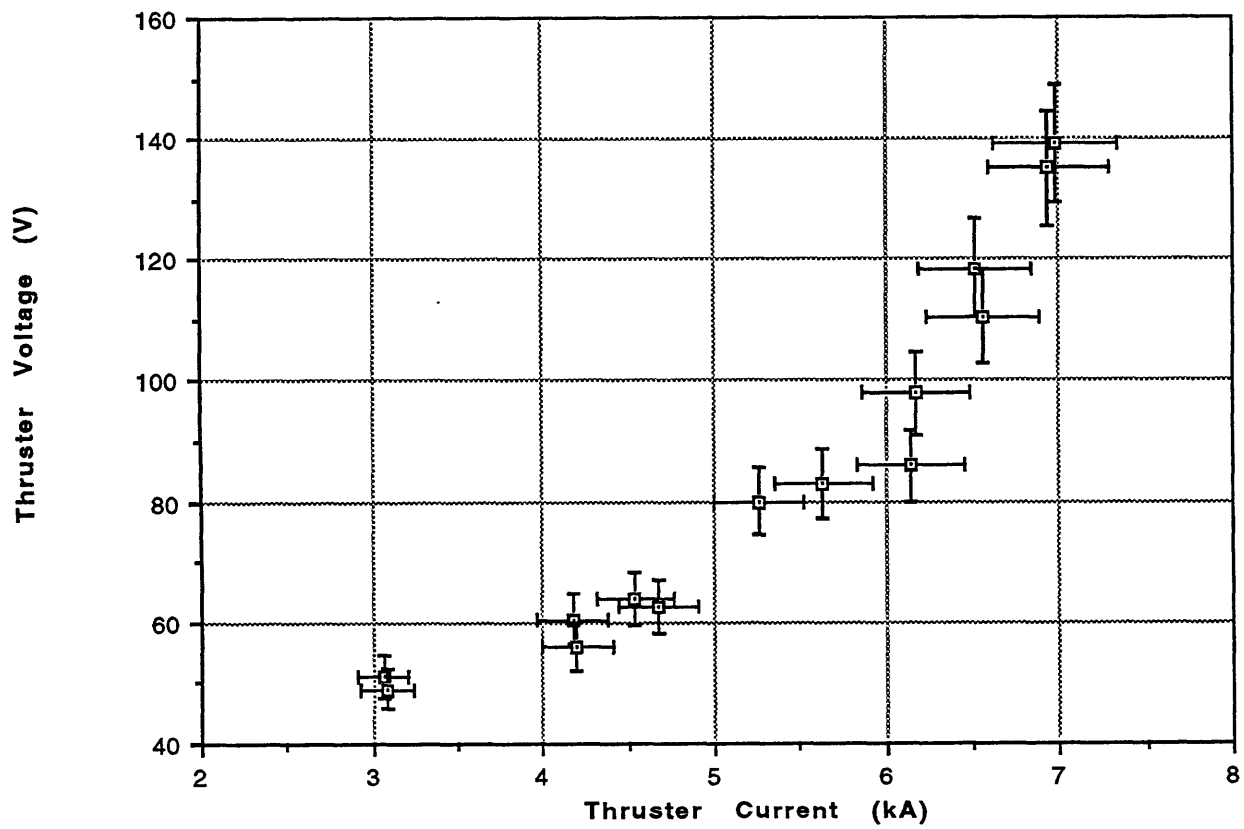
Figure 4-5: Voltage-Current Characteristic For The MPD At 1.0 grams/sec
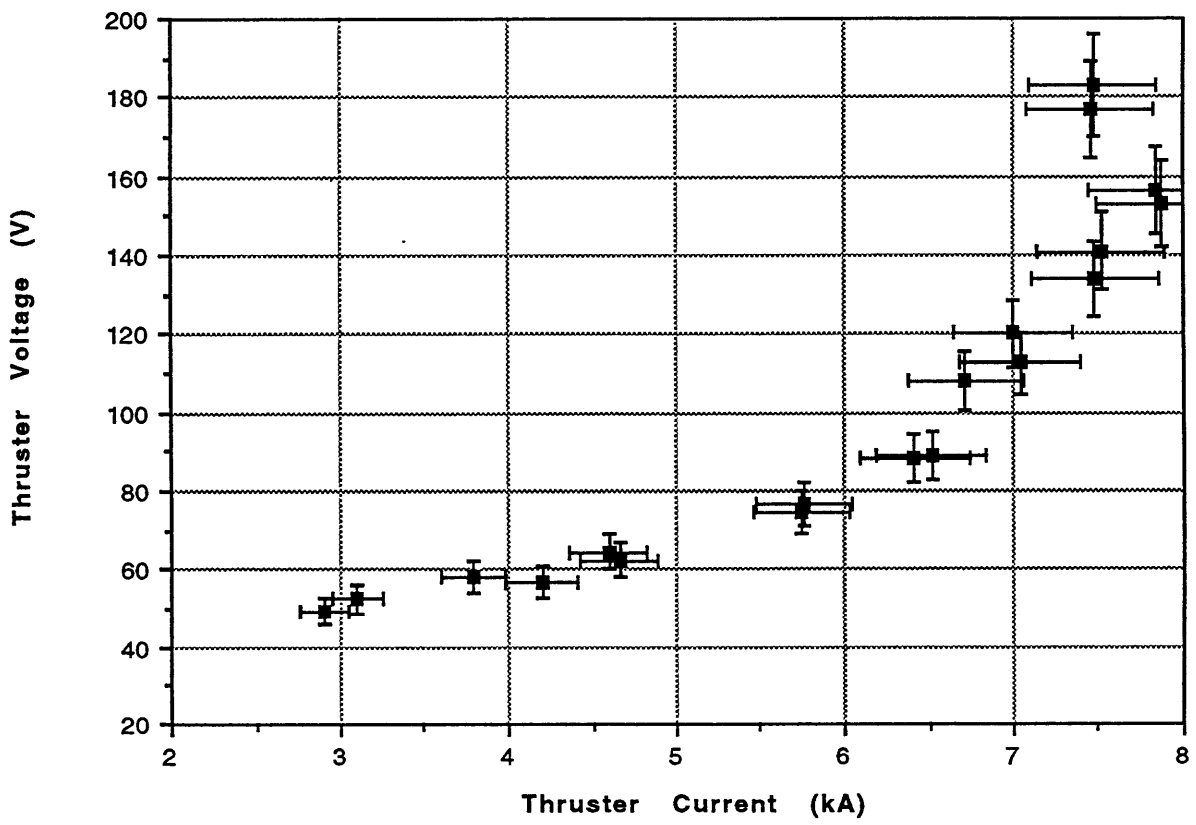
Figure 4-6: Voltage-Current Characteristic For The MPD At 1.5 grams/sec

for a given current ("underfed"), the flux of electrons from the adjacent plasma due to their thermal motion is inadequate to maintain the prescribed discharge current density. In this situation, according to Oberth[50], large electric fields (i.e. anode falls) form near the anode to enhance current conduction by both increasing the number of available current carriers through joule heating induced ionization, and by increasing the effective anode surface area (or conversely decreasing the prescribed current density). This effect, known as "anode starvation" has been described by other researchers as well [49, 56]. Since one of the primary goals of this investigation was to study the anode voltage drop through this anode starvation phenomenon, .5 grams per second was chosen as the mass flow rate for all probe measurements. Lower mass flow rate would in turn mean that the starvation regime of interest would be reached more quickly (i.e. at lower power level) than at higher flow rate. As mentioned previously, the criterion to be used for the triple probe and magnetic probe experiments was one where the anode drop as a fraction of the total thruster voltage exceeded 30%. Higher mass flow rates would result in that particular condition being satisfied at higher power levels which would result in greater physical damage and electrode erosion in the thruster.

The first set of experiments were conducted to determine the voltage drop as a fraction of the total thruster voltage. The results are described in the next chapter.

Chapter 5

Floating Probe Measurements

The initial set of probe experiments conducted were aimed at determining the near anode voltage drop. The physical limitation of the probe allowed the investigation to be done roughly 1 mm. from the anode surface. Time resolved local measurements of floating potential were obtained.

5.1 Anode Voltage Drop Results

The MPD thruster used in the experiments was 1.625 in. in length. Anode voltage drop experiments were conducted at 12 axial locations .125 in. apart. The thruster current was varied by varying the voltage on the Pulse Forming Network (PFN). The thruster was fired at eight different power levels corresponding to PFN voltage levels of 100, 125, 150, 160, 170, 180, 190, and 200 volts. The thruster current corresponding to the above PFN voltages was 2.2, 3.2, 4.4, 4.8, 4.9, 5.06, 5.11, and 5.34 kA, respectively. The thruster operation was kept below the onset level for .5 g/s determined previously to be 5.6 kA, to avoid damaging the electrodes. With the probe at each axial location, three shots were fired at each power level. The average of the three shots was used in the analysis. The random error associated with the repeatability of the data was ±5%. A typical floating probe signal is shown in Fig 5-1.

The goal of this set of experiments was to determine anode voltage drop as a
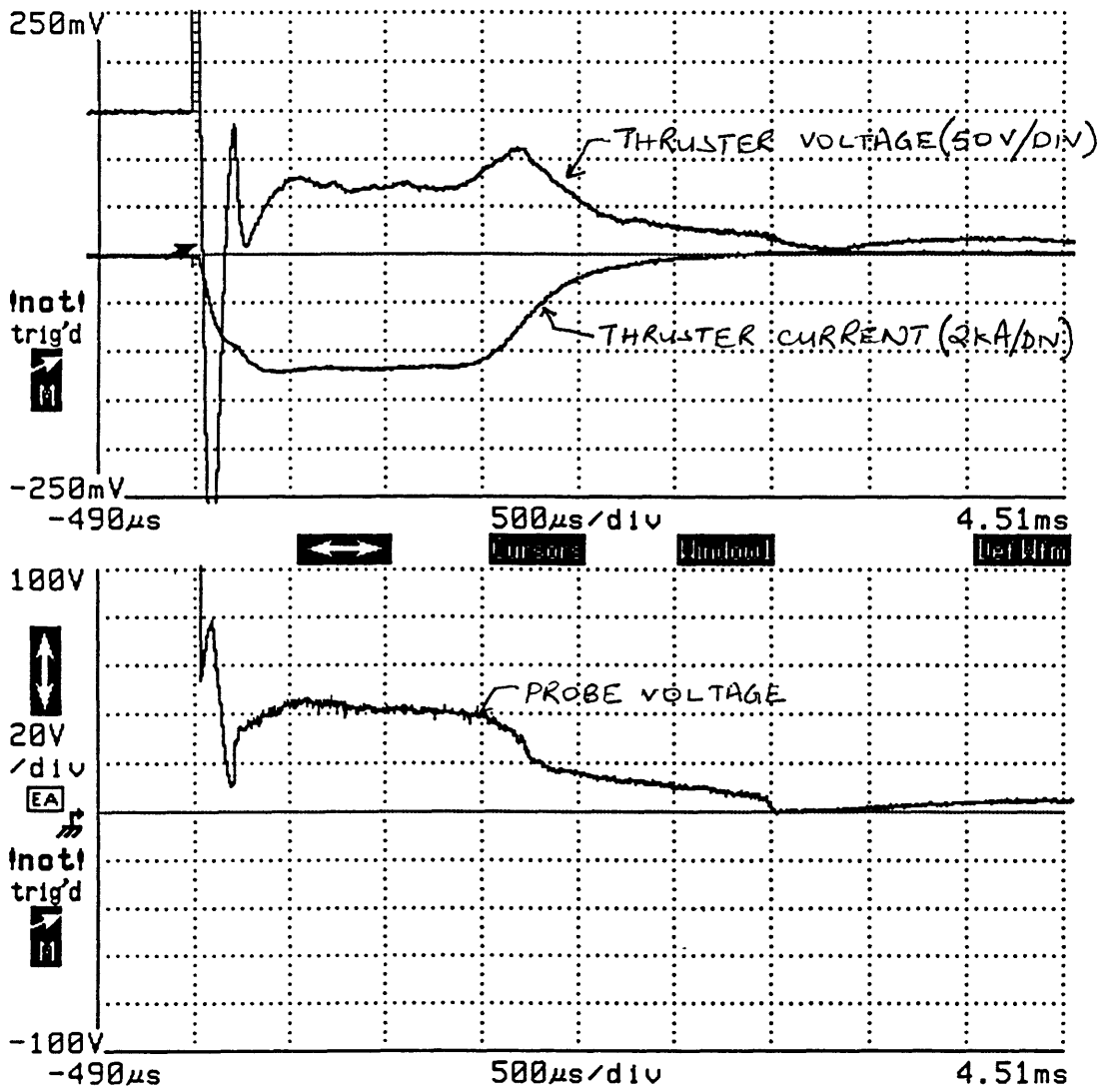
Figure 5-1: A Typical Floating Probe Signal
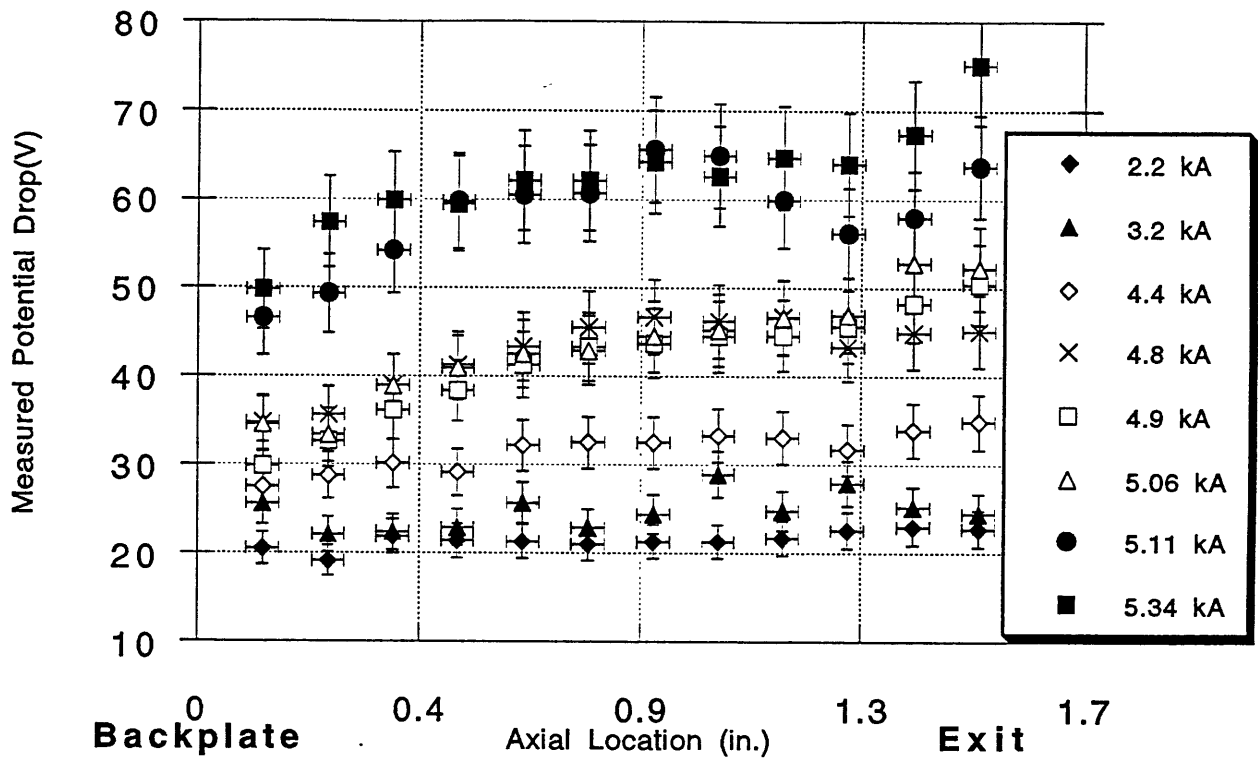
Figure 5-2: Near Anode Floating Potential Drop as a Function of Axial Location For Various PFN Voltages

function of increasing thruster current and determine an operating point where the anode drop rises rapidly.

The floating probe measurements as a function of axial location are shown below in Fig. 5-2. The plot represents the floating potential, not the plasma potential measurements, with respect to the anode.

Fig. 5-2 clearly shows a considerable jump in the floating potential drop between 150 V and 160 V PFN (4.4 and 4.8 kA) and again between 180 V and 190 V PFN (5.06 and 5.11 kA). As mentioned previously, an electron temperature correction is needed to convert from the floating potential measurement to the desired plasma potentials. Near anode electron temperature was acquired using a triple Langmuir probe and the results are described in the next chapter.

Knowing the near anode electron temperature, the correction was applied to the floating potentials. The axial anode voltage drop profiles are shown for the various current levels in Figs. 5-3 through 5-6.
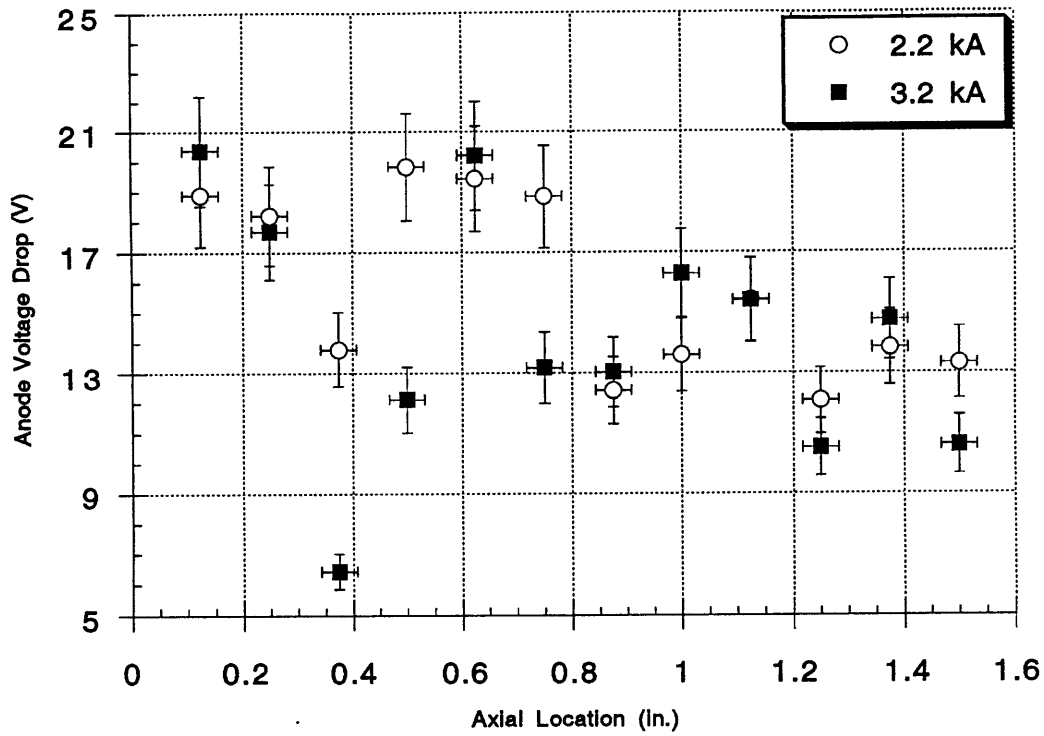
Figure 5-3: Near Anode Axial Voltage Drop Profiles for 2.2 and 3.2 kA
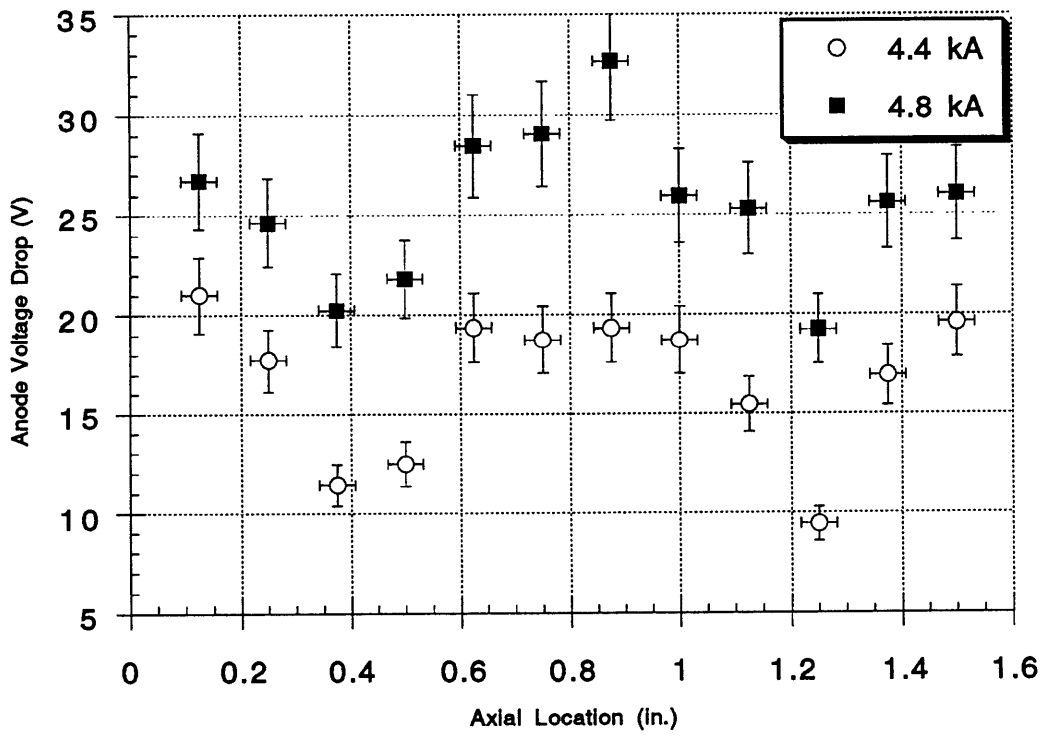
Figure 5-4: Near Anode Axial Voltage Drop Profiles for 4.4 and 4.8 kA
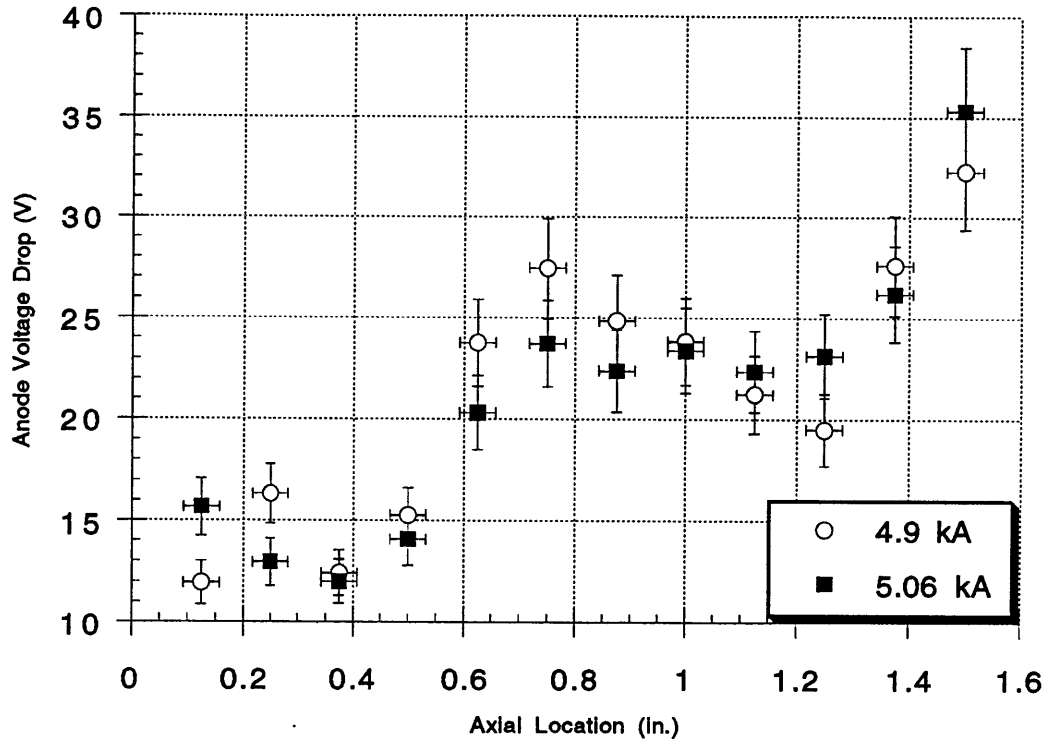
Figure 5-5: Near Anode Axial Voltage Drop Profiles for 4.9 and 5.06 kA
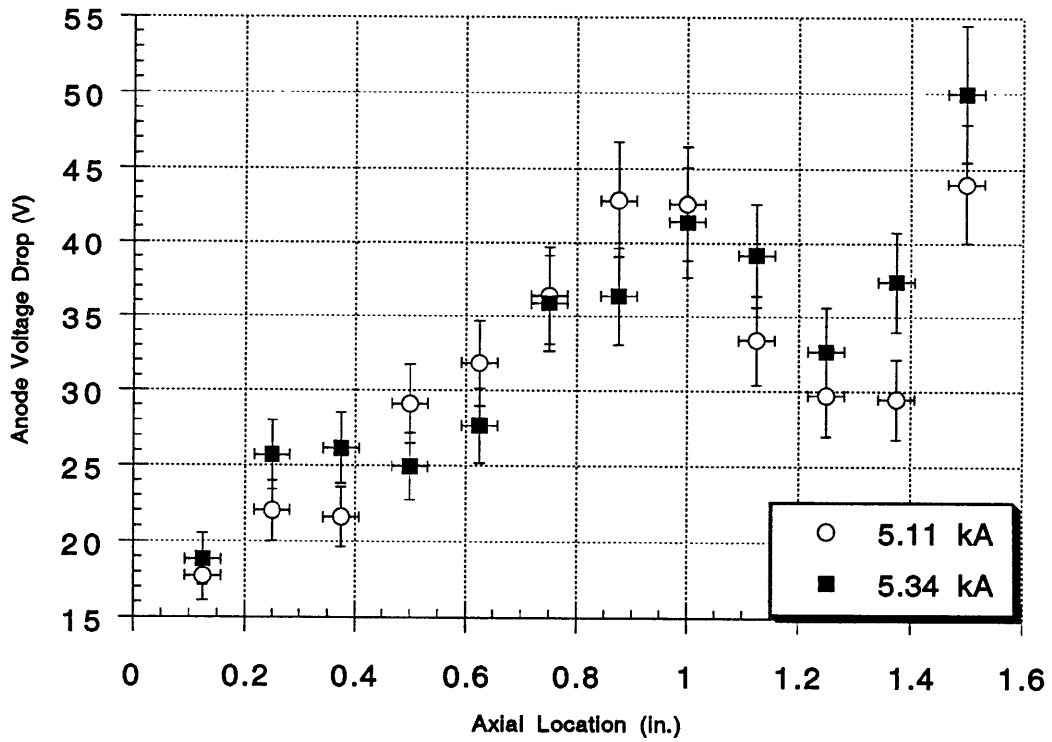
Figure 5-6: Near Anode Axial Voltage Drop Profiles for 5.11, 5.34 kA

73

PFN V	Thr. Volt.	Thr. Curr.	ΔV	$\Delta V/Vth$ (%)
100	65.5	2.17	15.8	24.1
125	74.9	3.21	14.2	19.0
150	76.0	4.40	16.7	21.98
160	84.9	4.80	25.5	30.0
170	88.3	4.90	21.4	24.2
180	94.3	5.06	20.95	22.2
190	103.7	5.11	31.7	30.61
200	110.7	5.34	33.0	29.8

Table 5.1: Summary of Floating Probe Results

The anode drop decreased substantially at .375 in. and 1.25 in. from the backplate for all current levels. That drop was not apparent in the floating potential drop profiles shown in Fig. 5-2, however. The reason for the drastic difference between the floating and the plasma axial profiles is due to the extremely high electron temperatures measured at the two axial locations, thereby increasing the correction factor to the floating potential measurements.

Figures 5-7 through 5-18 show the anode voltage drop as a function of increasing thruster current at all twelve axial locations. The plots show a noticeable increase in the anode voltage drop as a function of increasing thruster current. A jump in the anode voltage drop can be seen between 4.4 kA and 4.8 kA and again between 5.06 kA and 5.11 kA current levels at most axial locations.

The voltage drops seen were a significant fraction of the total thruster voltage. The results obtained from the near-anode floating probe experiments are summarized in Table 5.1.

The values for the anode voltage drops in the table above are axial averages of the

74
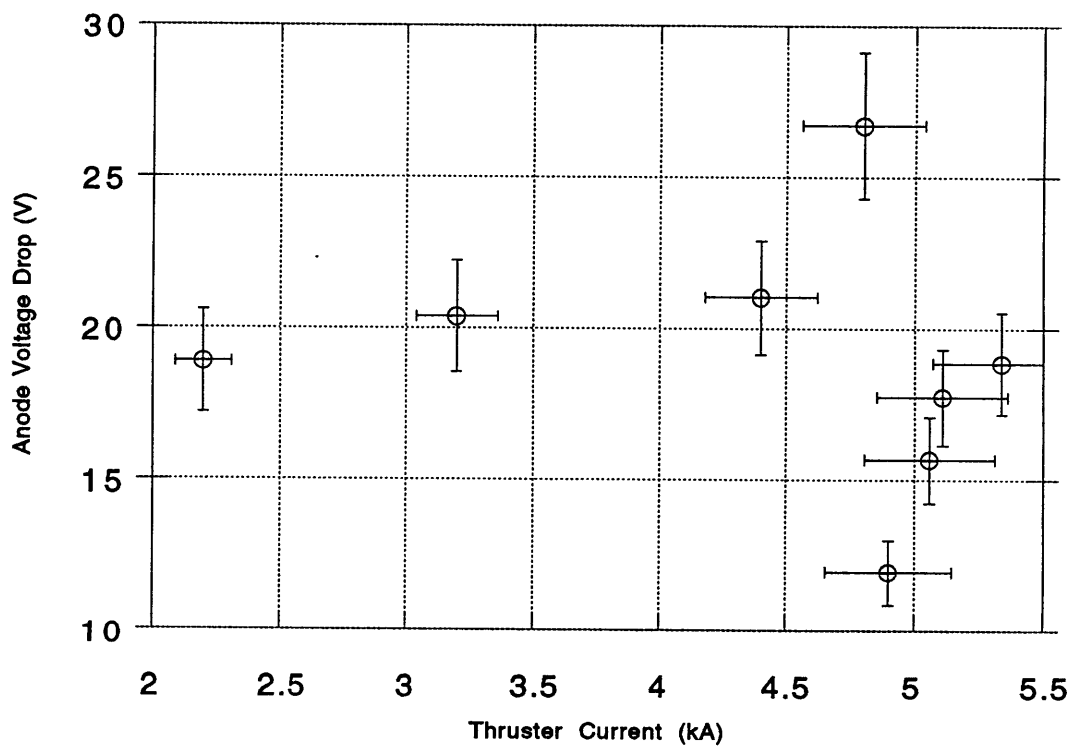
Figure 5-7: Near Anode Voltage Drop as a Function of Thruster Current at .125 in. From The Backplate
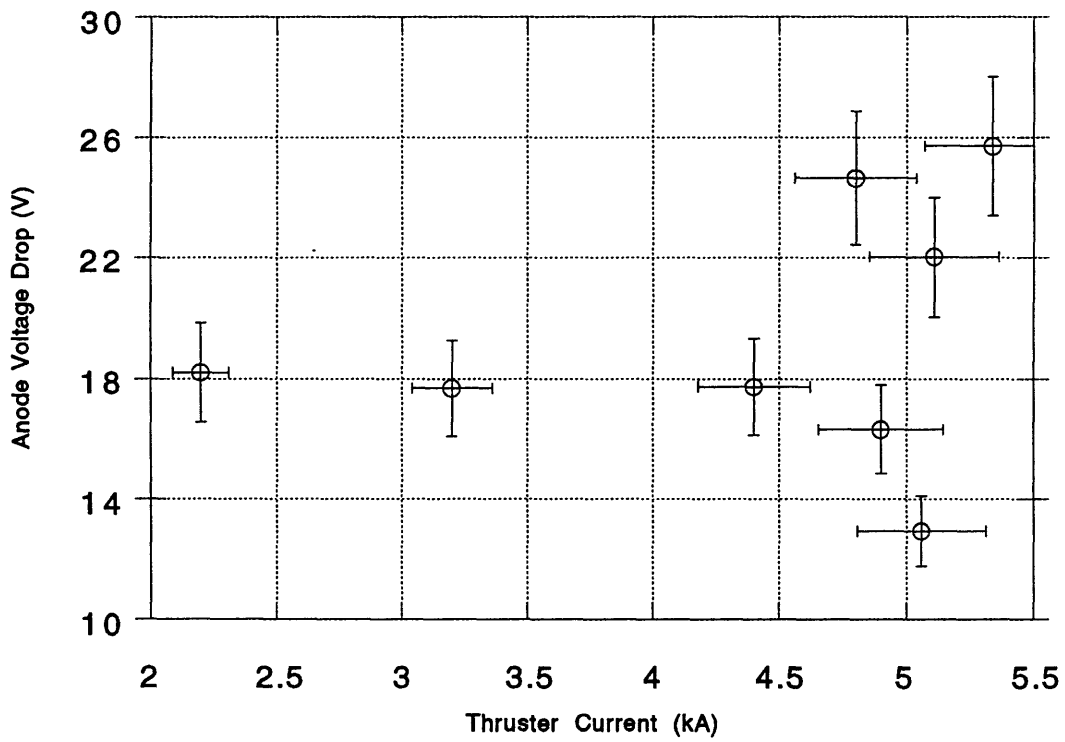
Figure 5-8: Near Anode Voltage Drop as a Function of Thruster Current at .25 in. From The Backplate
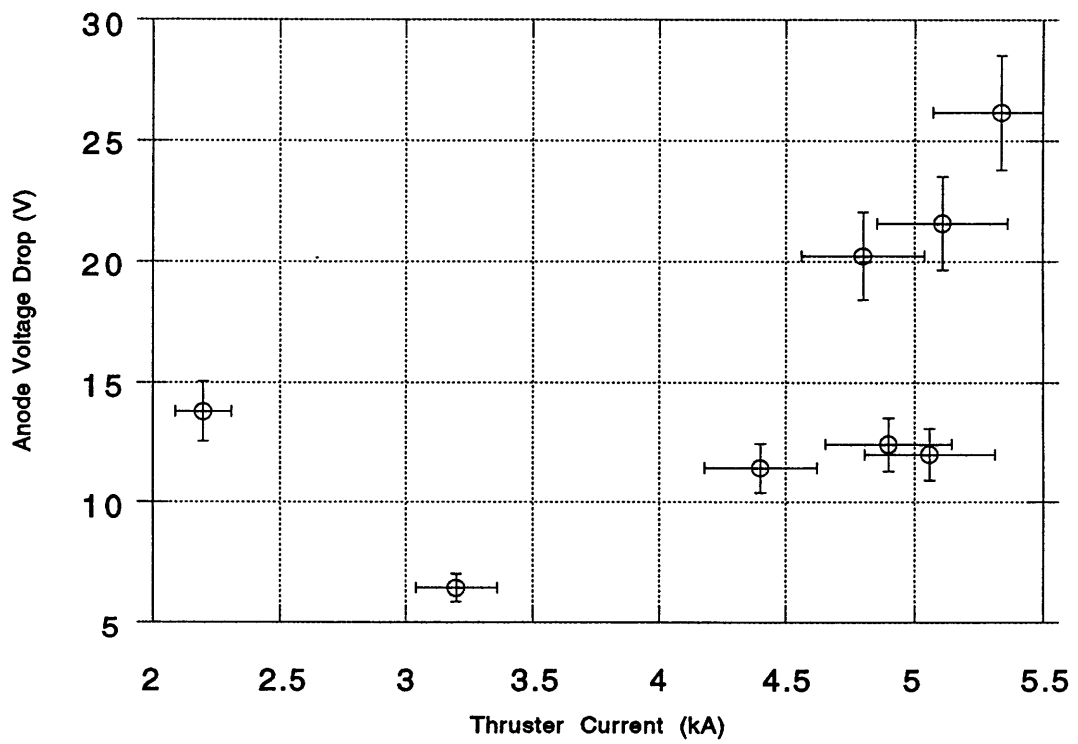
Figure 5-9: Near Anode Voltage Drop as a Function of Thruster Current at .375 in. From The Backplate
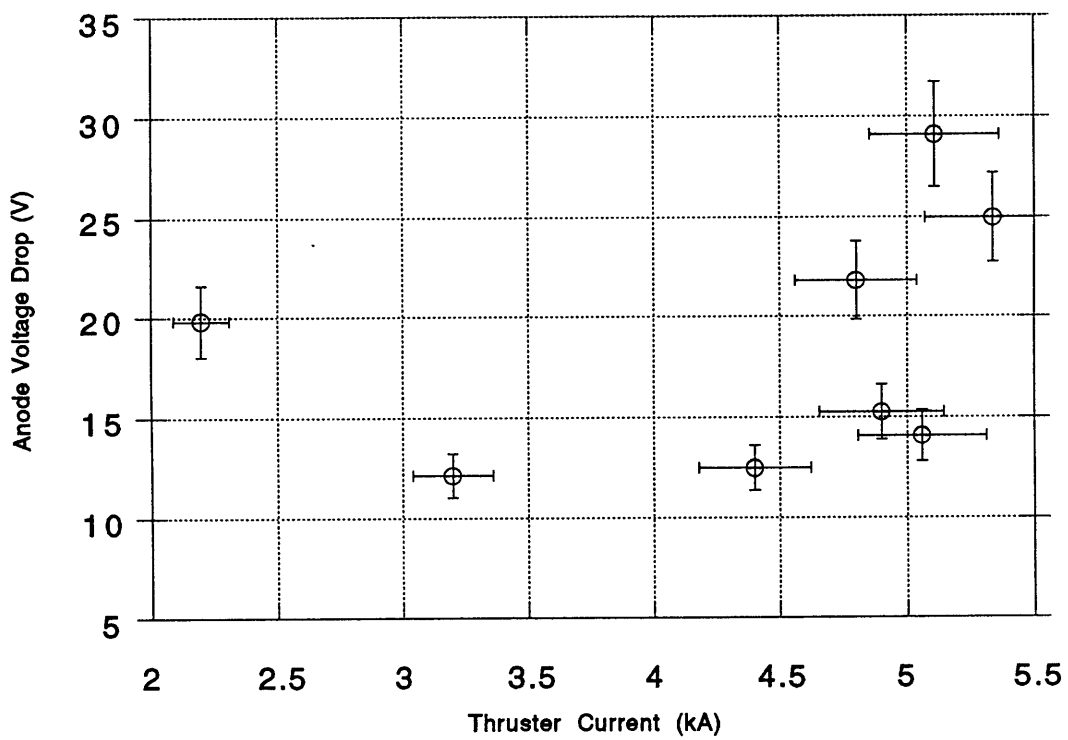
Figure 5-10: Near Anode Voltage Drop as a Function of Thruster Current at .50 in. From The Backplate

78
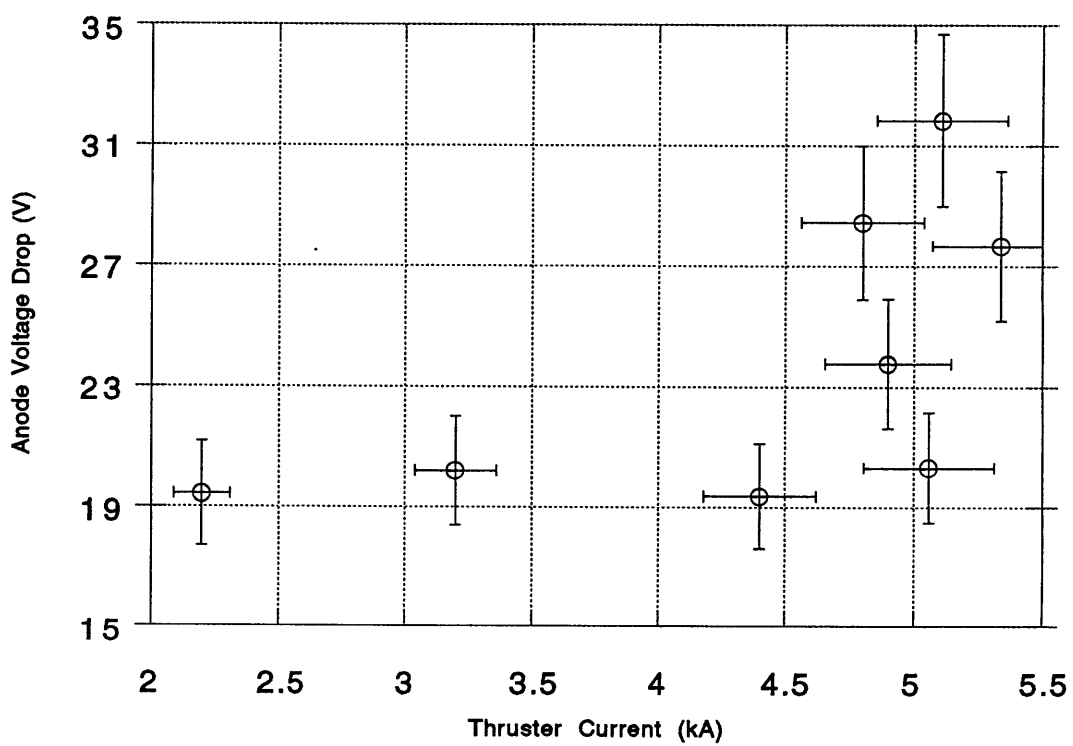
Figure 5-11: Near Anode Voltage Drop as a Function of Thruster Current at .625 in. From The Backplate
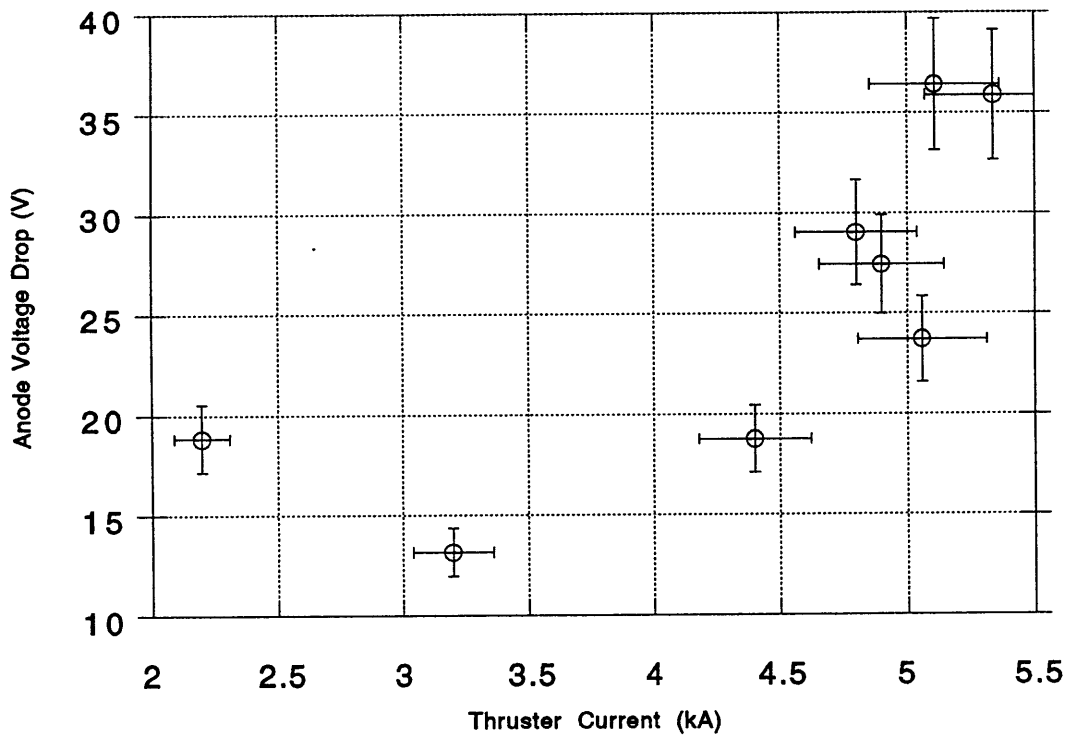
Figure 5-12: Near Anode Voltage Drop as a Function of Thruster Current at .75 in.
From The Backplate
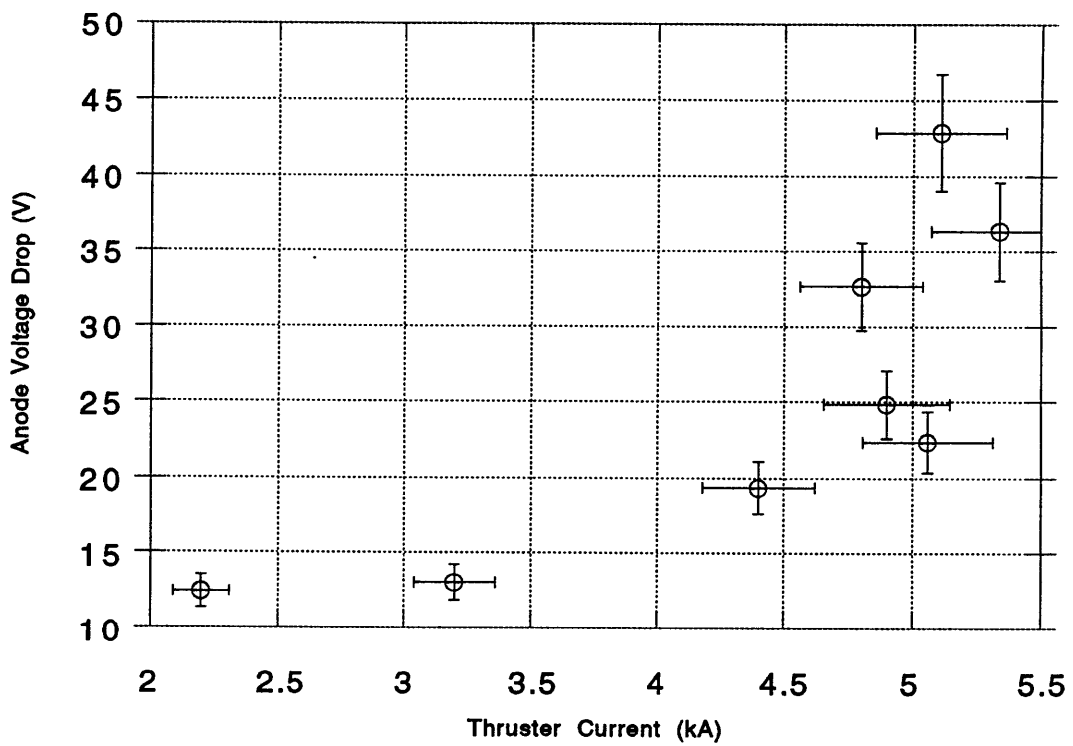
Figure 5-13: Near Anode Voltage Drop as a Function of Thruster Current at .875 in. From The Backplate
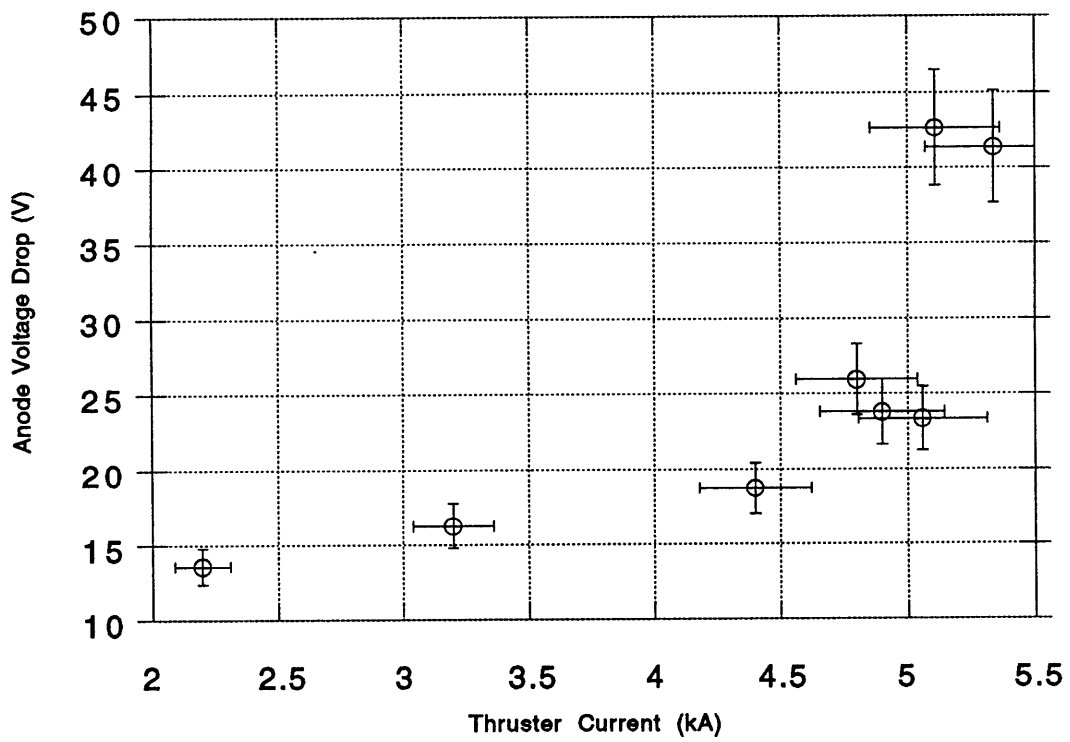
Figure 5-14: Near Anode Voltage Drop as a Function of Thruster Current at 1.0 in. From The Backplate
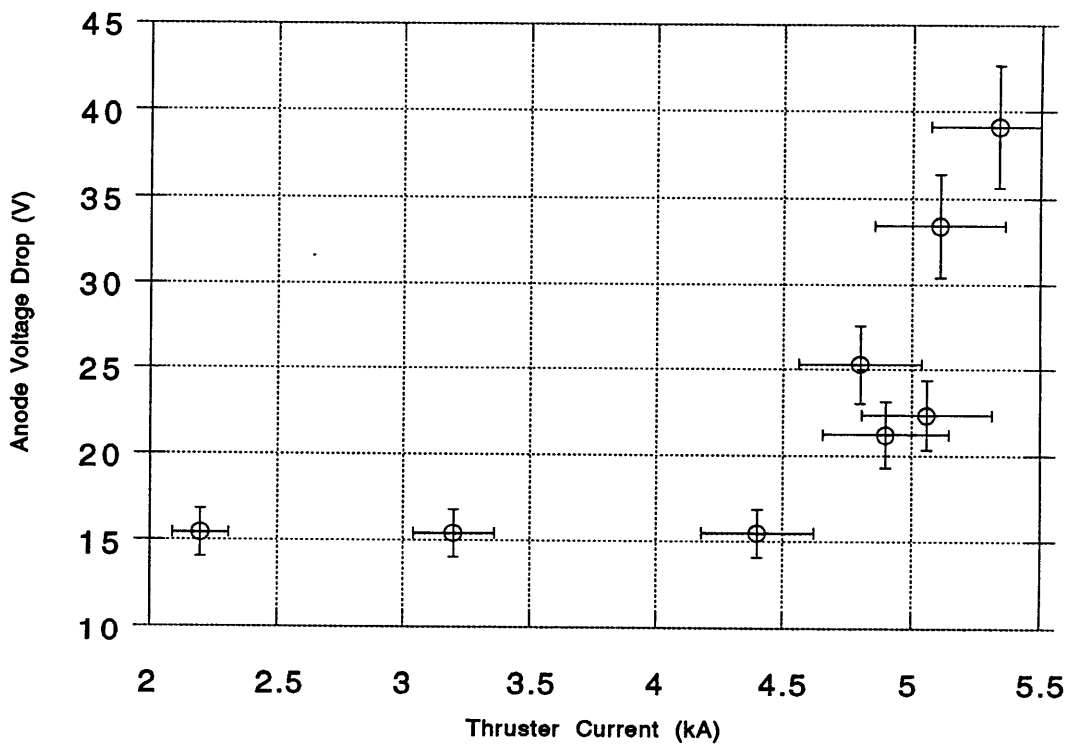
Figure 5-15: Near Anode Voltage Drop as a Function of Thruster Current at 1.125 in. From The Backplate
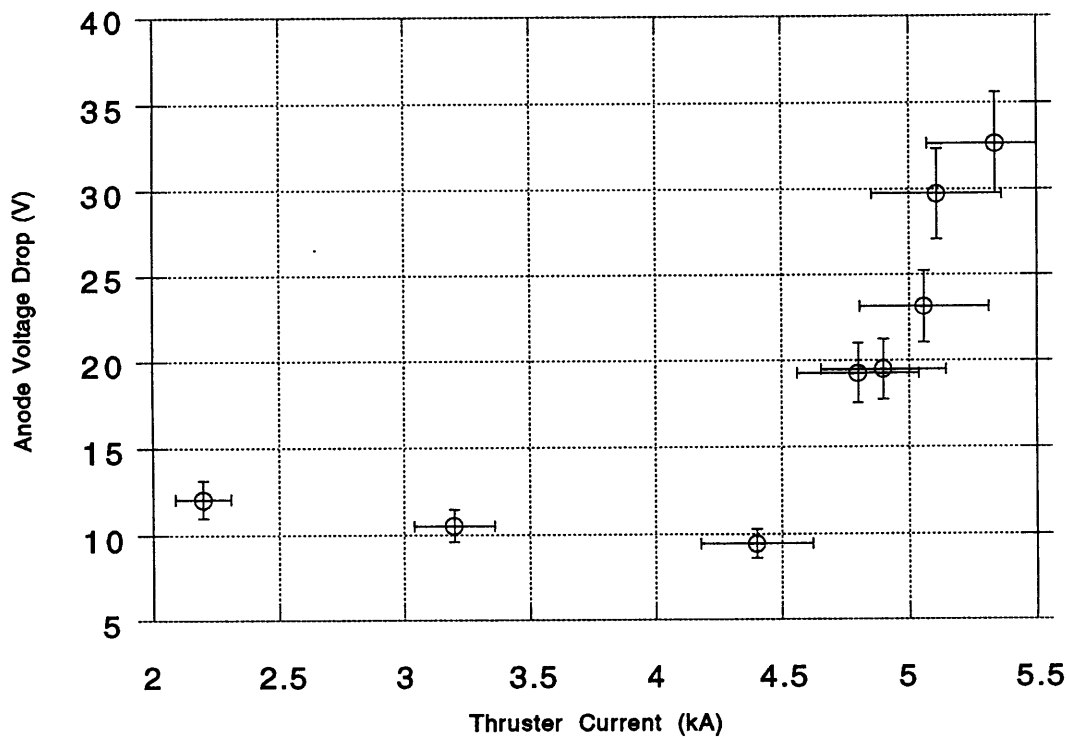
Figure 5-16: Near Anode Voltage Drop as a Function of Thruster Current at 1.25 in. From The Backplate
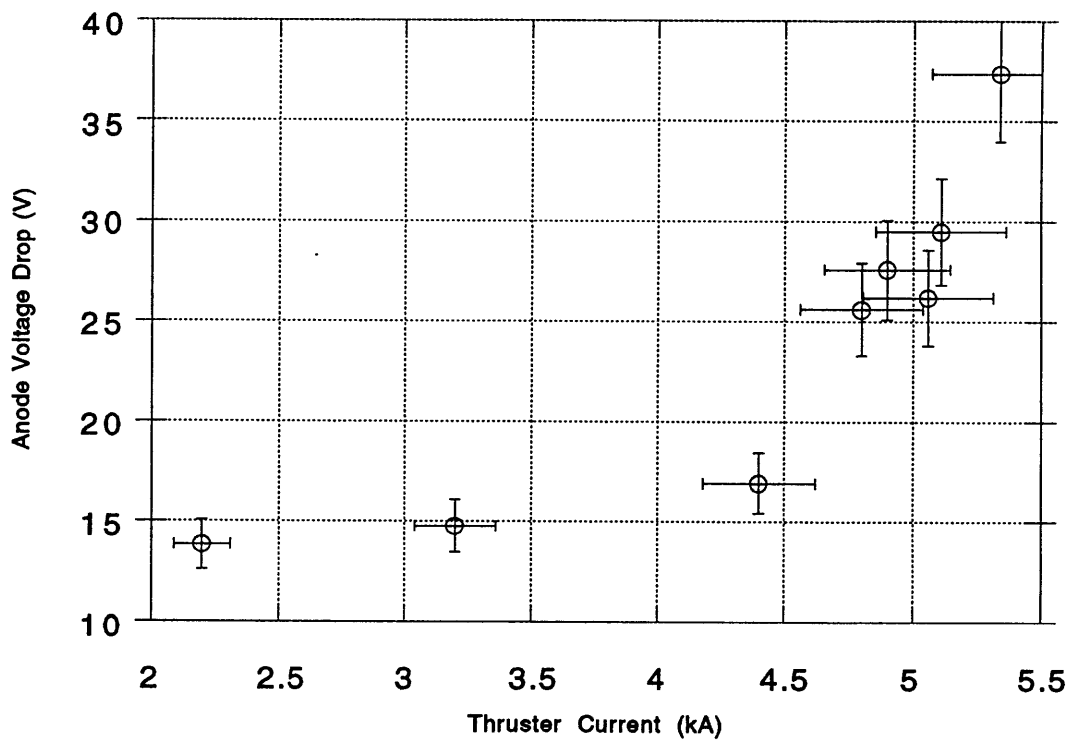
Figure 5-17: Near Anode Voltage Drop as a Function of Thruster Current at 1.375 in. From The Backplate
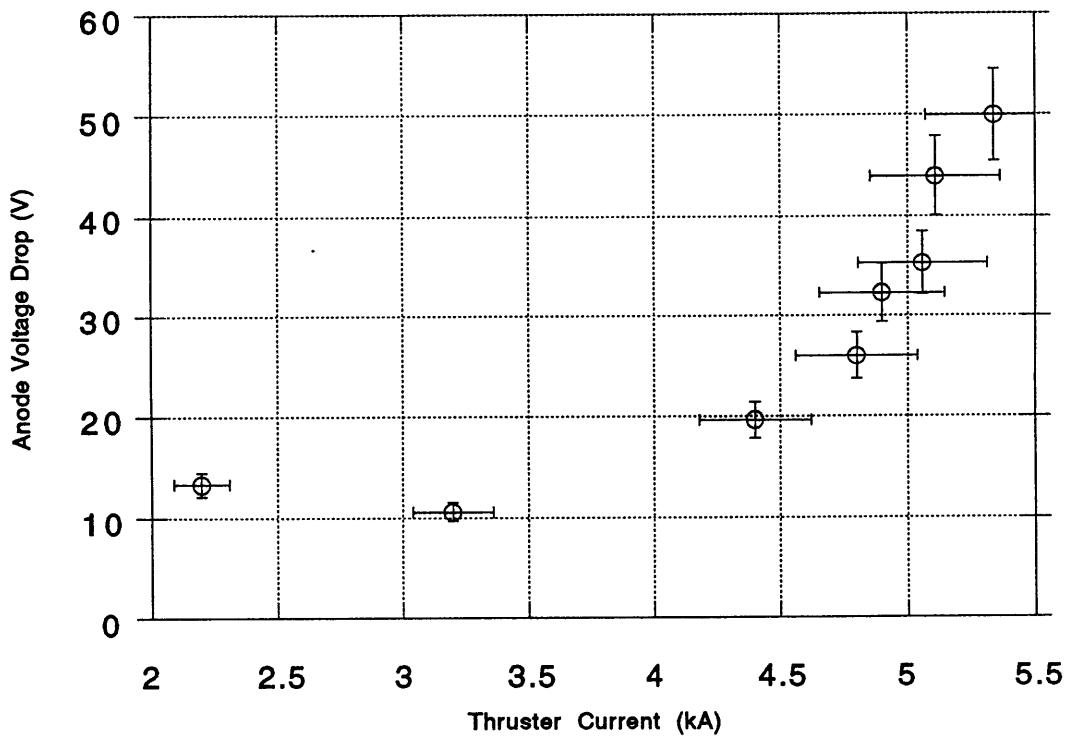
Figure 5-18: Near Anode Voltage Drop as a Function of Thruster Current at 1.5 in. From The Backplate

measured voltage drops at the twelve axial locations. The axial variation in the voltage drops is therefore not detectable in the table. An increased hashing of the probe signal was observed with increasing current level, even though the thruster voltage trace was relatively smooth. The hashing could be a result of probe contamination or a sheath effect. Time averaged values of the floating probe signal were used in the analysis. The measured floating potential drops varied from 21.5 volts for 100 V PFN (2.2 kA) to 57.2 V for 200 V PFN (5.34 kA). The electron temperature correction factor resulted in the corresponding plasma potential variation from 15.8 V for 100 V PFN to 33.0 V for 200 V PFN.

The measured anode drop was seen to be drastically different at different axial locations within the thruster as a function of thruster current. Near the backplate, the anode drop showed similar values at the lowest and highest current levels (18.9 V for 100 V PFN (2.2 kA) to 18.85 V for 200 V PFN (5.34 kA), respectively). It increased sharply, however, at the 160 V PFN (4.8 kA) level. For higher current levels (4.9 kA and above), however, a difference of 20 V or more was seen between the voltage drop values near the backplate and the exit. At 200 V PFN (5.34 kA), for example, the anode drop varied from 18.85 V near the backplate to 50 V near the exit. In the middle of the thruster, however (.5 in. to 1.0 in.), the voltage drop rose with thruster current until 160 V PFN (4.8 kA). The voltage decreased thereafter at 170 and 180 V PFN (4.9 and 5.06 kA, respectively) followed by another sharp increase in the voltage drop at 190 V PFN (5.11 kA). At the near-exit axial locations (1.25 in., 1.375 in. and 1.5 in.), the anode voltage drop increased considerably with thruster current. At the 1.5 in. axial location, the anode drop rose from 13.3 V at 2.2 kA to 50 V at 5.34 kA, showing an anode fall jump between 150 V and 160 V PFN and again between 180 V and 190 V PFN. This particular behavior indicates that the mechanism(s) for the anode fall magnifies with current everywhere except near the backplate region of the thruster.

An interesting contrast was seen for anode fall axial variation with current. For lower current levels (2.2 kA to 4.8 kA), the axial anode voltage drops stayed roughly constant, the exception being the .375 in. and 1.25 in. axial locations where a sub-
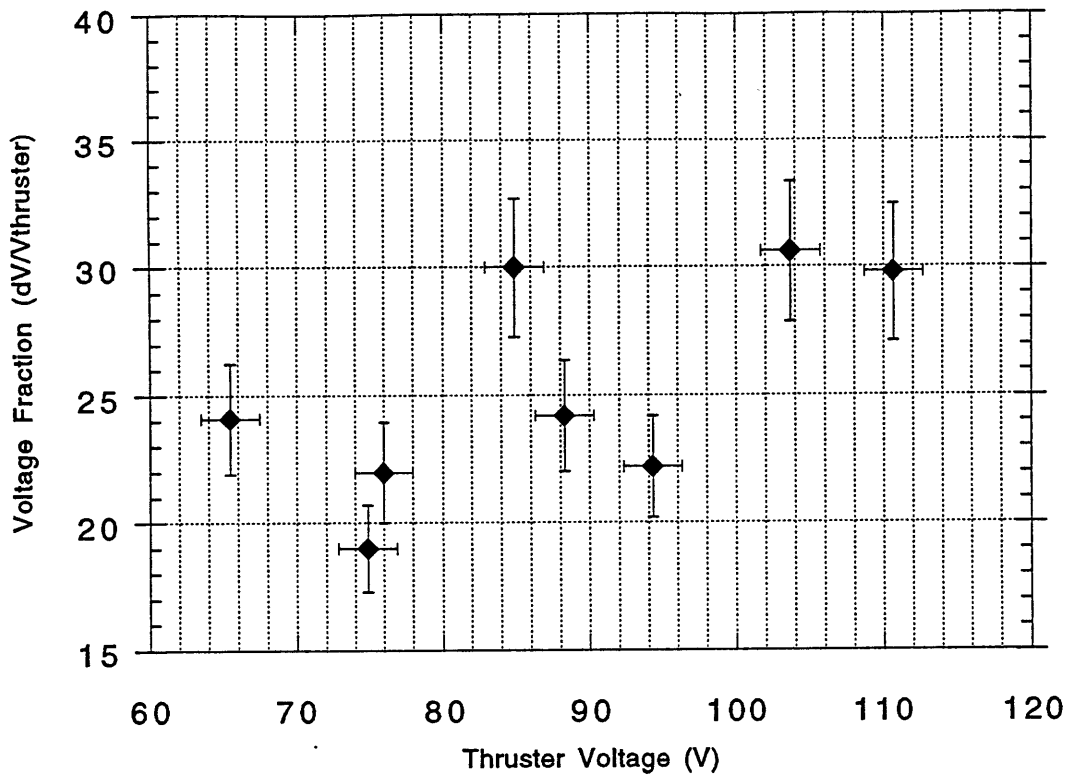
Figure 5-19: Anode Voltage Fraction as a Function of Thruster Current

stantial drop was observed due to the unusually high electron temperature correction. Higher current levels, however, showed a large axial anode fall variation.

More important than the magnitude of the voltage drop was the anode voltage fraction, i.e. the fraction of the total thruster voltage that is dissipated near the anode (i.e. the anode fall). Fig. 5-20 shows the anode voltage fraction as a function of thruster current identifying the two regions of anode fall increase (4.8 kA and 5.11 kA).

The voltage fraction jumped from 22.0% at 4.4 kA to 30.0% at 4.8 kA and then again from 22% at 5.06 kA to 30.6% at 5.11 kA.

5.2 Discussion of Near-Anode Results

Floating potential measurements obtained at 12 axial locations with the probe placed 1 mm from the anode surface yielded considerable anode drops at all current levels along with substantial axial variation in the anode drop profiles.

For the two lowest thruster current levels (2.2, 3.2 kA), the measured floating potential drop remained relatively constant throughout the axial traverse. At higher power levels (> 4.8 kA) however, a ramp in the voltage drop was observed between the Boron Nitride backplate and .5 in. from the backplate. The voltage drop near the backplate was considerably lower than .5 in. downstream from it. This could be due to lower temperatures near the inlet due to incoming cold gas, leading to a higher collision frequency ($\nu_e \sim T_e^{-3/2}$) and consequently a smaller Hall parameter in the region. The Hall parameter, as mentioned in an earlier chapter, is a measure of the tendency of the current to flow perpendicular to both electric and magnetic fields. With a smaller Hall parameter and lower resulting Lorentz pumping force, however, current flows radially and starvation is not induced in the region near the backplate. In addition, the insulating backplate itself forces j to be radial close to it.

Figures 5-7 through 5-18 show three particular phenomena of interest. Firstly, for current levels under 4 kA, very little change in the voltage drop is observed with axial variation; secondly, at axial locations under 1.25 in., a noisy transition is seen from relatively low anode fall to a much higher one. From 4.4 kA to 4.8 kA, a sharp rise was seen, dropping to a minimum at roughly 5 kA and rising sharply again at higher current levels. A third phenomenon was present from 1.25 in. axial location to the exit where a rapid rise in the anode fall was observed beyond the 4.4 kA level. No drop in the anode fall was apparent at 5.06 kA level as was the case in the mid-thruster axial locations. From the three different anode fall characteristics described above, it seems that under 4kA, the anode is not "depleted", and the ΔV_a is due to regular ohmic and sheath drops. Current levels higher than 5 kA, however, definitely correspond to a depleted or starved anode condition axially everywhere. A transition, although messy, does take place between 4 kA and 5 kA where both non-depleted (low anode fall) and depleted (high anode fall) regions are present.

At high power levels (> 4.4 kA), yet another ΔV ramp was noticed near the exit plane of the thruster. The voltage drop rose considerably from 1.25 to 1.5 in. axially from the backplate. This may be artificial due to the mechanical design of the thruster. The lip of the anode is rounded. As a result, during the near anode
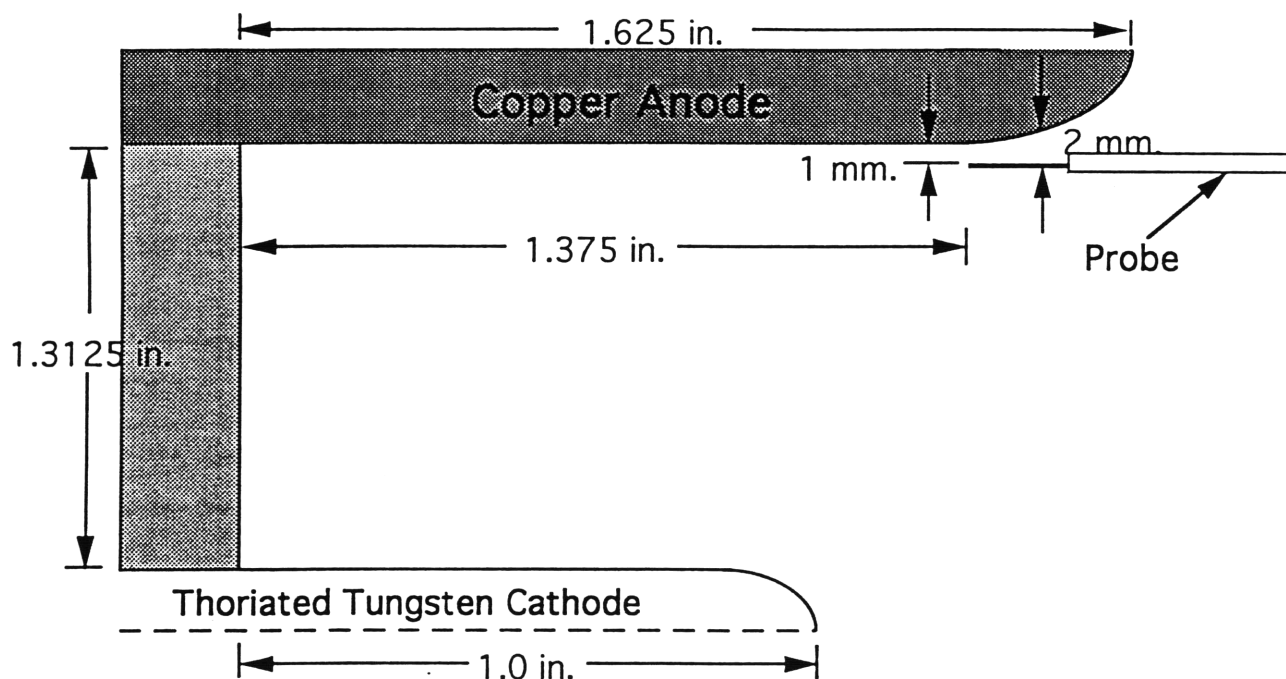
Figure 5-20: Near Exit Plane Probe Measurement Error

axial traverse near the exit plane, the probe was actually farther than 1 mm. from the anode as shown in Fig. 5-19.

The increased distance from the anode resulted in artificially high floating potential drops and subsequently high anode drops near the exit plane. Strangely enough, however, this behavior was observed only at high power levels ($>$ 150 V PFN). Since the thruster geometry is the same for all shots, some other plasma parameter must induce the increase in voltage drop near the exit. The Hall parameter has been related to the anode fall by Gallimore [22]. This may be the cause of the anode fall increase in the region.

The floating probe anode drop measurements were used as a gauge for the determination of an adequate operation point for the triple probe and magnetic induction probe experiments. This operating condition was determined to be 160 V PFN (4.8 kA) corresponding to the first voltage fraction jump in Fig. 5-20. Langmuir triple probe, induction probe and radial floating probe experiments were conducted at two power levels, however, corresponding to 150 V and 160 V PFN (4.4 and 4.8 kA, re-

90

spectively). The near-anode floating probe measurements indicated that a transition in the thruster behavior was taking place as the thruster current was increased from 4.4 kA to 4.8 kA. It was important, therefore, to monitor the plasma parameters of interest, namely electron temperature, electron density and enclosed current both before and after the transition. The idea was to see whether a sudden change in the near anode voltage drop behavior corresponded to an overall change in the MPD parameters through the bulk of the thruster.

5.3 Radial Plasma Potential Measurements

The second set of experiments with the floating probe involved radial traverses at three axial locations, .23 in., .98 in. and 1.47 in. ($\pm$.015) with reference to the exit plane. The measurements were conducted at eight radial locations separated by .15 in. ($\pm$.015) at 4.4 kA and 4.8 kA with Argon flowing at .5 g/sec. Once again, as with the anode fall measurements, the probe was referenced with respect to the anode. The electron temperature measurements acquired with the triple probe at the same radial and axial locations were used to determine the plasma potentials from the measured floating potentials.

The measured radial plasma potential profiles at the three axial locations for both 4.4 kA and 4.8 kA are shown in Figs 5-21 and 5-22, respectively.

The overall plasma potential profiles were roughly the same for both current levels. The near electrode voltage drops are summarized in the Table 5.2.

During the radial traverses, near electrode measurements were conducted with the probe approximately .125 in. ($\pm$.015) away. The cathode drop in the mid-thruster and near backplate axial locations was much greater than the anode drop. At 4.4 kA, the cathode voltage drop was 34.8 V ($\pm$2) near the backplate and 42.9 V ($\pm$2) at the mid-thruster location. The anode drop was found to be 6.2 V ($\pm$2) near the backplate and 18.1 V ($\pm$2) at the mid-thruster location. The corresponding cathode drops for 4.8 kA were 38.3 V and 43.7 V ($\pm$2) at the mid-thruster and near-backplate locations, respectively. The anode drops in this case are slightly larger than those
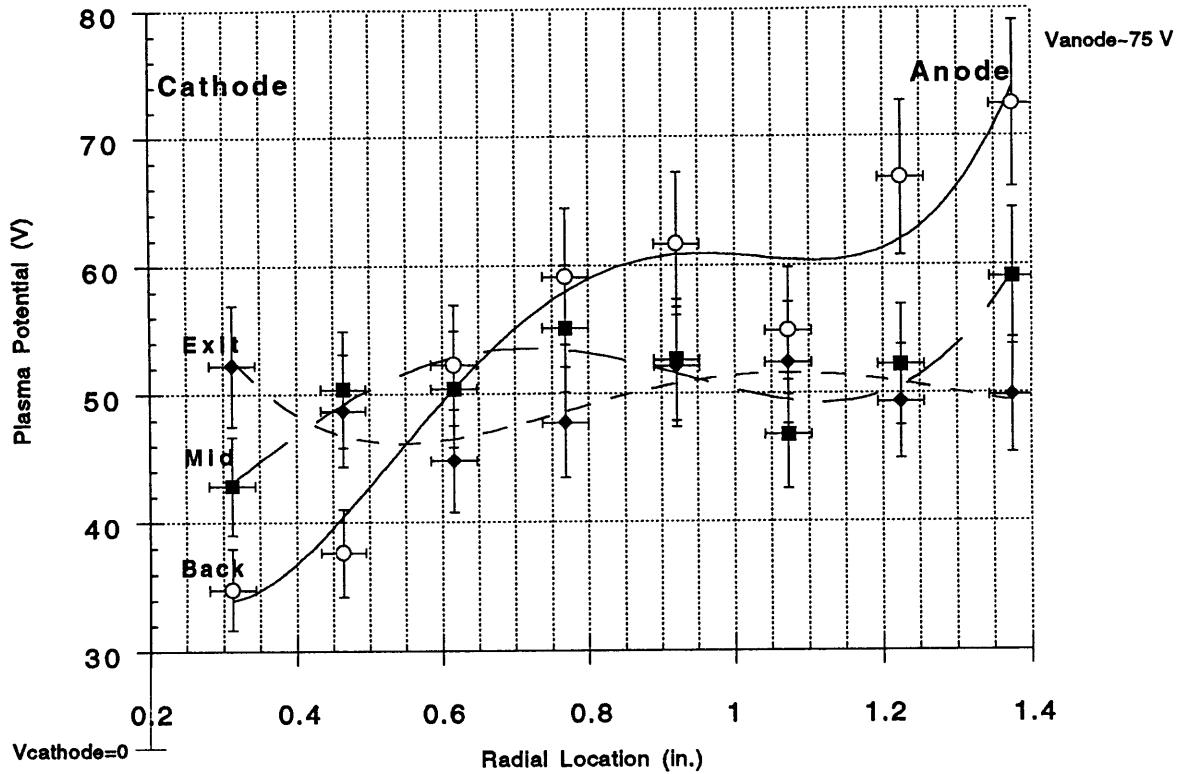
Figure 5-21: Radial Plasma Potential Measurements at Three Axial Locations For 4.4 kA

	Anode-back	Anode-mid	Anode-exit	Cathode-back	Cathode-mid
4.4 kA	6.2	18.1	25.36	34.81	42.85
4.8 kA	11.35	21.1	35.32	38.33	43.42

Table 5.2: Electrode Drops At Three Axial Locations For 4.4 kA and 4.8 kA During The Radial Traverse
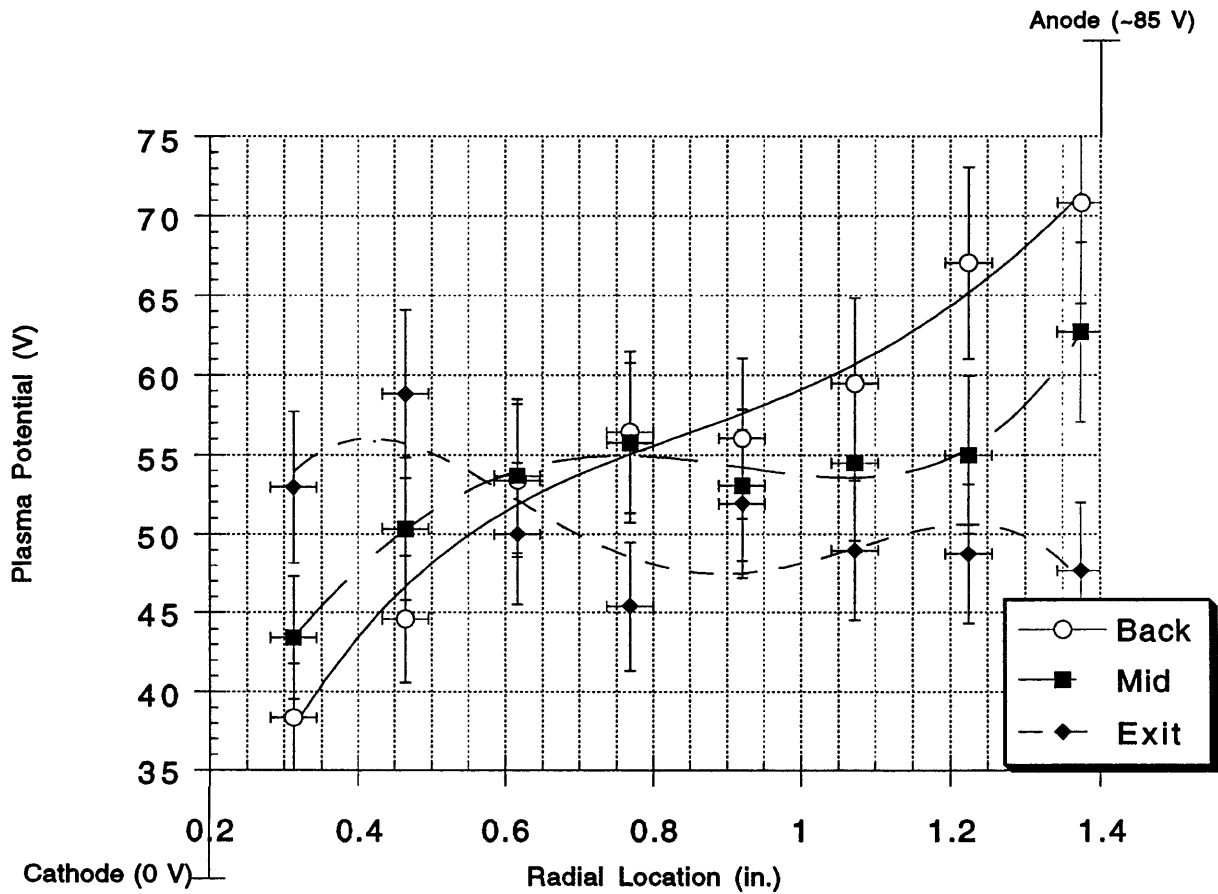
Figure 5-22: Radial Plasma Potential Measurements at Three Axial Locations For 4.8 kA

for 4.4 kA, measured to be 11.4 V near the backplate and 21.1 V at the mid-thruster location. The near exit measured values only make sense for the anode. As mentioned earlier, since the cathode was recessed .625 in. into the thruster (with respect to the exit plane), during the near exit floating probe scan, the probe was never closer than .4 in. to the cathode. The anode fall measurements according to the figures above are unusually high for the near exit axial location, due mainly to the rounded shape of the anode lip. As a result of the anode curvature at the exit plane, although the probe tip was .125 in. from the anode, the bulk of the probe electrode was greater than .125 in. from the anode (see Fig. 5-19).

Comparing the near anode voltage drop during the axial scan (with the probe approximately 1 mm. from the anode) and the outermost radial location during the radial scan (.125 in. or 3.2 mm. from the anode) show a large discrepancy. Near the backplate the values obtained during the axial near-anode traverse with the floating probe were approximately 21 V and 27 V for 4.4 and 4.8 kA respectively. At the mid-thruster levels, the respective anode drops were 19.5 V and 28.5 V. At the exit, the values were 17 V and 26 V for 4.4 and 4.8 kA, respectively. Comparing these values with those given in table 5.2 for the radial traverse, one can see a significant disparity, especially near the backplate and the exit.

5.4 Discussion of Radial Floating Probe Results

During the radial floating probe experiments, 60% and 80% of the thruster terminal voltage was observed lost within .125 in. of the two electrodes for 4.4 kA and 4.8 kA, respectively. A greater drop was observed near the cathode than the anode. Much research has been done to explain the anode fall and anode power deposition [22] in recent years. The anode fall has been explained recently both numerically and experimentally to scale with the Hall parameter [23, 49].

Previous research has tried to base the anode drop on phenomena such as sheaths and plasma microinstabilities. Not as much consideration has been given to the cathode phenomena and the cathode fall. There have been a few extensive MPD cathode

studies in the past twenty five years. The high cathode fall voltage has been theorized to be caused by the cold-cathode current emission phenomenon [65]. Photographic and spectroscopic investigations have shown that the majority of the cathode region lacks the incandescent temperatures, even though the current densities in the region exceed $100A/cm^2$. Since the cathode is cold, thermionic emission is absent [1]. To emit electrons off the cathode surface, therefore, large electric fields develop near the cathode to cause current emission. Near cathode probe measurements are also plagued by impurities (Tungsten) being boiled off and attaching to the probe itself. Contamination, especially near the cathode, is responsible for some error in both floating probe and triple probe results. The floating probe was cleaned after every ten shots using the electron bombardment technique described in chapter 2. Contamination of the probe may also be the cause for the disparity between the near-anode potential measurements during the axial and radial probe scans. Near the backplate and the exit, the outermost radial shots produced results drastically different than those obtained during the axial scan with the probe located roughly 1 mm. from the anode surface. Since neither the floating probe nor the thruster geometry was changed during the two sets of shots, it is unclear why the discrepancy occurs.

Next chapter describes the Langmuir triple probe results which were used to determine the electron temperature and density variations at 4.4 and 4.8 kA thruster current levels. The measured radial electron temperature profiles were used to determine radial plasma potentials (Figs. 5-21, 5-22) from the measured floating potentials.

Chapter 6

Triple Probe Experiments

6.1   Triple Probe Results

Two sets of triple probe experiments were conducted. The first set corresponded to the near anode axial traverse needed to determine the electron temperature correction factor for conversion from floating potential to plasma potential. Experiments were conducted at the same twelve axial locations and the eight current levels as used with the near-anode floating probe experiments. The second set of triple probe experiments were conducted to determine the radial electron temperature and electron density profiles in the MPD thruster for 4.4 kA and 4.8 kA thruster current levels. Laframboise's method along with the Peterson-Talbot curve fits [41, 53] and Bohm's thin sheath criterion [64] were used for T_e and N_e measurements. A detailed discussion of the triple probe theory is provided in Appendix A.

Overall thruster current and voltage characteristics were also recorded during these measurements. Radial traverses were made at three axial locations 1.47 in., .98 in. and .23 in. in from the exit plane. The three axial locations represent three very distinct regions of the thruster. The near backplate location represents the region where the gas transitions from unionized to a near fully ionized stage. The cathode root has also been identified by several researchers as an area of large current concentration [49, 65]. A triple probe scan through that region would yield an understanding of the radial electron temperature and density gradients. The mid-thruster axial location
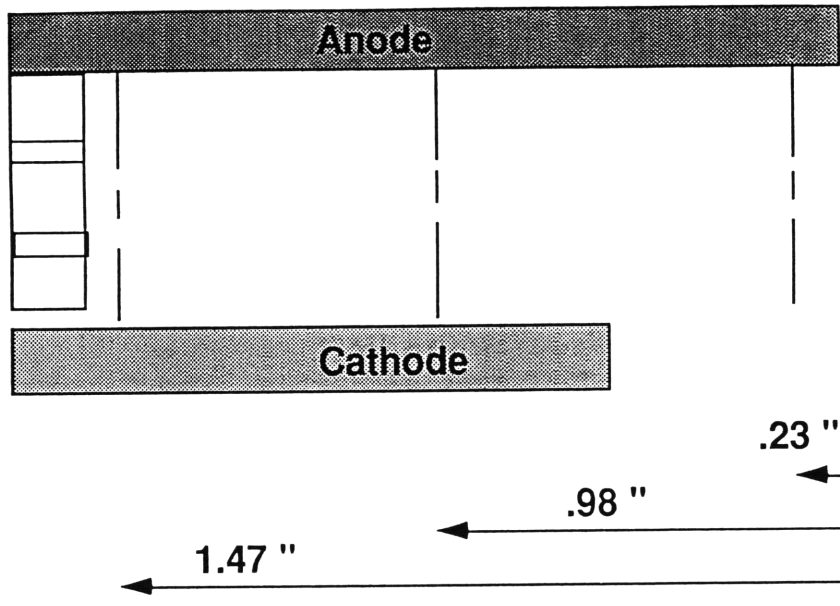
Figure 6-1: Triple Probe Radial Traverse Locations

is used to represent the bulk of the thruster where the propellant is close to fully ionized and the region is not ridden with current or temperature concentrations. The near exit plane traverse represents a region of relatively low magnetic field but a high current concentration near the anode lip.

The thruster schematic in Fig. 6-1 shows the axial locations of the three traverses described above.

As in the floating probe experiments, three shots were fired at each physical location at each current level with Argon flowing at .5 g/sec. The average of the three shots was used as the ultimate value for the electron temperature and electron density for analysis purposes. Voltage and current traces from the triple probe were expected to look similar, i.e. with a fast rise , a flat quasi-steady-state region and a slower exponential decay. The probe signals behaved as expected. A typical Langmuir triple probe trace is shown in Fig. 6-2.

The error associated with the triple probe measurements has been described in reference [64] (also see Appendix A). The random error associated with data repeatability was found to be 5% for the electron temperature measurements and 10% for the electron density measurements. The overall error which includes the random error with the so-called schematic error (i.e. error associated with the interpretation of the
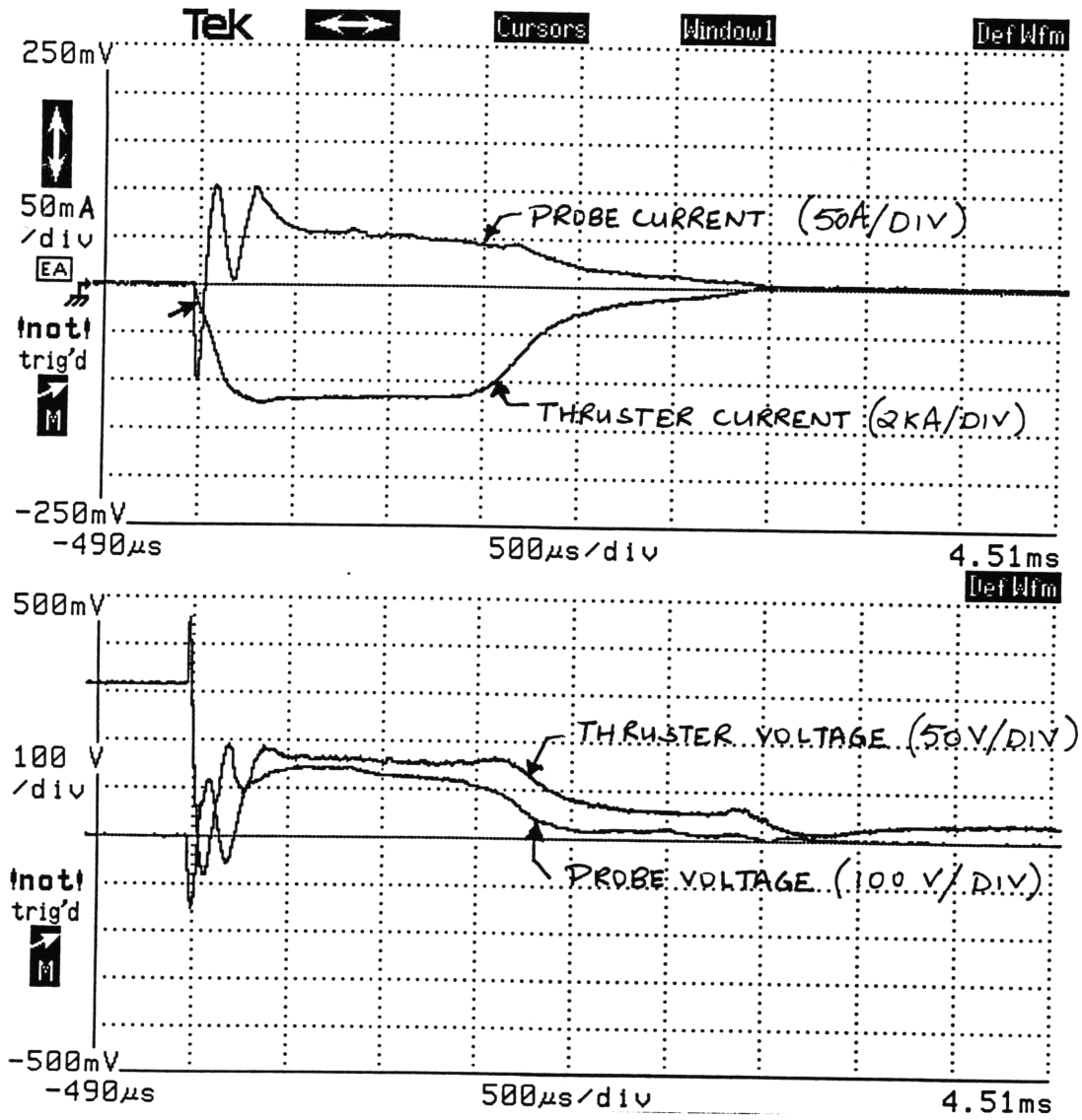
Figure 6-2: A Typical Triple Probe Response
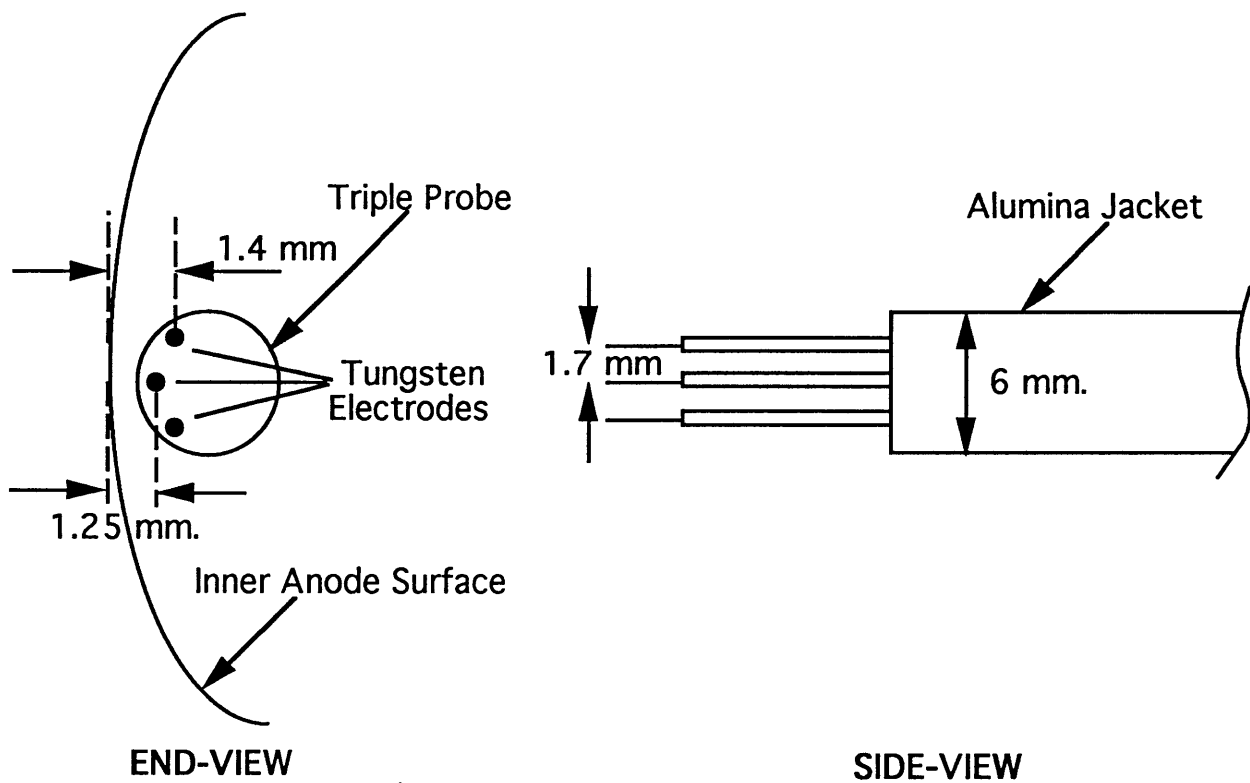
Figure 6-3: Triple Probe Orientation and Critical Dimensions

triple probe output using Laframboise's theory) was determined to be 20% and 80% for electron temperature and density, respectively. The probe was cleaned after every ten shots with the electron bombardment technique described in chapter 2.

6.1.1 Near Anode T_e and n_e Results

Due to the physical dimensions of the probe, during the near anode traverse, the electrodes were placed approximately 1.25 mm. from the anode surface. with an inter-electrode separation of 1.6 mm as shown in Fig. 6-3.

The probe was aligned to keep the distance between each electrode and the anode surface roughly equal. The outer two electrodes were a little bit farther from the anode surface ($\sim$ 1.4mm.) than the one in the middle. Measurements were obtained at twelve axial locations separated by .125 in. and at eight current levels corresponding to PFN voltage variation from 100 to 200 V.

Figures 6-4 through 6-7 show the near-anode axial electron temperature profiles
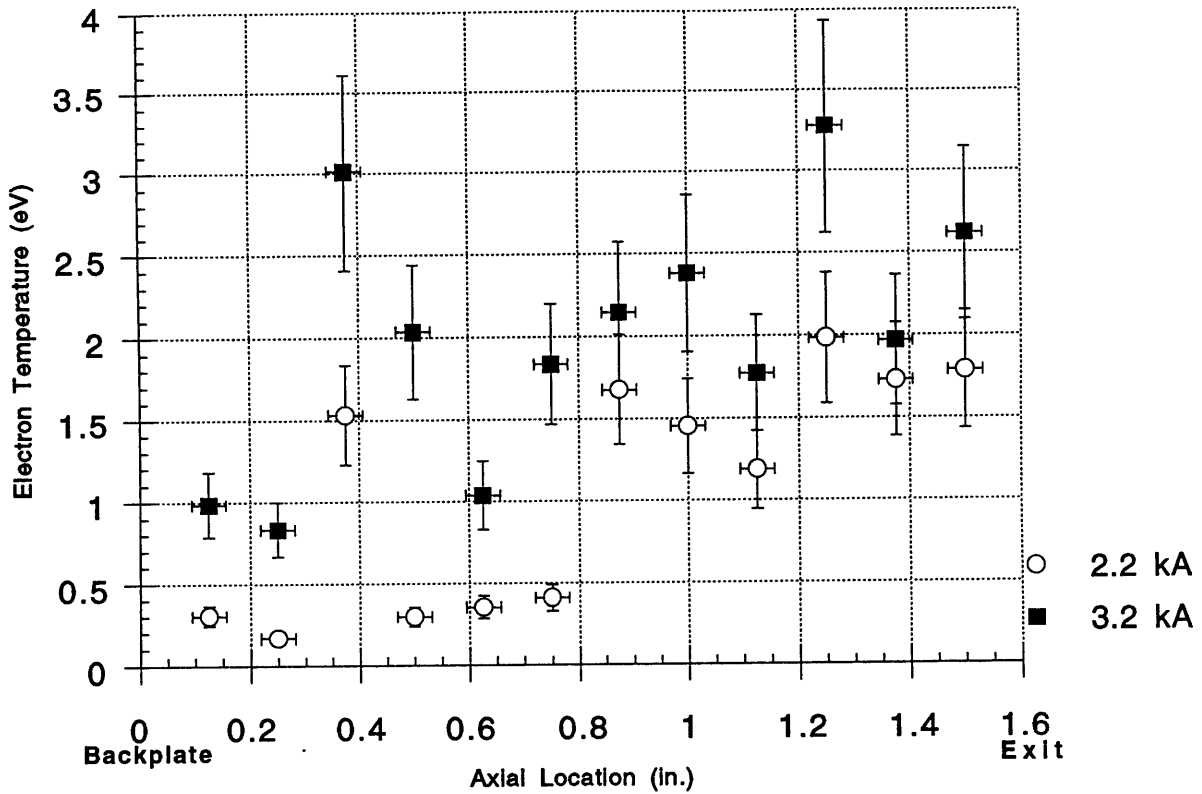
Figure 6-4: Near Anode Axial Electron Temperature Profiles at 2.2 and 3.2 kA

for various thruster current levels.

The thruster was fired with Argon flowing at .5 g/s. Thruster operation was kept under the onset regime (5.6 kA) to avoid electrode damage.

Near-anode electron temperatures varied from .2 eV to over 6 eV with increasing thruster current. All axial temperature profiles displayed a dual hump behavior corresponding to a sharp electron temperature rise at .375 in. and 1.25 in. locations. High electron temperature at those two locations, in turn, led to a rather high correction factor $(5.3kT_e/e)$ to the floating probe measurements. The large correction factor resulted in a dip in the axial anode voltage drop profiles seen in Fig. 5-2 through 5-5 at the same two axial locations. The fact that the electron temperature behavior is repeatable for all current levels seems to indicates that the phenomenon is real and not a probe error.

Electron Temperature as a function of increasing thruster current at each axial location is shown in Figs. 6-8 through 6-19.

Electron temperature increased noticeably with thruster current. The temper-

Figure 6-5: Near Anode Axial Electron Temperature Profiles at 4.4 and 4.8 kA

Figure 6-6: Near Anode Axial Electron Temperature Profiles at 4.9 and 5.06 kA

Figure 6-7: Near Anode Axial Electron Temperature Profiles at 5.11 and 5.34 kA

atures indicated by the triple probe are higher than expected for Argon since the multiple ionization levels present in Argon provide an energy buffer. That is, an increase in energy in an Argon plasma results in secondary ionization rather than an increase in electron temperature. It is possible that due to probe contamination, probe misalignment with plasma flow or due to charge interaction between the probe and the anode surface, there was an overprediction in T_e. In the near-anode case, therefore, attention should be given to the temperature profiles rather than the absolute magnitudes. An axial electron temperature variation was observed at each given current level. Near the backplate, where the incoming gas is cold, electron temperature at 2.2 kA and 3.2 kA was less than 1 eV. The near backplate axial locations (.125 in. and .25 in.) showed a steep temperature rise from roughly .2 eV at 2.2 kA to almost 6 eV at 5.34 kA. At .375 in. location, as has been mentioned before, the electron temperature jumped to 1.5 eV at 2.2 kA rising to 6.4 eV at 5.34 kA. The .50 in. and .625 in. axial locations showed a sharp increase in the electron temperature rising from under 1 eV at 2.2 kA to 6.5 eV at 5.34 kA. At the next four axial

102
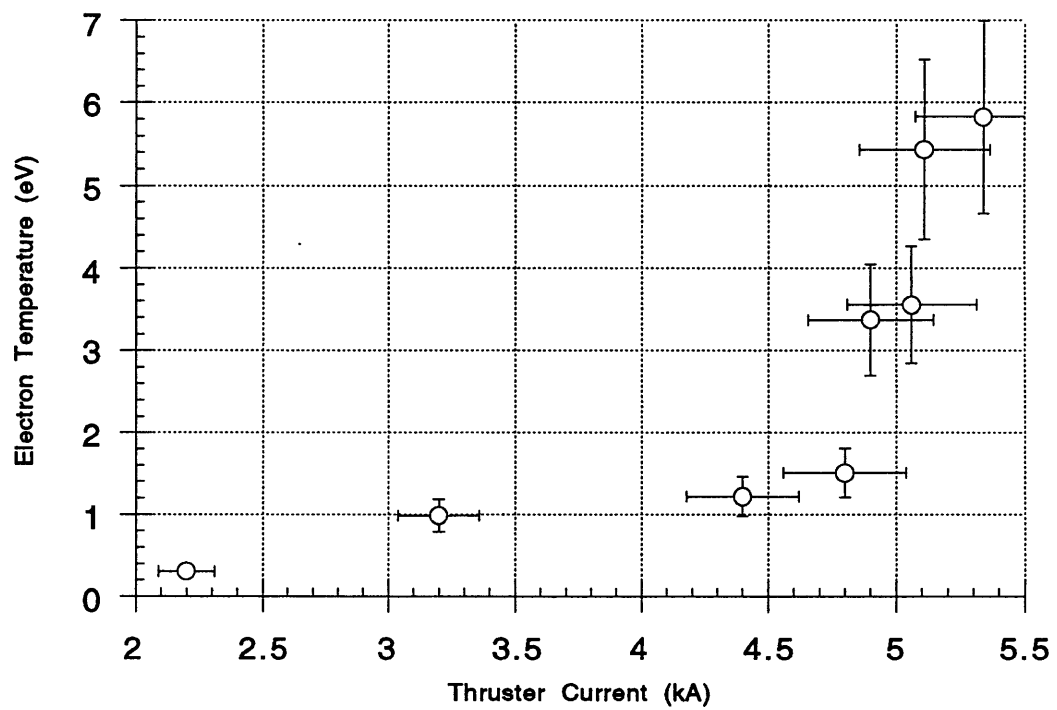
Figure 6-8: Near Anode Electron Temperature as a Function of Thruster Current at
.125 in. From the Backplate

Figure 6-9: Near Anode Electron Temperature as a Function of Thruster Current at .25 in. From the Backplate

Figure 6-10: Near Anode Electron Temperature as a Function of Thruster Current at .375 in. From the Backplate

Figure 6-11: Near Anode Electron Temperature as a Function of Thruster Current at .50 in. From the Backplate

106

Figure 6-12: Near Anode Electron Temperature as a Function of Thruster Current at .625 in. From the Backplate

Figure 6-13: Near Anode Electron Temperature as a Function of Thruster Current at .75 in. From the Backplate

Figure 6-14: Near Anode Electron Temperature as a Function of Thruster Current at .875 in. From the Backplate

Figure 6-15: Near Anode Electron Temperature as a Function of Thruster Current at 1.0 in. From the Backplate
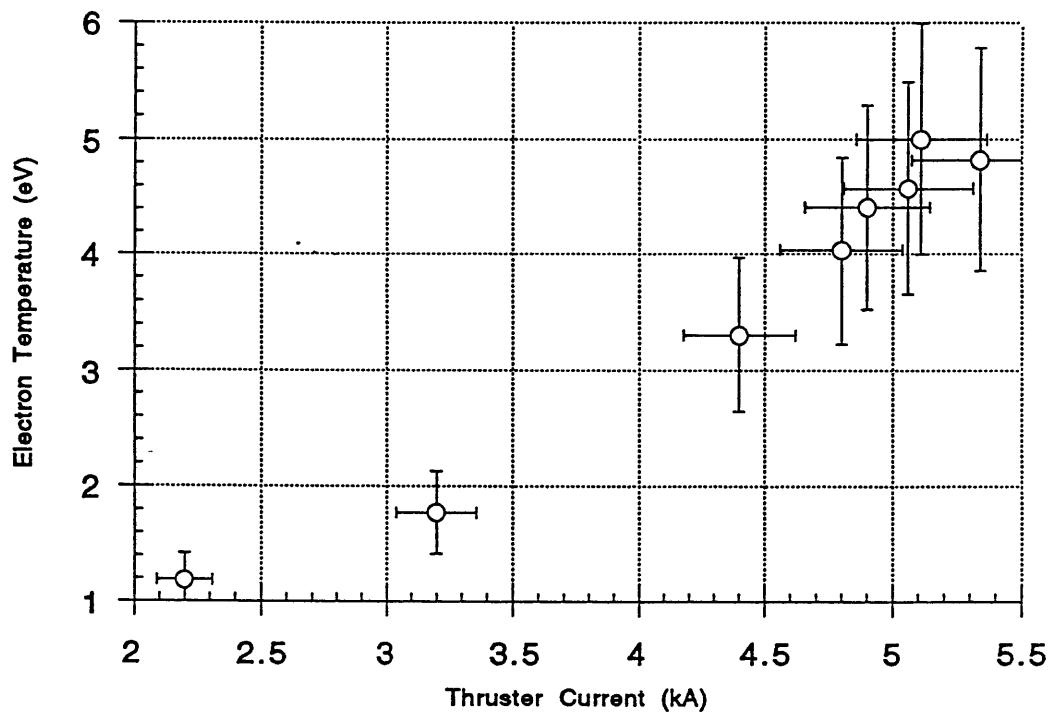
Figure 6-16: Near Anode Electron Temperature as a Function of Thruster Current at 1.125 in. From the Backplate
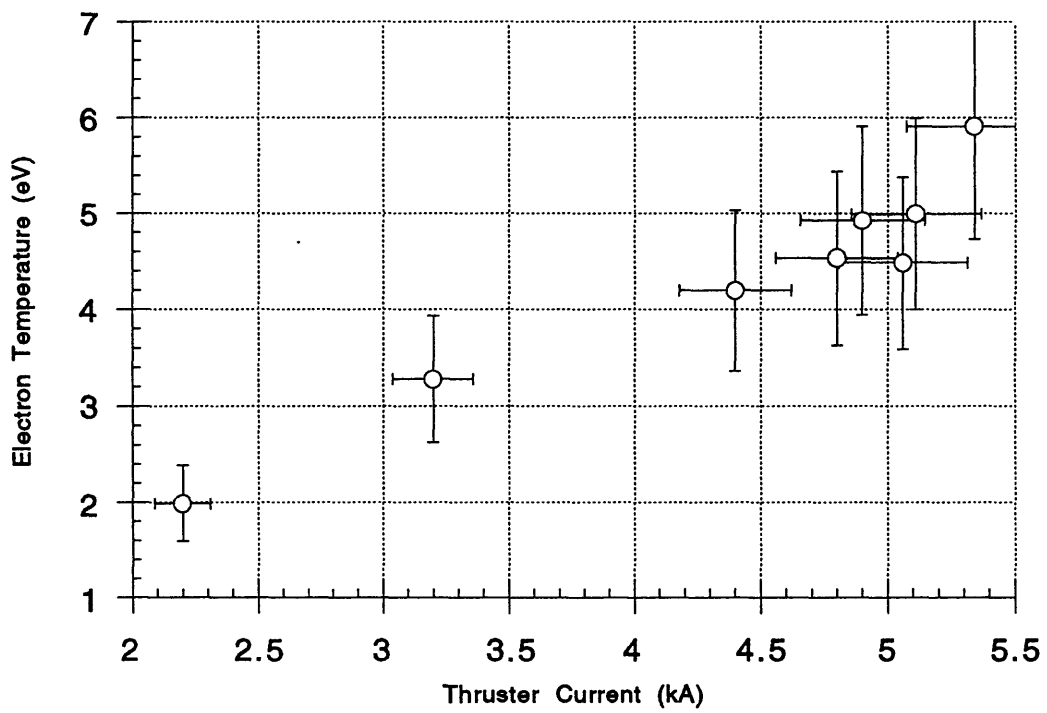
Figure 6-17: Near Anode Electron Temperature as a Function of Thruster Current at 1.25 in. From the Backplate
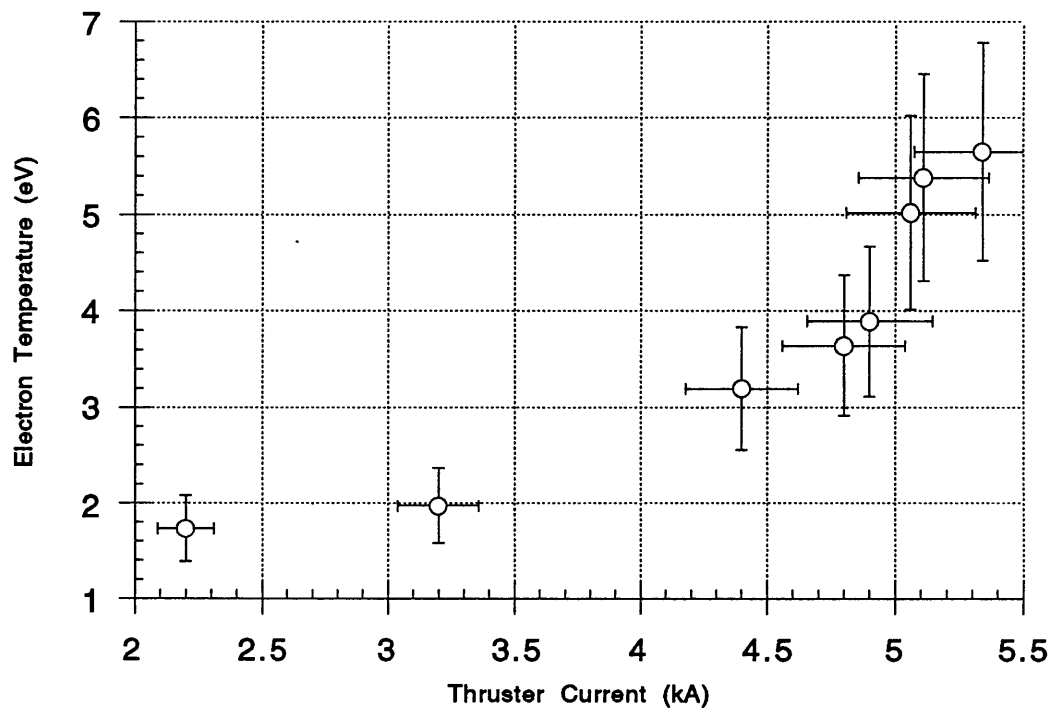
Figure 6-18: Near Anode Electron Temperature as a Function of Thruster Current at 1.375 in. From the Backplate
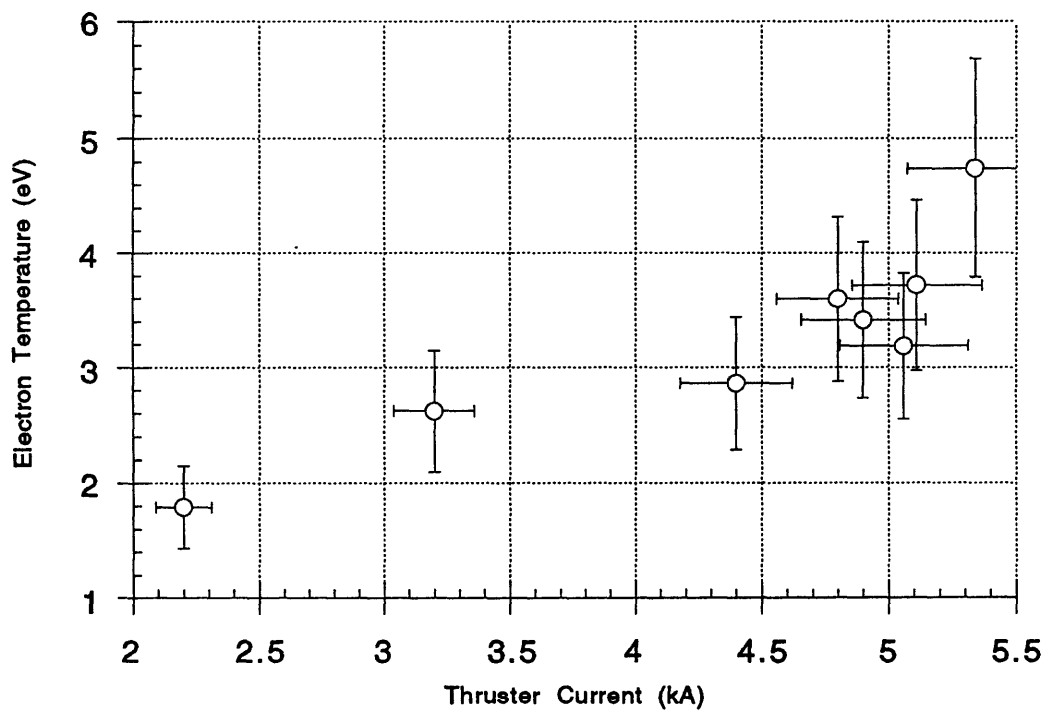
Figure 6-19: Near Anode Electron Temperature as a Function of Thruster Current at 1.5 in. From the Backplate

locations (.75 in through 1.125 in.), the temperature varied from roughly 1.5 eV at 2.2 kA to approximately 5 eV at the highest current. At 1.25 in. location, a jump of more than 1 eV in the electron temperature was detected from the previous location. The temperature drops again further towards the exit plane. The temperature rise noticed at .375 in. and 1.25 in. was repeatable for all current levels.

An electron temperature transition from cold to hot was clearly observed during operation at various current levels. At 2.2 kA, the first half of the thruster showed temperature less than 1 eV, with the exception of the jump to 1.5 eV at .375 in. Electron temperature jumped in the second half of the thruster to 1.5 eV. At 3.2 kA, once again, the first half of the thruster was "cold" with roughly 1 eV electron temperature, jumping to roughly 2.25 eV in the second half of the thruster. During firings at 4.4 and 4.8 kA, the transition from cold to hot was limited to .25 in. from the backplate. At the near backplate locations (.125 in. and .25 in.), the temperature was approximately 2 eV, rising after the first jump at .375 in. to 2.75 eV for 4.4 kA and 3.5 eV for 4.8 kA. T_e measurements at 4.9 and 5.06 kA showed no clear transition from cold to hot, however. All axial locations showed T_e above 3 eV rising to almost 5 eV at the two temperature hump locations. A dip in the temperature was apparent at the mid-thruster location (.75 in.) followed by a gradual rise to 1.25 in., the location of the second temperature hump. At 5.11 and 5.34 kA current levels, the electron temperature remained above 4 eV in all but one case. Even at the near backplate locations (.125 in. and .25 in.), the temperature stayed above 5 eV in both cases.

Near anode axial electron density profiles for various current levels are shown in Figs. 6-20 through 6-23. The values in the plots represent the average of three firings at each axial location at each current level.

Although T_e increased dramatically with current, no such behavior was seen in the N_e profiles. In general, N_e decreased with increasing current. The axial N_e profiles are different for 2.2 and 3.2 kA than all other current levels. There was a decrease in number density observed for the two current levels at .375 in. and 1.25 in. locations corresponding to the axial locations of sharp T_e rise shown in the last section. This behavior was observed only for the 2.2 and 3.2 kA firings. For the
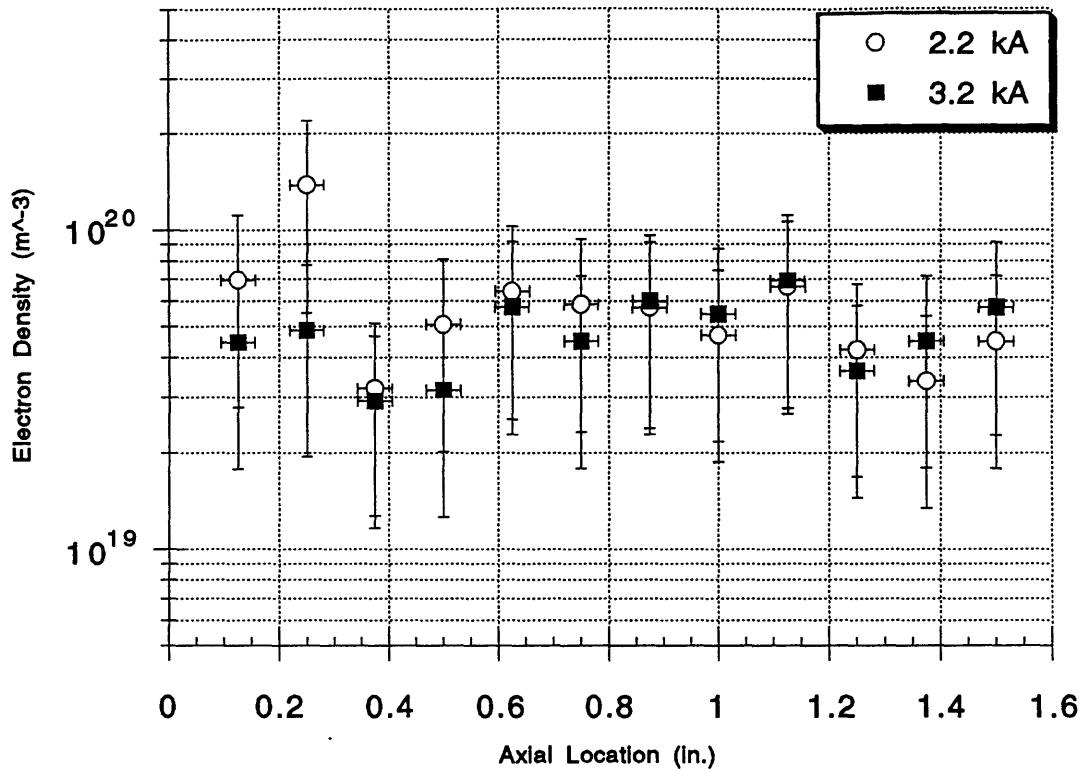
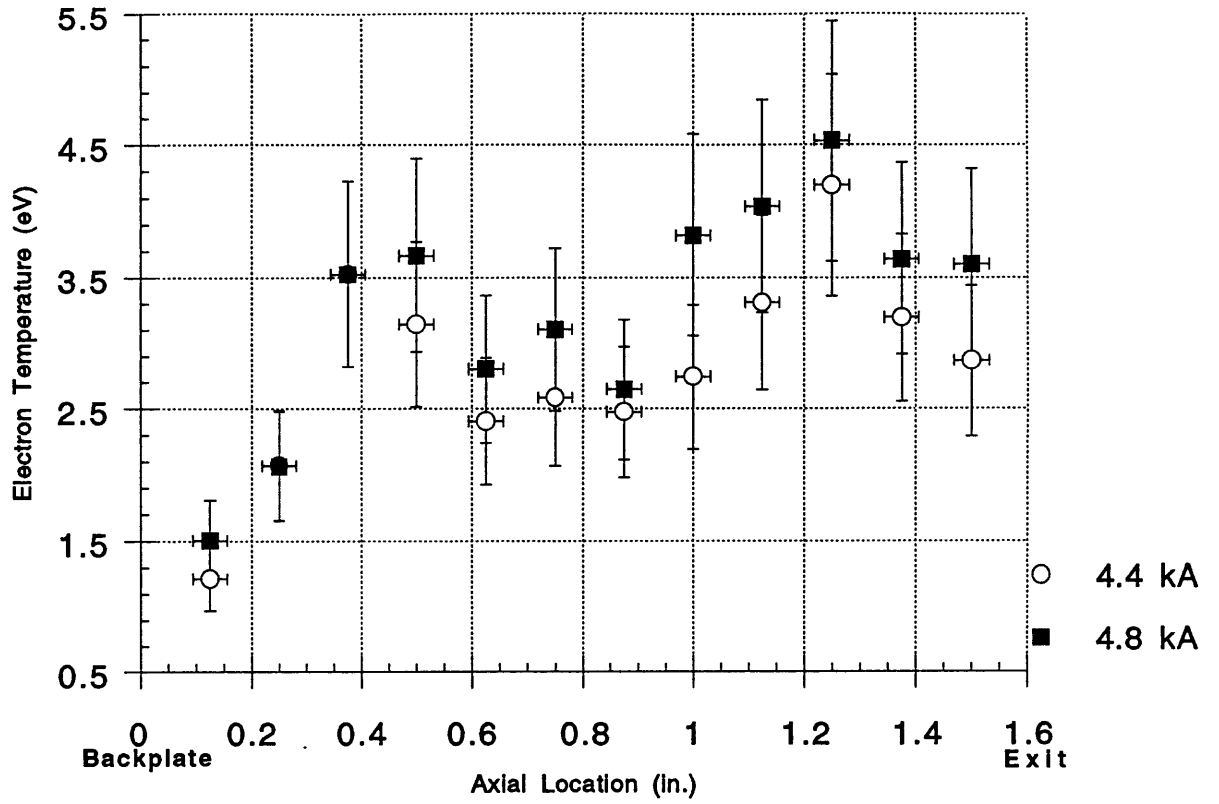Figure 6-20: Near Anode Axial Electron Density Profiles at 2.2 and 3.2 kA
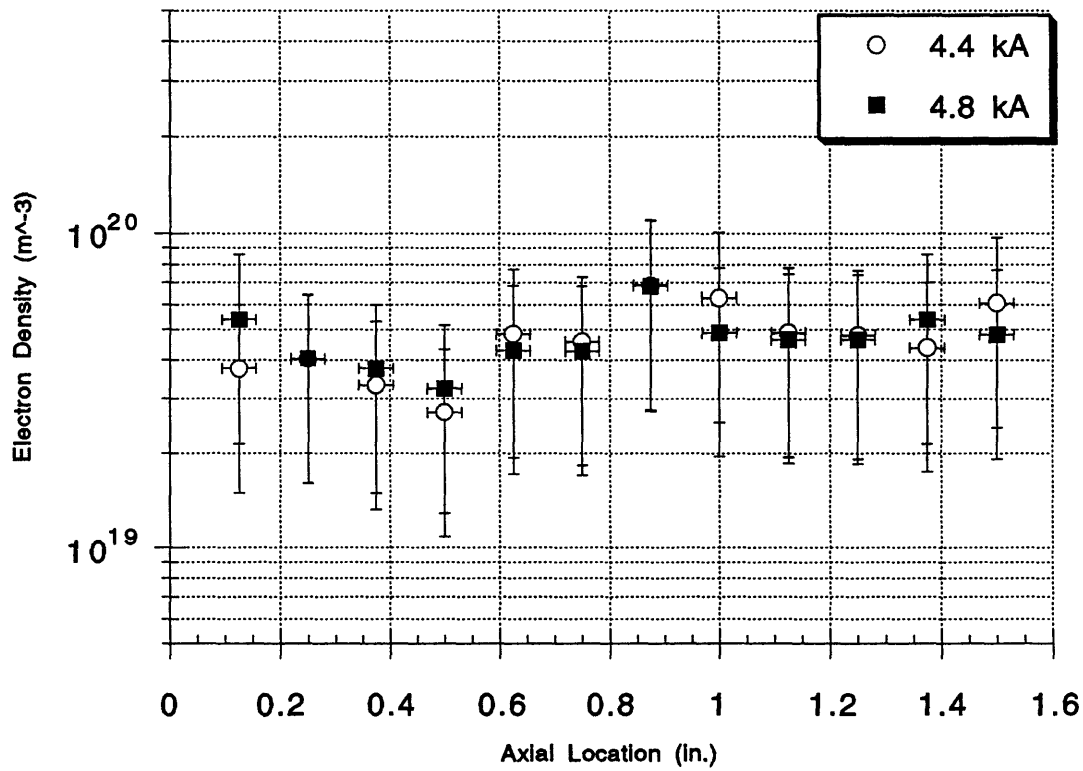
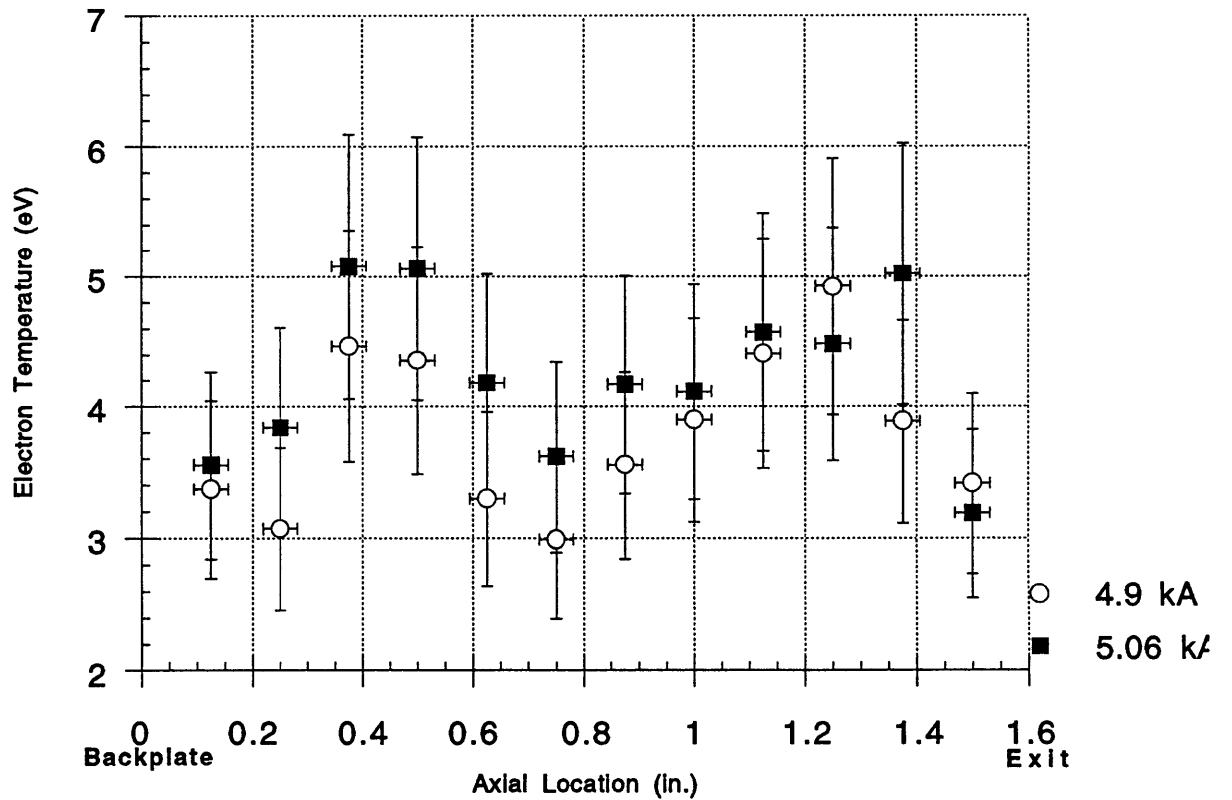Figure 6-21: Near Anode Axial Electron Density Profiles at 4.4 and 4.8 kA
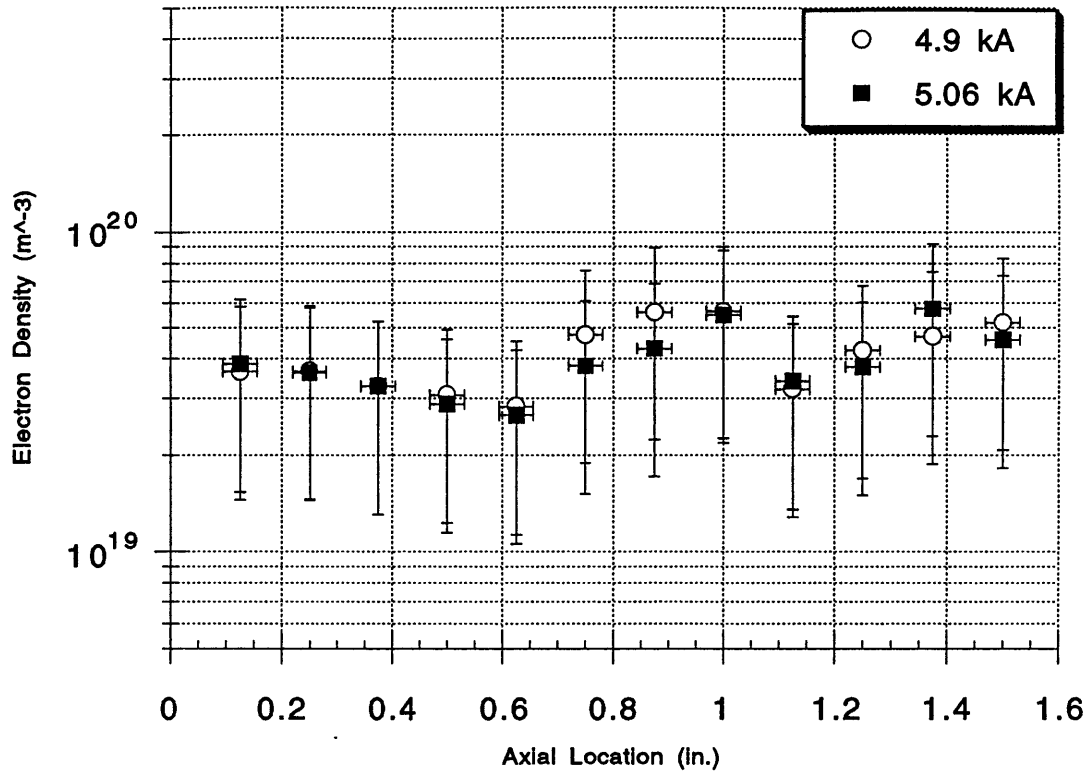
Figure 6-22: Near Anode Axial Electron Density Profiles at 4.9 and 5.06 kA
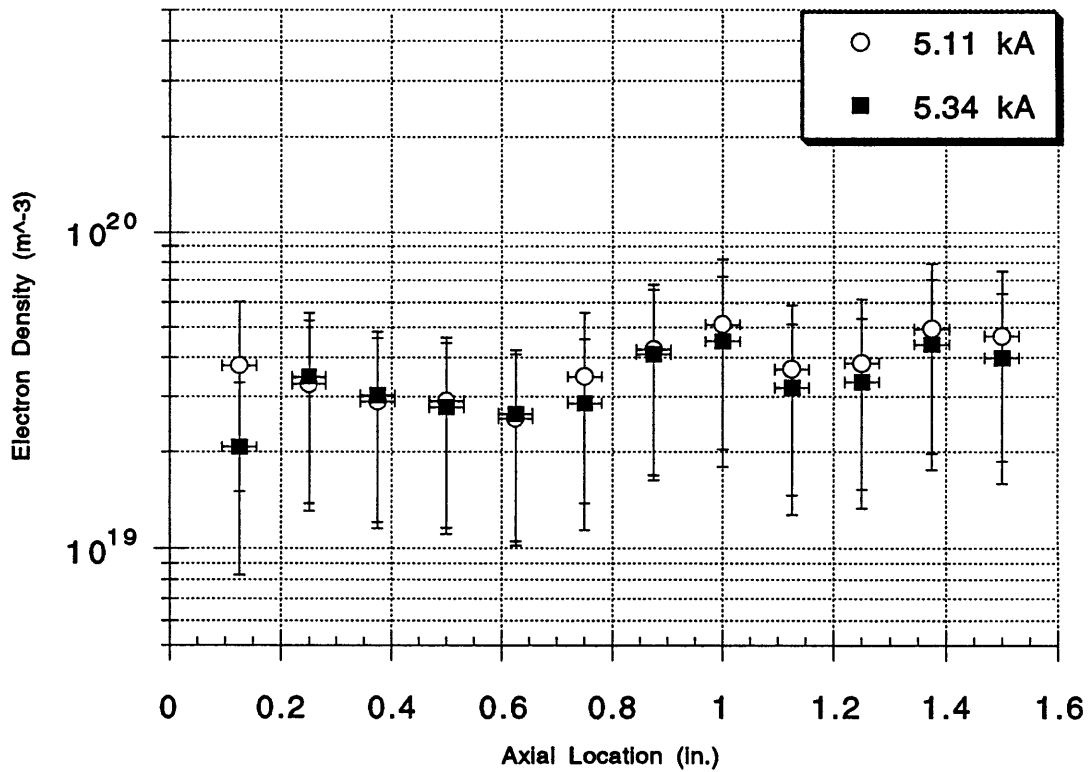
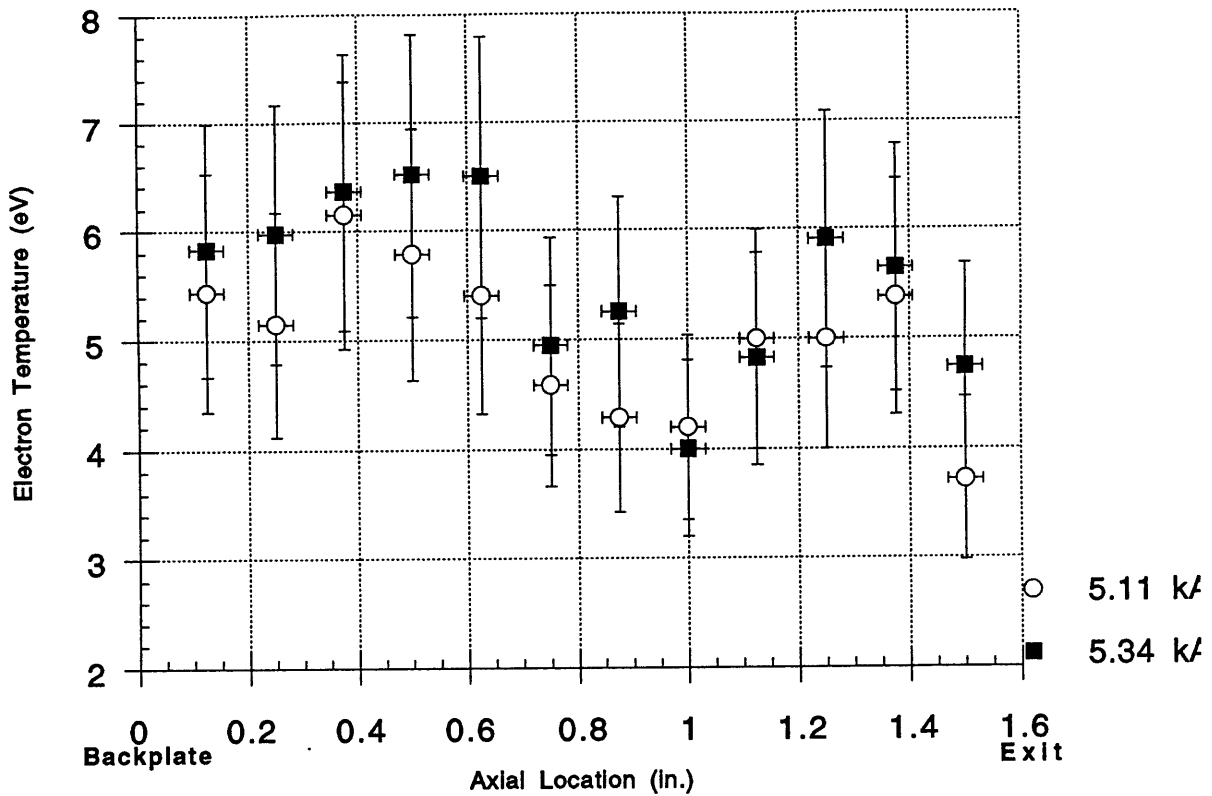Figure 6-23: Near Anode Axial Electron Density Profiles at 5.11 and 5.34 kA
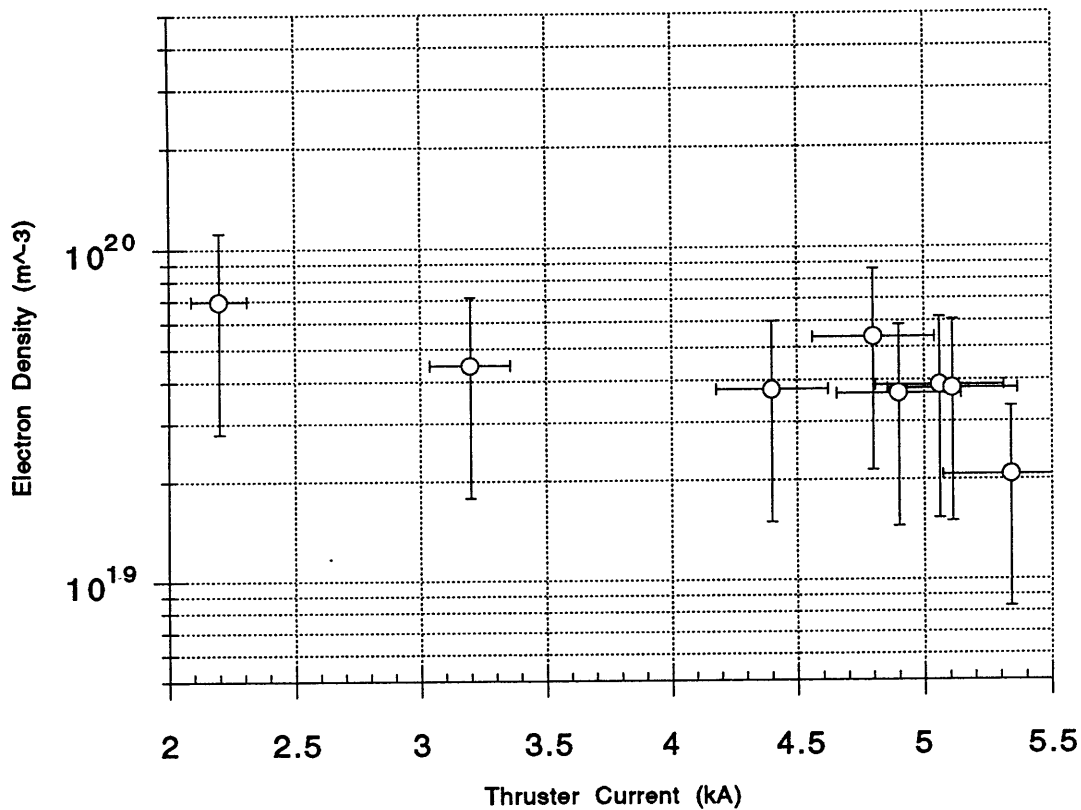
Figure 6-24: Near Anode Electron Density as a Function of Thruster Current at .125 in. From the Backplate

remaining six current levels, a pattern was observed. The electron density dropped from the backplate to roughly .5 in. axial location rising gradually thereafter to 1.0 in. location followed by another slight dip at 1.125 in. and then a gradual rise towards the exit plane. The electron density for 4.4 kA through 5.34 kA varied from 3 x $10^{19} m^{-3}$ to 7 x $10^{19} m^{-3}$.

Figures 6-24 through 6-35 show electron density profiles as a function of increasing thruster current at each of the twelve near-anode axial locations.

The near anode electron density, as mentioned before, decreased with increasing thruster current from 7 x $10^{19} m^{-3}$ to 3 x $10^{19} m^{-3}$, except for the 2.2 kA case, where
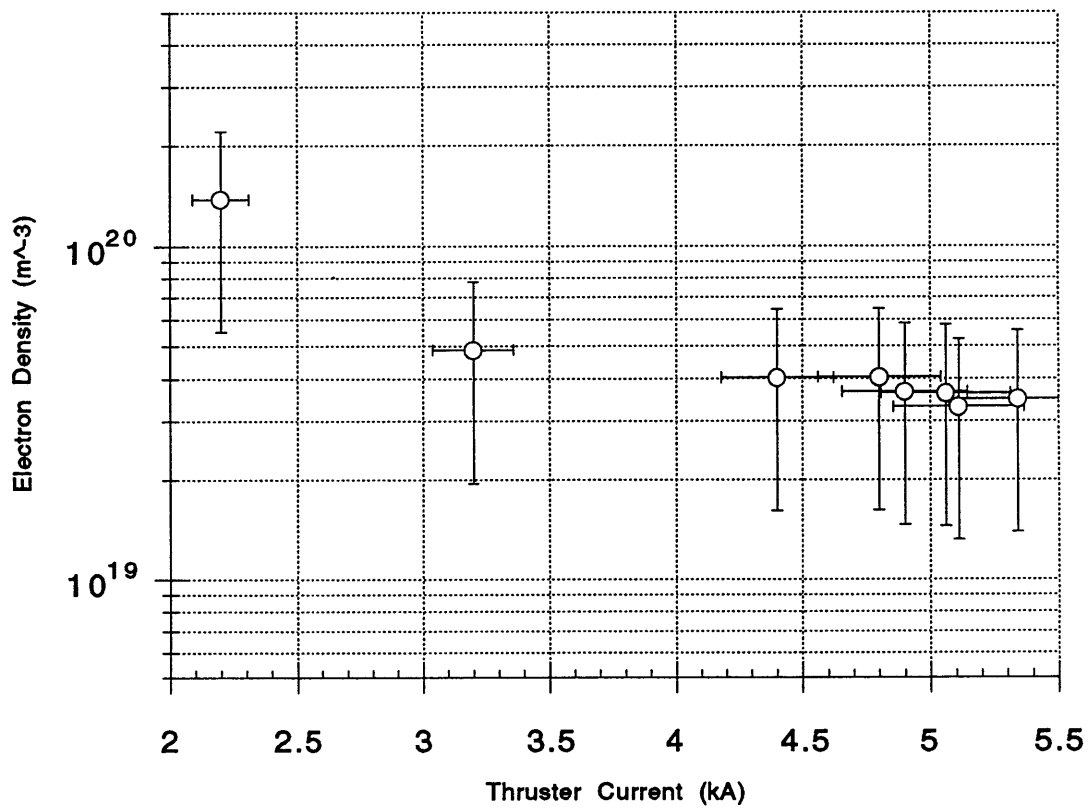
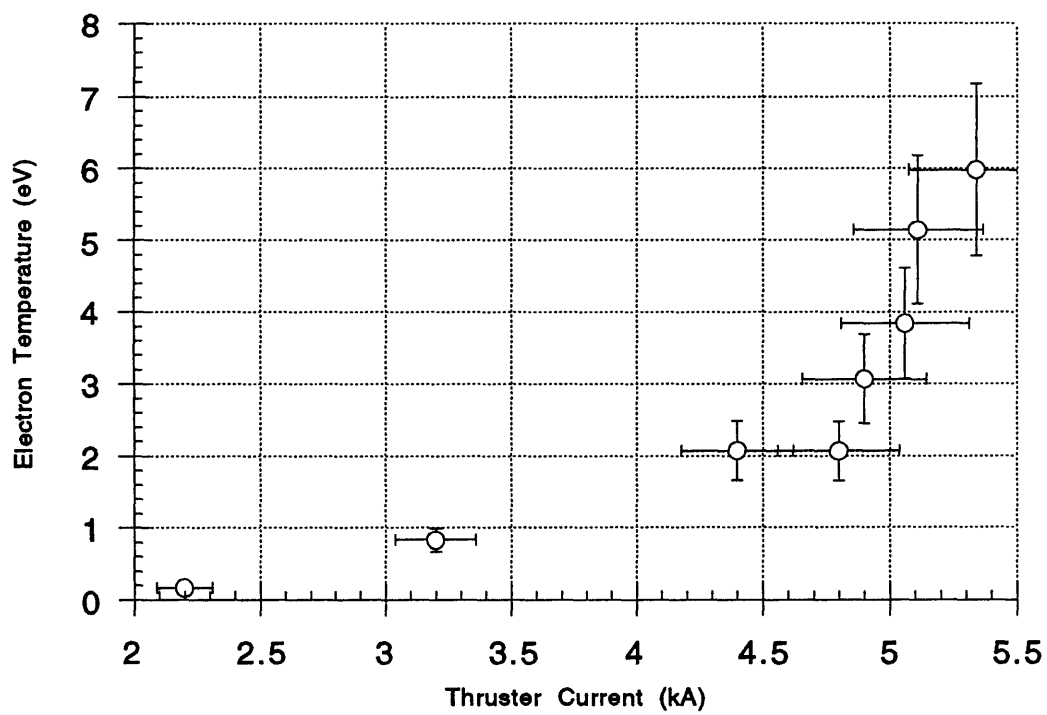Figure 6-25: Near Anode Electron Density as a Function of Thruster Current at .25
in. From the Backplate
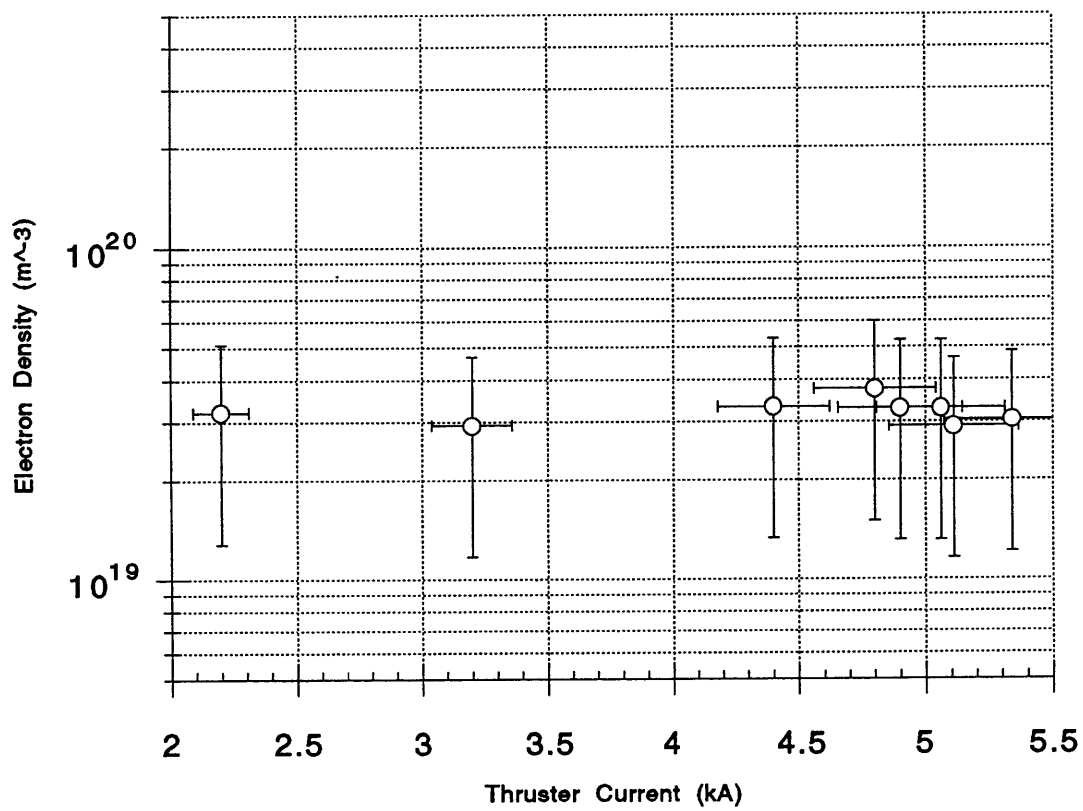
Figure 6-26: Near Anode Electron Density as a Function of Thruster Current at .375 in. From the Backplate
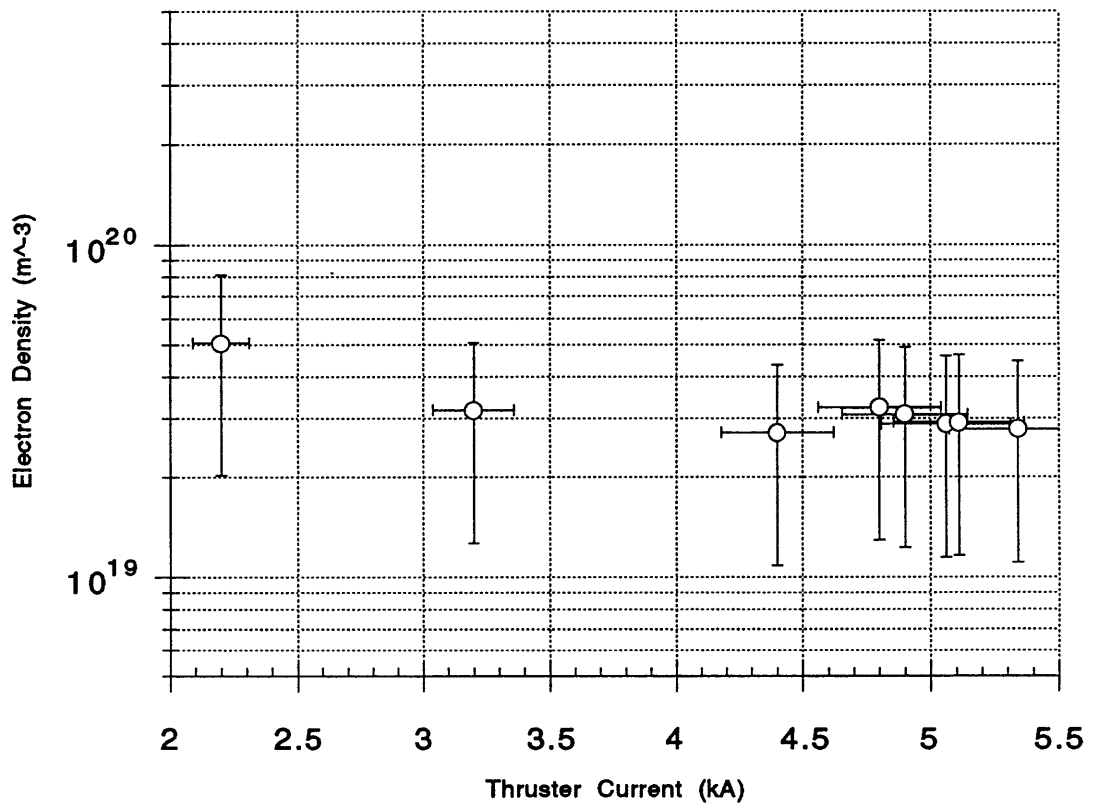
Figure 6-27: Near Anode Electron Density as a Function of Thruster Current at .50 in. From the Backplate
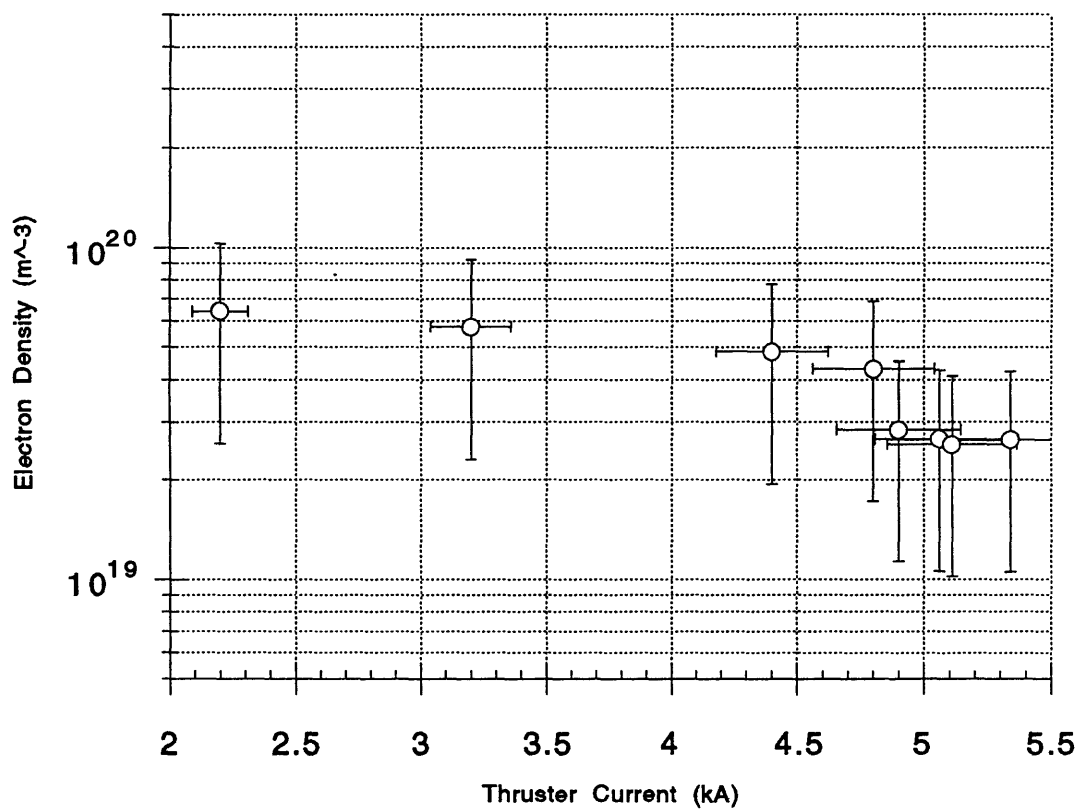
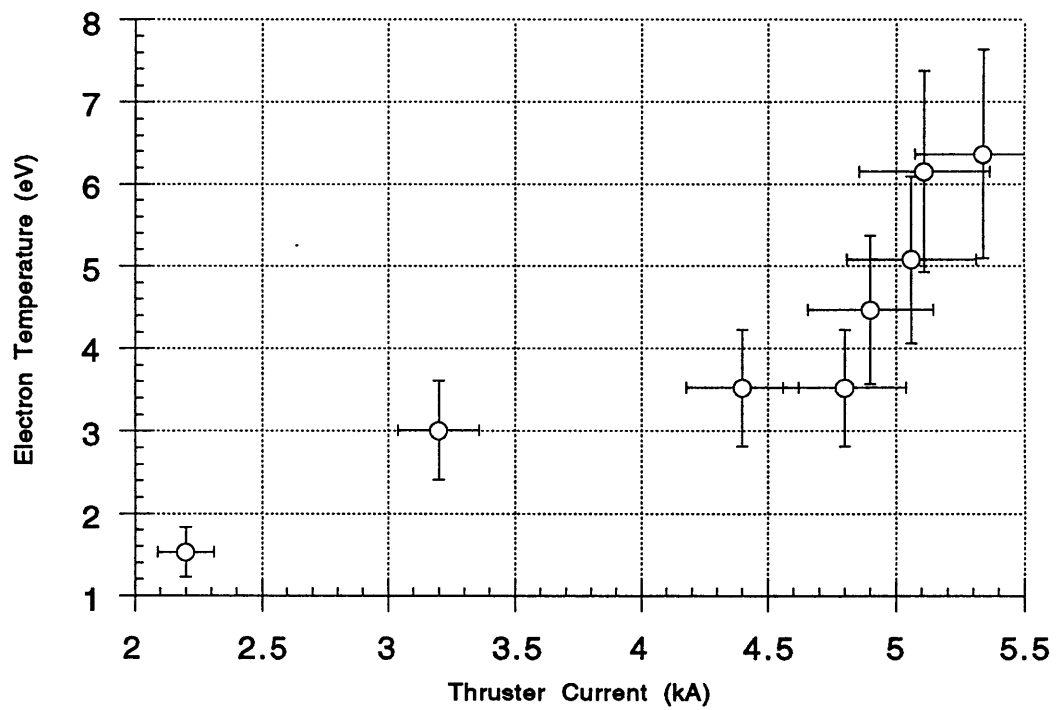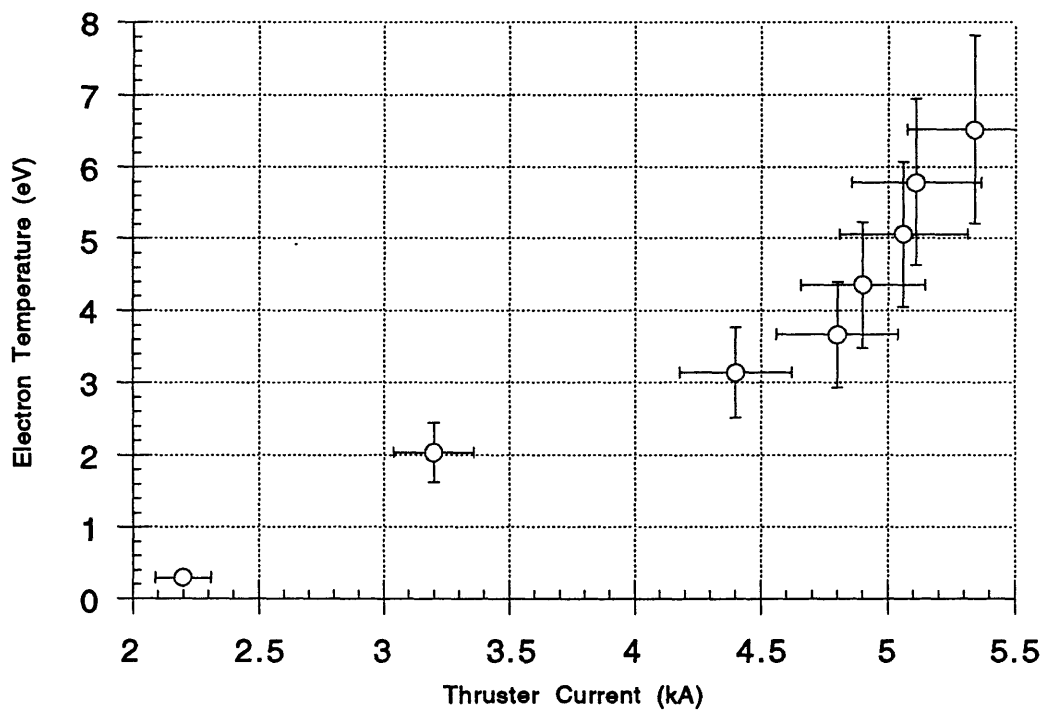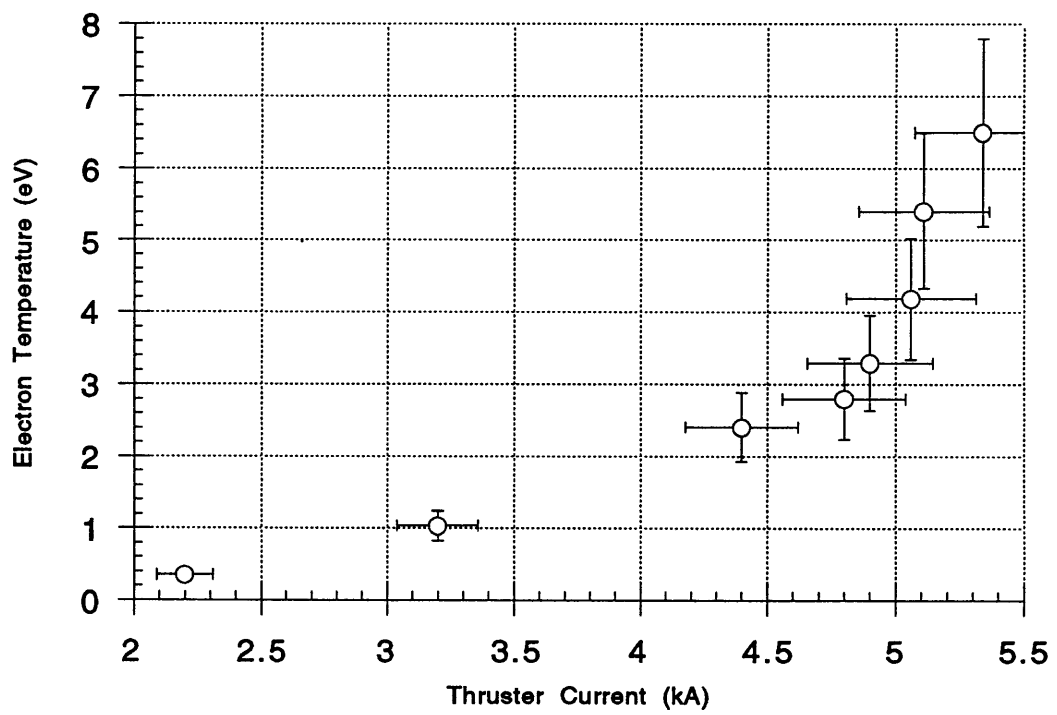Figure 6-28: Near Anode Electron Density as a Function of Thruster Current at .625 in. From the Backplate
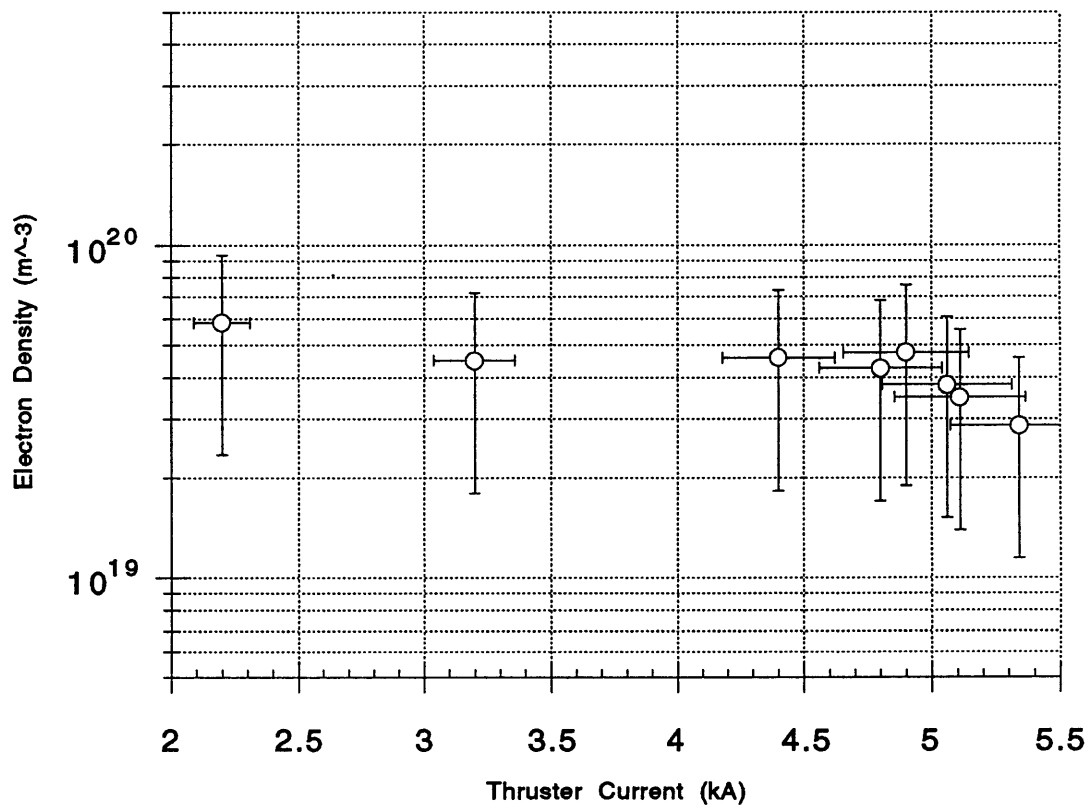
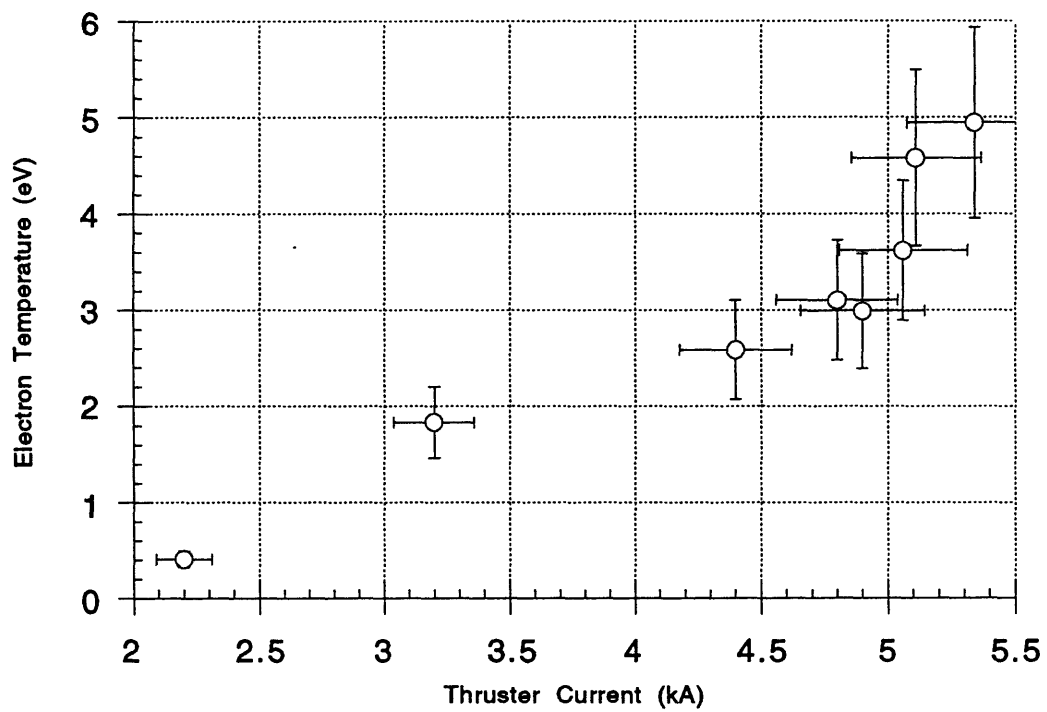Figure 6-29: Near Anode Electron Density as a Function of Thruster Current at .75 in. From the Backplate
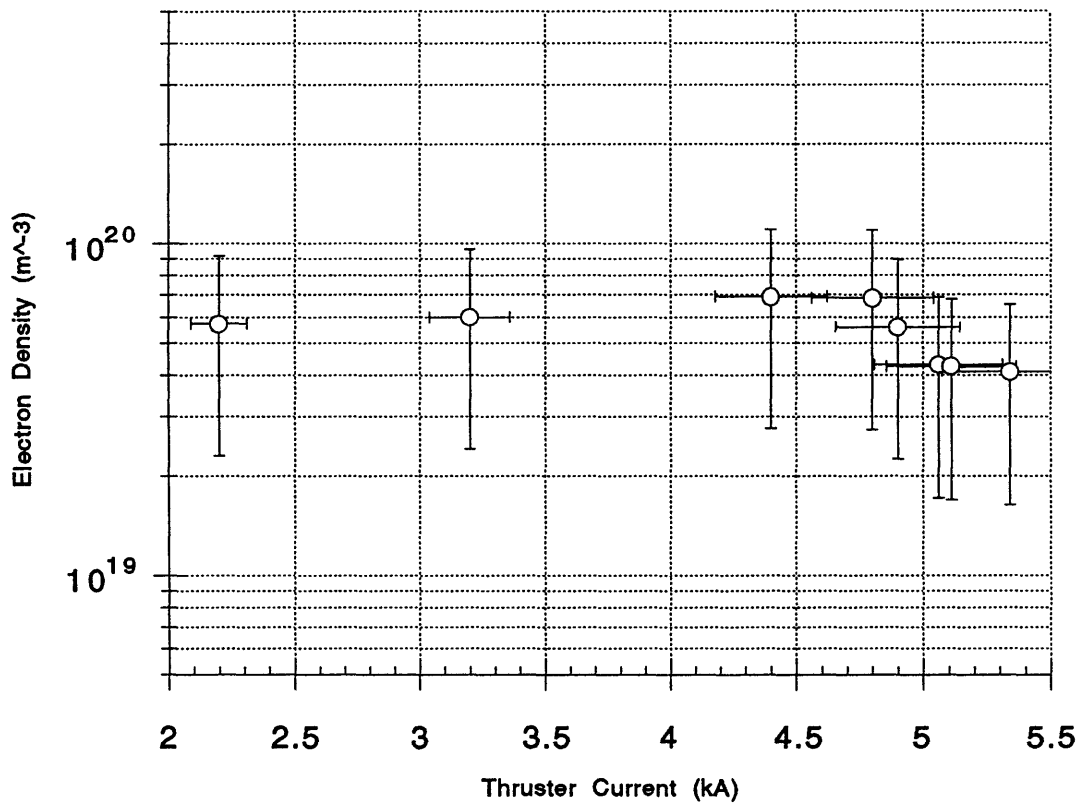
Figure 6-30: Near Anode Electron Density as a Function of Thruster Current at .875 in. From the Backplate
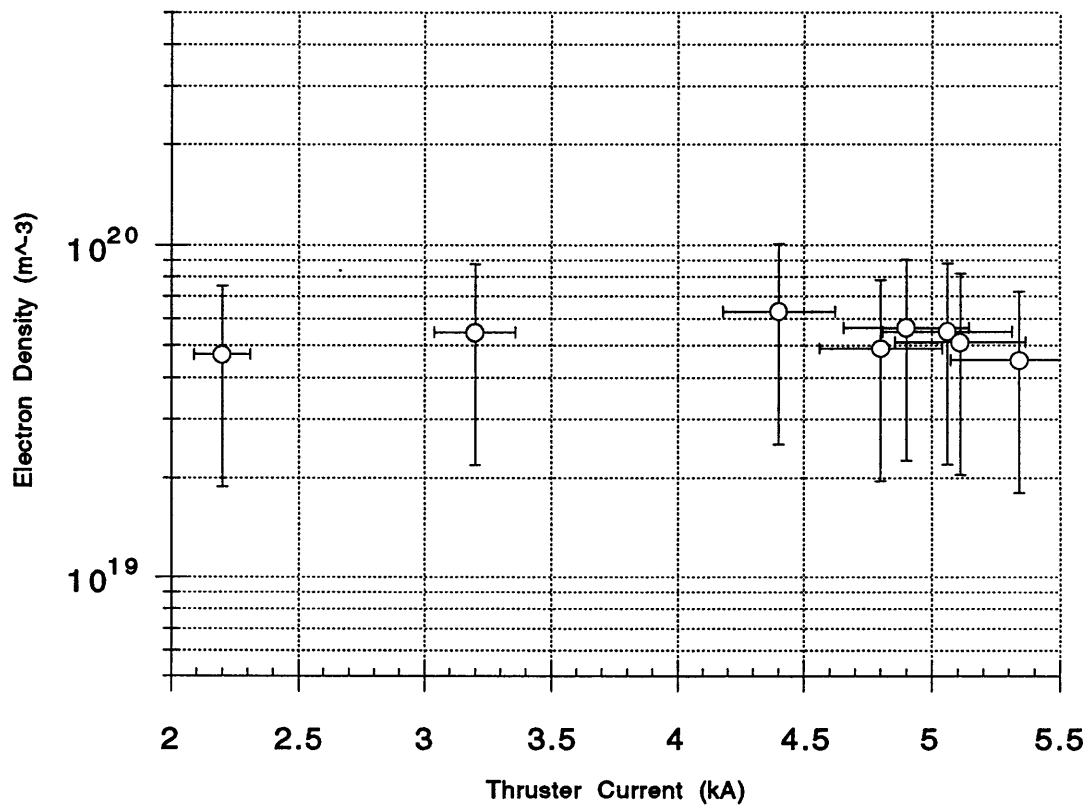
Figure 6-31: Near Anode Electron Density as a Function of Thruster Current at 1.0 in. From the Backplate
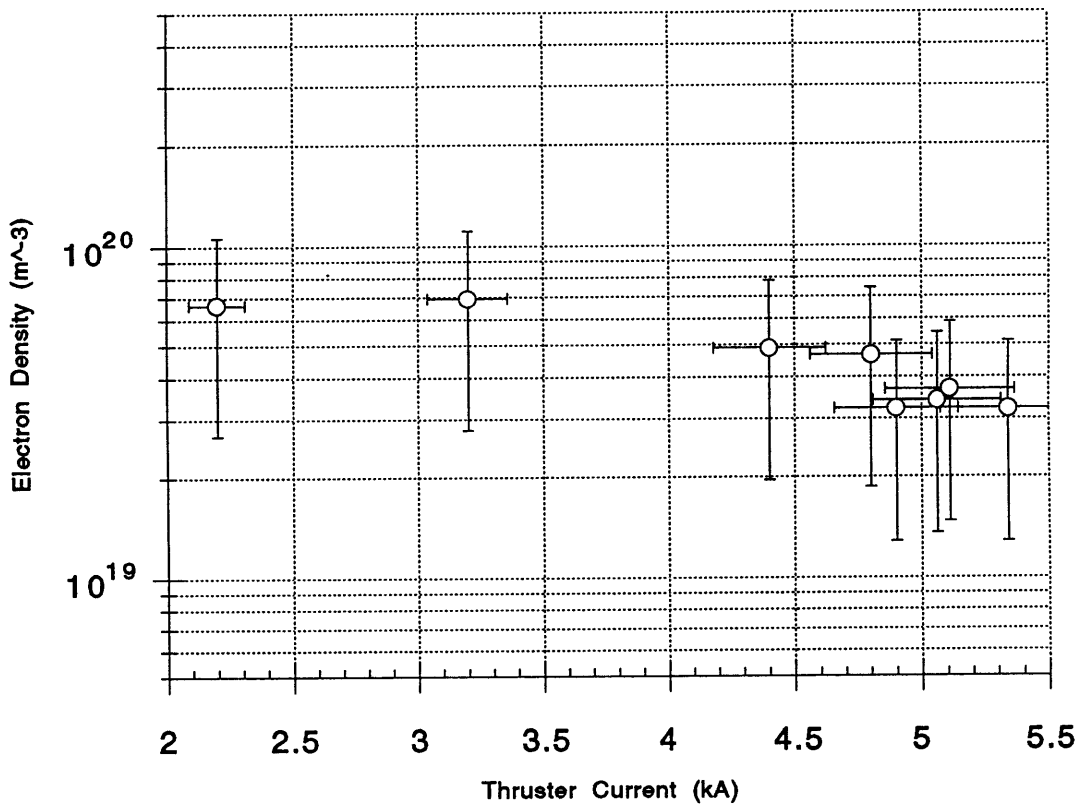
Figure 6-32: Near Anode Electron Density as a Function of Thruster Current at 1.125 in. From the Backplate
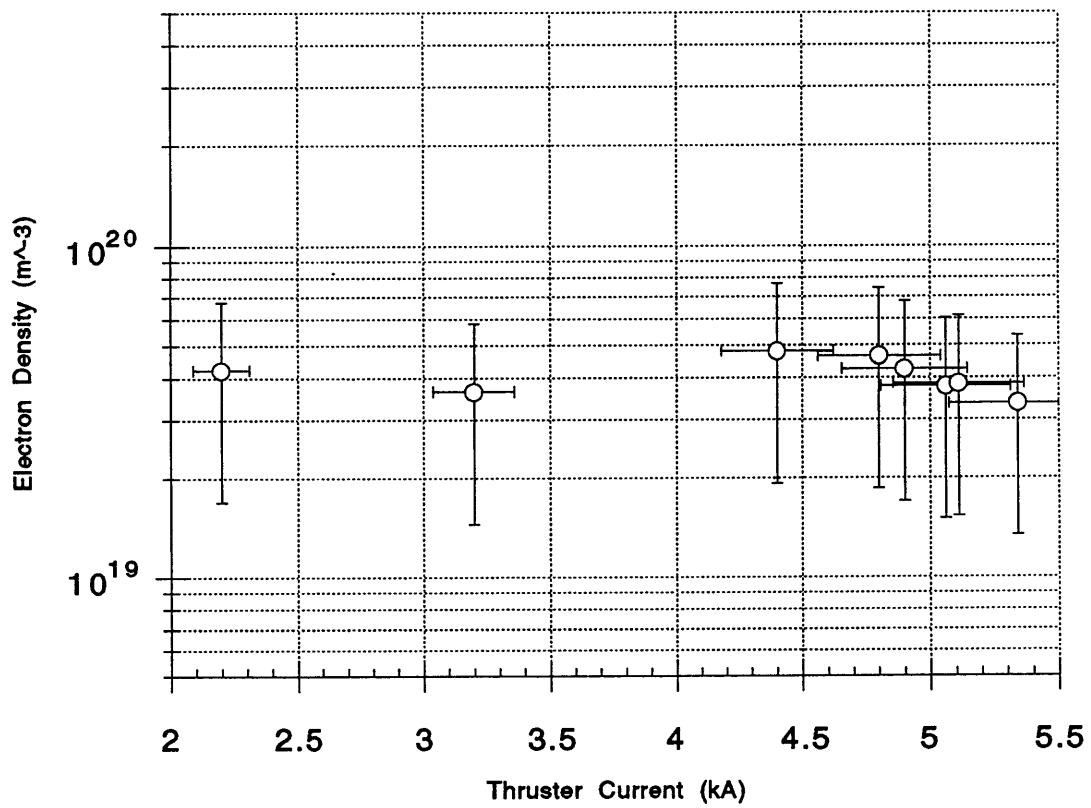
Figure 6-33: Near Anode Electron Density as a Function of Thruster Current at 1.25 in. From the Backplate
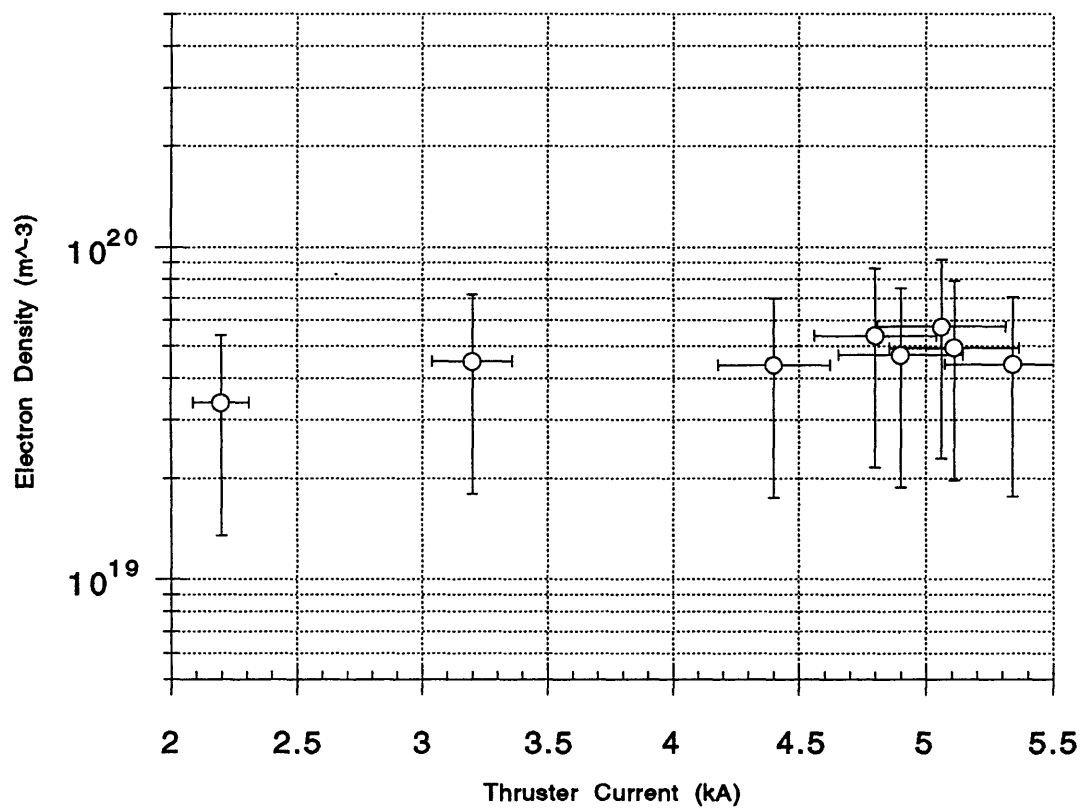
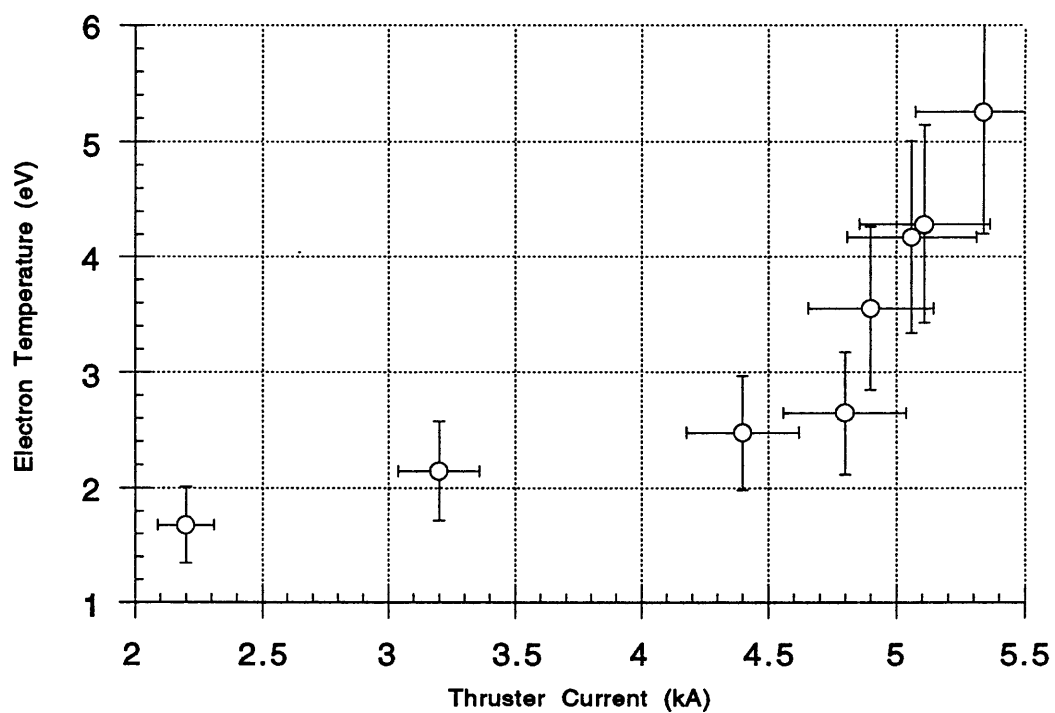Figure 6-34: Near Anode Electron Density as a Function of Thruster Current at 1.375 in. From the Backplate
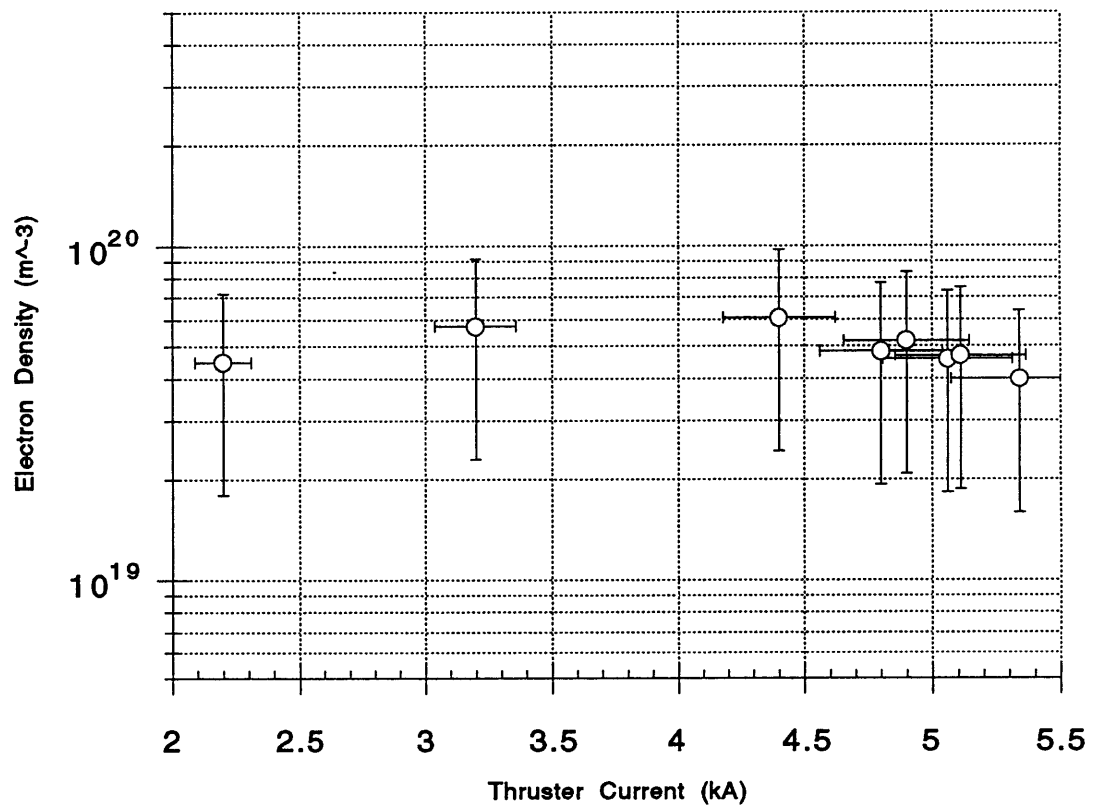
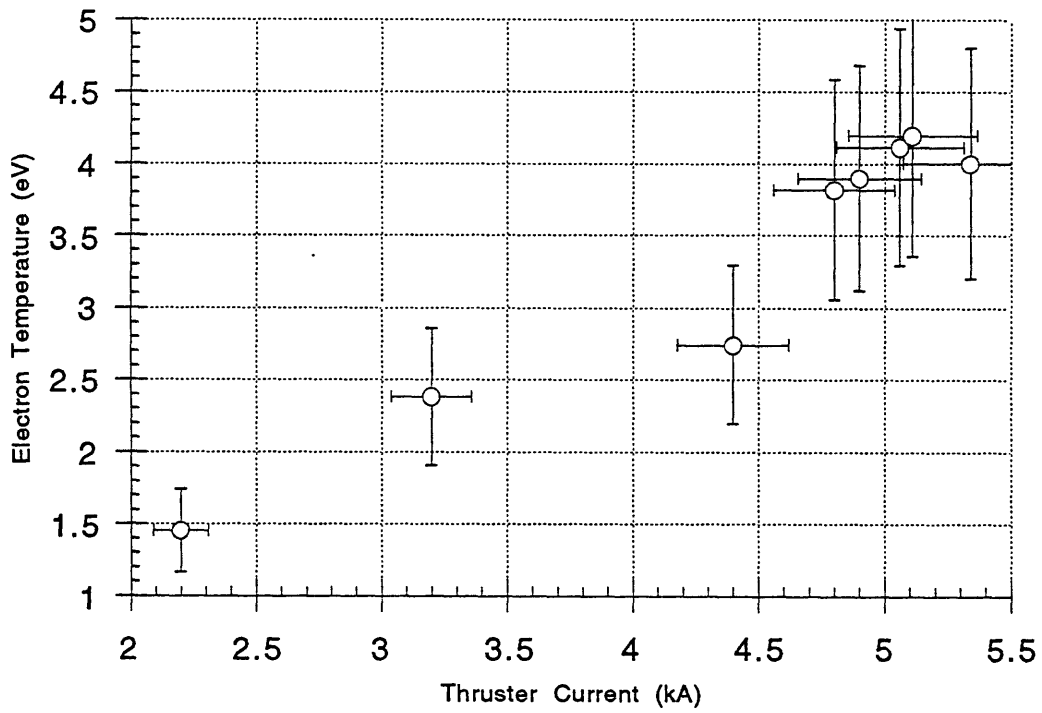Figure 6-35: Near Anode Electron Density as a Function of Thruster Current at 1.5 in. From the Backplate

Axial loc.(in.)	2.2 kA	3.2 kA	4.4 kA	4.8 kA	4.9 kA	5.06 kA	5.11 kA	5.34 kA
0.12500	4.9174e-07	1.1053e-06	1.3406e-06	1.2447e-06	2.2635e-06	2.2586e-06	2.8241e-06	3.9412e-06
0.25000	2.5967e-07	9.7297e-07	1.6894e-06	1.6823e-06	2.1559e-06	2.4222e-06	2.9420e-06	3.0836e-06
0.37500	1.6261e-06	2.3873e-06	2.4235e-06	2.2804e-06	2.7453e-06	2.9268e-06	3.4274e-06	3.4066e-06
0.50000	5.6901e-07	1.8854e-06	2.5326e-06	2.5063e-06	2.7990e-06	3.1180e-06	3.3173e-06	3.6004e-06
0.62500	5.5100e-07	9.9838e-07	1.6572e-06	1.9003e-06	2.5377e-06	2.9507e-06	3.4179e-06	3.6857e-06
0.75000	6.2152e-07	1.5028e-06	1.7676e-06	2.0063e-06	1.8675e-06	2.2972e-06	2.7001e-06	3.0919e-06
0.87500	1.2726e-06	1.4063e-06	1.4090e-06	1.4626e-06	1.8746e-06	2.3153e-06	2.3624e-06	2.6646e-06
1.0000	1.3084e-06	1.5532e-06	1.5520e-06	2.0780e-06	1.9556e-06	2.0364e-06	2.1318e-06	2.2169e-06
1.1250	9.9285e-07	1.1886e-06	1.9354e-06	2.1908e-06	2.7561e-06	2.7276e-06	2.7437e-06	2.8846e-06
1.2500	1.6129e-06	2.2328e-06	2.1996e-06	2.3228e-06	2.5338e-06	2.5668e-06	2.6845e-06	3.1257e-06
1.3750	1.6845e-06	1.5566e-06	2.0089e-06	1.9343e-06	2.1397e-06	2.1997e-06	2.4546e-06	2.6630e-06
1.5000	1.4857e-06	1.5913e-06	1.6157e-06	2.0324e-06	1.9072e-06	1.9638e-06	2.0965e-06	2.5633e-06

Table 6.1: Calculated Near-Anode Debye Lengths

the density rose to over 1 x $10^{20}m^{-3}$. In the first half of the thruster (.125 in. through .75 in.), the electron density was highest at the lowest current level and gradually decreased with increasing thruster current. In the second half of the thruster, however (.875 in. through 1.5 in.) the electron density rose from 2.2 kA to 4.4 kA before dropping again. Based on the T_e and N_e measurements, the electron Debye length and electron collision frequency could be calculated. The electron Debye length, λ_d is given by:

$$\lambda_d = (\frac{\epsilon_o k T_e}{e^2 n_e})^{1/2} \qquad (6.1)$$

where ϵ_o is the permittivity of free space, n_e is the electron density, k is the Boltzmann constant and T_e is the electron temperature. The Debye length is an important parameter in Langmuir probe theory as shown in Appendix A. The calculated Debye lengths for the near anode axial traverse are shown in Table 6.1.

The electron-ion collision frequency was calculated using the following equation

130

Axial Loc. (in.)	2.2 kA	3.2 kA	4.4 kA	4.8 kA	4.9 kA	5.06 kA	5.11 kA	5.34 kA
0.12500	6.3604e+09	9.6280e+08	6.2153e+08	6.6002e+08	1.5736e+08	1.5474e+08	8.5638e+07	4.4191e+07
0.25000	2.3525e+10	1.2963e+09	3.2971e+08	3.3280e+08	1.7893e+08	1.3152e+08	8.0998e+07	6.9771e+07
0.37500	3.9756e+08	1.4872e+08	1.3591e+08	1.5249e+08	9.7702e+07	8.2238e+07	5.6416e+07	5.6297e+07
0.50000	4.9228e+09	2.7018e+08	1.3075e+08	1.2553e+08	9.5129e+07	7.3020e+07	6.1521e+07	5.0196e+07
0.62500	4.9400e+09	1.1424e+09	3.2299e+08	2.3529e+08	1.2782e+08	8.7458e+07	5.9732e+07	4.8062e+07
0.75000	3.7808e+09	4.3050e+08	2.7820e+08	2.0414e+08	2.3709e+08	1.4881e+08	9.9843e+07	7.4890e+07
0.87500	6.0817e+08	4.5948e+08	4.3371e+08	3.9397e+08	2.2010e+08	1.3865e+08	1.3205e+08	9.6952e+07
1.0000	6.0917e+08	3.6636e+08	3.4751e+08	1.7615e+08	1.9598e+08	1.7774e+08	1.6176e+08	1.5300e+08
1.1250	1.0994e+09	6.7692e+08	2.1315e+08	1.5598e+08	9.7493e+07	9.8008e+07	9.3559e+07	8.6304e+07
1.2500	3.6571e+08	1.6325e+08	1.5244e+08	1.3337e+08	1.0945e+08	1.1083e+08	9.7518e+07	6.8307e+07
1.3750	3.5517e+08	3.9217e+08	2.0136e+08	2.0556e+08	1.6549e+08	1.4203e+08	1.1224e+08	9.4290e+07
1.5000	4.4388e+08	3.3747e+08	3.1684e+08	1.8801e+08	2.1641e+08	2.1031e+08	1.7503e+08	1.0872e+08

Table 6.2: Calculated Near-Anode Electron Collision Frequencies

[20]:

$$\nu_{ei} = 2.91 \times 10^{-6} \frac{n_e ln\Lambda}{T_e^{3/2}} \qquad (6.2)$$

where $ln\Lambda$ is the Coulomb collision parameter calculated from:

$$ln\Lambda = ln(12\pi n_e \lambda_d^3) \qquad (6.3)$$

where n_e is the electron density in m^{-3} and λ_d is the debye length in m. In using the above formula, it is assumed that only singly charged ions are present. Only electron-ion collision frequency is needed since the electron-electron collisions only redistribute energy among electrons and do not affect the electrical conductivity or the Hall parameter. Calculated electron collision frequencies for the near anode experiments are given in Table 6.2.

The collision frequency is necessary in determining the Hall parameter, as calculated in the next chapter.

6.1.2   Radial Ne and Te Results

Radial triple probe experiments were conducted at 150 V PFN (4.4 kA) and 160 V PFN (4.8 kA) at .5 g/sec Argon flow rate. Three axial locations were chosen for triple probe radial traverses. These locations were .23 in., .98 in. and 1.47 in. from the thruster exit plane. One of the major goals for this particular series of tests was to not only get radial temperature profiles but also some idea of the axial variation in temperature. The three axial locations were chosen because they represent three quite different regimes of the MPD. Near the backplate (1.47 in.), the incoming gas is cold and the gas is in the process of going from completely unionized to fully ionized. The mid thruster represents the bulk of the thruster where the gas is fully ionized and free from current or temperature concentrations. The near-exit location allows for the measurement of temperature and density gradients in the region of high current concentration near the anode lip. To get a sense of the axial variation in temperature and density, it makes sense to conduct radial traverses at the backplate, at the mid-thruster level and near the exit plane. Ideally, one should conduct a complete temperature and density map of the thruster at any given operation level. Due to time constraints, however, the three aforementioned locations were selected. The experiments were conducted at 4.4 and 4.8 kA thruster current level. The electron density radial profiles at the three axial locations are shown below in Figs. 6-36 and 6-37.

Electron density was maximum closest to the cathode and decreased radially in all cases. A profound "hump" was noticed .25 in. from the anode in the electron density. Numerical simulations of MPD thruster behavior such as the one being conducted by Niewood [49] have shown the so-called starvation regime near the anode. The density profile in the near exit-plane experiments shows a drop only near the anode, however. The reason that there is no obvious decline in electron density near the middle of the thruster in Fig. 6-36 is that even at the middle of the thruster the probe is still .4 in. from the cathode. In the MPD device being used for these tests, the cathode was recessed in the thruster such that the cathode tip was .625 in. inside the thruster and not aligned with the exit plane.
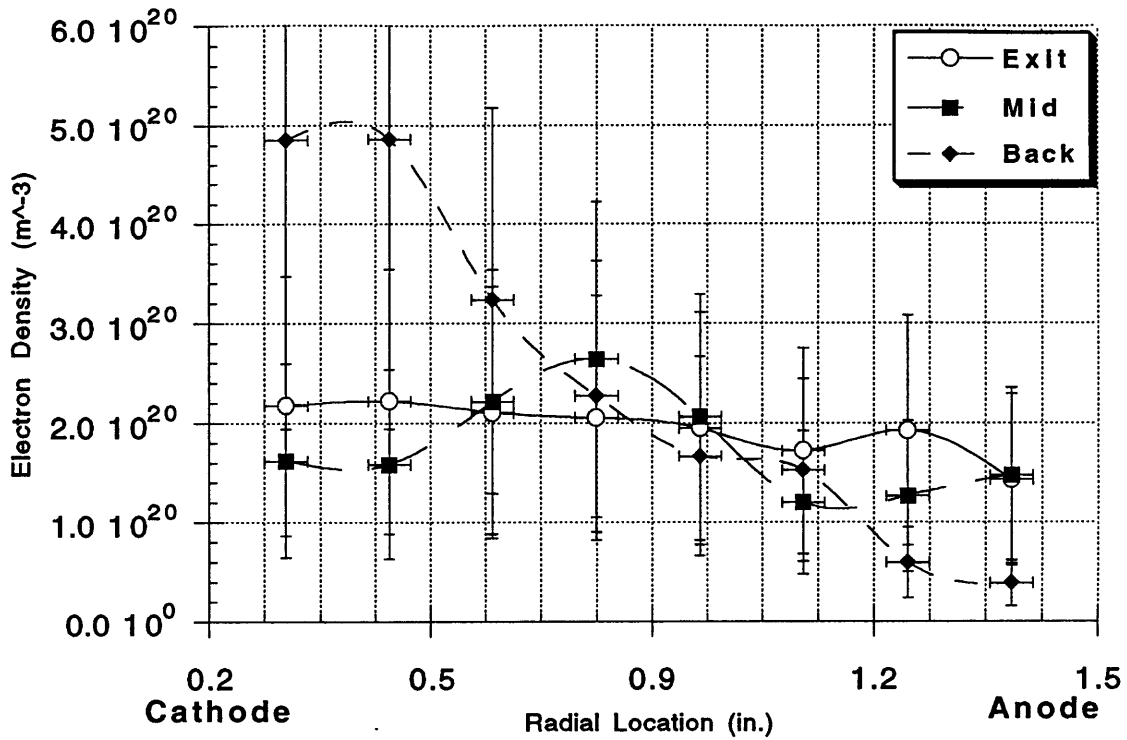
Figure 6-36: Radial Electron Density Profiles at Three Axial Locations for 4.4 kA
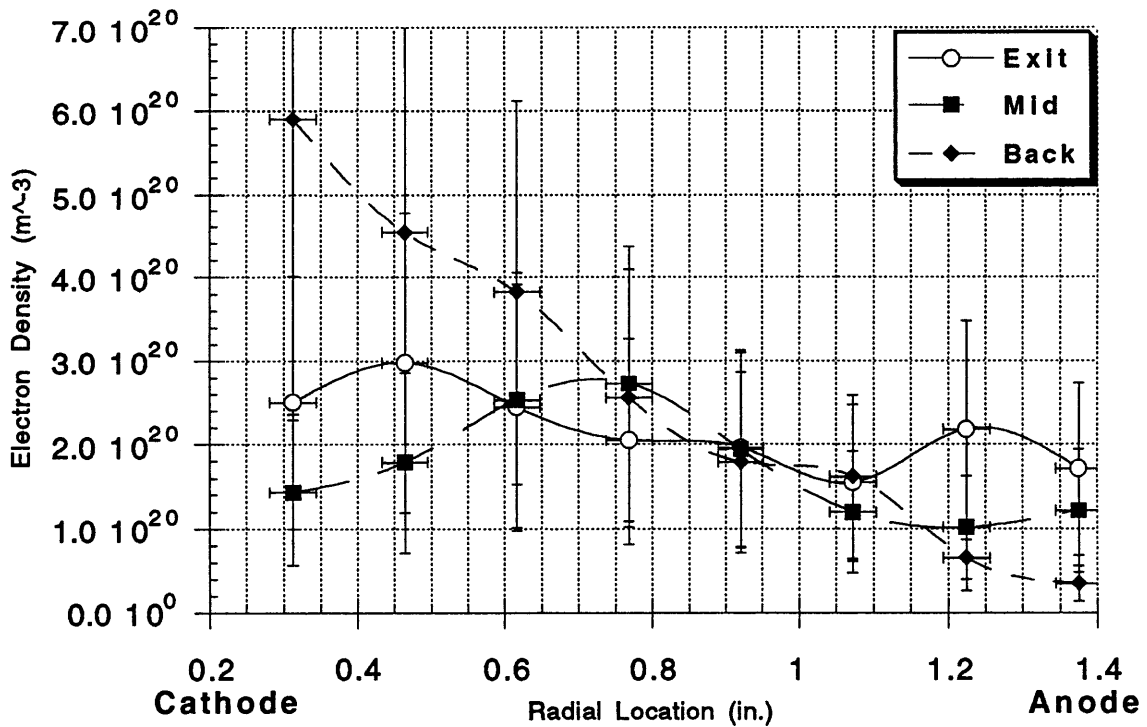
Figure 6-37: Radial Electron Density Profiles at Three Axial Locations for 4.8 kA

133

The density profiles and magnitudes for the two current levels are very similar. The jump in the near anode voltage drop from 4.4 kA to 4.8 kA current levels did not seem to correspond to any change in the electron density profile away from the anode. As can be seen in the figures above, the electron density profiles change significantly from one axial location to the next. Near the backplate, the density is extremely high near the cathode and drops sharply radially towards the anode. The near backplate electron density varied from 5 x $10^{20}m^3$ near the cathode to 3.5 x $10^{19}m^3$ near the anode. The reason for the high density near the cathode root is twofold: Nearly half the gas enters the MPD chamber through the .1875 in. thick annulus around the cathode; in addition, a high current concentration near the cathode root leads to high ionization and rise in electron density. The mid thruster level radial profile shows a sharp drop in electron density near both electrodes with the electron density rising from 1.6 x $10^{20}m^{-3}$ near the cathode to 2.64 x $10^{20}m^{-3}$ at the mid-radius level and dropping again to 1.47 x $10^{20}m^{-3}$ near the anode. The drop in the electron density near the cathode explains the large voltage drop near the cathode. The electron density, near the exit plane, varied from 2.2 x $10^{20}m^{-3}$ near the cathode to 1.4 x $10^{20}m^{-3}$ near the anode. It should be pointed out that the near-anode shot during the radial traverses at the three axial locations does not correspond to the near-anode location during the axial traverse. During the anode fall measurements, the floating probe was place roughly 1 mm. from the anode surface while the triple probe was placed such that the middle electrode was approximately 1.25 mm. from the anode surface while the outer two electrodes were roughly 1.4 mm. away. During the radial traverses, however, the triple probe was never closer than 3.2 mm. from the anode surface. As a result, the values for the electron density are different for the two sets of experiments.

In addition to the electron density measurements, the triple probe was used to acquire values for electron temperature as well. The radial electron temperature profiles at 4.4 and 4.8 kA are given in Fig. 6-38 and 6-39.

Near the backplate, the electron temperature varied from 4.2 eV near the cathode to 1 eV near the anode for the 4.4 kA current level. For the 4.8 kA current level, the
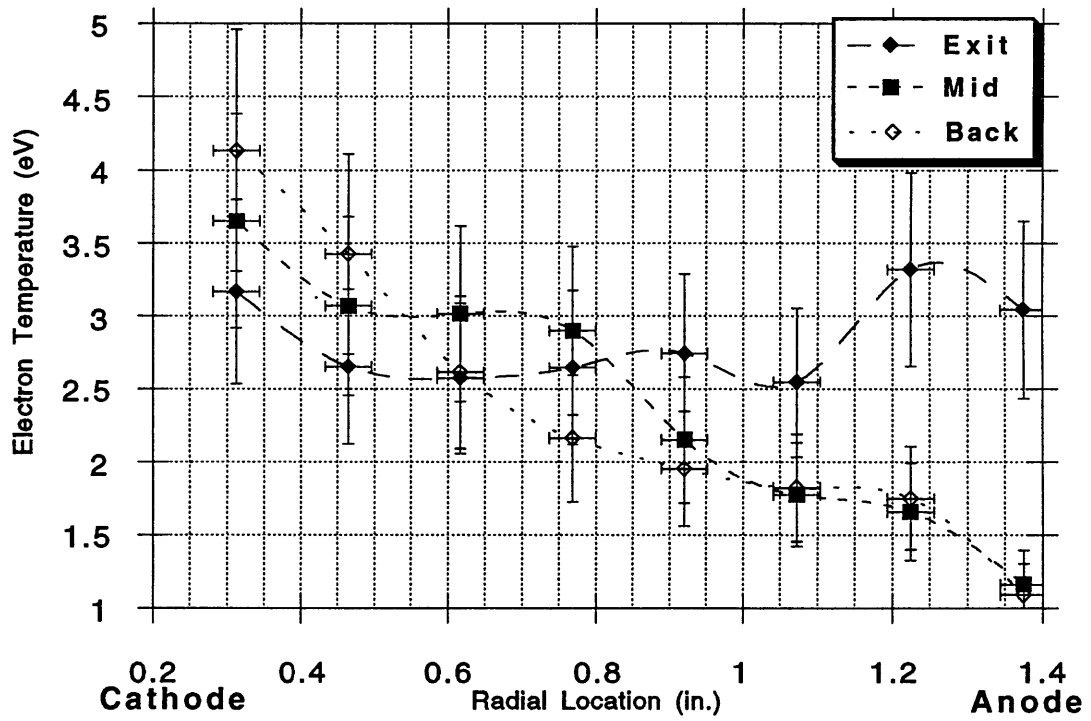
Figure 6-38: Radial Electron Temperature Profile at Three Axial Locations for 4.4 kA
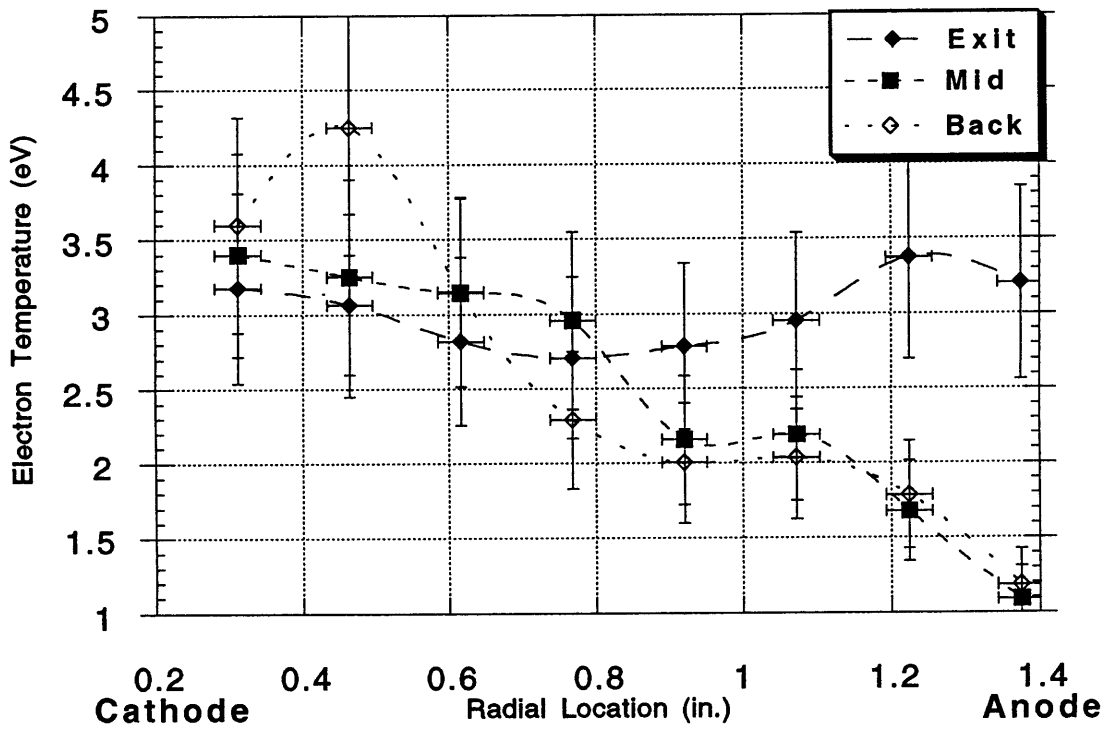
Figure 6-39: Radial Electron Temperature Profile at Three Axial Locations for 4.8 kA

values were roughly the same varying from 4.25 eV to 1.2 eV. At the mid-thruster location, the temperature decreases a bit near the cathode to 3.7 eV for both current levels dropping to 1 eV near the anode for both cases. Near the exit plane the temperature profiles looked very different than in the other two cases. The temperature decreased from 3.2 eV at the thruster centerline (.4 in. axially from the cathode) to 2.6 eV midway between the two electrodes and then rose again near the anode to 3.3 eV for both 4.4 kA and 4.8 kA cases. The near-anode shots during the radial traverse correspond to a distance of roughly 2 mm. from the anode. The near-anode axial traverse performed to determine the anode fall corresponded to the floating and triple probes being placed about 1 mm. from the anode. The T_e measurements near the anode are roughly the same for the axial traverse and radial traverse for the near-backplate and near exit locations. For the mid-thruster location, however, the axial traverse produced T_e values much higher than those measured during the radial traverse at the near-anode location ($\sim$3 mm. from anode surface). The reason for that discrepancy is not very clear but contamination and/or probe interaction with the anode surface may be to blame.

Once again, based on the radial electron temperature and density profiles, the Debye lengths and electron collision frequencies could be obtained. Radial profiles of the Debye length are shown in Figs. 6-40 and 6-41 for 4.4 and 4.8 kA, respectively. The corresponding collision frequency variations are shown in Figs. 6-42 and 6-43. A rise in the electron collision frequency is noticeable for the mid-thruster axial location near the anode for both 4.4 and 4.8 kA levels due primarily to the low electron temperatures ($\sim 1eV$).

6.2   Discussion of Triple Probe Results

Both near-anode axial scan and radial scans with the triple probe yielded reasonable results. A very profound dual hump behavior in the temperature was seen during the near-anode axial traverse. The fact that the profile was repeatable for all current levels indicates that the effect was real and not a probe error. The magnitudes of
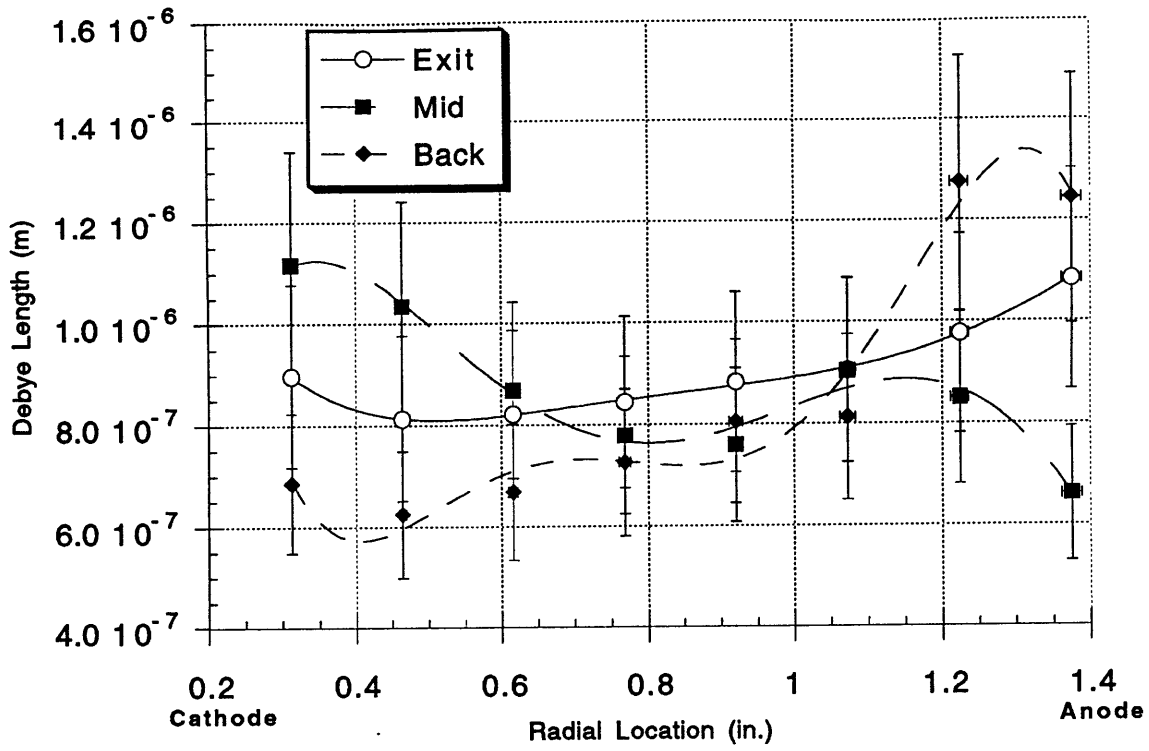
Figure 6-40: Radial Debye Length Profiles For 4.4 kA
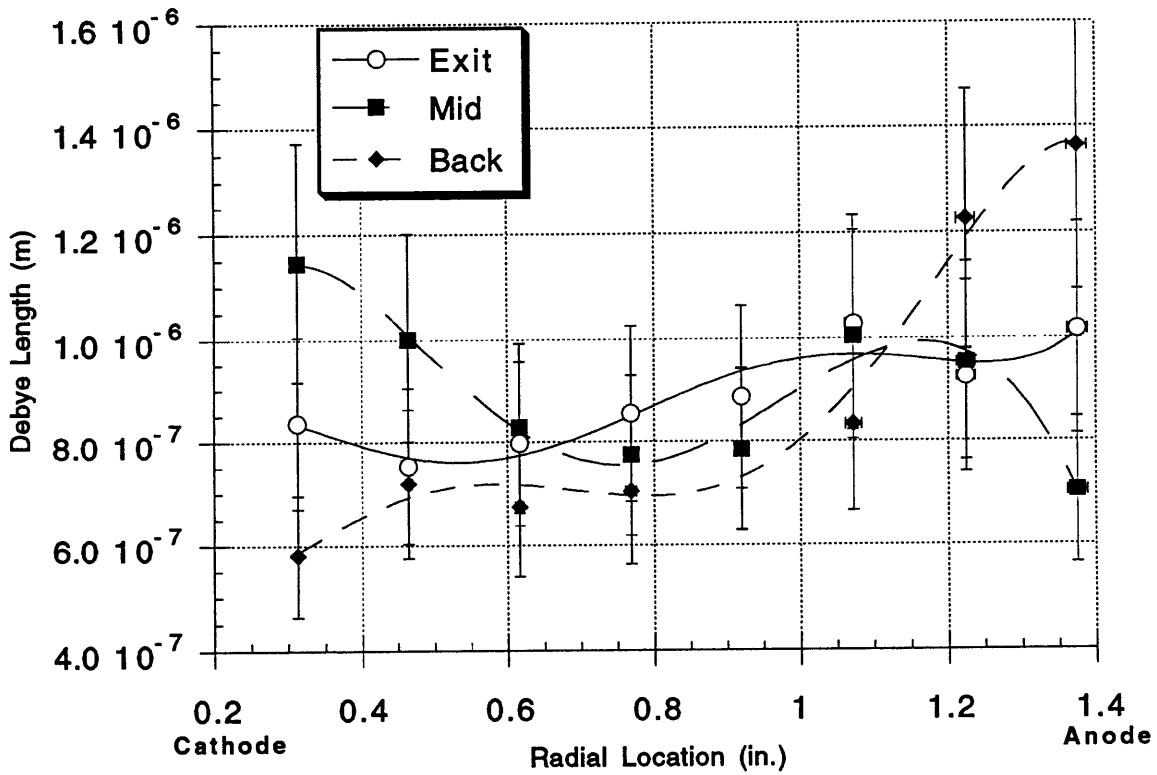
Figure 6-41: Radial Debye Length Profiles For 4.8 kA

138
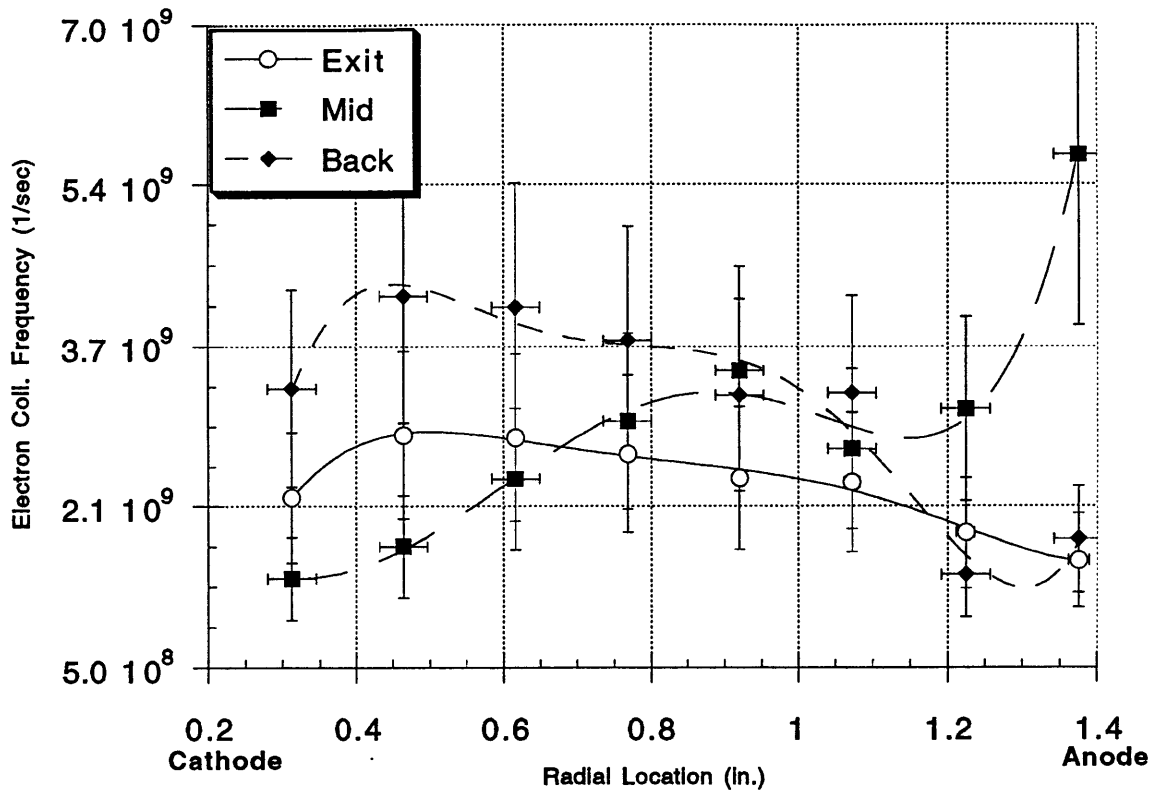
Figure 6-42: Radial Electron Collision Frequency Profiles For 4.4 kA
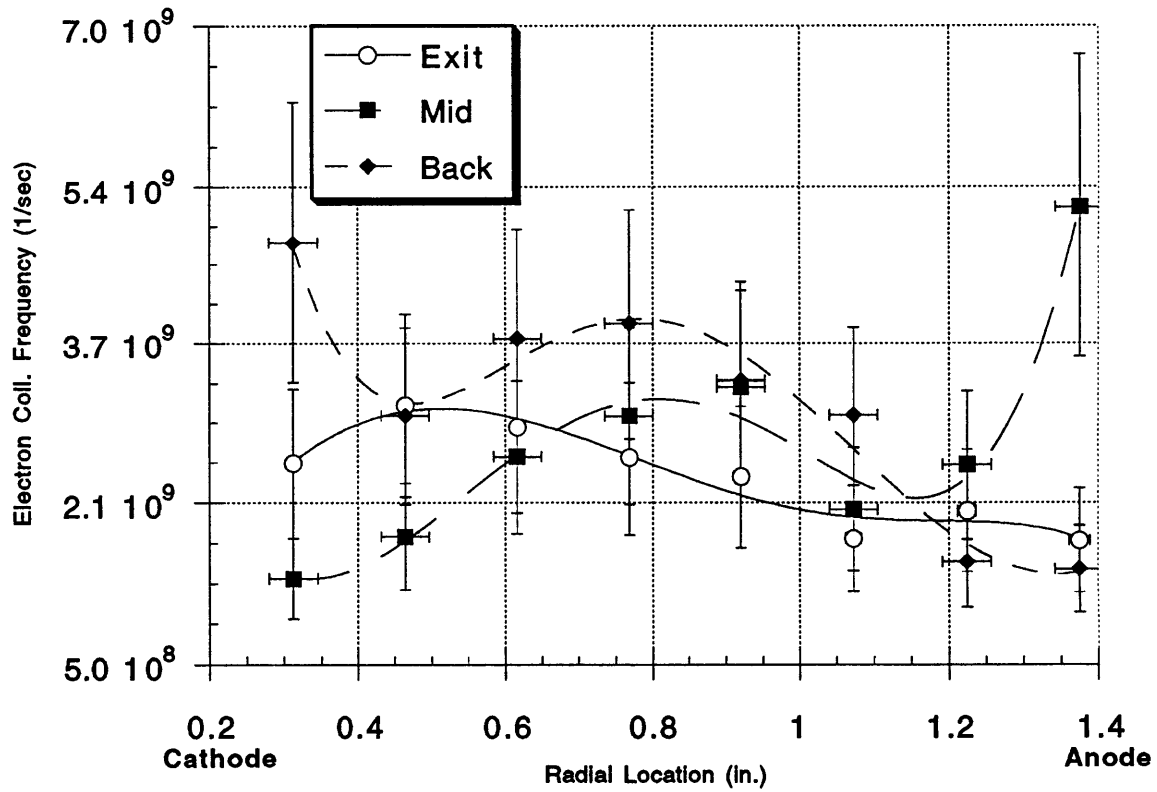
Figure 6-43: Radial Electron Collision Frequency Profiles For 4.8 kA

the indicated electron temperature are questionable, however. For Argon, electron temperature in excess of 4 eV or so are unlikely since several energy levels provide an energy buffer. In other words, the excessive energy present in the Argon plasma goes into exciting the species to higher energy levels rather than a temperature rise.

Probe errors may be to blame, then, for the unusually high T_e values at high current levels. Near the anode, the probe was visually aligned with the thruster axis. For accurate results, however, the triple probe needs to be aligned with the ion flow. Gallimore [21] conducted extensive triple probe experiments inside the Princeton benchmark thruster and found that a ten degree probe angle deviation with respect to the flow could alter the T_e value by a factor of two. Ideally, therefore, several shots should be fired with the probe at different angles with respect to the thruster and the average of the shots corresponding to the lowest probe voltage signal should be used for analysis. Time constraints, however, negated the use of that process. In addition to the alignment problem, contamination of the probe can lead to an over estimation of both electron temperature and electron density[64]. During experimentation, the probe should be cleaned after every shot via either ion-bombardment or electron-bombardment technique. For this study, due to time constraints, the probe was cleaned after every ten shots.

The reason for the temperature rise at the two axial locations in not completely clear. Theoretical efforts in the field have indicated that near the backplate, the flow transitions from subsonic to supersonic [49]. With the presence of a shock, the ions can have a larger perpendicular than parallel flow component with respect to the probe, leading to higher voltage and current signals. Although the above argument may apply to the temperature jump at the first axial location (.375 in.), the jump at 1.25 in. has to be explained differently. Large ohmic dissipation, due to large radial current density, low electrical conductivity or a combination of both, could result in the higher temperature at that location. In the next chapter, this issue will be addressed with the measurement of magnetic fields in the region.

During the near-anode triple probe experiments, electron density decreased, in general, with increasing current. This could be attributed to the anode starvation

mechanism (Hall parameter) which increases with increasing thruster current corresponding to higher temperature and lower electron collision frequency ($\sigma \sim T_e^{-1.5}$). A current concentration was expected to lead to higher ionization and consequently an increase in electron density at the anode lip. Current concentration induced ionization may explain the rise in N_e seen at 1.375 in.

Radial temperature and density profiles were determined at .23 in., .98 in. and 1.47 in. from the exit plane for 4.4 and 4.8 kA thruster current levels. The electron temperature decreased radially from the cathode to the anode in all three cases. Highest temperatures were observed near the cathode root where large current concentration is expected. A slight increase in T_e was also noticed near the anode lip which is another high current concentration area. As mentioned earlier, the probe was cleaned after every ten shots with the glow discharge technique. Probe contamination was unavoidable, however, especially near the cathode where contaminant concentration was expected to be high. Mass spectroscopy conducted on a MPD thruster similar to the one used for this study has indicated the presence of the aforementioned materials [40]. After each radial scan, the probe housing (alumina tubes, plexiglass holder etc.) were seen covered with contaminants. Contamination is expected to have caused an increase in the indicated electron temperature and density values.

The high electron density near the cathode root can be attributed to two major factors: 1) Nearly 60% of the incoming gas enters the chamber through the annulus around the cathode and 2) Due to high current concentration at the cathode root, subsequent ionization causes a rise in the electron density in the region. At the mid-thruster axial location (.98 in.), the electron density drops near both the cathode and the anode. This result is especially interesting because it clearly shows a drop in electron density near both the cathode and the anode. The anode density drop could be due to the anode starvation mechanism that has been described previously. The mechanism present near the cathode is quite different, however. Low electron density near the cathode could be due to the relatively low ionization fraction present. Current concentration near the anode lip and the cathode root cause high ionization in those regions increasing the number of electrons in those region. A comparable

mechanism for electron production is absent from the middle of thruster channel at the thruster axis. The high electrode voltage drops observed at the mid-thruster location with the floating probe can now be related directly to low electron density observed near both electrodes.

Although a majority of the results obtained through the triple appear reasonable, error sources as discussed in Appendix A must be kept in mind. Bowman [8], who conducted triple probe experiments with the same thruster as used in this study found that in certain regions of the thruster, the presence of the probe caused global plasma characteristics to change considerably. He found that with the probe at the 1.0 in. location, onset was induced in the thruster. He argues that the presence of the probe causes the current paths to shift resulting in onset. Although, no exceedingly high probe voltage signals were observed during the experiments, signal noise was very apparent except at very low power levels.

The last set of experiments were performed to measure the magnetic field strengths and enclosed current profiles throughout the thruster. The values for electron collision frequencies calculated in this chapter can be used in conjunction with the measured magnetic field to deduce the Hall parameter. In addition, current density values calculated from the measured magnetic field, along with the classically calculated electrical conductivity can be used to yield the near-anode ohmic dissipation. These experiments are described in the next chapter.

Chapter 7

Magnetic Induction Probe Results

Induction probe measurements were conducted within the thruster on a grid of seven axial and eight radial locations. The magnetic field measurements made could be used to yield the Hall parameter, which has been related to large anode falls by several researchers [22, 49]. In addition, the measurements can be used to calculate the enclosed current profiles throughout the thruster indicating regions of current concentration that have been speculated previously to be near the cathode root and the anode tip. Furthermore, knowing the current profiles and the Hall parameter, ohmic dissipation can be calculated near the anode to determine whether the temperature rise measured at .375 in. and 1.25 in. near-anode axial locations were due to high ohmic heating. The obtained measurements and calculated parameter values are presented in the section to follow.

7.1   Induction Probe Measurements

The magnetic field measurements were obtained throughout the thruster via a magnetic probe consisting of a 75 turn cylindrical copper coil sealed within a quartz tube. The probe was calibrated to yield magnetic field strengths from the measured probe voltage output. A sample induction probe output is shown in Fig. 7-1.

The probe signal was sent through an amplifier-integrator circuit (see Appendix A) and recorded on a Tektronix DSA601 digitizing oscilloscope.
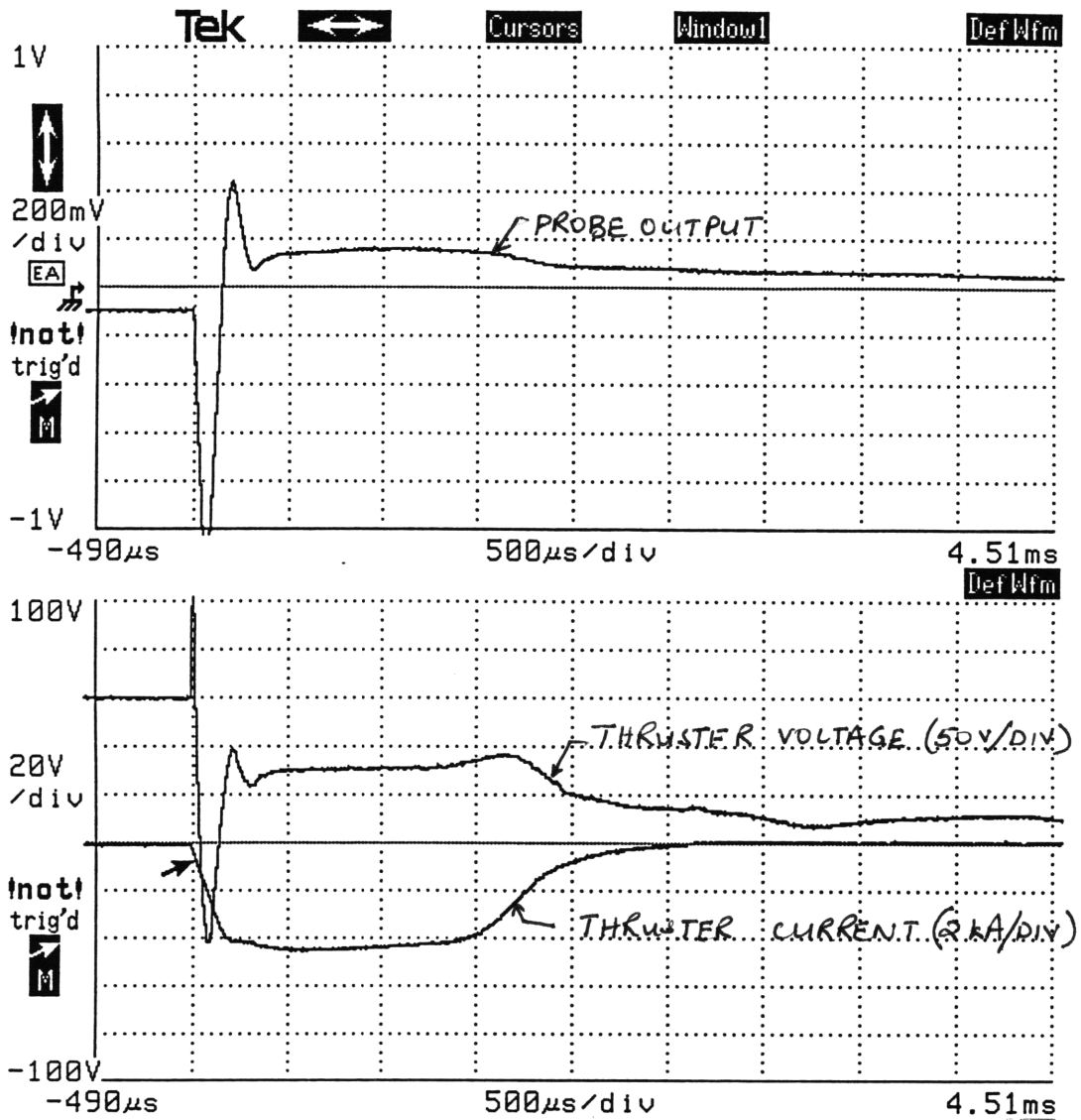
Figure 7-1: A Typical Induction Probe Output
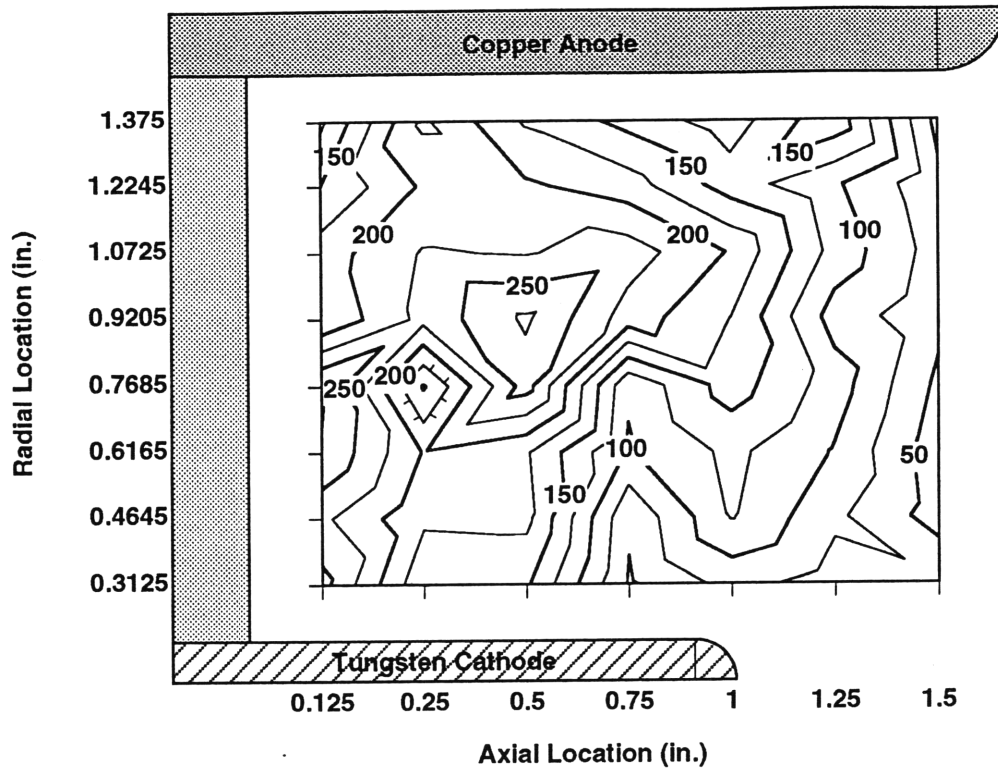
Figure 7-2: Constant Magnetic Field (Gauss) Line Contours at 4.4 kA

Three shots were fired at each spatial location for each current level with Argon flowing at .5 g/sec. The average of the three shots was recorded as the magnetic field strength for analysis. Constant magnetic field contours (in Gauss) for both 4.4 kA and 4.8 kA are shown in Figure 7-2 and 7-3.

The measured values for the magnetic field are presented in Tables 7.1 and 7.2 for 4.4 kA and 4.8 kA, respectively. The magnetic field, in general, decreased radially from the cathode to the anode and axially from backplate towards the exit plane.

Knowing the magnetic field strengths in conjunction with the electron temperature and density obtained from triple probe measurements, the Hall parameter could now be calculated ($\Omega = \omega_e/\nu_e$). Although twelve near-anode axial locations were used for the floating probe and triple probe experiments, due to time constraints, only seven locations separated by .25 in. were used for the Induction probe scans. Therefore, only those seven near-anode Hall parameter values could be calculated. The near-anode axial variation in the Hall parameter at 4.4 and 4.8 kA is shown in Fig. 7-4.

145
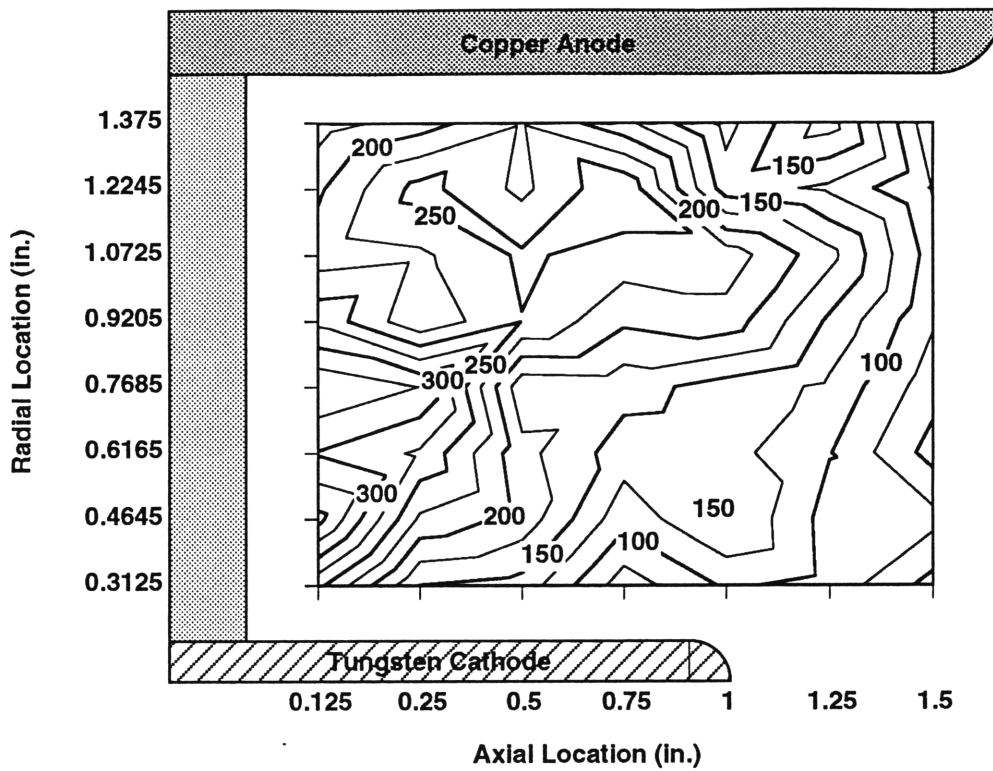
Figure 7-3: Constant Magnetic Field (Gauss) Line Contours at 4.8 kA

Rad. Location	B@.125 in.	B@.25 in.	B@ .5 in.	B@ .75 in.	B@ 1.0 in.	B@ 1.25 in.	B@ 1.5 in.
0.3125	258	154	153	47	84	64	72.5
0.4645	230	179.3	182	54	126.67	80	38.67
0.6165	274	198	178	96	131.33	98	35
0.7685	278	147.3	261.3	105	162.5	112.67	45
0.9205	178	232	279.3	214	174.67	89	57
1.0725	187.33	227.3	223	238	198	116	64
1.2245	150	203.3	204	187	138	104	56.67
1.375	119.3	230	172	142	111	169.3	42

Table 7.1: Measured Magnetic Field Strengths (Gauss) at 4.4 kA

146

Rad. Location	B@.125 in.	B@.25 in.	B@ .5 in.	B@ .75 in.	B@ 1.0 in.	B@ 1.25 in.	B@ 1.5 in.
0.3125	256	256	140	60.67	104	91.3	40.67
0.4645	358	358	191	108.7	153.3	89.3	83.33
0.6165	298	298	183.3	137	134	101.3	40
0.7685	348	348	157.3	160	140	120	60.67
0.9205	268.67	268.67	249.3	204.7	215.3	146	78
1.0725	212	212	254	239	239.3	183.3	88
1.2245	196	196	218.67	271.3	137	120	73
1.375	162.67	162.67	223.3	182	116	187	54

Table 7.2: Measured Magnetic Field Strengths (Gauss) at 4.8 kA
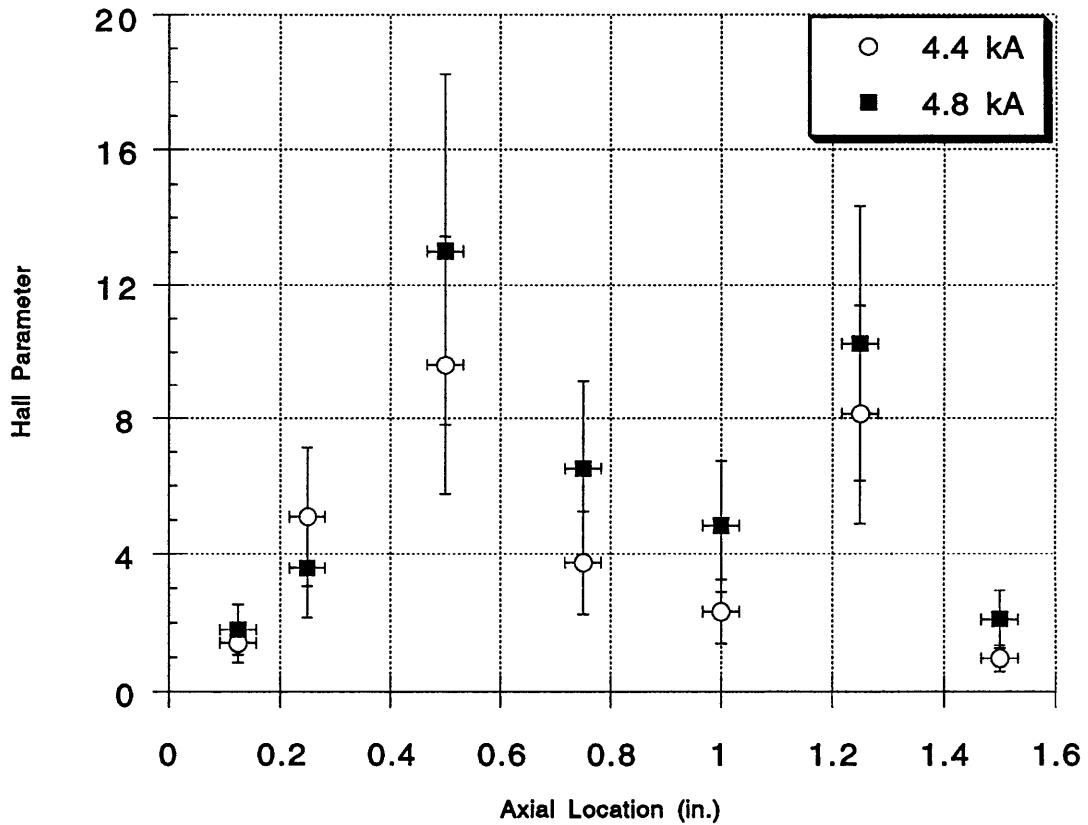
Figure 7-4: Near-Anode Axial Hall Parameter Profiles For 4.4 and 4.8 kA
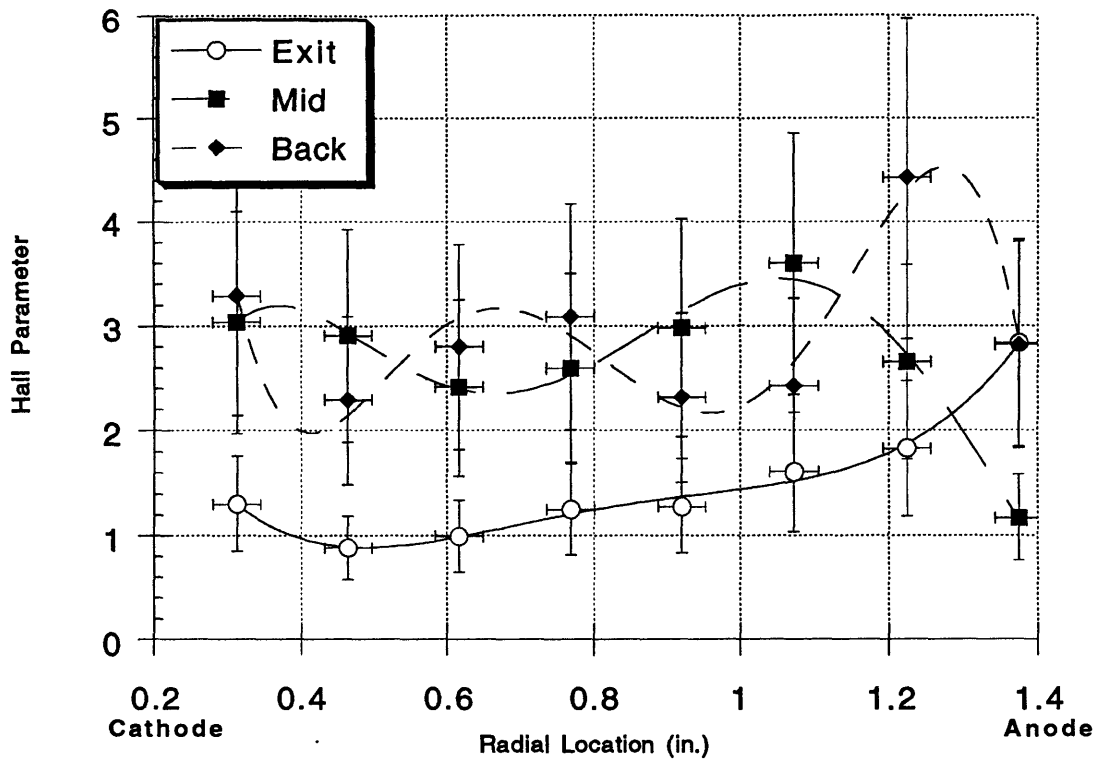
Figure 7-5: Radial Electron Hall Parameter Profiles For 4.4 kA

The electron gyrofrequency ($\omega_e = eB/m_e$) was calculated from the measured magnetic field strength and electron collision frequency (ν_e) was determined based on the measured near-anode electron temperature and density. A large variation was seen in the Hall parameter axially. For 4.4 kA, the parameter varied from 1.0 to 9.6. For 4.8 kA, a variation from 1.8 to 13.0 was observed. A rise in the parameter was seen at .5 in. and 1.25 in. axial locations.

In addition to the near anode values, radial Hall parameter profiles at the three axial locations were obtained for 4.4 and 4.8 kA and are shown in Figs. 7-5 and 7-6, respectively.

The Hall parameter was measured to be greater than one almost everywhere in the thruster. Hall parameters values varied from .8 to 5.4 during the radial traverses, dropping under one only for the near-exit shots near thruster axis.

Magnetic field measurements were also used to calculate enclosed current profiles using the following equation:
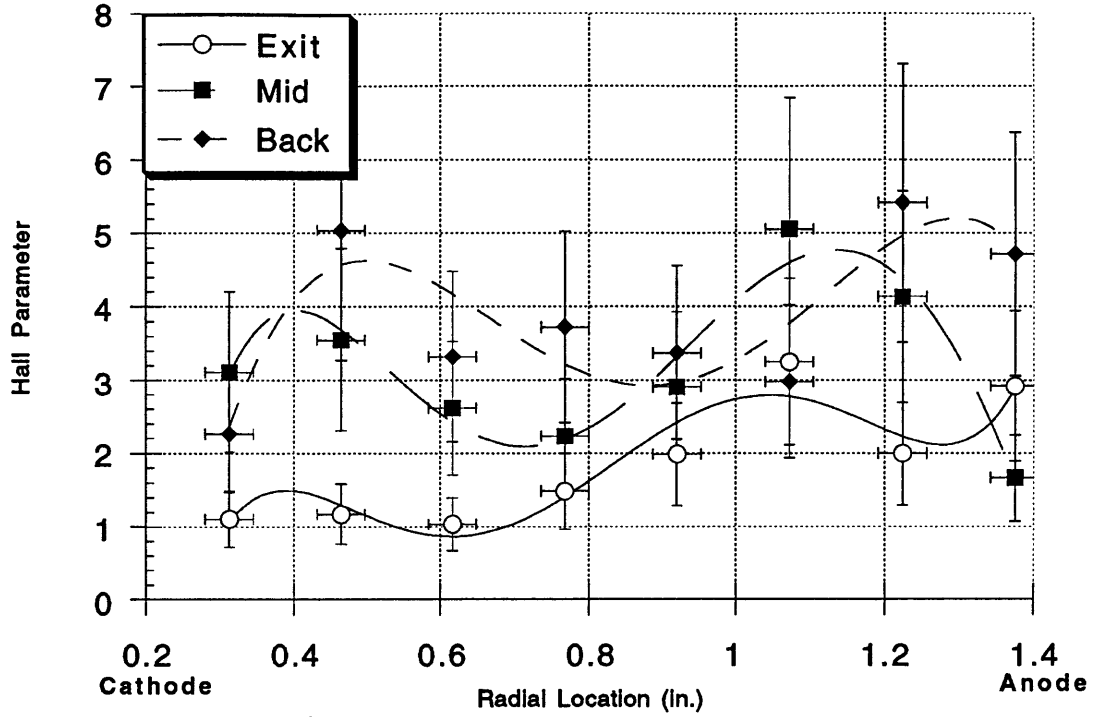
Figure 7-6: Radial Electron Hall Parameter Profiles For 4.8 kA

$$I_{encl} = \frac{2\pi r_p B_{meas}}{\mu_o} \tag{7.1}$$

where r_p is the probe radial location, B_{meas} is the measured magnetic field in Tesla and μ_o is the permittivity of free space $(4\pi \times 10^{-7} H/m)$. The resulting enclosed current contours are shown in Figs. 7-7 and 7-8 for 4.4 kA and 4.8 kA, respectively. As expected, enclosed current values increased radially from cathode to anode and axially from the exit towards the backplate.

To further verify the current concentration behavior, radial current density near the two electrodes was calculated using the following equation:

$$J_y = \frac{1}{\mu_o} \frac{dB}{dx} \tag{7.2}$$

where dB/dx was approximated by:
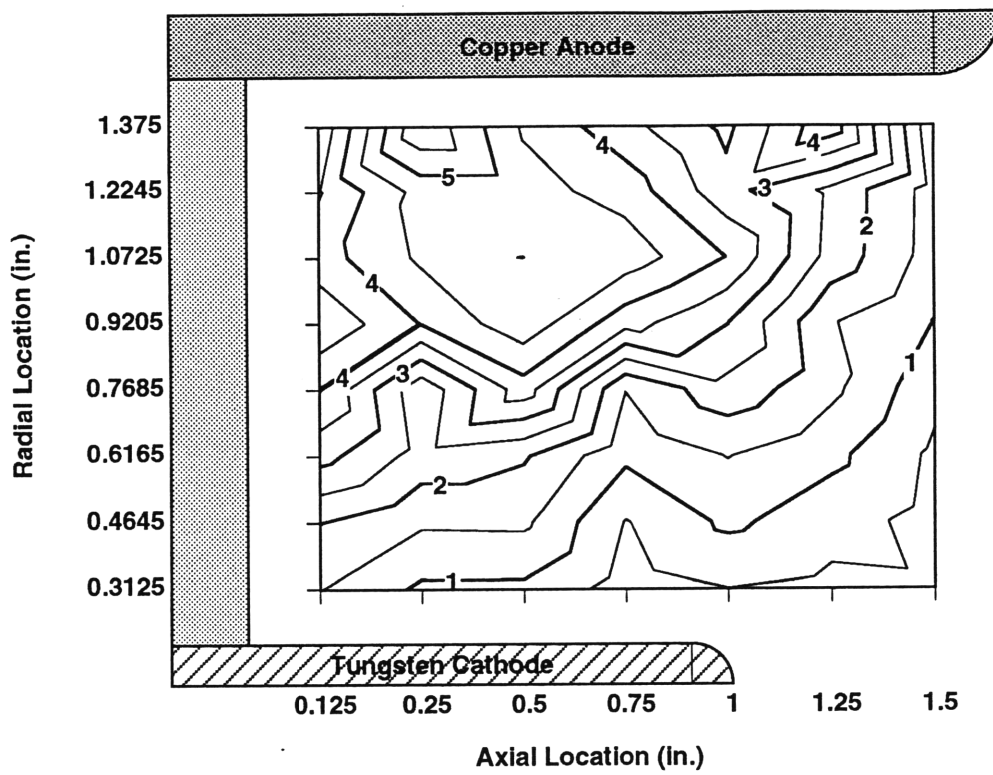
Figure 7-7: Enclosed Current (kA) Line Contours at 4.4 kA
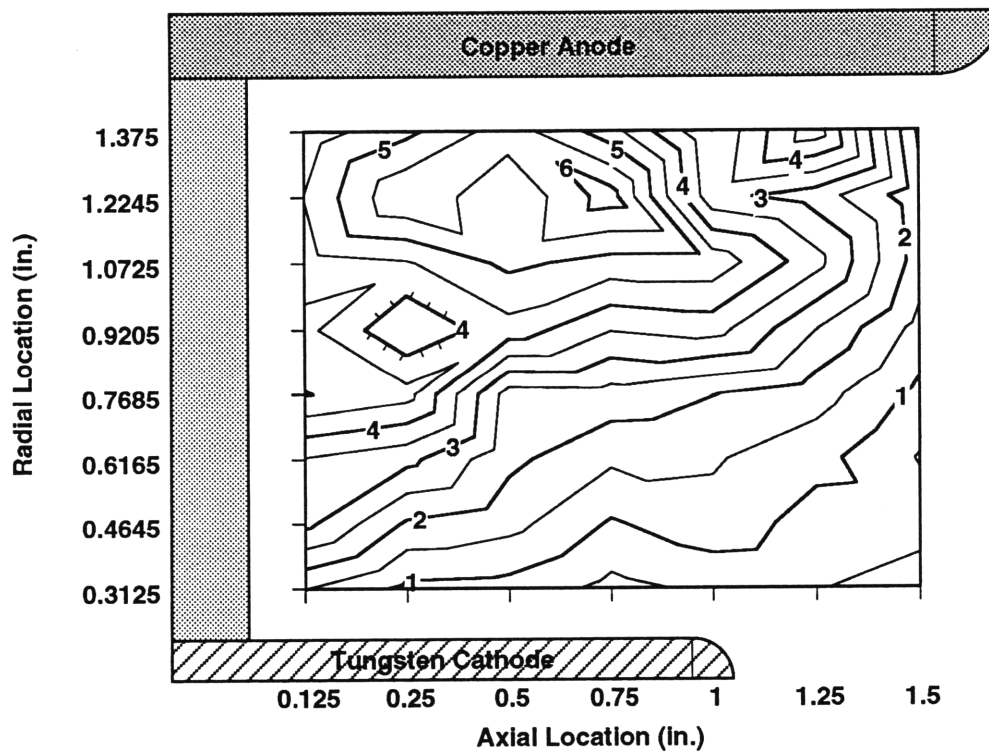
Figure 7-8: Enclosed Current (kA) Line Contours at 4.8 kA

150
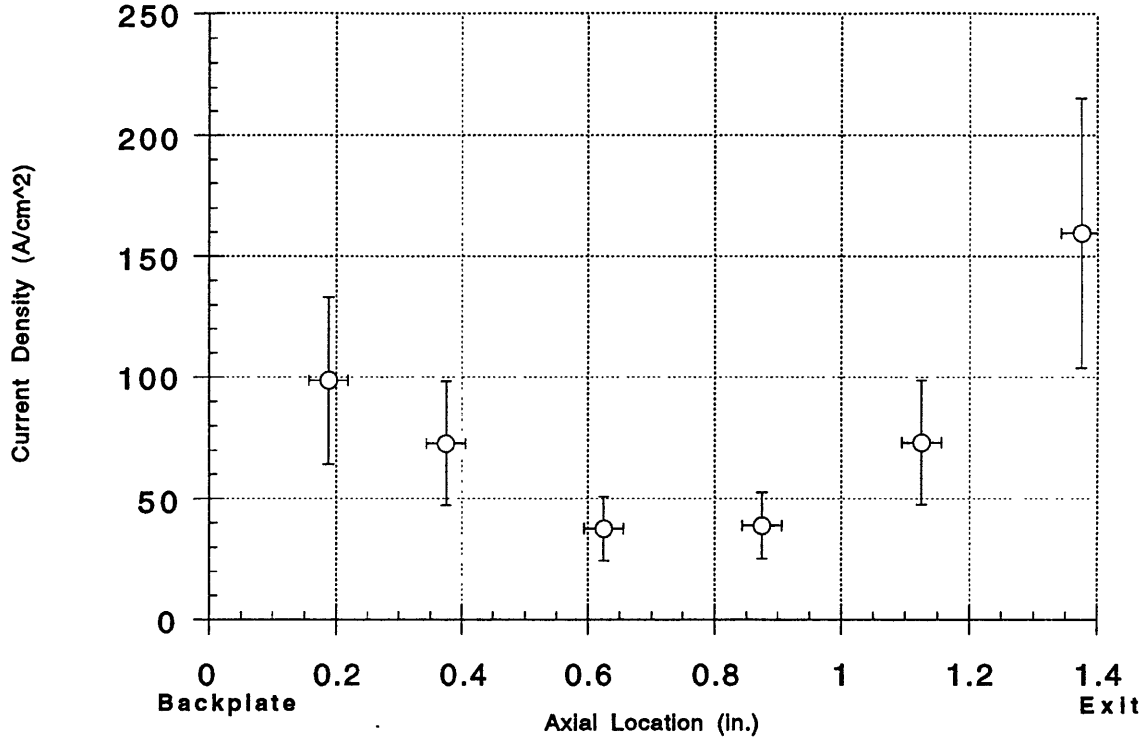
Figure 7-9: Near Anode Radial Current Density For 4.4 kA

$$\frac{dB}{dx} = \frac{\Delta B}{\Delta x} = \frac{B(x) - B(x + \Delta x)}{\Delta x} \tag{7.3}$$

Radial current density (J_y) profiles near both electrodes for 4.4 and 4.8 kA are shown in Figs. 7-9 through 7-12.

Figs. 7-9 through 7-12 clearly show a sharp rise near the anode lip and the cathode root, as expected. The current density varied from over $250 A/cm^2$ near the cathode root to about $50 A/cm^2$ near the exit plane. One must be reminded that the cathode was recessed .625 in. from the exit plane. The values for current densities beyond the 1.0 in. axial location in the near-cathode cases correspond to a distance of .125 in. or more from the cathode surface. Near-anode current density rose gradually from roughly $100 A/cm^2$ for 4.4 kA and $65 A/cm^2$ for 4.8 kA near the backplate to a value of $180 A/cm^2$ for both 4.4 and 4.8 kA at the anode lip.

Measured values of current densities were used to determine the anode power fractions, in conjunction with the floating probe data (anode fall) using the following

151
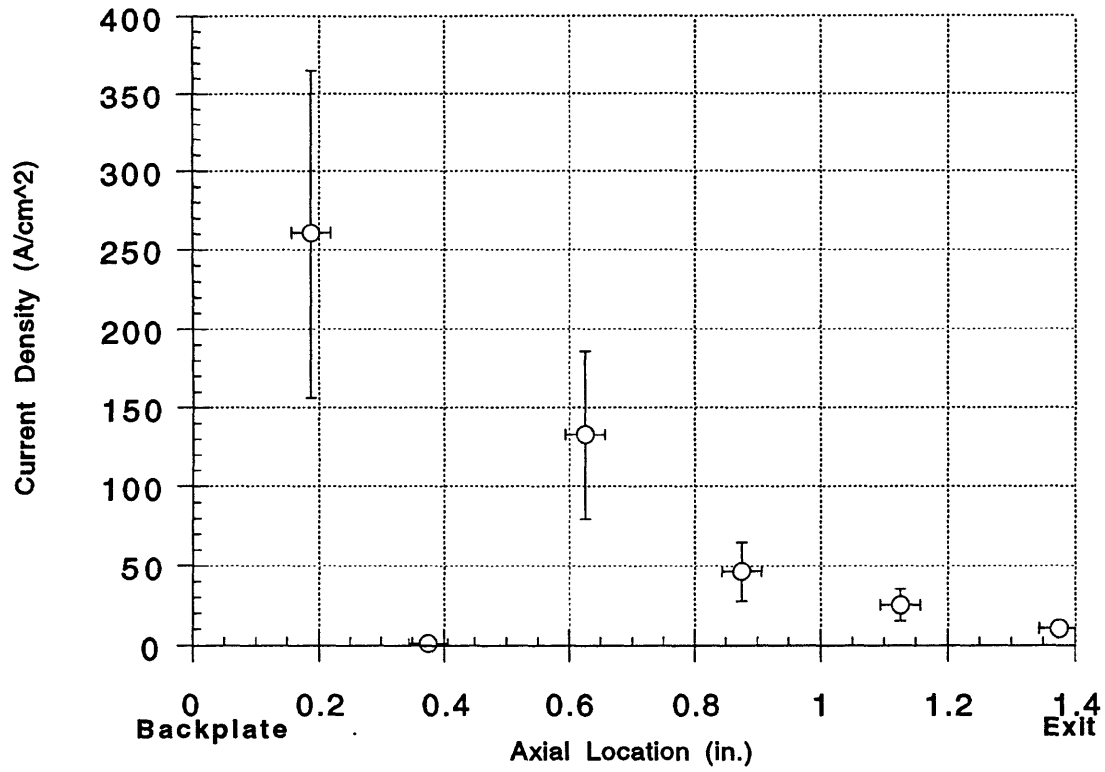
Figure 7-10: Near Cathode Radial Current Density For 4.4 kA
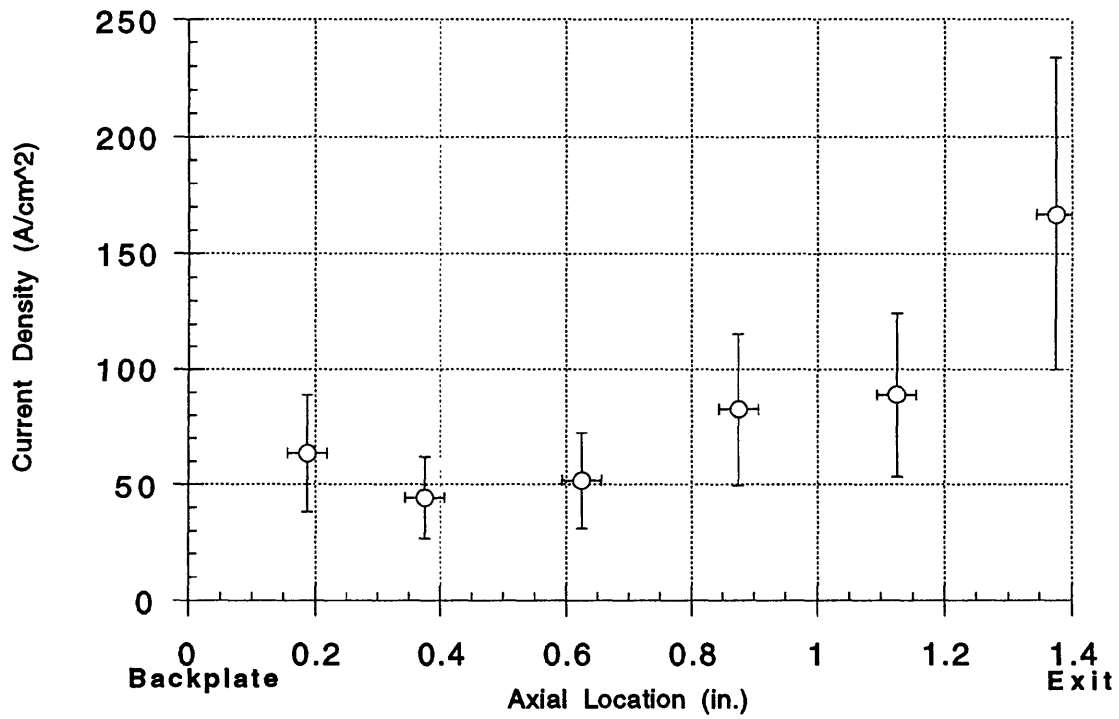
Figure 7-11: Near Anode Radial Current Density For 4.8 kA
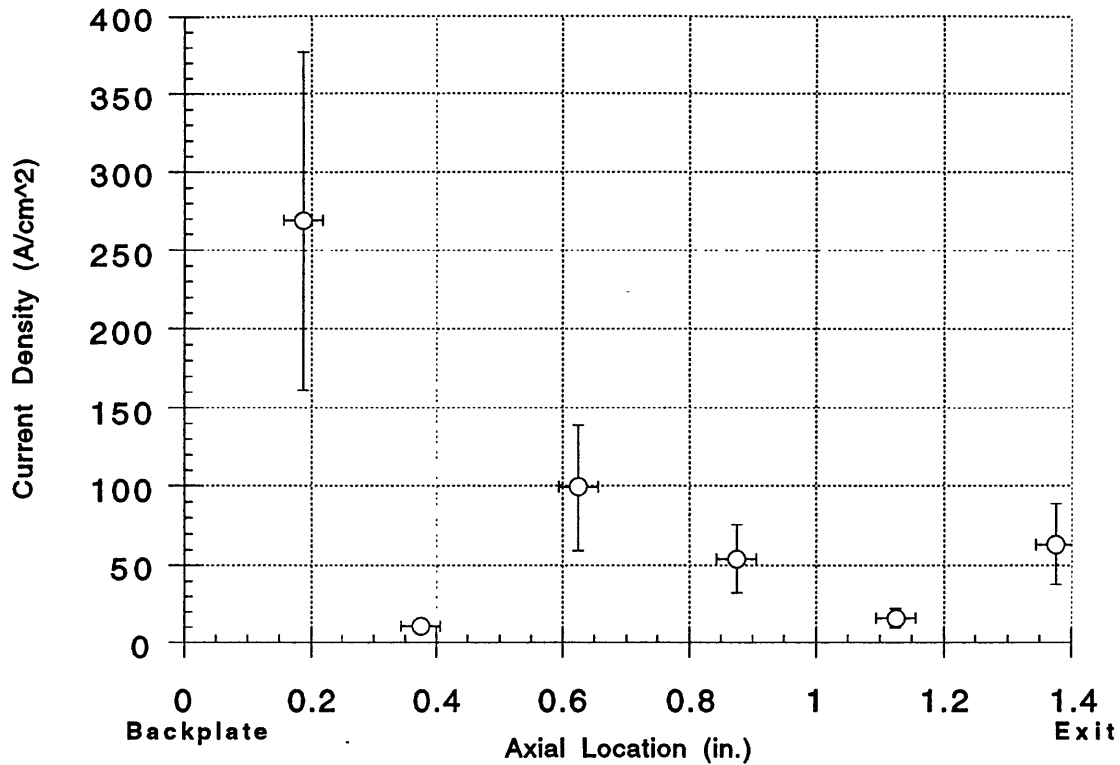
Figure 7-12: Near Cathode Radial Current Density For 4.8 kA

equation:

$$P_{anode} = \sum_i \Delta V_i (J_i 2\pi r_{anode} \Delta x) \tag{7.4}$$

where i represents a slice of the thruster of thickness Δx (.25 in.) and r_{anode} is the magnetic probe near-anode radial location, J_i is the radial component of the current density and ΔV_i is the measured anode fall for each thruster slice. In the above equation, the power deposition to the anode by the random electron thermal energy (kT_e/e) and the heat liberated due to the work function of the anode material (ϕ) has been neglected. The anode power fraction, due to the anode fall, was calculated to be 33% and 40% ($\pm$5%) for 4.4 and 4.8 kA, respectively.

Finally based on the calculated current density near the anode and the electrical conductivity which could be calculated classically based on triple probe results, ohmic dissipation at the anode was determined as given by:

153

$$Q_{ohmic} = \frac{j^2}{\sigma_o} \qquad (7.5)$$

where j is the current density calculated using the following equation:

$$j^2 = j_x{}^2 + j_y{}^2 \qquad (7.6)$$

where j_x and j_y are the axial and radial current density components, respectively. The electrical conductivity (σ_o) was calculated using the following equation:

$$\sigma_o = \frac{e^2 n_e}{m_e \nu_e} \qquad (7.7)$$

where n_e is the electron density and m_e is the electron mass. ν_e is the electron collision frequency calculated from the following equation [20]:

$$\nu_e = 2.91 \times 10^6 n_e (T_e)^{-1.5} ln\Lambda \qquad (7.8)$$

In the above equation, T_e is the electron temperature and $ln\Lambda$ is the coulomb collision parameter:

$$ln\Lambda = ln\left(12\pi n_e (\lambda_d)^3\right) \qquad (7.9)$$

where λ_d is the Debye length. The values for j^2/σ_o are plotted in Figs. 7-13 and 7-14 for 4.4 and 4.8 kA, respectively.

7.2 Discussion of Induction Probe Results

Scans with the Induction probe provided reasonable profiles for both magnetic fields and enclosed current values. These results, in conjunction with the triple probe experiments were used to calculate the near-anode Hall parameter and ohmic dissipation values.

A major point of interest during these experiments was the fact that the enclosed current at certain locations exceeded the total measured thruster current, indicating

154
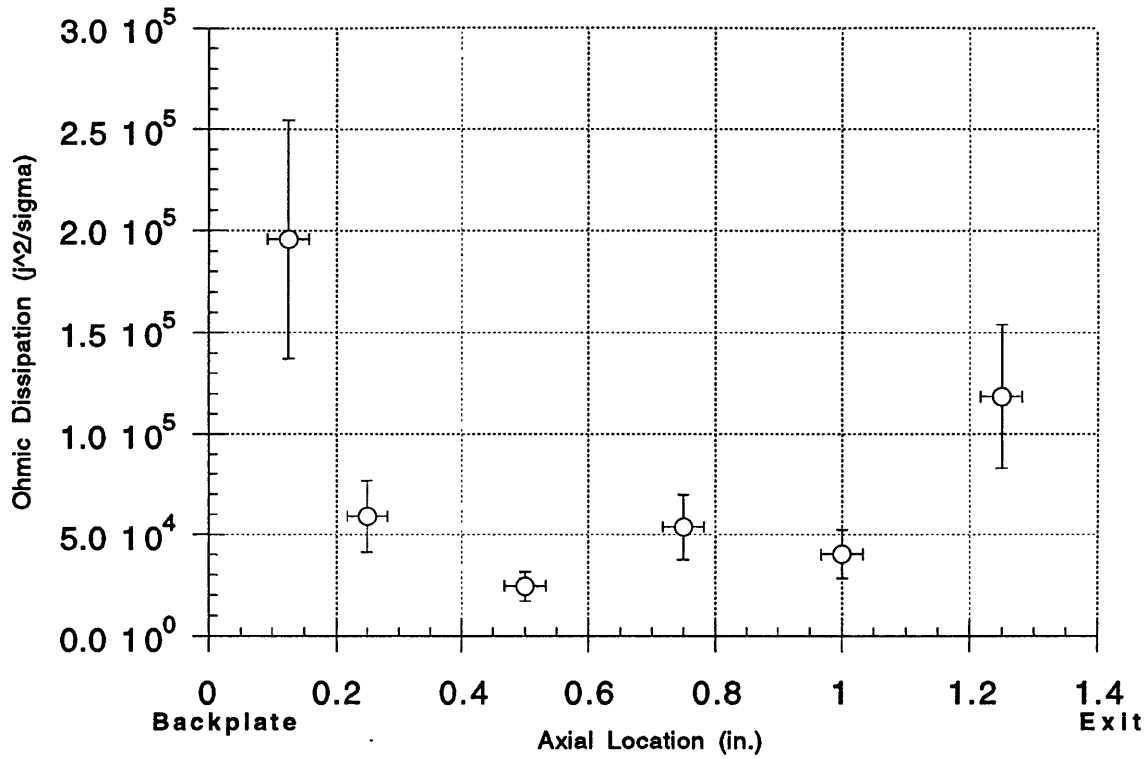
Figure 7-13: Axial Ohmic Dissipation Profile at 4.4 kA
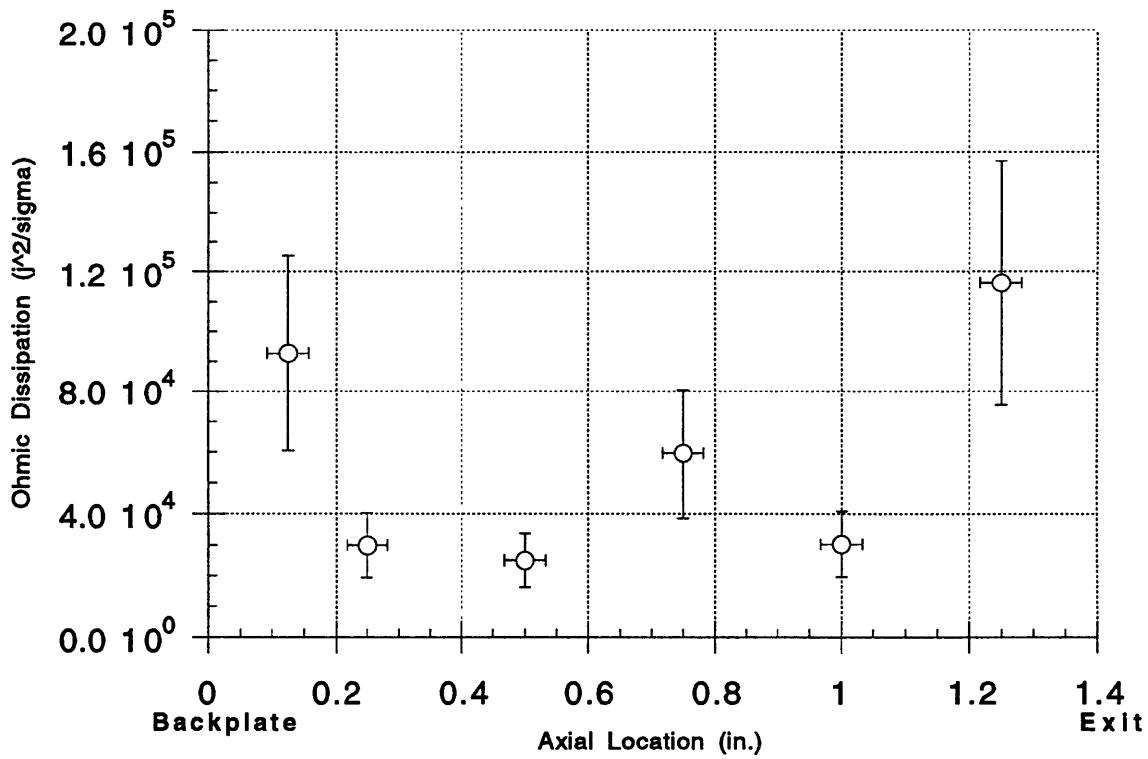
Figure 7-14: Axial Ohmic Dissipation Profile at 4.8 kA

155

an error in the calibration process. During the calibration process, the probe was placed very close to the backplate and as close to the anode surface as possible. This was done to ensure that the entire thruster current was being enclosed by the probe. The coil itself, however, was buried roughly .125 in. inside the sealed edge of the quartz tube. It is possible, therefore, that some of the current escaped without being measured by the probe. This, in turn, would suggest an overprediction of enclosed current values at all locations. The total error in the magnetic field measurement due mainly to calibration is estimated to be 40%.

Figs 7-7 and 7-8 show regions where apparent current loops occur in the core of the thruster or current contours begin and end at the anode. The former cannot be true during steady state operation and therefore must be treated as an artifact of the induction probe experimentation and must be included in the error estimate for the magnetic field values. Current contours that seem to begin and end at the anode may have a logical explanation, however. The induction probe was never brought closer than .125 in. from the backplate axially and the anode surface radially. There is a possibility, therefore, that the current lines actually do connect between the two electrodes but the induction probe was never in the region (either close to the anode surface or the backplate) to actually measure them. A possible enclosed current profiles that may explain the enclosed current contours beginning and ending at the anode is shown in Fig. 7-15. This would still involve the enclosed current contours to bend in an unusual manner. Supplemented by the temperature rise and corresponding decrease in voltage drop seen at .375 and 1.375 in. axial locations, one can conclude that the overall plasma behavior changes rather drastically at those two axial locations. The reason for the strange behavior, however, is unclear.

Calculated ohmic dissipation profiles show a definite rise at .125 in. and 1.25 in. axial locations corresponding roughly to the locations of the T_e rise seen during the triple probe experiments. A large dissipation was expected near the anode lip since the enclosed current contours showed a large concentration in that region. Although no current concentration was observed at .375 in. axial location, low electrical conductivity does lead to high dissipation at the .125 in. location. In addition,
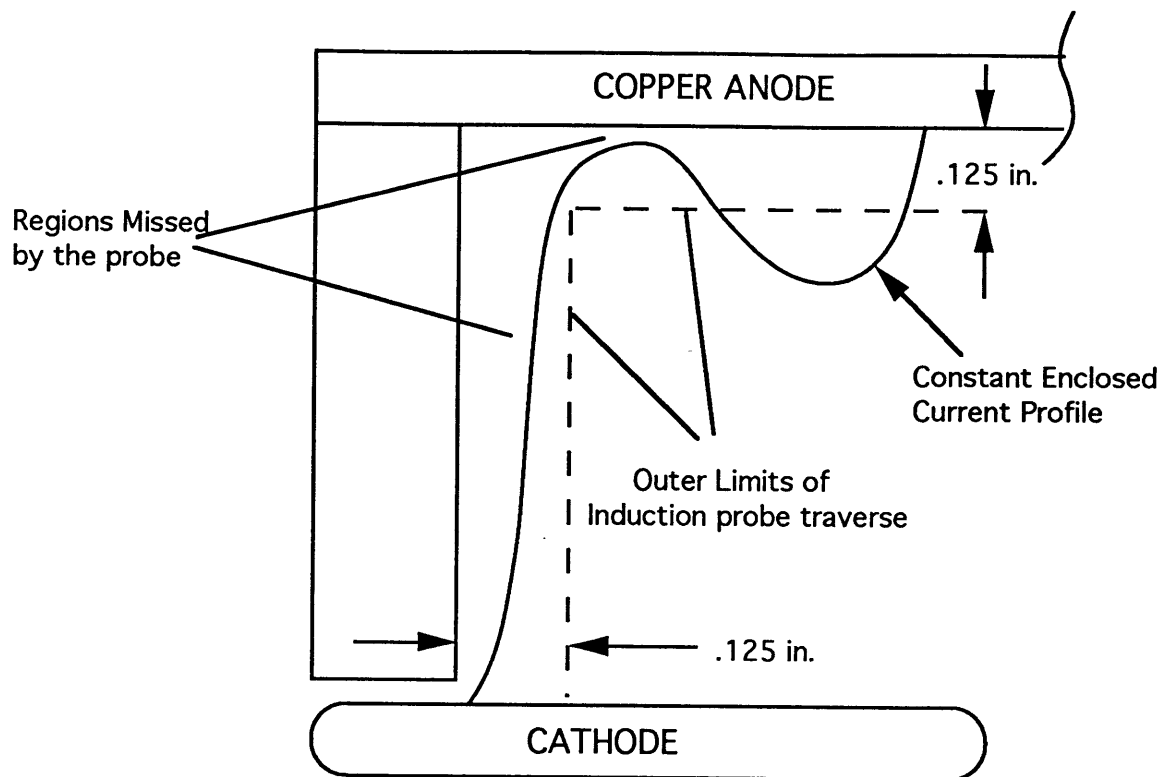
Figure 7-15: Enclosed Current Contour Bend

a transition from subsonic to supersonic flow might be responsible. Numerical calculations being performed on a thruster similar to the one used in this study, show that a sonic transition does take place near the backplate [48]. During this transition a shock may occur forcing current lines to shift, resulting in ion motion perpendicular to the probe rather than parallel, as is desired. Gallimore has shown that ion motion perpendicular to the probe can result in the indicated electron temperature being off by as much as a factor of two.

If the electrons near the anode are assumed to be governed by a Maxwell-Boltzmann distribution, then, in the absence of magnetic fields, the radial electron current density at the anode surface due to random motion is

$$j_e = \frac{1}{4} e n_e \bar{C}_e \qquad (7.10)$$

where $\bar{C}_e$ is the electron thermal speed $\left(\sqrt{8kT_e/\pi m_e}\right)$ and n_e is the electron number density. Figures 7-15 and 7-16 show comparisons between the random electron flux to
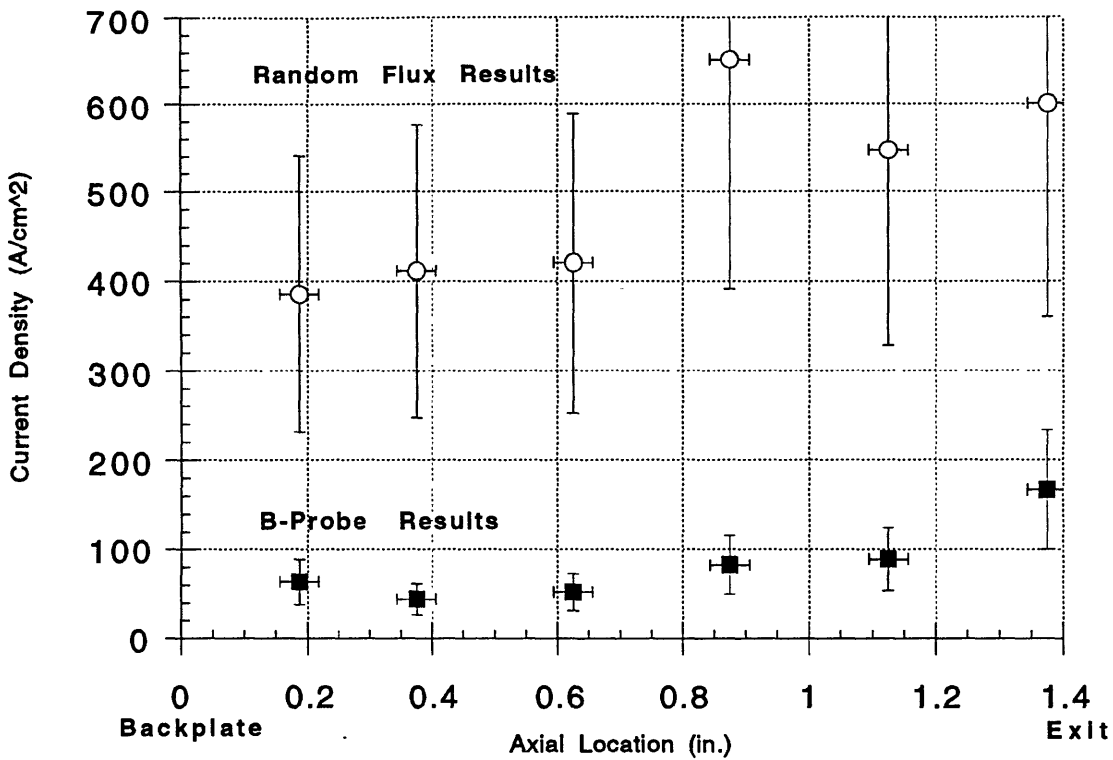
Figure 7-16: Measured Anode Radial Current Density Distribution with Estimated Random Electron Current at 4.4 kA

the anode, estimated from triple probe data (assuming $n_e = n_i$), with current density values calculated from magnetic probe results for 4.4 and 4.8 kA, respectively.

Figures 7-15 and 7-16 clearly show that the electron flux required by the thruster for current conduction is easily supplied by the ambient plasma. In all cases, the current density due to random electron flux is greater than that measured with the magnetic probe. According to Langmuir probe theory, this should result in a negative (electron repelling) anode voltage drop. All floating probe experiments done during this study indicated a positive anode fall. The discrepancy between measured current density and estimated random electron flux density may be explained by the highly non-isotropic nature of current conduction in a magnetized plasma. The presence of a strong magnetic field tends to inhibit the flow of current carrying electrons across field lines, making the analysis of anode current conduction on the basis of unrestricted random flux of electrons to a surface inadequate. The observation that magnetization of the electrons may be a significant feature of anode current conduction is qualita-
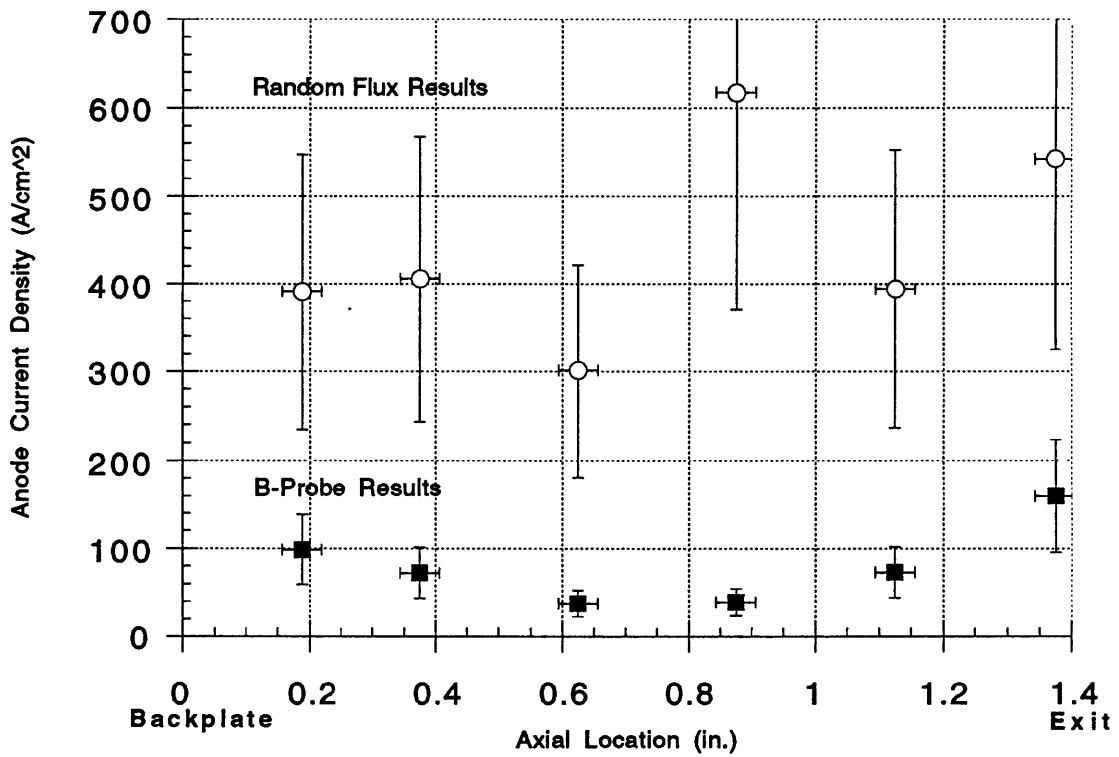
Figure 7-17: Measured Anode Radial Current Density Distribution with Estimated Random Electron Current at 4.8 kA

tively justified by the fact that the Hall parameter at the anode has been calculated with probe data to be higher than 1 in almost all cases and higher than 10 in some.

Researchers in the past [23, 13] have linked the large anode drops in MPD thrusters with an "anomalous conductivity" phenomenon which has to do with scattering of electrons by waves, resulting in unusually high collision frequencies and a large deviation from the classically calculated values for the Hall parameter and electrical conductivity. Waves with oscillating electric fields of exponentially increasing amplitude (plasma instabilities) impede the passage of current carrying electrons within the plasma, resulting in anomalously high electron collision frequencies. As a result of these high collision frequencies, the resistivity of the plasma is increased, requiring, in turn, the presence of large electric fields to maintain current continuity. The values for the electrical conductivity and Hall parameter calculated classically and inferred using the generalized Ohm's law are presented in the next two sections.

7.2.1 Inferred Electrical Conductivity

With the magnetic strengths in the thruster measured, the electrical conductivity could be determined in conjunction with the floating probe and triple probe results. Work in the past has linked large voltage drops at the anode to large electron Hall parameters and consequently low electrical conductivity. Anode starvation has been theorized to relate the anode power deposition and the Hall parameter. Anode starvation refers to a depletion of charge carriers near the anode due to a high Lorentz pumping force. At large Hall parameter, significant axial Hall currents exist which create radial components of the Lorentz force that drive charged particles away from the anode region. In response to this depletion of charged carriers, large electric fields are needed near the anode to maintain radial current density at the necessary level. This effect can be shown by manipulation of Ohm's law:

$$J = \sigma_o(E + v \times B) - \frac{\Omega}{|B|}(j \times B - \nabla p_e) \qquad (7.11)$$

where J is the current density vector, σ_o is the electrical conductivity, E and B are

	Ne (1.23 in.)	Ne (1.375 in.)	Te (1.23 in.)	Te (1.375 in.)
4.4 kA Exit	1.92E+20	1.43E+20	3.32	3.04
4.4 kA Mid	1.27E+20	1.47E+20	1.66	1.16
4.4 kA Back	5.97E+19	3.89E+19	1.75	1.09
4.8 kA Exit	2.18E+20	1.72E+20	3.37	3.2
4.8 kA Mid	1.02E+20	1.21E+20	1.68	1.09
4.8 kA Back	6.56E+19	3.51E+19	1.79	1.18

Table 7.3: T_e and n_e Values To Justify Exclusion of ∇P_e in The Generalized Ohm's Law

the electric and magnetic fields, respectively, v is the plasma bulk velocity and p_e is the electron pressure. The "z" axis is selected to align with the magnetic field, which is assumed to be purely in the azimuthal direction (parallel with the anode), and the "x" and "y" axes are chosen to be in the axial and radial directions, respectively. The gradients in both electron temperature and electron density are relatively small at the 1.23 in. and 1.375 in. radial locations so the ∇p_e term in Eq. 7.6 can be neglected. Values for n_e and T_e at those two radial locations at three axial locations are presented in table 7.3.

Ohm's law can be written in a tensor form:

$$ J = \sigma_o \begin{pmatrix} \frac{1}{1+\Omega^2} & \frac{\Omega}{1+\Omega^2} & 0 \\ -\frac{\Omega}{1+\Omega^2} & \frac{1}{1+\Omega^2} & 0 \\ 0 & 0 & 1 \end{pmatrix} (E + v \times B) \qquad (7.12) $$

where the current-induced magnetic field is assumed azimuthal. An axisymmetric current discharge is assumed allowing for the "z" components of E, v and j to be neglected. Manipulation of the above equation yields the following equation for the electrical conductivity:

$$\sigma_o = \frac{(1 + \Omega^2)j_y}{\Omega(E_x + B_z v_y) + E_y - B_z v_x} \tag{7.13}$$

which relates the electrical conductivity to the "x" and "y" components of the current density obtained from the magnetic probe measurements. The radial current density j_y was calculated based on the measured magnetic field strengths incorporated into Eq. 7.2. The magnetic field strengths B_z were obtained from magnetic probe measurements, and n_e was obtained from the Langmuir triple probe data. The radial electric field ($E_y = \Delta V_y / \Delta y$) was obtained from floating probe measurements at 1.23 in. and 1.375 in. radial locations at the three axial locations (.23 in., .98 in. and 1.47 in. from the exit plane). The axial electric field (E_x) was determined from the near-anode traverse. The assumption made was that the axial electric field is independent of the radial location and therefore at 1.375 in. radial location E_x is the same as the radial location during the floating probe measurements (~ 1 mm. from the anode surface). The magnitude of the flow velocities were obtained from reference [21]. The effect of the magnitudes of the back EMF term (vB) is small compared to the magnitudes of the electric fields (i.e. $E_x \gg v_y B_z$ and $E_y \gg v_x B_z$). The velocity values in reference [21] corresponding to the $J^2/\dot{m}$ from this study were used in the analysis ($v_x = 10,000 m/sec; v_y = -1800 m/sec$). The electrical conductivity is classically defined in Eq. 7.6.

The inferred electrical conductivity was determined to be a few times smaller but of the same order of magnitude as the calculated value for almost all cases. Figs. 7-18 and 7-19 show the inferred electrical conductivity plotted against the calculated value.

The values for electrical conductivity used for Figs. 7-13 and 7-14 were the ones calculated classically, not the inferred values. In addition to the electrical conductivity, the Hall parameter has been seen as a major scaling parameter for the anode fall [23]. Both calculated and inferred values of the Hall parameter are described in the next section.
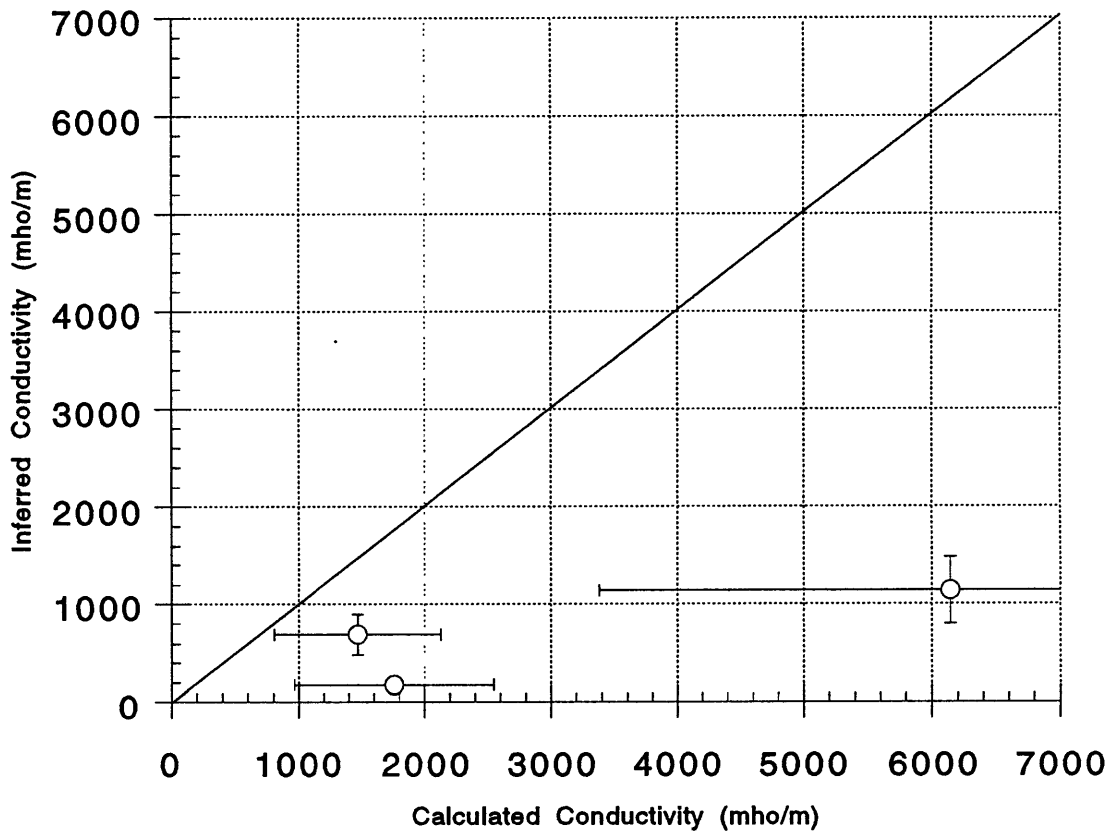
Figure 7-18: Inferred vs. Calculated Values For The Electrical Conductivity at 4.4 kA
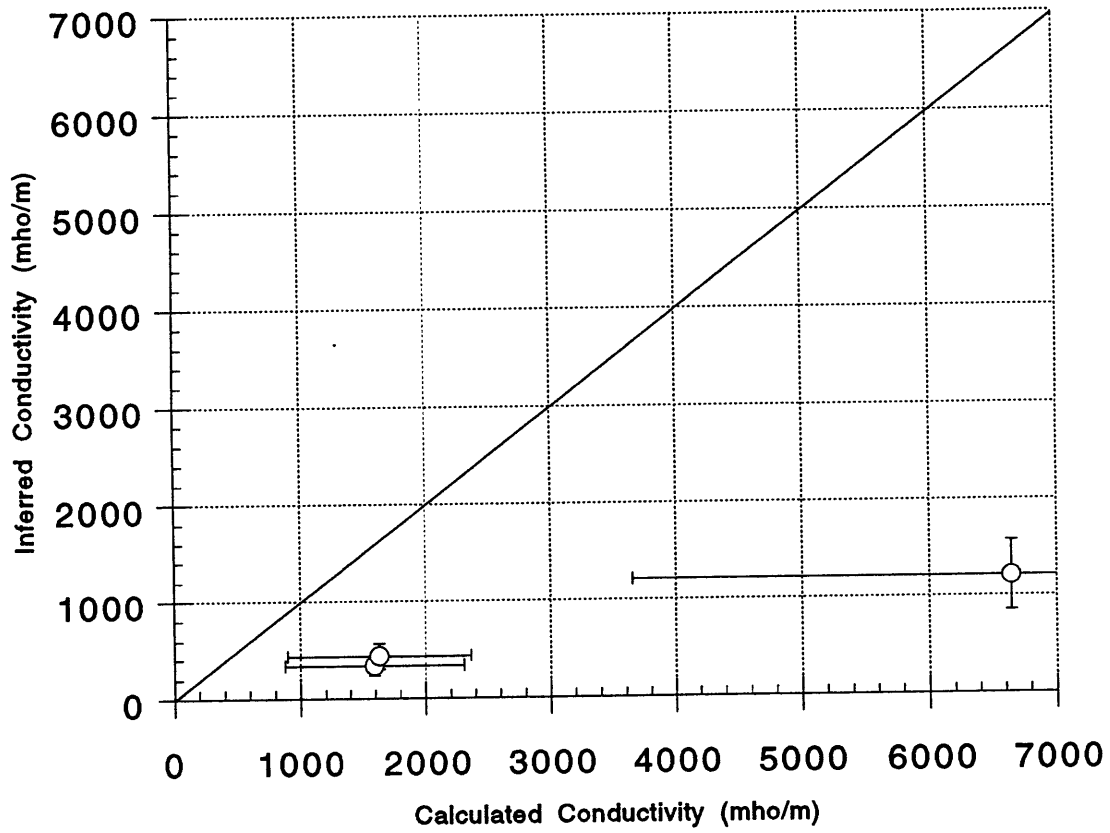
Figure 7-19: Inferred vs. Calculated Values For The Electrical Conductivity at 4.8 kA

7.2.2 The Hall Parameter

Work in the past has linked large voltage drops at the anode to large electron Hall parameters [49, 23]. In all cases, however, the magnetic field is predominantly parallel to the anode. Therefore, current conduction to the anode requires electrons to diffuse across magnetic field lines. The Hall parameter (Ω) is a response of the electron to electric and magnetic fields. For plasmas characterized by a low Hall parameter, electrons, in general flow parallel with the electric field. For plasmas with a large Hall parameter, electrons tend to migrate in a direction that is perpendicular to both electric and magnetic fields. The Hall parameter can be determined from the following equation.

$$\Omega = \frac{\omega_{ce}}{\nu_e} = \frac{eB}{m_e \nu_e} \tag{7.14}$$

where Ω is the electron Hall parameter, ν_e is the electron collision frequency, B is the measured magnetic field strength, and ω_{ce} is the electron gyrofrequency.

The Hall parameter, which was determined to exceed unity most everywhere in the MPD chamber tends to turn the enclosed current profile axially near the electrodes. As mentioned in chapter I, studies with a variety of plasma producing devices have found that the anode fall increases with Hall parameter [22, 49, 45].

The electrical conductivity can be written as a function of the Hall parameter as given below:

$$\sigma_o = \frac{e n_e \Omega}{B_z} \tag{7.15}$$

Using the above equation, Eq. 7.11 can be manipulated to yield the value for the Hall parameter:

$$\Omega = \frac{(1 + \Omega^2) j_y B_z}{e n_e (\Omega(E_x + B_z v_y) + E_y - B_z v_x)} \tag{7.16}$$

Since the magnetic fields used to calculate either set of Hall parameters are identical, the difference between the two sets is due to the discrepancy between inferred

	Hall Calc	Hall Inf.	Conduct. Calc	Conduct. Inf.
4.4 kA Back	2.82	1.3	1472	690
4.4 kA Mid	1.17	0.1	1759.2	177.2
4.4 kA Exit	2.83	0.5	6145.5	1141
4.8 kA Back	4.72	1.3	1632.3	440
4.8 kA Mid	1.66	0.4	1593.1	340.5
4.8 kA Exit	2.92	0.5	6645.6	1214.6

Table 7.4: Inferred vs. Calculated Values For The Hall Parameter and Electrical Conductivity At Three Axial Locations

electron collision frequencies and those calculated assuming only coulombic collisions.

The results of the calculations for electrical conductivity and the Hall parameter are presented in table 7.4.

The calculated and inferred values for the Hall parameter for both 4.4 and 4.8 kA current levels are plotted in Figs. 7-20 and 7-21.

The two values for the Hall parameter, as the values for the electrical conductivity found previously, are of the same order of magnitude in almost all cases, although there still exists a considerable disparity between the two sets of values.

Based on the calculated and inferred values for the electrical conductivity derived earlier, it is unclear whether anomalous conductivity exists .125 in. from the anode surface. The results do show reduced conductivity and Hall parameter values, but only by factors of two to five. Nothing can be concluded, however, very close ($\sim .0625in.$) to the anode, because the radial electric field is an unknown there. To resolve the issue of anomalous conductivity, a clearer understanding of the radial electric field very close to the anode is required.

166
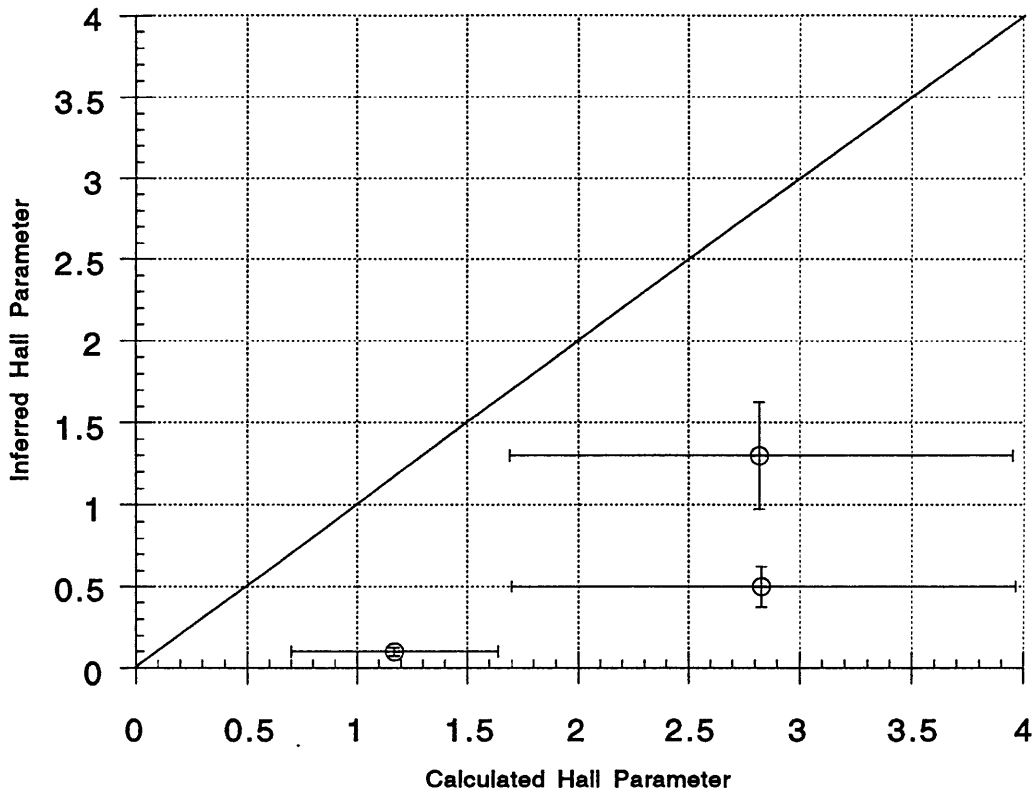
Figure 7-20: Inferred vs. Calculated Values For The Hall Parameter at 4.4 kA
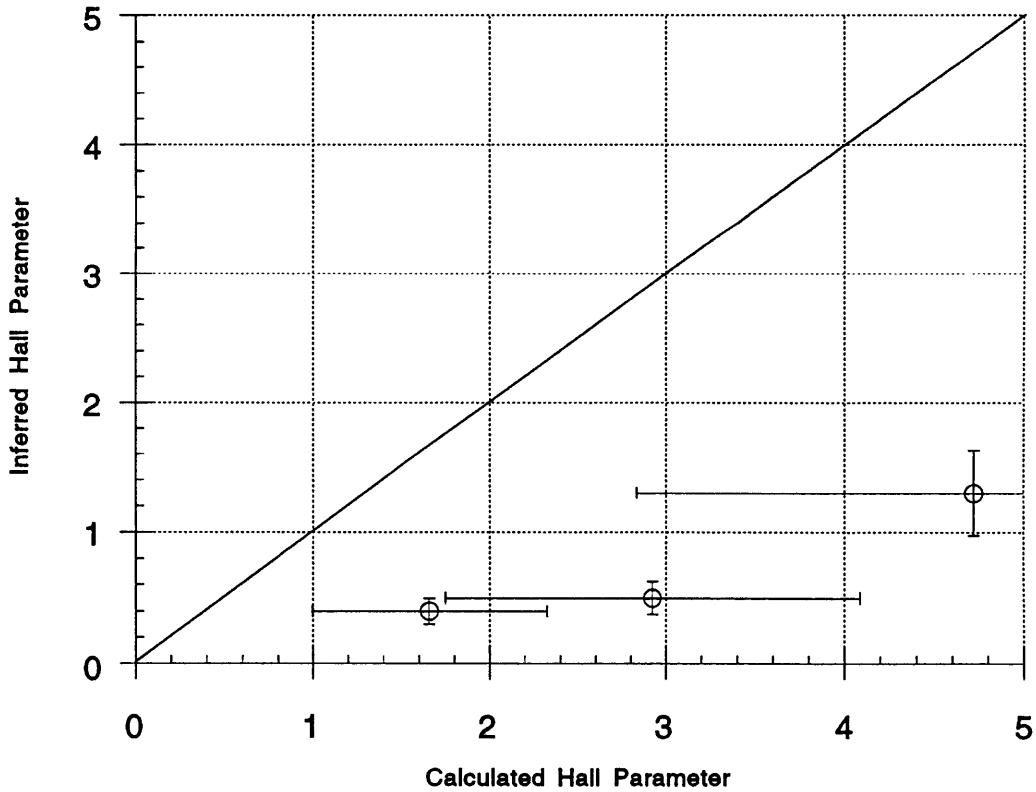
Figure 7-21: Inferred vs. Calculated Values For the Hall Parameter at 4.8 kA

Chapter 8

Conclusions and Recommendations

8.1 Conclusions

Extensive experimental data have been provided for important plasma parameters including electron temperature, electron density, enclosed current and plasma potential. The goals set forth for the study were met. The stable regime (below Onset) for the thruster was identified for .5, 1.0 and 1.5 g/sec flow rates. .5 g/sec was chosen as the flow rate for the study. Anode fall data were obtained using a floating probe in conjunction with a Langmuir triple probe to determine the electron temperature correction factor needed to convert from measured floating potentials to plasma potentials. Anode fall was seen to increase with thruster current at all axial locations accompanied by an increase in electron temperature and a gradual decrease in number density. A direct correlation between anode fall and reduction in number density was therefore obtained. Two transition points (jumps) in the anode fall were observed corresponding to 4.8 and 5.11 kA current levels. 4.8 kA was chosen as the point of operation for the remaining probe experiments. Radial plasma potential measurements were obtained at three axial locations corresponding to near-backplate, mid-thruster and near-exit locations. The measured temperature decreased sharply from the cathode to the anode. A rise in temperature was observed near the anode

lip. Induction probe measurements show a considerable rise in current density near the anode lip which could presumably be causing localized high ohmic dissipation resulting in higher temperature at that location.

The electron density varied considerably both radially and axially. Near the back-plate, near the cathode, where high current concentration and a resulting high ionization exists, the number density is highest dropping sharply towards the anode. At the mid-thruster location, however, a drop in density is seen both near the cathode and the anode. A drop in density can, therefore, be directly related to the observed voltage drops near the electrodes. The mechanisms for the voltage drop near the cathode and anode are quite different. Starvation or lack of charge carriers due to the Lorentz pumping force can be cited as a reason for the reduced density near the anode. To maintain current continuity, large electric fields are created in the region very close to the anode leading to large voltage drops. The reason for a low number density near the cathode may be reduced ionization in the region due to lack of current concentration that is seen at the cathode root and the anode lip. There is no observable ionization mechanism, therefore, in the near-cathode region. A higher voltage drop was seen .125 in. from the cathode than the same distance from the anode at all three axial locations. The voltage drop mechanism for the cathode is quite different than that at the anode, however. The fact that the cathode is cold and cannot thermionically emit can be cited as the cause for the large cathode drop [1]. For the electrons to be detached from the cathode, large electric fields are created.

The probe experiments were not without considerable errors. The temperature values gotten during the near-anode axial scan indicated electron temperatures exceeding 6 eV in some cases. For Argon, temperatures of that magnitude are highly unlikely since multiple ionization acts as an energy buffer. Therefore, in the axial traverse, the trends for T_e rather than the absolute magnitudes should be considered. Additional errors were apparent during the radial traverses with both floating and triple probes. The anode fall measured during the axial traverse with the probe roughly 1 mm. from the anode produced results different from the radial traverse at the near-anode locations. During the radial traverses both floating and triple probes

were .125 in. away from the anode at the outermost radial location. During the axial scan, both probes were roughly .0625 in. away from the anode. The anode fall values measured during the axial scan should have been lower than those measured during the radial traverses since the probe was closer to the anode surface. For the near-exit and near-backplate locations, the inverse happened. The radial outermost point yielded ΔV values less than those measured during the axial traverse. The mid-thruster anode fall values were comparable, however. Similar behavior was observed during the triple probe experiments. A large discrepancy was seen between the near anode values for electron temperature during the axial scan and at the outermost radial location during the radial scan. This was true for both 4.4 and 4.8 kA levels. During the radial scans, T_e dropped to approximately 1 eV near the anode at the near-backplate and mid-thruster axial locations. During the axial near-anode traverse with the triple probe, T_e was measured to be approximately 2 eV. Probe contamination and misalignment of the probe with ion flow can be pointed to as causes for the over-prediction of the electron temperature. The electron density values, on the other hand, gave expected results. At the outermost radial location (.125 in. from anode), the density was higher than that measured during the axial near-anode scan (.0625 in. from anode).

An induction probe was used to determine magnetic field strengths and current contours throughout the thruster. A large current concentration was identified near the cathode root and the anode lip. The Hall parameter which has been related to large anode drops and skewing of the current lines, was calculated from measured plasma parameters. It exceeded unity everywhere near the anode. No consistent radial pattern in the Hall parameter was observed, however. "Strange" behavior was observed at .375 in. and 1.25 in. axial near-anode locations throughout the series of probe experiments. A large jump in electron temperature was seen at the two locations corresponding to a large temperature correction factor for the floating potentials. As a result, the anode fall dropped considerably at the two locations for all current levels. In addition, current contours obtained from the induction probe measurements show the enclosed current being highest at the .375 in. location

and increasing sharply at the 1.25 in. axial location as well. It may be concluded, therefore, that a transition in the plasma flow (perhaps a sonic transition) takes place at .375 in. from the backplate causing the charge carriers to flow perpendicular to the probe rather than give the desired parallel flow. Ion flow perpendicular rather than parallel to the probe has been seen to cause an error in the T_e by as much as a factor of two. The fact that induction probe measurements yielded strange behavior at the two axial locations as well seems to indicate a distinct plasma effect rather than a probe error. In addition, the results obtained at those two locations showed similar behavior at all current levels. Therefore, a large random error cannot be associated with the temperature rise at those locations. Ohmic heating can also be identified as the cause of the temperature rise at the 1.25 in. axial location where the second T_e jump was observed. Current density values obtained from the magnetic field measurements near the anode along with electrical conductivity values obtained from the electron temperature and density measurements were used to determine the ohmic heating at the anode. A sharp rise in the ohmic dissipation was observed at the 1.25 in. axial location along with a smaller rise at the .375 in. location.

8.2   Recommendations For Future Work

Although this study has provided much needed information about plasma parameter variations in an MPD thruster at one particular operating condition, many more questions have been raised.

Two transitions were observed in the anode fall behavior as a function of increasing thruster current. The first transition at 4.8 kA was used for the set of experiments conducted for this study. A similar set of measurements should be made at the 5.11 kA current level corresponding to the second observed transition. It could be that the 4.8 kA level was not the sharp rise in anode fall that was the objective of the initial anode-fall experiments with the floating probe. The fact that the anode fall actually dropped between 4.8 and 5.11 kA may mean that the anode fall behavior is in mid-transition and that the jump from stable anode fall to a sharp rise is messy

(i.e. over a large thruster current range).

The triple probe experiments conducted in this study should be verified, especially for the near-anode axial scan. The probe contamination problem which leads to inaccurate electron temperature and density values should be resolved as best as possible. Care should be taken to either clean the probe using ion or electron bombardment techniques after every shot, or the probe should be replaced after every few shots. In order to obtain the best results possible, the probe should be aligned with the flow. That is, the probe angle with respect to the thruster should be varied until the lowest probe voltage is observed. The problem of a temperature jump at the two axial locations could have been further verified or resolved with the mentioned rotational degree of freedom. One should, therefore, repeat the triple probe experiments done here to verify the rise in the temperature seen at the two locations. A velocity study, either using probes or spectroscopy via Doppler broadening, should be conducted within the thruster to identify the region of transition from subsonic to supersonic flow. An understanding of the current paths during the transition is desired. A better calibration for the magnetic probe should be used. The fact that some of the current may not have been enclosed by the coil during the calibration led to a large error in the magnetic field and enclosed current measurements.

A great deal of fundamental understanding of electrode phenomena is missing. Although much effort has been put forth in examining the anode loss phenomenon, cathode phenomena have remained relatively untouched. A larger fall at the cathode than the anode has to be further validated and studied. Whether the cause for the electrode drops is a sheath effect or caused by plasma instabilities should be resolved.

Finally, computer simulations for the thruster geometry used in this study should be conducted and completed in order to compare the numerical and experimental results.

Appendix A

Theoretical Analysis

A.1　Introduction

The theoretical basis employed in the set of experiments conducted during the course of this study was developed over six decades ago by Joseph Langmuir. Plasma diagnostics serve a wide variety of roles. At one extreme, for applications in basic plasma experiments, they are needed to determine the details of the electron and ion parameters. At the other extreme, in plasma processing control, they may be needed to just give an indication that a plasma processing device has the same plasma charactersitics as on a previous occasion, but it may not be necessary to know the characteristics. It is extraordinary that one type of diagnostic, Langmuir probes have been used to serve the full range of roles over such a wide range of plasma densities [27]. Although a triple Langmuir probe was used for the determination of electron temperature and density for this particular study, knowledge of the single Langmuir probe technique is imperative in order to understand the triple probe theory. Both theories are discussed in some detail below. The Langmuir probe is a plasma diagnostic tool that can be used to measure electron density and temperature. A typical langmuir probe is illustrated in Fig. A-1.

In its simplest form, the single Langmuir probe consists of a piece of metallic wire surrounded by a ceramic jacket (Alumina) for structural integrity. The jacket protects the insulator (also Alumina) from the plasma and provides a vacuum sealing surface.
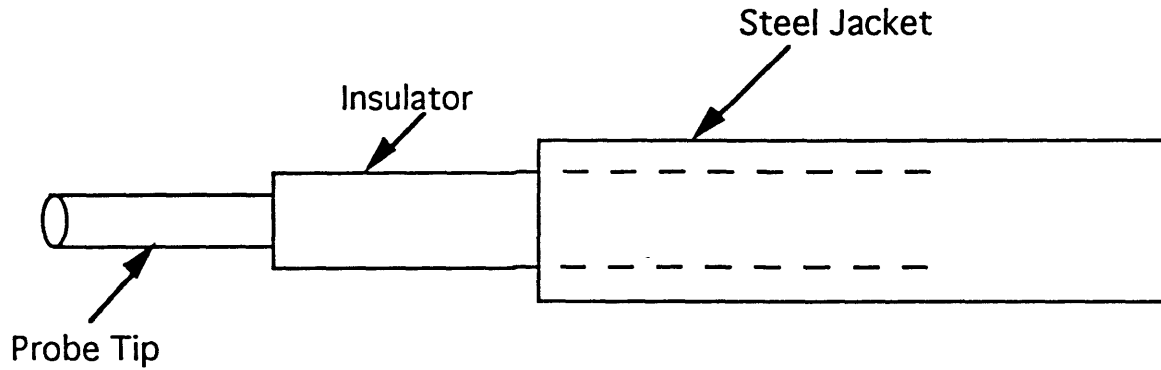
Figure A-1: A Typical Single Langmuir Probe Schematic

Under normal operation the probe is inserted directly into the plasma and electrical current flowing from the probe is measured. The circuit of a typical Langmuir probe is shown in Fig. A-2.

The electron number density and temperature can be deduced from a plot of the probe current vs. the bias voltage V as shown in Fig. A-3.

Although the measurements are relatively simple to make, they are not quite as straightforward in interpretation. The reason is that the purpose of the probe is to measure the parameters at a local point of insertion. However, due to the shielding tendency of the plasma, the parameters are altered in the presence of the probe. One then needs a sophisticated theory to relate the measured quantities to the density and temperature if there were no probe current.

There are therefore two underlying principles to be outlined, namely Debye shielding and Langmuir probe theory[51].

A.1.1   Debye Shielding

As mentioned earlier, a plasma has enormous tendency to shield itself from applied electric potentials. With the insertion of a potential, very strong fields are generated that tend to rearrange the plasma in such a way that the effect of the potential is
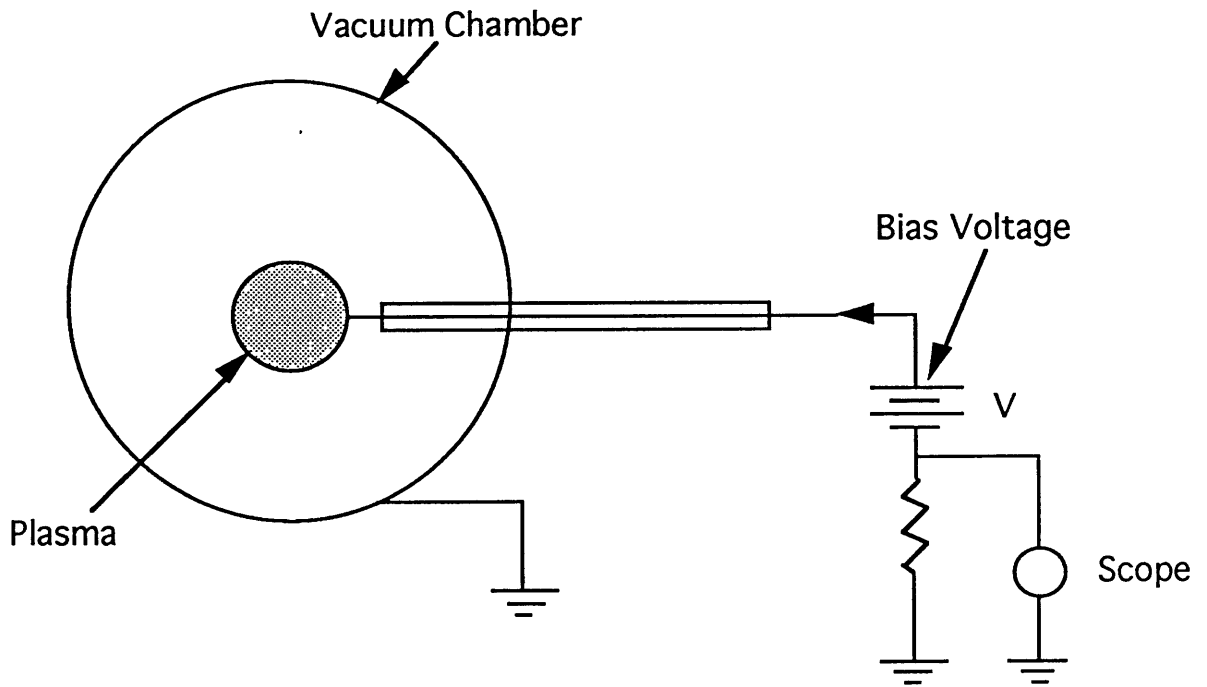
Figure A-2: The Overall Single Langmuir Probe Circuit
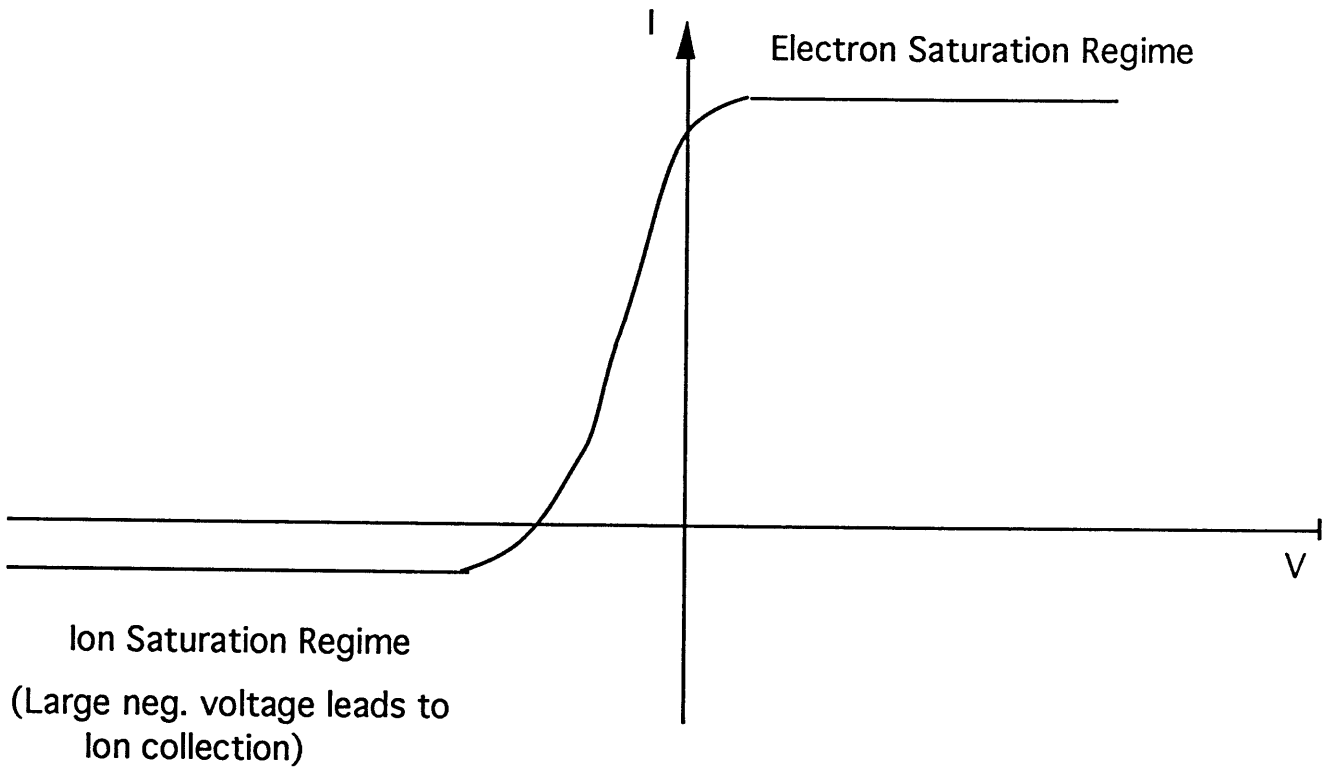
Figure A-3: Two Limiting Regimes of Operation For a Langmuir Probe
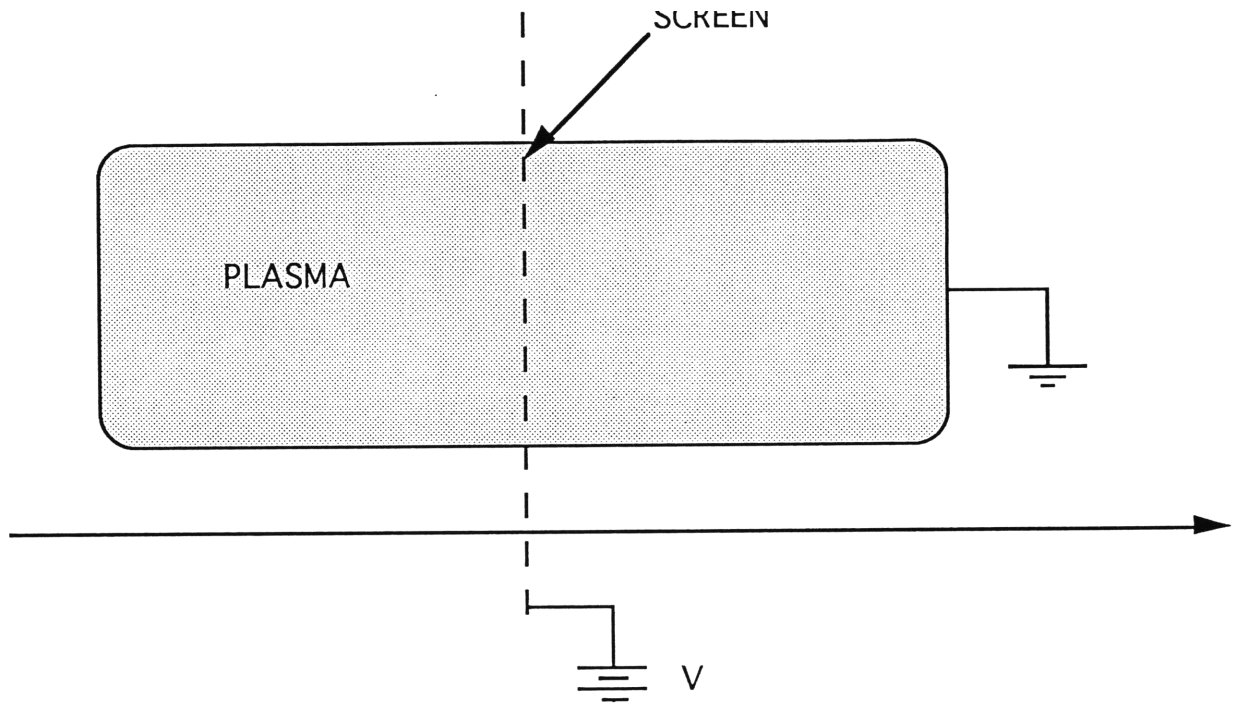
Figure A-4: Schematic For Theoretical Derivation of The Debye Length

negated. The shielding normally takes place over a Debye length, derived below.

Consider inserting a conducting screen into an infinite one dimensional plasma as shown in Fig. A-4.

Assume that the screen is maintained at a potential V with respect to the potential far from the plasma, where $\phi(\pm\infty) = 0$. For mathematical simplicity, one can assume that the ions have infinite mass and are therefore stationary. The electrons will either be attracted or repelled from the screen depending upon the sign of the applied potential. For a positive potential, electrons will accumulate in the form of a thin negative charge sheet near the screen as shown in Fig. A-5.

The electric field caused due to these charge sheets is in the direction opposing the applied electric field. In fact, electrons will continue to accumulate until the applied field is essentially cancelled exactly: that is, the plasma is perfectly shielded. The thickness of the charge sheet is defined as the Debye length.

Since the ions are assumed to be heavy and at rest, they produce a uniform background charge density given by:

$$\sigma_i = en_o \tag{A.1}$$

The electrons, with no external field, produce a canceling charge density, thus

176
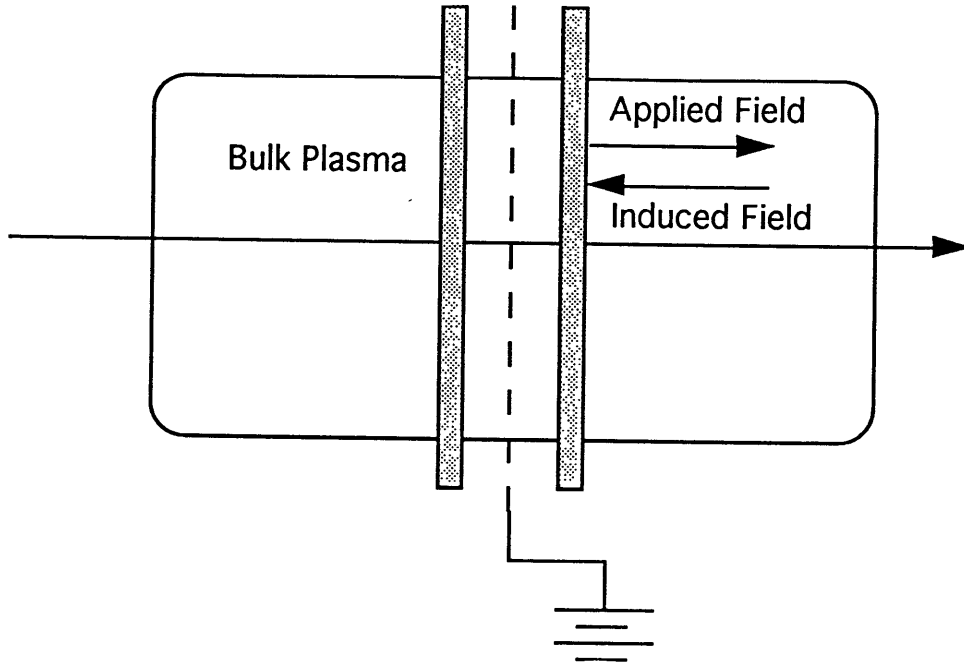
Figure A-5: Electron Accumulation Near a Positive Bias

satisfying the well known condition of charge neutrality ($n_o = n_e = n_i$). To calculate the effect of the applied field, one can assume that the electrons have a Maxwellian distribution function given below. A gas in thermal equilibrium has particles of all velocities and the most probable distribution of these velocities is Maxwellian[20].

$$f_e = n_o(\frac{m_e}{2\pi kT_e})^{1.5} exp(-\epsilon/kT_e) \tag{A.2}$$

In the above formula, ϵ is the total particle energy. With no applied field $\epsilon = m_e v^2/2$. With an applied field, however, $\epsilon = m_e v^2 - e\phi(x)$ where $e\phi$ is the self consistent potential energy due to the applied potential and the redistribution of the electron charge density,σ_e is given by

$$\sigma_e = -e \int_{-\infty}^{\infty} f_e dv = -en_o exp(e\phi/kT_e) \tag{A.3}$$

This is the Boltzmann distribution formula. When $\phi = 0, \sigma_e = -en_o$ as required by the overall plasma neutrality condition. When $\phi > 0, \sigma_e$ increases, showing that electrons are attracted to a positive potential and vice versa.

The net charge density can now be substituted into Poisson's equation to determine the potential $\phi(x)$

$$\frac{d^2\phi}{dx^2} = -\frac{\rho}{\epsilon_o} = -\frac{en_o}{\epsilon_o}[1 - exp(e\phi/kT_e)] \qquad (A.4)$$

The boundary conditions are:

$$\phi(0) = V$$

$$\phi(\pm\infty) = 0$$

In the limit where $e\phi/kT_e \ll 1$, the exponential term in the above equation can be Taylor expanded as $(e\phi/kT_e) = 1 + e\phi/kT_e$. Poisson's equation then reduces to

$$\frac{d^2\phi}{dx^2} - \frac{\phi}{(\lambda_d)^2} = 0 \qquad (A.5)$$

where $\lambda_d = (\epsilon_o kT_e/e^2 n_o)^{.5}$. The solution to the above equation 3.5, satisfying the above boundary conditions is given by

$$\phi = V exp(-|x|/\lambda_d) \qquad (A.6)$$

as shown in Fig. A-6.

The main bulk of the plasma is shielded from the applied potential over a distance of the order of λ_d known as the Debye length. For a 3 eV plasma with density $10^{20}m^{-3}$, $\lambda_d \sim .002mm$. The region between x=0 and several Debye lengths is called the "Sheath region" and the deviations from charge neutrality are substantial. Such a region is created, for example, when the Langmuir probe is inserted into a plasma and potential disturbance is created. In the ion saturation region, an estimate of the sheath thickness can be determined by using space charge limited arguments.

For $e\phi/kT_e \gg 1$, the sheath region near the probe consists primarily of ions. In this region the ion current is space charge limited and can approximately be described by the Child-Langmuir current.

178
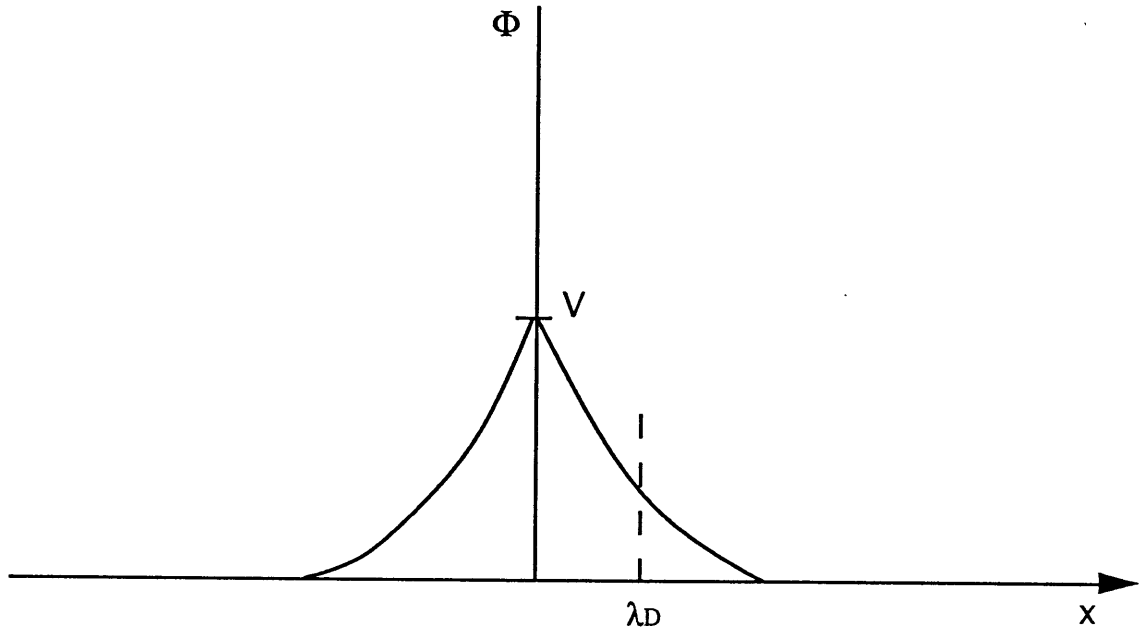
Figure A-6: Exponential Drop in Potential Due to Debye Shielding

$$J_{cl} = \frac{\frac{4}{9}\sqrt{\frac{2e}{m_i}}\epsilon_o \phi^{3/2}}{d^2} \qquad (A.7)$$

where e is the electron charge, m_i is the ion mass, d is the separation of the probe surface and the plane at which the electron density cannot be neglected and ϕ is the sheath drop. In other words, Child-Langmuir law determines the sheath thickness given the current density and the sheath drop.

A.1.2 Langmuir Probe Analysis

The general analysis of the Langmuir probe is quite complicated. A number of approximations can be made, however, to simplify the analysis considerably.

The main goal of the analysis is to calculate the V-I characteristic of a Langmuir probe in the ion saturation regime and determine electron density and temperature from it. The simplifying assumptions have to do with the relative size of several different length scales which enter the plasma physics. The shortest length scale is assumed to be the Debye length of roughly .002 mm. Next in size is the diameter of the probe, "a", which was .125 mm. for this study. When $\lambda_d \ll a$, the geometry can be accurately approximated as a one dimensional planar configuration. The next

length scale of interest is the electron-ion mean free path, λ_{ei}.

$$\lambda_{ei} = \frac{12.7\pi\lambda_d}{[.715g ln(12\pi/g)]} \quad\quad (A.8)$$

where the plasma parameter "g" is defined as:

$$g = (\frac{1}{n_e\lambda_d})^3 \quad\quad (A.9)$$

One can assume that $a << \lambda$, implying that in the vicinity of the probe, the plasma is collisionless. This is also a major assumption in the triple probe theory as is shown in a later section. Particles can free stream to and away from the probe surface under the influence of the electric field. For a 2 eV Argon plasma with $10^{20}m^{-3}$ density, $\lambda \sim 1.5mm$. The last length scale of interest is the gyro radius. In the ion saturation region where most electrons are repelled, only the ion gyroradius is important.

$$r_{Li} = \frac{v}{\omega_i} \quad\quad (A.10)$$

where

$$v = \sqrt{\frac{2kT_i}{m_i}} \qu\quad (A.11)$$

and ω is the ion cyclotron frequency given by the equation below.

$$\omega = \frac{eB}{m_i} \quad\quad (A.12)$$

Above e is the ion charge, B is the magnetic field and m_i is the ion mass. When $a << r_{Li}$, the magnetic field effects can be neglected. For Argon with B = .04 Tesla and Te = 3 eV, $r_{Li} \sim 3$ cm.

Under these assumptions, the probe geometry is modeled as shown in Fig. A-7. The current leaving the probe is defined as

$$I = -\pi a^2 e(n_i v_i - n_e v_e) \quad\quad (A.13)$$

180
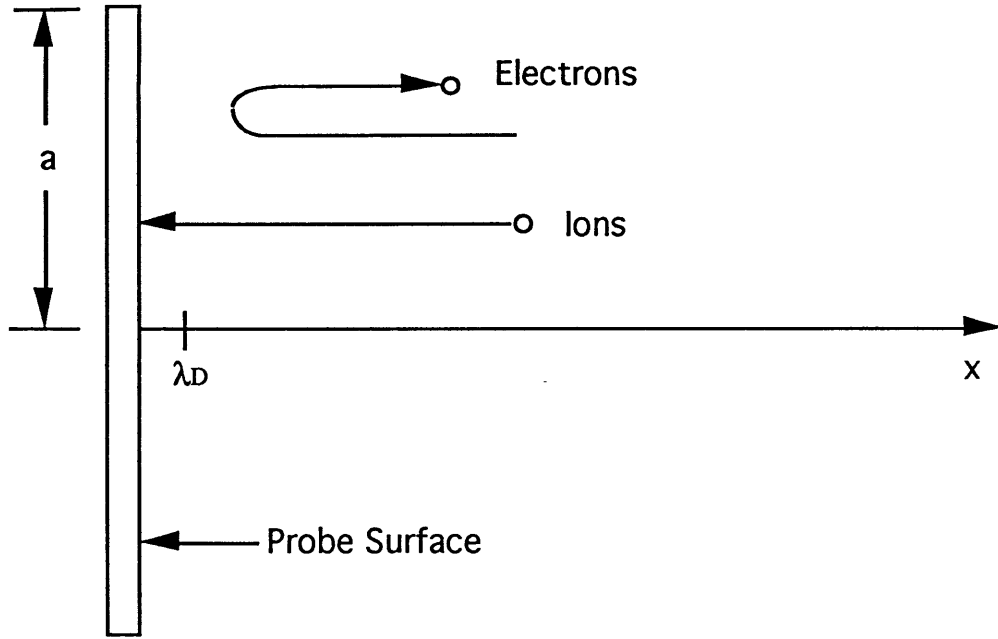
Figure A-7: Probe Geometry In The Ion Saturation Regime

The goal now is to determine the electron and ion flux (nv) as a function of the bias voltage V. To do this, separate solutions have to be calculated for the electron and ion number densities (ne, ni), and then substituted into Poisson's equation to determine the self-consistent potential (ϕ).

The electron distribution at a position x, a short distance from the probe is illustrated in Fig. A-8. Particles with negative v move towards the probe. Due to the large negative potential, almost all are reflected back. Only those with energy high enough to overcome the probe potential are collected. Thus, the return distribution for positive v is almost symmetric to the original distribution of the negative moving particles, except for the small high energy tail which represents the electrons collected by the probe.

If the probe is at a potential ϕ_o with respect to the bulk plasma, then electrons with energy $m_e v^2/2 > -e(\phi_o - \phi)$ are collected. Assuming the initial electron distribution is Maxwellian, then the electron charge and current densities are given by the following equations.

$$\sigma_e = -e \oint_{-v_o}^{\infty} f_e dv \qquad (A.14)$$

181

Incident
Electrons

Reflected
Electrons

X
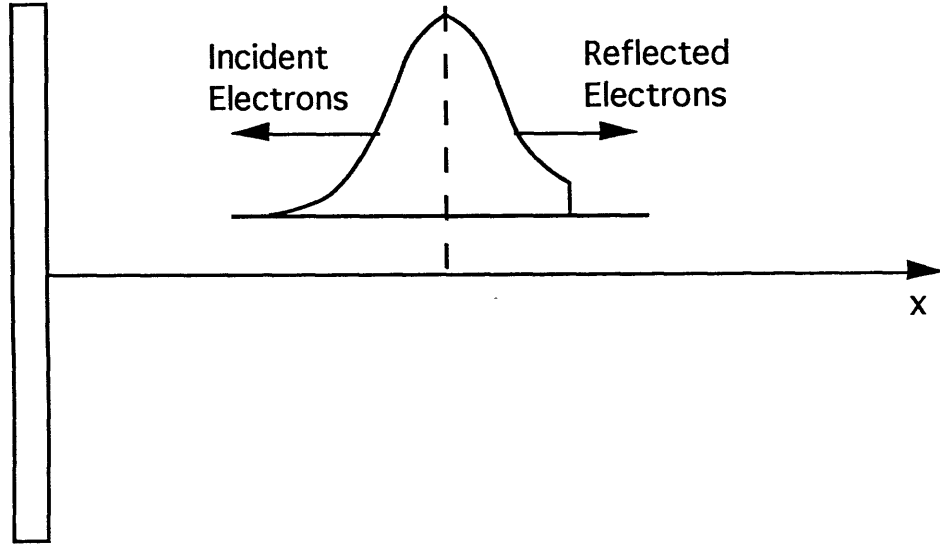
Figure A-8: Electron Distribution a Short Distance From The Probe

$$J_e = -e \oint_{-v_o}^{\infty} v f_e dv \qquad (A.15)$$

where $v_o = [2e(\phi - \phi_o)/m_e]^{1/2}$ and

$$f_e = n_o(\frac{m_e}{2\pi kT_e})^{1/2} exp(-\frac{m_e v^2}{2kT_e} + \frac{e\phi}{kT_e}) \qquad (A.16)$$

The quantity n_o represents the bulk plasma density far from the probe ($\phi \to 0$). In the ion saturation regime $-e\phi_o >> T_e$ in order for most electrons to be reflected. This implies, as in the Debye shielding case, that

$$\sigma_e = -en_o exp(e\phi/kT_e) \qquad (A.17)$$

Evaluation of eq. A.17 is a bit more subtle since both limits of the integral nearly cancel. Using the conservation of current (or charge) $Je(x) = const.$, eq. A.17 can be easily evaluated by choosing x to lie in the bulk plasma region ($\phi = 0$). Letting u $= (m_e/2kT_e)^{1/2}v$ in eq. A.17 yields

$$J_e = -en_o(\frac{2kT_e}{\pi m_e})^{1/2} \int_{-\infty}^{\infty} ue^{-u^2} du \qquad (A.18)$$

182
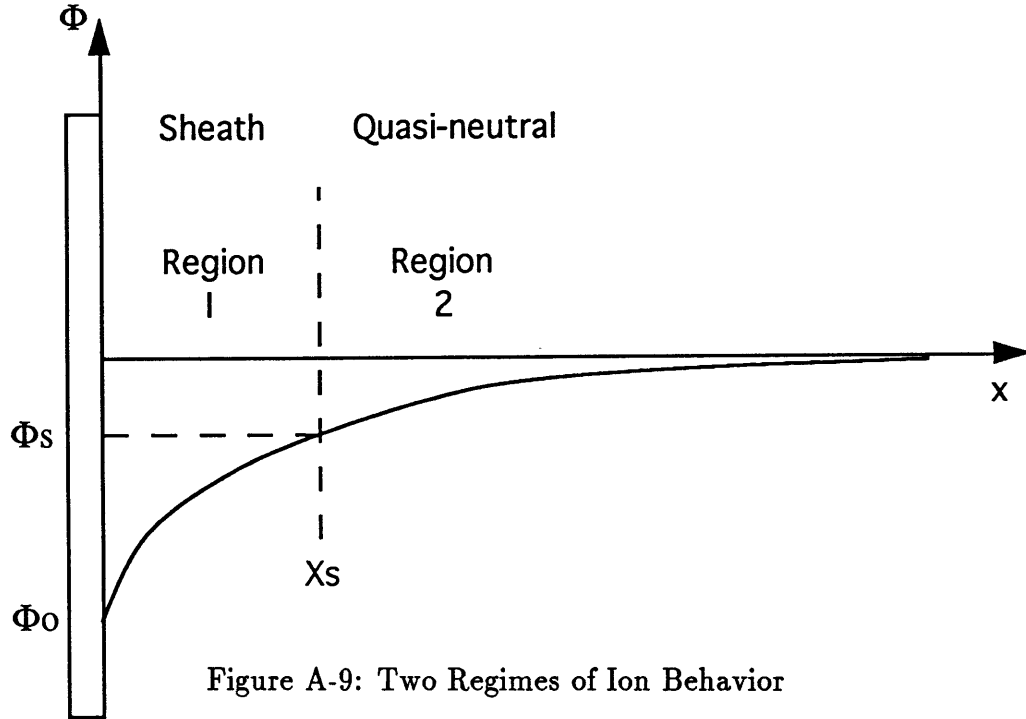
Figure A-9: Two Regimes of Ion Behavior

where $u_o = (-e\phi_o/kT_e)^{1/2}$. Integrating we find

$$J_e = -en_o(\frac{kT_e}{2\pi m_e})^{1/2}exp(\frac{e\phi_o}{kT_e})$$ (A.19)

The ions are considerably more complicated than the electrons and their behavior must be separated into two regions as shown in Fig. A-9.

Region 1 corresponds to the sheath regions where charge neutrality assumption breaks down and the full Poisson's equation must be solved. Region 2 is the quasi-neutral region with $n_e = n_i$. The transition point between the two regions is not sharply defined. The reason for two regions is that it is difficult to construct a simple model for the ion distribution function that is valid in both regions and can be solved analytically. A simple model can be constructed, however, for Region 1, and charge and current densities can be subsequently determined by requiring the boundary conditions to match at the edge of the two regions.

Once again, simplifying assumptions can be made. The ions can be assumed cold $(Ti << Te)$. Each ion enters the sheath region with the same initial velocity v_s and satisfies the conservation of energy relation

$$\frac{1}{2}m_iv_i^2 + e\phi(x) = e\phi_s + \frac{1}{2}m_iv_s^2 = 0 \tag{A.20}$$

where ϕ_s is the sheath potential. The integration constant in the solution was chosen to be zero since the ions are assumed at rest deep in the bulk of the plasma. The ion current density J_i, is yet undetermined, a consequence of the conservation of particles: $J_i(x) = J_i = const$. The ion charge density can be written in terms of the current density from the definition

$$\sigma_i = \frac{J_i}{(-2e\phi/m_i)^{1/2}} \tag{A.21}$$

J_i is determined, as stated before, by solving Poisson's equation and matching the solution to the quasi-neutral region 2:

$$\frac{d^2\phi}{dx^2} = -\frac{1}{\epsilon_o}(\sigma_i + \sigma_e) \tag{A.22}$$

Substituting equations A.17 and A.21, and introducing dimensionless variables $\psi = -e\phi/kT_e > 0$ and $y = x/\lambda_d$ one obtains

$$\frac{d^2\psi}{dy^2} = \frac{\alpha}{\psi^{1/2}} - e^{-\psi} \tag{A.23}$$

$$\alpha = \left(\frac{m_i}{2kT_e}\right)^{1/2}\frac{J_i}{en_o} \tag{A.24}$$

The boundary conditions require $\psi(0) = -2e\phi_o/kT_e$ and that ψ match smoothly onto a quasi-neutral region at some $y_s = x_x/\lambda_d$. It is this matching condition that determines $\alpha(J_i)$. The matching condition can be obtained by manipulating Eqs. A.22 and A.23 and sketching

$$f(\psi) = \frac{n_i - n_e}{n_i + n_e} = \frac{\alpha - \psi^{1/2}e^{-\psi}}{\alpha + \psi^{1/2}e^{-\psi}} \tag{A.25}$$

as a function of ψ for various α as shown in Fig. A-10.

To match onto a quasi-neutral region, $f(\psi)$ must vanish, or at least be very small

184
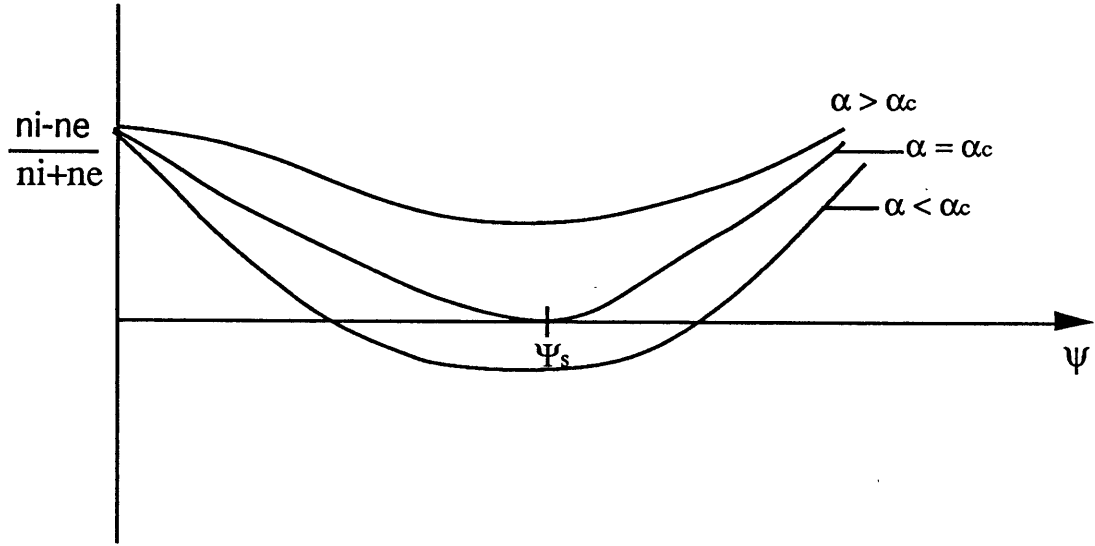
Figure A-10: Boundary Value Problem For The Neutrality Condition

at some point in space. When $f(\psi_s) = 0$, then $n_e = n_i$ and matching is possible. For large $\alpha < \alpha_c, f(\psi)$ becomes negative implying a negative charge density. This definitely violates the assumption of an electron repelling sheath and in fact, it can be shown that no sheath solution exists. Only for $\alpha = \alpha_c$ does $f(\psi)$ vanish. The value of ϕ_s and α_c are easily found from eq. A.25.

$$\psi_s = 1/2 \tag{A.26}$$

$$\alpha_c = \frac{e^{-1/2}}{\sqrt{2}} \tag{A.27}$$

Equation 29 can be rewritten to give the value of J_i

$$J_i = .61en_o(\frac{kT_e}{m_i})^{1/2} \tag{A.28}$$

Equation 25 can now be integrated numerically and the results are qualitatively similar to Fig. A-9.

The electron and ion current densities can be finally combined to give the probe current as a function of probe voltage ϕ_o. From eq. A.13, we find

185
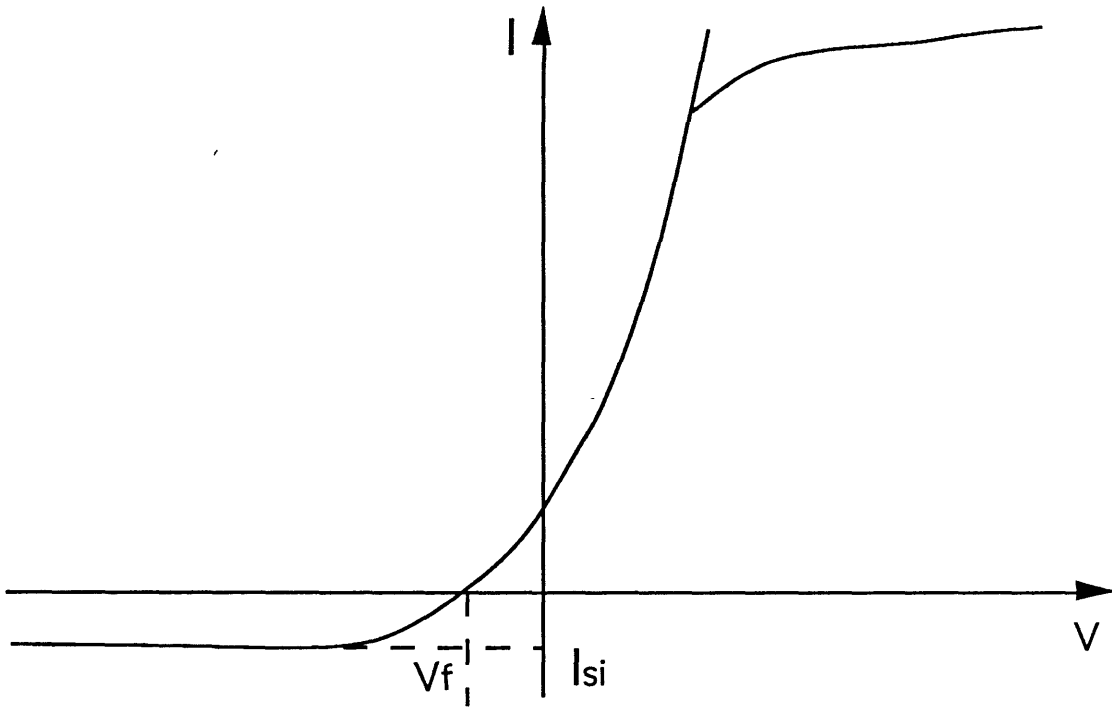
Figure A-11: Probe Current-Potential Characteristic

$$I = \pi a^2 e n_o [(\frac{kT_e}{2\pi m_e})^{1/2} exp(\frac{e\phi_o}{kT_e}) - .54(\frac{kT_e}{m_i})^{1/2}] \qquad (A.29)$$

Note the slightly more accurate coefficient .54 instead of .61 is obtained from numerical results[51]. This is the desired relationship $I = I(\phi_o)$, and is sketched in Fig. A-11.

A.1.3   Interpretation of The Langmuir V-I Curve

Probe V-I relationship can be used to determine the plasma density and temperature. From the V-I plot in the experiment, the open circuit voltage can be determined. This gives the proper reference point for the plasma potential with respect to the vacuum chamber ground connection. Using eq. A.29, one can see that at open circuit conditions, $\phi_o = \phi_f$ satisfies

$$(\frac{kT_e}{2\pi m_e})^{1/2} exp(\frac{e\phi_f}{kT_e}) = .54(\frac{kT_e}{m_i})^{1/2} \qquad (A.30)$$

where $\phi_f = V_f - V_p$ where V_p is the unknown plasma potential (with respect to the vacuum ground) and V_f, known as the floating potential, is the measured open circuit voltage (determined from the V-I plot). Substituting into eq. A.30 yields

$$V_f = V_p + \frac{kT_e}{2e}(ln(\frac{m_e}{m_i}) + .61) \qquad (A.31)$$

This particular correction factor was mentioned earlier and is necessary for conversion from measured floating potentials to actual plasma potential values. The ion saturation current can be measured by making ϕ_o sufficiently negative so that the electron contribution is negligible. This leads to

$$I_{si} = -.54\pi a^2 e n_o(\frac{kT_e}{m_i})^{1/2} \qquad (A.32)$$

In a typical Langmuir probe experiment, the theory for which has been described above, the probe voltage has to be swept to a get a V-I characteristic. Assuming that the characteristic is of the form given by eq. A.29, then a simple calculation shows that

$$\frac{dI}{dV} = \pi a^2 e n_o(\frac{kT_e}{2\pi m_e})^{1/2}(\frac{e}{kT_e})exp(\frac{e(V - V_p)}{kT_e}) \qquad (A.33)$$

By substitution, we get

$$\frac{dI}{dV} = \frac{e}{kT_e}(I - I_{si}) \qquad (A.34)$$

The above equation can be inverted to obtain the electron temperature as given by

$$T_e = \frac{e(I - I_{si})}{dI/dV} \qquad (A.35)$$

The measurements given in eqs. A.33, A.34, and A.37 are sufficient to determine Te, n_o and V_p. The electron temperature can be measured through graphical techniques as shown in Fig. A-12.

Knowing Te, probe area, and ion saturation current (Isi), the number density can be found from eq. A.32. The plasma potential can then be found from eq. A.31 using the electron temperature value and the measured V_f.

A cross check can be made for the value of plasma density. The value V_p corre-
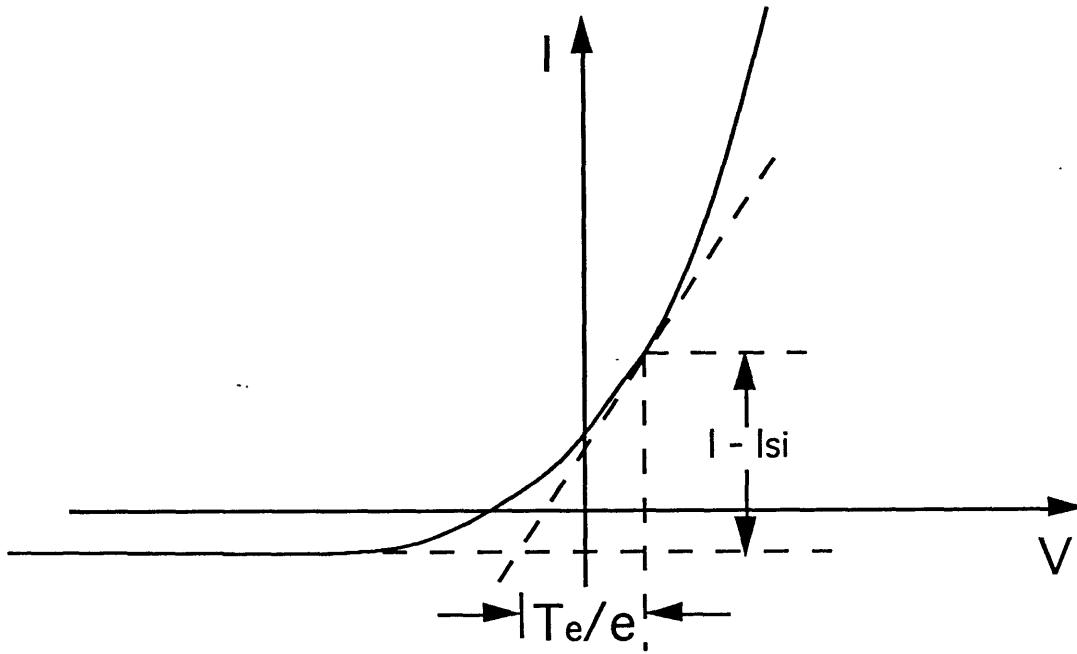
Figure A-12: Electron Temperature Determination From The Probe V-I Curve

sponds to the plasma potential with no probe present; that is, if the probe is biased with a voltage V_p, no sheath develops and the plasma is quasi-neutral right up to the probe surface; the potential $\phi = 0$ everywhere. The current flowing into the probe then is just the flux of the electrons corresponding to a half of Maxwellian distribution:

$$J_e = -e \oint_0^\infty u f_e(\phi = 0) du = -e n_o (\frac{kT_e}{2\pi m_e})^{1/2} \qquad (A.36)$$

The electron saturation current $I_{se} = -\pi a^2 J_e$ is then read as the intersection of the characteristic at the voltage V_p (see Fig. A.13).

Using the values of V_p and T_e deduced from ion saturation and the measured value of I_{se} in eq. A.36 gives an alternate value for n_o.

A.2 Triple Probe Theory

With the single Langmuir probe theory known, one can apply a similar analysis to the triple probe technique. A triple probe is a step up from the conventional Langmuir probe described above. It consists of three electrodes that are electrically configured to eliminate the need for a voltage sweep as required by a single probe. That fea-

188
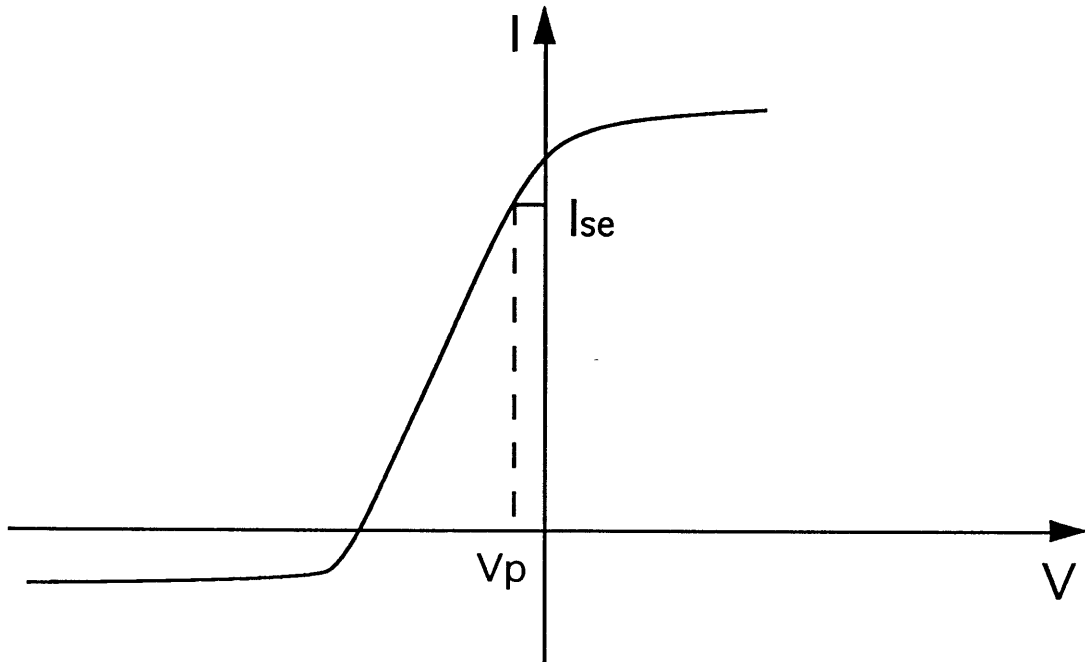
Figure A-13: Determination of Electron Saturation Current Through The Measured Plasma Potential

ture allows the Triple probe to be used as a diagnostic tool in quasi-steady MPD experiments for electron temperature and density measurements. Knowledge of these parameters is essential for the study of MPD plume physics, such as electromagnetic acceleration mechanisms and plasma instabilities. The triple probe method of Chen and Sekiguchi[12] is a straightforward and accurate technique to obtain the aforementioned parameters.

Even though the triple probe method is over twenty-five years old, only recently has it been applied to MPD studies [64]. It has been used effectively in several other applications including coaxial guns, edge plasmas in tokamaks, metal vapor lasers and discharge tubes [64]. The theoretical basis for the triple probe application to MPD thrusters is presented below.

A.2.1 Triple Probe Theory in the Thin Sheath Limit

The triple probe consists of three separate electrodes such that the electron temperature and density can be directly deduced from the measured voltage between electrodes 1 and 2 and the current flowing through electrode 3, respectively. The triple probe schematic is shown in Fig. A-14.

189
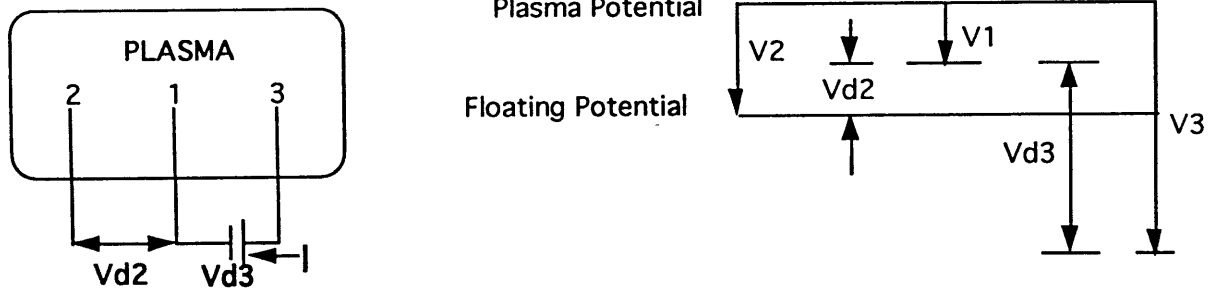
Figure A-14: Triple Probe Schematic

Above electrode 2 is floating while there is current flowing between electrodes 1 and 3. The triple probe circuit is floating such that no net current is transferred between the plasma and the probe meaning that the net charge lost by electrode 1 is gained by electrode 3. All electrodes are biased negative with respect to the plasma. Simple circuit theory along with plasma physics can be used to obtain Te and n_e from probe measurements. From Kirchoff's law, assuming only one ionized species, the following equations can be written for the three electrodes:

$$Electrode1 : 0 = J_{eo}exp(-\chi_1) - J_i(\chi_1) \qquad (A.37)$$

$$Electrode2 : 0 = J_{eo}exp(-\chi_2) - J_i(\chi_2) \qquad (A.38)$$

$$Electrode3 : \frac{I}{A_3} = -J_{eo}exp(-\chi_3) + J_i(\chi_3) \qquad (A.39)$$

where $J_{eo} = en_e(kT_e/2\pi m_e)^{1/2}$ is the electron current at the sheath edge due to random thermal motion, $\chi = eV/kT_e$ is non-dimensional potential of the electrode with respect to the plasma potential, $J_i(\chi)$ is the ion flux to the surface of the electrode, and A is the total collection area of the electrode.

190

In MPD thrusters, previous experiments have shown mean free paths on the order of a millimeter and debye lengths around $2\mu m$. The collisionless thin sheath theory can be used, therefore, to interpret the probe results. In the thin sheath limit, J_i is independent of χ, allowing for the electron temperature to be expressed implicitly as a function of V_{d2} and V_{d3}. Assuming that all three electrodes are the same dimensions, when equation A.37 is divided by equation A.37 and A.39, the left hand side is equal to 1/2; the right hand side can be further modified by eliminating J_{eo} with equation A.38 which leads to:

$$\frac{1}{2} = \frac{1 - exp(-\chi_{d2})}{1 - exp(-\chi_{d3})} \qquad (A.40)$$

where $\chi_{d2} = \chi_2 - \chi_1$, and $\chi_{d3} = \chi_3 - \chi_1$. To obtain the electron number density, Chen and Sekiguchi have modeled the ion current using the Bohm sheath criterion which has been described previously: $J_i = exp(-.5)en_e(kT_e/M_i)^{1/2}$. Using this expression for the ion current, substitutions can be made into equations A.37 and A.38 above to determine the electron number density:

$$n_e = \frac{exp(0.5)\frac{I}{A_3}}{e(\frac{kT_e}{M_i})^{1/2}(1 - exp(-(\chi_{d3} - \chi_{d2})))} \qquad (A.41)$$

Eqns. A.38 and A.39 can be manipulated to yield another expression for the electron number density:

$$n_e = \frac{exp(0.5)\frac{I}{A_3}}{e(\frac{kT_e}{M_i})^{1/2}(exp(\chi_{d2} - 1))} \qquad (A.42)$$

In the above expression, A_1 is the probe surface area, k is Boltzmann's constant, and I is the probe current. The formulae for T_e and n_e assume a Maxwellian electron distribution and thin collisionless sheath. (i.e. $r_p >> \lambda_d$) and $\lambda_e >> \lambda_d$ where λ_d is the electron Debye length). The additional requirement that the electron mean free path be much larger than the probe radius ($\lambda_e > r_p$) may not be satisfied in the quasi-steady MPD thruster where the charged particle densities can approach 1 x $10^{21}m^{-3}$. This effect is expected to have only a minor effect on ion current collection

of the probe, however [23].

In solving the equations for n_e and T_e, the following assumptions are made:

- J_i is independent of χ in the thin sheath limit.

- $A_1 = A_3$.

- V_{d3} is set negative to repel enough electrons to make the flux of electrons and ions to the probe surface comparable.

In an effort to obtain the most accurate interpretation of the probe results, the following criteria were considered while designing the probe:

$$\frac{r_p}{\lambda_d} \gg 1 \qquad \text{(A.43)}$$

$$\frac{\lambda_{ii}}{r_p} \gg 1 \qquad \text{(A.44)}$$

$$\tau = \frac{L_p}{r_p} \sqrt{\frac{Z_i K T_e}{M_i}} \frac{1}{U_{di}} \gg 1 \qquad \text{(A.45)}$$

$$\frac{S}{\lambda_d} \gg 1 \qquad \text{(A.46)}$$

$$\frac{r_{le}}{r_p} \gg 1 \qquad \text{(A.47)}$$

$$\frac{eV_{d3}}{kT_e} \gg 1 \qquad \text{(A.48)}$$

where r_p is the probe radius, λ_{ii} is the ion-ion mean free path, τ is an end effect parameter for the probe, Z_i is the ion charge number, L_p is the probe length and S is the inter-electrode spacing. The first two equations are necessary for the thin collisionless sheath criterion to hold true. Equation A.45 allows for the probe end effects to be ignored. Equation A.46 assures that the sheath surrounding one electrode does not affect either of the other electrodes. Equation A.47 is required for the

magnetic fields to not interfere with electron motion to the probe. This particular criterion is hardest to fulfill in an MPD near the anode where high magnetic fields can lead to the electron Larmour radius to approach the probe radius in magnitude. The last equation results in the eV_{d3} being dropped from the equation for T_e, thereby allowing the electron temperature calculation based solely on V_{d2}.

The crucial assumption in the derivations above is the underlying assumption of a thin sheath. In reality, the ion saturation current is a function of several parameters, changing the functional form of $J_i(\chi)$. The functional form of the ion current can be represented by the equation below, for a finite cylinder, two temperature, Maxwellian plasma, and perfectly absorbing surface.

$$J_i(\chi) = \sum_i J_{io}\nu_i(\chi, S_{\perp i}, \frac{r_p}{\lambda_d}, \frac{T_i}{Z_iT_e}, \frac{\lambda_i i}{r_p}, \tau, \frac{s}{\lambda_d}, \frac{r_{li}}{r_p}) \qquad (A.49)$$

where

$$J_{io} = n_iZ_ie(\frac{Z_ikT_e}{2\pi M_i})^{1/2} \qquad (A.50)$$

In the above equations, $S_{\perp i}$ is the ratio of the ion drift velocity perpendicular to the probe axis, $U_{\perp i}$, to the most probable ion thermal velocity $(2kT_i/M_i)^{1/2}$, r_p/λ_d is the ratio of the probe radius to the debye length, T_i/Z_iT_e is the ratio of the ion to electron temperature divided by the ion charge number, λ_{ii}/r_p is the ion-ion Knudsen number (ratio of the ion-ion mean free path to the probe radius), τ is an end effect parameter for a cylindrical probe aligned with the flow, s/λ_d is the probe spacing divided by the Debye length, and r_{Li}/r_p is the ratio of the ion Larmour radius to the probe radius. As seen by the equation above, the ion current to the probe is affected by many parameters. The effect of the parameters on the electron temperature and density measurements is given in detail in reference [64].

As with the ion current, the electron current can be significantly affected by magnetic fields, electron drift, and electron-ion collisions, yielding an equation analogous to the one above:

$$J_e(\chi) = \sum_i j_{eo} \nu_e(\chi, \frac{r_{Le}}{r_p}, \frac{\lambda_{ei}}{r_p}, S_{\perp i}) \qquad (A.51)$$

where r_{Le}/r_p is the ratio of the electron Larmour radius to the probe radius, λ_{ei}/r_p is the electron ion Knudsen number, and $S_{\perp e}$ is the electron drift perpendicular to the probe, $U_{\perp e}$, divided by the most probable electron velocity $[(2kT_e/m_e)^{.5}]$. In this study, V_{d3} was set high to make sure that the electron flux at electrode 3 was negligible compared to the ion flux. This results in the formation of an explicit relation for V_{d2}.

$$\frac{eV_{d2}}{kT_e} = ln(\frac{I_{i1} + I_{i3}}{I_{i2}}) + ln(\frac{A_2}{A_1}) + ln(\frac{O_e(\chi_2)}{O_e(\chi_1)}) + \frac{eV_{cont}}{kT_e} \qquad (A.52)$$

where I_{ij} is the ion current to electrode j, A_j is the collection area of electrode j and ΔV_{cont} is the contact potential difference. The first term reduces to $ln2$ in the thin sheath limit, the second term accounts for the difference in electrode areas and the third taken into account the deviation of the electron flux from $A_j J_{eo} exp(-\chi_j)$. When using the simplified theory, the assumption is made that the last two terms in the expression above are negligible in a clean probe and if the probe was fabricated with equal electrode dimensions.

In an effort to obtain the most accurate interpretation of the probe results, curve fits of Laframboise's exact solution of current collection by a cylindrical probe in an unmagnetized, two temperature, collisionless plasma have been applied to the triple probe results along with the Peterson-Talbot curve fits[53]. The curve fits are as follows:

$$J_i(\chi_j) = [B_p + \chi_j]^\alpha \qquad (A.53)$$

where

$$\alpha = \frac{2.9}{ln\frac{r_p}{\lambda_d} + 2.3} + .07(\frac{T_i}{Z_i T_e})^{.75} - 0.34 \qquad (A.54)$$

and

194

$$B_p = 1.5 + (0.85 + 0.135(ln(\frac{r_p}{\lambda_d}))^3)(\frac{T_i}{Z_i T_e}) \qquad (A.55)$$

Laframboise's theory is based on the assumption that only one ionized species exists and that end effects and sheath interactions are negligible. The following equations can be solved simultaneously to obtain the corrected values for n_e and T_e.

- Implicit relation for the electron temperature:

$$\frac{1}{2} = \frac{1 - \frac{1}{2}([1 - \beta_p V_{d2} - V_{d3}]^{\frac{1}{2}})exp(-\chi_{d2})}{1 - exp(-\chi_{d2})} \qquad (A.56)$$

where

$$\beta_p = \frac{e\eta_{probe}}{kT_e} \qquad (A.57)$$

$$\eta_{probe} = (\frac{dJ_i^2(\chi_j)}{d\chi_j})_f(\frac{1}{J_i^2(\chi_f)}) \qquad (A.58)$$

and χ_f is the dimensionless floating potential.

- The Peterson-Talbot curve fit yields the following expression:

$$\eta_{probe} = \frac{2\alpha}{B_p + \chi_f} \qquad (A.59)$$

- The fact that the triple probe must be floating with respect to the plasma and consequent lack of charge exchange with the plasma yields the following expression:

$$[B_p + \chi_f]^{2\alpha} - \frac{M_i}{m_e}exp(-2\chi_f) = 0 \qquad (A.60)$$

- The number density equation based on Laframboise's results:

$$n_e = \frac{1}{e}\sqrt{\frac{2\pi M_i}{kT_e}} \frac{\frac{I_{probe}}{A_3}}{([B_p + (\chi_{d3} - \chi_{d2}) + \chi_f]^\alpha - [B_p + \chi_f]exp[\chi_{d2} - \chi_{d3}])} \quad (A.61)$$

The above equations can be solved numerically to yield the values for n_e and T_e. The last check to be made is that r_p/λ_d is consistent. This value should be updated based on the calculation of n_e and T_e and this process iterated until convergence. The flow chart for the process just described is given in Fig. A-15.

The corrections to the Bohm model (Equations A.56 and A.61) introduced by Laframboise's solution take into account phenomena which affect ion collection such as finite ion temperature and sheath thickness. For the dense plasma such as the one present in quasi-steady MPD thrusters, this correction is minimal, changing T_e and n_e by 5% and 10%, respectively [23]. The final values of T_e and n_e via the triple probe technique are estimated to be accurate to within 10% and 60%, respectively for a probe aligned with ion flow.

In general, Laframboise's theory may be considered exact for r_p/λ_d between 5 and 100 and is valid for values greater than 100 with a relatively small error involved. One should also note that for $\chi_{d3} < 3$, the above equations do not converge self-consistently with r_p/λ_d. V_{d3} was set high enough for this particular study so that χ_{d3} was always greater than 3.

Application of Laframboise's solution to a flowing plasma can yield inaccurate data if special care is not taken during analysis. The probe axis should be aligned parallel with the flowing plasma to minimize the convective ion current perpendicular to the probe leading to artificially high number density measurements. In addition, the minimum probe aspect ratio (L/r_p) for which Laframboise's results are valid has been estimated to be twenty for a quiescent plasma [41],[53],[64]. For a flowing plasma where $r_p >> \lambda_d$ (probe radius is much greater than the Debye length), the additional current due to the convection of ions through the end of an aligned probe is

$$\frac{I(L)}{I(\infty)} = 1 + \frac{r_p}{L}\frac{U_p}{\sqrt{\frac{kT_e}{M_i}}} \quad (A.62)$$

196
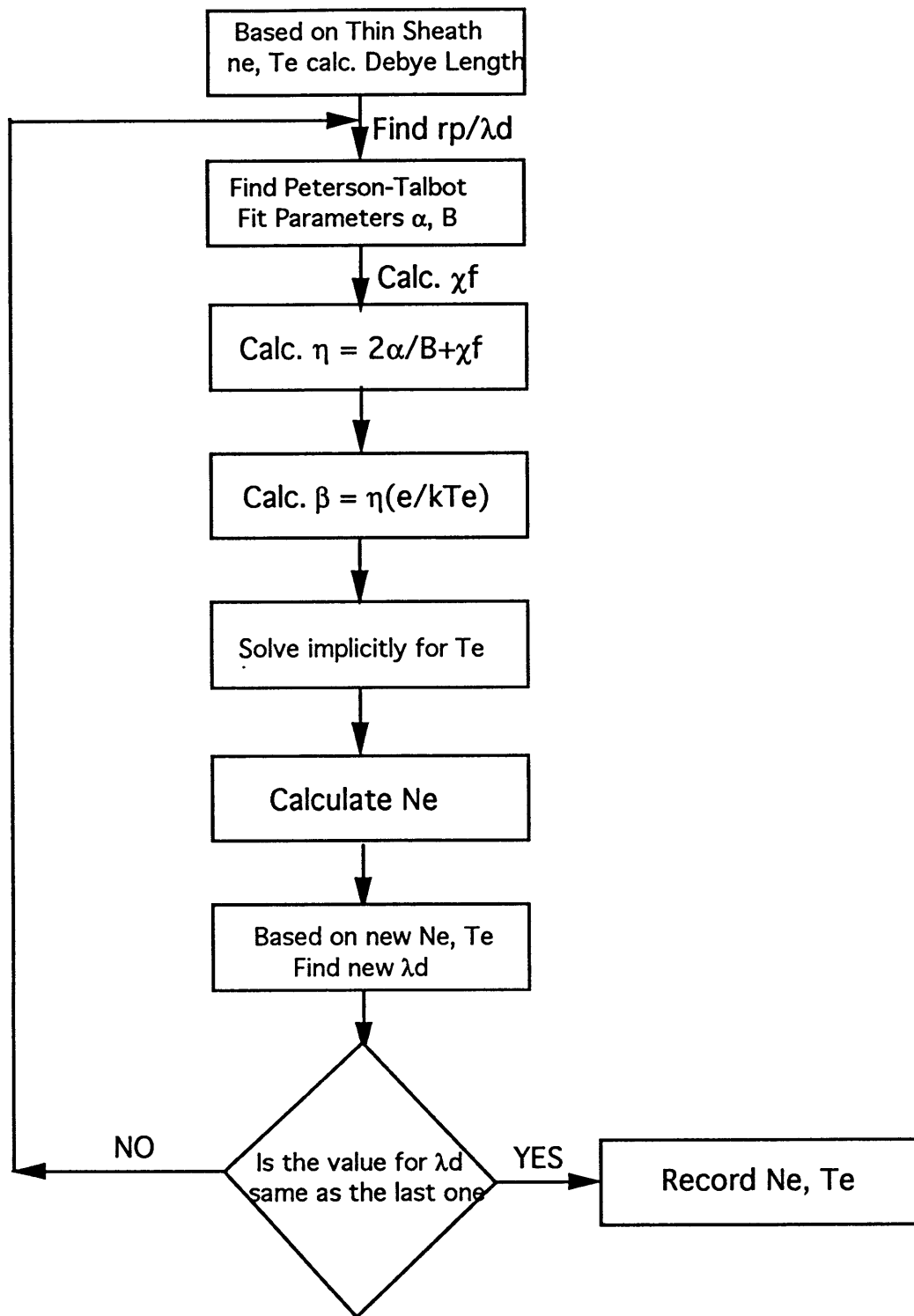
Figure A-15: Flow Chart For The Calculation of Ne and Te Based on Laframboise
Solution With The Peterson-Talbot Curve Fit

where the ratio $\frac{I(L)}{I(\infty)}$ is the finite length correction to Laframboise's currents [41]. For typical MPD thruster conditions near the axis $kT_e \sim 3$ eV, $U_p \sim 10,000$ m/s, $L/r_p \sim 50$, this correction predicts a 10% increase in current[23].

The values obtained with the triple probe aligned with the flow are expected to be accurate to within 10% for T_e and 60% for n_e. It is important, however, to estimate the additional errors in the measurements of these quantitities with a misaligned probe. Errors in number density can be roughly estimated with the following analysis from reference [23]. For $C_i \ll U_p \ll C_e$, where C_i and C_e are the ion and electron thermal velocities, respectively, and U_p is the plasma bulk velocity, the total current to a probe is approximately

$$I(\theta) = I_{p\|} + (I_{p\perp} - I_{p\|})sin\theta \qquad (A.63)$$

where θ is the angle of the probe axis with respect to that of the plasma bulk flow and $I_{p\|}$ and $I_{p\perp}$ are measured probe currents when the probe axis is parallel with and perpendicular to the flow, respectively. The current definitions are as follows:

$$I_{p\|} \sim \kappa q A_\| n_i \sqrt{\frac{kT_e}{M_i}} \qquad (A.64)$$

$$I_{p\perp} \sim q A_\perp n_i U_p \qquad (A.65)$$

where $A_\|$ and $A_\perp$ are effective probe areas for either extreme in probe orientation, and κ is a dimensionless proportionality constant (~ 0.5). Assuming that $A_\| \sim 2\pi r_p L$ and $A_\perp \sim 2 r_p L$, then

$$\frac{I_{p\perp}}{I_{p\|}} \sim \frac{2U_p}{\pi\sqrt{kT_e/M_i}} \qquad (A.66)$$

For the typical thruster operating conditions, ($C_i \sim 2,200 m/s, U_p \sim 10,000 m/s$ and $C_e \sim 100,000 m/s$), the above equation yields $I_{p\perp}/I_{p\|} \sim 3$ which is consistent with the experimental results cited in Reference [23]. Alignment of the probe with the flow is therefore imperative if one is to get reasonably accurate results. The over-

all error for T_e and n_e for this particular study comprised of two categories, namely "random error" and "systematic error". Random error is associated with the repeatability of the probe signals at any given operating condition. The random error for T_e and n_e was determined to be 5% and 10%, respectively. The schematic error, on the other hand, is associated with the probe fabrication and interpretation of the probe signal in deducing the values for electron temperature and density. As mentioned previously, several assumptions were made in calculating the two key plasma parameters from measured probe signals. Each assumption adds error to the eventual result. The schematic error associated with the T_e and n_e measurements was 15% and 70%, respectively. The overall error, therefore, for the temperature and density measurements was 20% and 80%, respectively.

A.3   Magnetic Induction Probe Theory

A magnetic induction probe can be used to determine the current distribution via the magnetic field strength measurements throughout the MPD thruster. The probe usually consists of a several turn cylindrical coil inserted into a sealed quartz tube for protection from the plasma. Due to the small coil cross-section, magnetic field is assumed that the magnetic field does not vary over it. As a result, the voltage induced in the coil by a magnetic field can be represented by:

$$V_i = -A_{eff}\frac{dB_\perp}{dt}(t) \tag{A.67}$$

where V_i is the induced voltage, A_{eff} is the effective cross sectional area of the coil, and $B_\perp$ is the magnetic field perpendicular to the coil. As the equation indicates, the voltage induced is proportional to the time derivative of the magnetic field. The signal, therefore, must be time integrated to obtain a value for the actual magnetic field as a function of the induced voltage. An electronic schematic for the induction probe is shown in Fig. A-16.

A calibration has to be performed to determine the magnetic field as a function of this induced voltage. The probe can be calibrated in a known varying magnetic
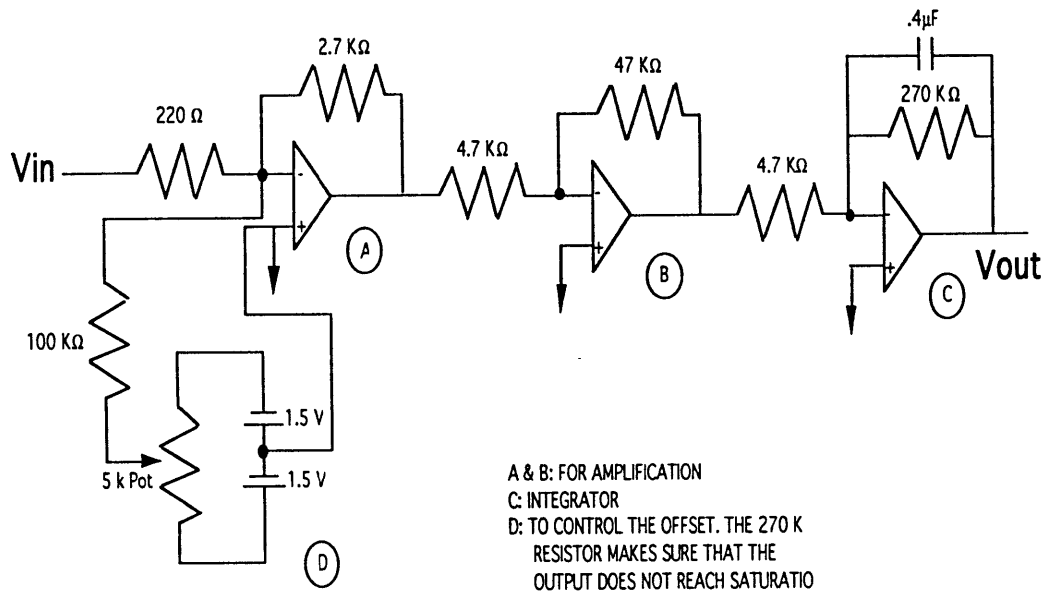
Figure A-16: Induction Probe Electronics

field and a calibration curve of $B(V_i)$ can be obtained.

Ampere's law can be used to calibrate the induction probe and also to determine current densities from the measured magnetic field strengths. To measure magnetic fields, the probe output signal is integrated with an electronic integrator as shown in Fig. A-16. A 50 Ω terminator was used to match the impedance of the coaxial cable line with that of the integrator. This ensures that the error associated with signal reflection is minimized [43, 59].

A.3.1 B-Probe Calibration

The probe was calibrated in a simple manner. The induction probe was place at the very back of the thruster close to the anode such that ideally the entire thruster current would be enclosed by the coil. The thruster was fired at various current levels and linear relationship was obtained between the measured thruster current and the induction probe voltage output using a linear fit. In addition, Ampere's law was used to get the magnetic field as a function of thruster current as given by the equation below.

$$B = \frac{\mu_o I}{2\pi r_{th}}$$

(A.68)

where μ_o is the permittivity of free space, I is the measured thruster current and r_{th} is the thruster radial location where the probe is placed. The two equations were then used to get the experimental relationship between the induction probe voltage output and the magnetic field. The experimental value was then compared to the theoretical voltage output as a function of the magnetic field as given by eq. A.69.

$$V_{out} = \frac{1}{RC}\pi r^2 n B \qquad (A.69)$$

where r is the coil radius, R and C are the integrator resistor and capacitor values, respectively. The right hand side would have to be multiplied by a gain factor (G) if the probe output was sent through an amplifier prior to going through the integrator. The magnetic probe theory rests entirely on Ampere's law which states that the line integral of the magnetic field B around any closed path C is proportional to the total current I flowing through the area of which C is the perimeter. That is,

$$\oint_c B \cdot ds = \mu_o I \qquad (A.70)$$

Nearly all plasmas open to diagnostic methods are penetrated by magnetic fields. These magnetic fields stem either from current flowing in external conductors or are generated from electrical current flowing in the plasma itself as is the case with the MPD. A full description of a plasma under investigation must therefore contain information on the spatial distribution and temporal variation of these magnetic field and subsequently the current.

Induction probes can produce voltages much higher than the electrical noise level of the plasma [8], but the actual voltage is a function of the effective area of the coil and dB/dt.

As mentioned earlier, one can go from the measured field distribution to the wanted current densities using Maxwell's equations. Since the spatial resolution of induction probe measurements is limited to about 2 mm, a meaningful measurement of the distribution of the distribution of the magnetic field strength B is restricted to plasmas with a diameter of at least several centimeters. Nearly all measurements of

magnetic field distributions in pulsed discharges, such as quasi-steady MPD devices, have been made with inductive probes [1-5] because these probes are easily produced in the laboratory. The error associated with the induction probe measurements consists of "random" and "schematic" parts. The random error during this particular set of experiments was found to be 15% and the schematic error associated primarily with the calibration procedure was determined to be 25%, leading to an overall error of 40% for the magnetic field and enclosed current values.

Appendix B

List of Symbols and Constants

Symbol Description

A	Electrode Area (m^2)
B	Peterson-Talbot Curve Fit Parameter
$\mathbf{B}$	Magnetic Field Strength (Gauss)
$\bar{C}_e$	Electron Thermal Velocity $\sqrt{\frac{8kT_e}{\pi m_e}}$ (m/sec)
C_i	Ion Thermal Velocity (m/sec)
e	Elementary Charge, $1.6 \times 10^-19 C$
E	Electric Field (V/m)
f_e	Distribution Function
I	Thruster Current (kA)
I_3	Triple Probe Current (A)
I_e	Total Electron Current to An Electrode (A)
I_i	Total Ion Current to Electrode (A)
I_{se}	Electron Saturation Current (A)
I_{si}	Ion Saturation Current (A)
J_a	Total Anode Current (A)
j	Current Density (A/cm^2)
j_a	Anode Current Density (A/cm^2)
J_e	Electron Flux at the Surface of an Electrode
J_{eo}	Random Electron Thermal Current $(en_e\sqrt{(8kT_e/\pi m_e)}$

J_i	Ion Flux at the Surface of an Electrode
J_{io}	Random Ion Thermal Current
k	Boltzmann's Constant, $1.38 \times 10^{-23} J/K$
k_n	Knudsen Number, $\lambda_{ei}/r_p \, or \, \lambda_{ii}/r_p$
L_p	Probe Length (m)
$\dot{m}$	Thruster Mass Flow Rate (g/sec)
m_e	Electron Mass, $9.11 \times 10^{-31} kg$
m_i	Argon Ion Mass, $6.626 \times 10^{-26} kg$
n_e	Electron Number Density (m^{-3})
n_i	Ion Number Density (m^{-3})
r_a	Anode Radius (m)
r_c	Cathode Radius (m)
r_{le}	Electron Larmour Radius (m)
r_{li}	Ion Larmour Radius (m)
r_p	Probe Radius (m)
$r_t h$	Probe Radial Location (m)
s	Inter-Electrode Spacing (m)
$S_\perp$	$U_{\perp i}/(2kT_i/m_i)$
p_e	Electron Pressure (Pa)
P_t	Total Anode Power (W)
$\dot{Q}_a$	Anode Heat Flux (W/cm^2)
$\dot{Q}_c$	Convective Anode Heat Flux (W/cm^2)
$\dot{Q}_r$	Radiative Anode Heat Flux (W/cm^2)
T_e	Electron Temperature (K)
T_g	Heavy Species Temperature (K)
t_s	Sheath Thickness (m)
U_j	Drift Velocity of Species j (m/sec)
V_i	Potential of ith Electrode (V)
V_p	Plasma Potential (V)
V_f	Floating Potential (V)

v_x	Plasma Bulk Velocity (Axial Component) (m/sec)
v_y	Plasma Bulk Velocity (Radial Component) (m/sec)
V	Thruster Voltage (V)
V_a	Anode Fall (V)
α	Peterson-Talbot Curve Fit Parameter
ϵ	Total Particle Energy (eV)
ϵ_o	Permittivity of Free Space, $8.85 \times 10^{-12} F/m$
ϕ	Anode Material Work Function (eV)
λ_d	Debye Length (m)
Λ	Coulomb Collision Parameter
λ_{ei}	Electron-ion Mean Free Path (m)
λ_{ii}	Ion-Ion Mean Free Path (m)
ω_e	Electron Gyrofrequency (sec^{-1})
Ω	Hall Parameter
Ω_{calc}	Classically Calculated Hall Parameter
Ω_{inf}	Inferred Hall Parameter
$\phi(x)$	Potential as a Function of Distance
σ_{calc}	Spitzer-Harm Electrical Conductivity (mho/m)
σ_{inf}	Inferred Electrical Conductivity (mho/m)
σ_i	Background Charge Density
ν_{ei}	Electron-ion Collision Frequency (sec^{-1})
μ_o	Permeability of Free Space $4\pi \times 10^{-7}$ H/m
χ_i	Non-Dimensional Electrode Potential

Appendix C

Schematics of Thruster Components

Figures 11-1 through 11-6 show the different components of the MPD thruster used in this study. Fig. 11-1 shows the entire MPD thruster assembly. The anode, cathode, boron-nitride backplate, cathode stub and plexiglass mounting components are shown in Figs. 11-2 through 11-6, respectively.

The anode and cathode stub were made from high purity copper; the cathode was 2% thoriated Tungsten; the insulating backplate was made from Boron Nitride and the pieces used to mount the thruster to the chamber floor were made from plexiglass.
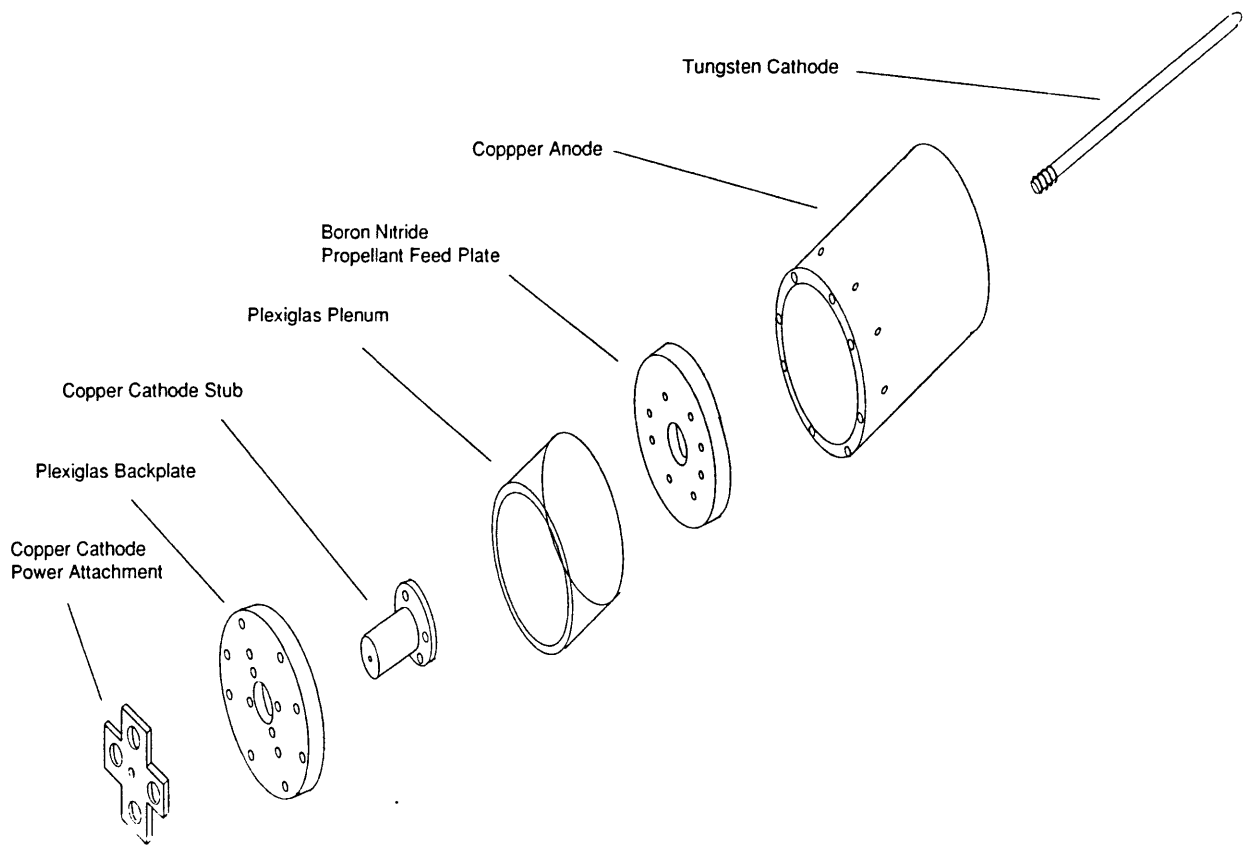
Figure C-1: MPD Thruster Assembly Drawing
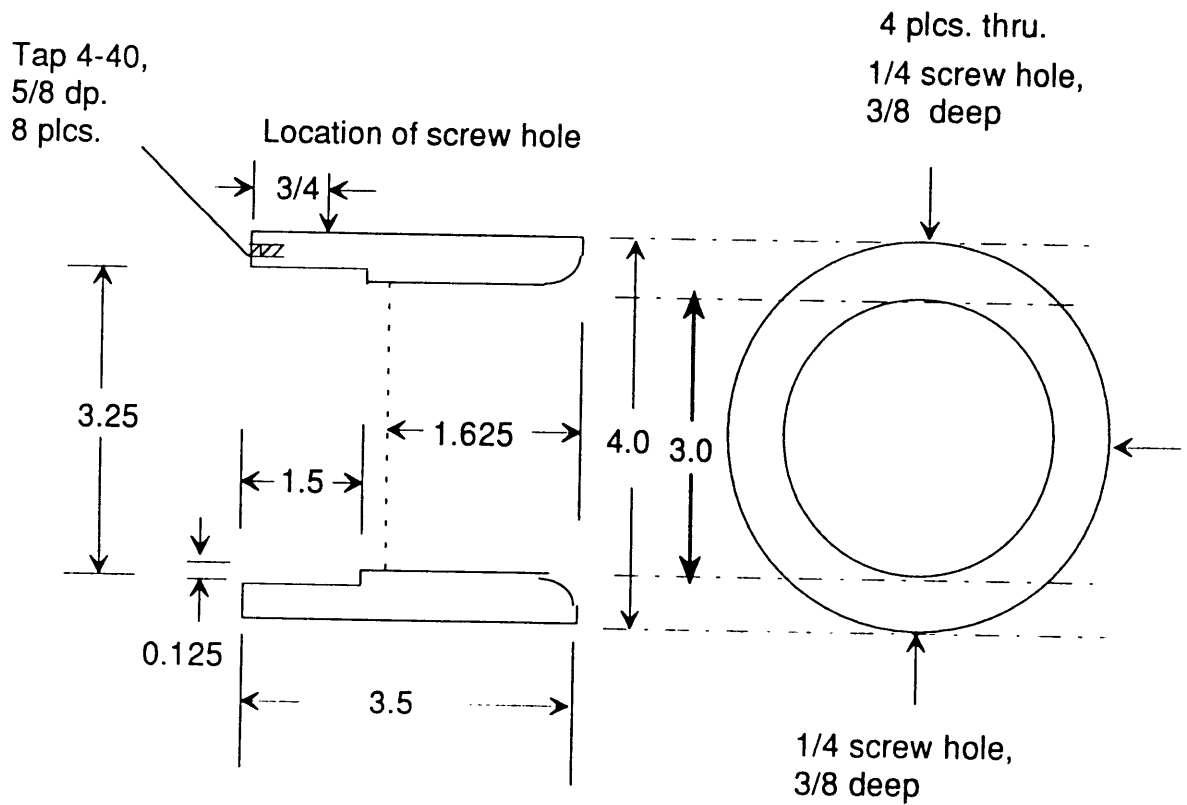
Figure C-2: Anode and Cathode

2

3.25

2.75

.125 square groove cut out

→| .5 |←

3.0
0.75

1/8 inch propellant holes
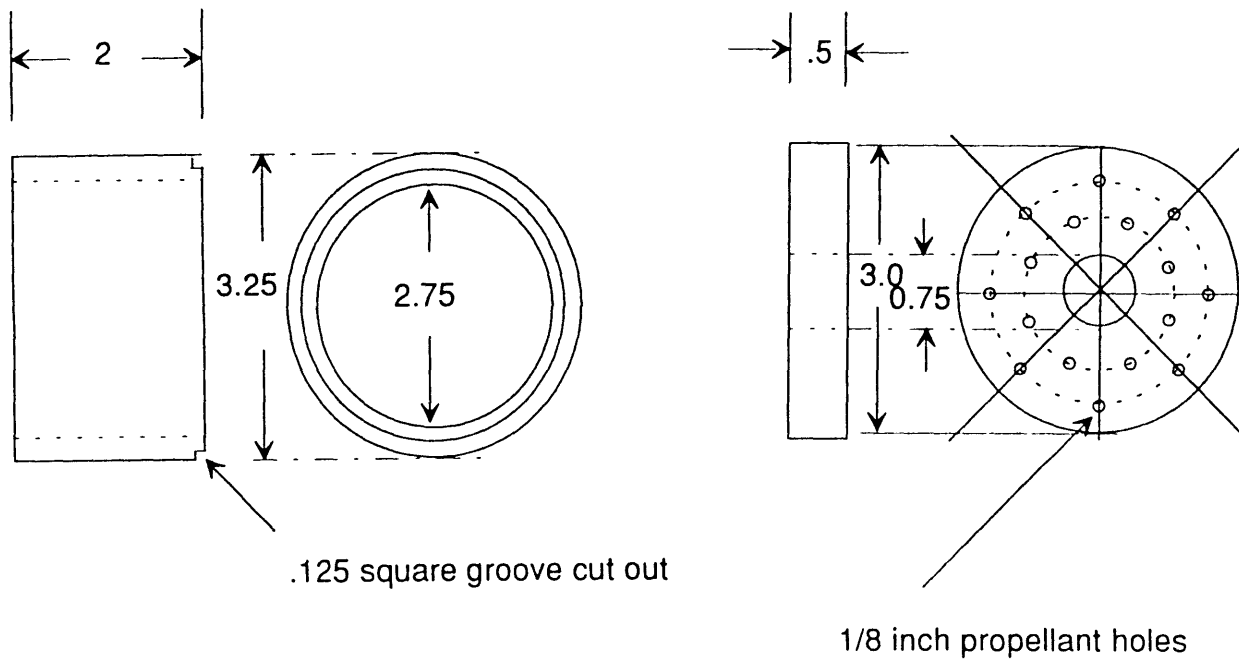
Figure C-3: Plexiglass Plenum and Boron Nitride Backplate

Drill for 1/8 inch bolt

1→|←1→|

1/8 inch bolt hole

1/2 inch punched hole

0.25

0.25

0.5

1

0.5

0.25

2

Drill for screw end of cathode

Figure C-4: Cathode Stub

208

1/4 inch hole

0.25 wide groove,
0.5 deep

1/8 inch propellant/spark wire holes
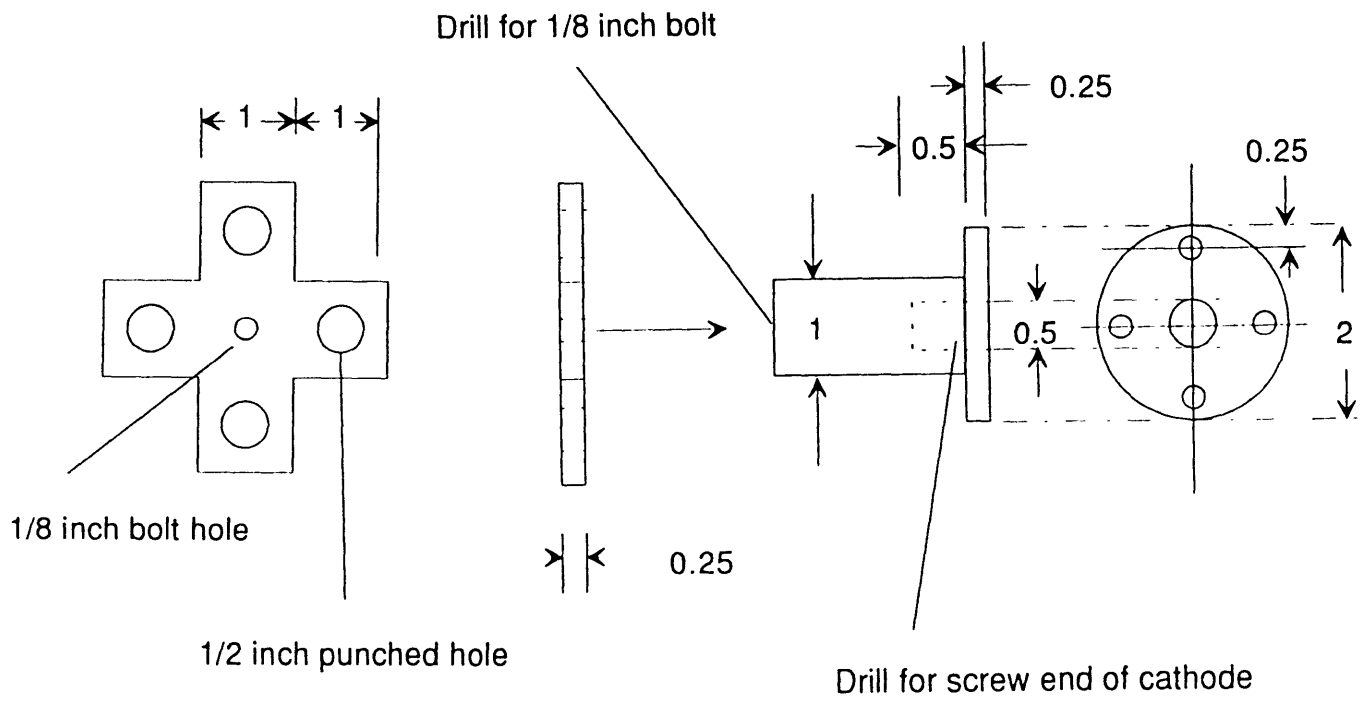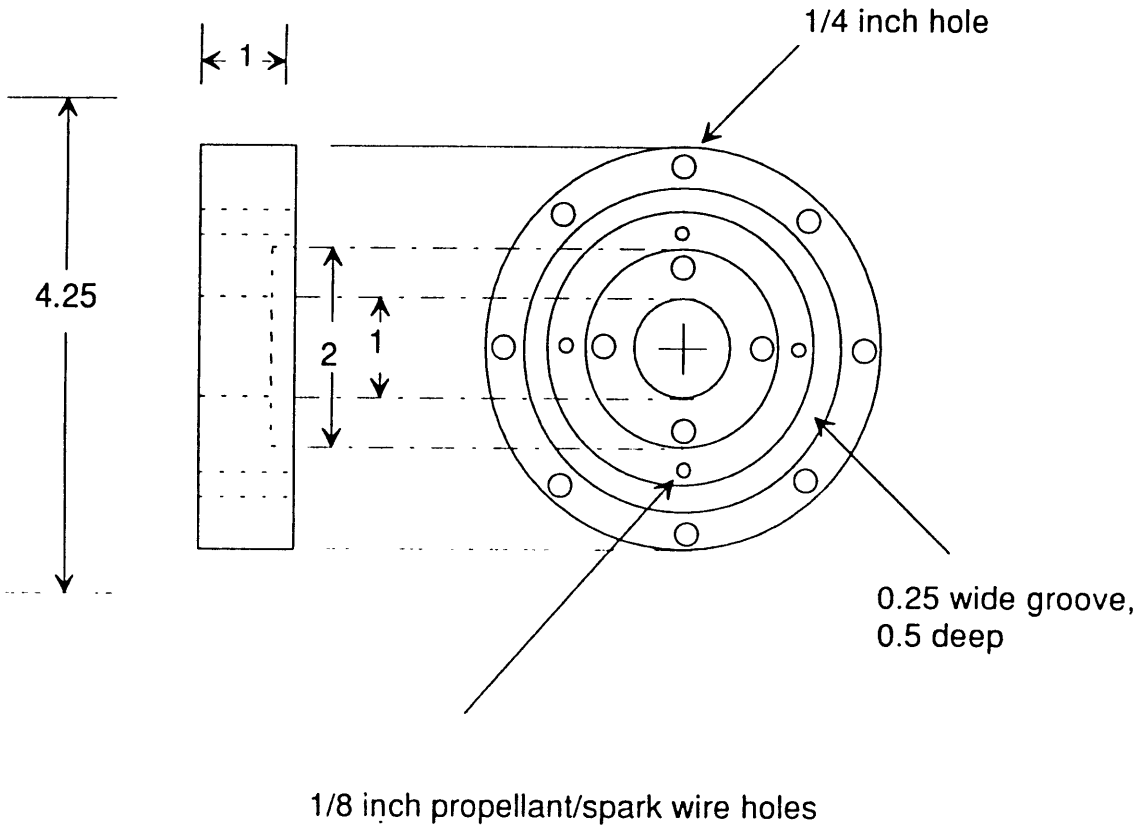
Figure C-5: Plexiglass Mounting Backplate

2.0 Rad

1/4 inch bolt holes

Figure C-6: Plexiglass Thruster Saddle

Bibliography

[1] Paganucci F. Andrenucci M. and G. La Motta. Mpd thruster performance with cathode heating. *AIAA/SAE/ASME/ASEE 28th Joint Propulsion Conference*, (AIAA-92-3458), July 6-8 1992.

[2] J. Garner C. Aston, G. Brophy and L. Pless. A xenon ion propulsion module for enhanced spacecraft capability. *22nd Joint Propulsion Conference*, (AIAA-86-3821), July 16-18 1986.

[3] G. R. Babb and W. R. Stump. Comparison of mission design options for manned mars missions. *Manned Mars Mission, Working Group Papers*, (NASA TM-89320), 1986.
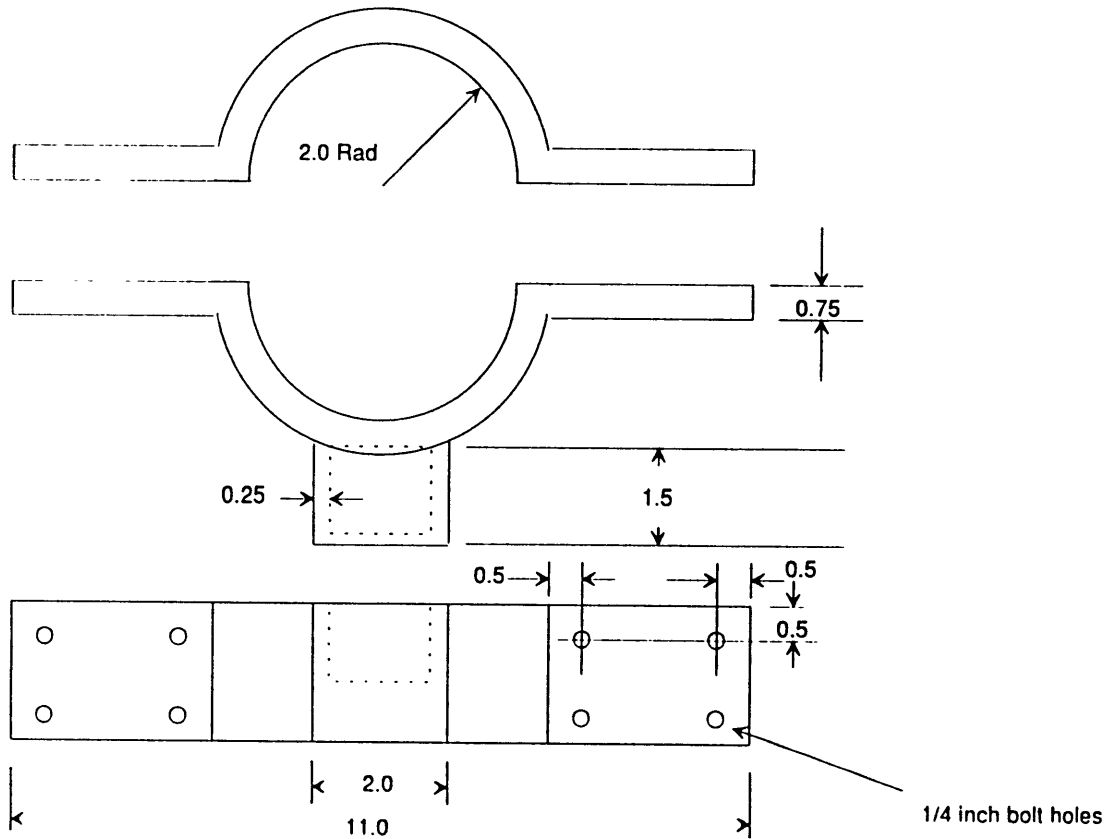
[4] B.Y. Baksht, F.G. Moizhes and A.B. Rybakov. Critical regime of a plasma accelerator. *Sov. J. Plasma Phys.*, Vol. 18(No. 12):pp. 1613–1616, June 1974.

[5] J.N. Beattie, J.F. Matossian and R. R. Robinson. Status of xenon ion propulsion technology. *19th AIAA/DGLR/JSASS Internation Electric Propulsion Conference*, (AIAA-87-1003), May 1987.

[6] M. Birkan and M. M. Micci. Survey of electric propulsion thruster applicability to near earth space missions. *DGLR/AIAA/JSASS 20th International Electric Propulsion Conference*, (IEPC-88-065), October 3-6 1988.

[7] T.K. Bose and E. Pfender. Direct and indirect measurements of the anode fall in a coaxial arc configuration. *AIAA Journal*, Vol. 7(No. 8):pp 1643–1645, August 1969.

[8] E. Bowman. *Microinstabilities in High-Power MPD Systems: Preliminary Diagnostics.* School of Aeronautical and Astronautical Engineering, Purdue University, 1992.

[9] E.Y. Kelly A.J. Caldo, G. Choueiri and R.G. Jahn. An mpd code with anomalous transport. *22nd International Electric Propulsion Conference*, (AIAA-91-102), October 14-17 1991.

[10] L. M. Carney and J. M. Sankovic. The effects of arcjet thruste operating conditions and constrictor geometry on the plasma plume. *25th Joint Propulsion Conference*, (AIAA-89-2723), July 10-12 1989.

[11] S Castillo. Mpd propulsion facility at edwards air force base. (AIAA-91-0054), 1991.

[12] S.L. Chen and T. Sekiguchi. Instantaneous direct-display system of plasma parameters by means of triple probe. *Journal of Applied Physics*, Vol. 36(No. 8):pp. 2363–2375, Aug. 1965.

[13] E.Y. Choueiri. *Electron-Ion Streaming Instabilities of an Electromagnetically Accelerated Plasma.* Ph. D. Thesis, Dept. of Mechanical and Aerospace Engineering, Princeton Univ., 1991.

[14] S. R. Haag T. W. Sarmiento C. J. Curran, F. M. Bullock and J. M. Sankovic. Medium power hydrogen arcjet performance. *27th Joint Propulsion Conference*, (AIAA-91-2343), June 24-27 1991.

[15] Buden D. Nuclear thermal rocket propulsion. *26th Joint Propulsion Conference*, (AIAA-90-2755), July 16-18 1990.

[16] S.M. Dyuzhev, G.A. Shkol'nik and V.G. Yur'ev. Anode phenomena in the high-current arc i. *Sov. Phys. Tech. Phys.*, Vol. 23(No. 6):pp 667–671, July 1978.

[17] S.M. Dyuzhev, G.A. Shkol'nik and V.G. Yur'ev. Anode phenomena in the high-current arc ii. *Sov. Phys. Tech. Phys.*, Vol. 23(No. 6):pp. 672–677, July 1978.

[18] Tosti E. and W. D. Deininger. Plume analysis of a 10 kwe/n arcjet using emission spectroscopy. *AIDAA/AIAA/DGLR/JSASS 22nd International Electric Propulsion Conference*, (IEPC-91-092), October 14-17 1991.

[19] E.R.G. Eckert and E. Pfender. *Advances in Heat Transfer*, volume Vol. 2. Academic Press, New York, NY, 1967.

[20] Chen F.F. *Plasma Diagnostic Techniques*. Academic Press, New York, NY, 1965.

[21] A. Gallimore. *Anode Power Deposition in Coaxial MPD Thrusters*. Dept. of Mechanical and Aerospace Engineering, Princeton Univ., 1992.

[22] A.J. Gallimore, A.D. Kelly and R.G. Jahn. Anode power deposition in quasi-steady mpd thrusters. *21st International Electric Propulsion Conference*, (AIAA-90-2668), July 18-20 1990.

[23] R.M. Gallimore, A.D. Myers and R.G. Jahn. Anode power deposition in an applied field segmented anode mpd thruster. *27th Joint Propulsion Conference*, (AIAA-91-2343), June 24-27 1991.

[24] P. W. Garrison and J. F. Stocky. Future spacecraft propulsion. *J. Propulsion*, Vol. 4(No. 6), Nov-Dec 1988.

[25] R. H. Garrison, P. W. Frisbee and M. F. Pompa. Ultra high performance propulsion for planetary spacecraft. *FY '81 Final Report*, 10(JPL D-2123), 1987.

[26] J. A. Riehl J. P. Hack, K. J. George and J. H. Gilland. Evolutionary use of nuclear electric propulsion. *AIAA Space Programs and Technologies Conference*, (AIAA-90-3821), September 25-28 1990.

[27] E. Hershkowitz. *Plasma Diagnostics*. Academic Press, 1992.

[28] H.B. Kenny B.H. Hickman, J.M. Curtis and R.J. Sefcik. Systems analysis of mars solar electric propulsion vehicle. *AIAA Space Programs and Technologies Conference*, (AIAA-90-3824), September 25-28 1986.

[29] Griem H.R. *Plasma Spectroscopy*. McGraw Hill Book Company, New York, NY, 1964.

[30] Eds. R. H. Huddlestone and S. L. Leonard. *Plasma Diagnostic Techniques*. Academic Press, New York, NY, 1965.

[31] H. Hugel. Effect of self-magnetic forces on the anode mechanism of a high current discharge. *IEEE Transactions on Plasma Science*, Vol. PS-8(No. 4):pp. 437–442, Dec. 1980.

[32] Patterson M. J. Performance characteristics of ring-cusp thrusters with xenon propellant. *22nd Joint Propulsion Conference*, (AIAA-86-90), July 16-18 1986.

[33] R. G. Jahn. *Physics of Electric Propulsion*. McGraw Hill Book Company, New York, 1968.

[34] Lawless J.L. and V.V. Subramaniam. A review of the theory of self-field mpd thrusters. *AIDAA/AIAA/DGLR/JSASS 22nd International Electric Propulsion Conference*, (IEPC-91-019), October 14-17 1991.

[35] R.M. Jones. A comparison of potential electric propulsion systems for orbit transfer. *AIAA/JSASS/DGLR 16th Internation Electric Propulsion Conference*, (AIAA-82-1871), Nov. 1982.

[36] H.R. Kauffman and R.S. Robinson. Electric thruster performance for orbit raising and manouvering. *AIAA/SAE/ASME 18th Joint Propulsion Conference*, (AIAA-82-1247), June 1982.

[37] D. B. Kilfoyle and M. Martinez-Sachez. Spectroscopic investigation of the exit plane of an mpd thruster. *DGLR/AIAA/JSASS 20th International Electric Propulsion Conference*, (IEPC-88-027), October 3-6 1988.

[38] D.Q. King and J.C. Sercel. A review of the multi-megawatt mpd thruster and current mission applications. *22nd Joint Propulsion Conference*, (AIAA-86-1437), July 16-18 1986.

[39] M. Kuriki, K. Onishi and S. Morimoto. Thruster measurement of k iii mpd arcjet. *AIAA/JSASS/DGLR 15th International Electric Propulsion Conference*, (AIAA-81-0683), April 1981.

[40] Chemistry Laboratory. Inspection of mpd thruster contaminants. 1991.

[41] J. Laframboise. Theory of cylindrical and spherical probes in a collisionless plasma at rest. *ITIAS Report*, (No. 100), 1966.

[42] J.L. Lawless and V.V. Subramaniam. Theory of onset in magnetoplasmadynamic thrusters. *J. Propulsion*, Vol. 3(No. 2):pp. 121–127, March-April 1987.

[43] R.H. Lovberg. *Plasma Diagnostic Techniqes*. Academic Press, New York, NY, 1965.

[44] R.G. Garrison R.L. Malliaris, A.C. Jahn and D.R. Libby. Performance of quasi-steady mpd thrusters at high powers. *AIAA Journal*, Vol. 10(No. 2), Feb 1972.

[45] M. Martinez-Sanchez and D.J. Heimerdinger. Analysis of performance limiting factors in mpd thrusters. *IEEE International Conference on Plasma Science*, 1985.

[46] J.F. Mondt. Space reactor power, sp-100 ges phase ii project, afosr space power workshop. June 1988.

[47] S. Nakanishi and E. Pawlik. Experimental investigation of a 1.5 m diam. kaufman thruster. *J. Spacecraft*, Vol. 5(No. 7):pp 801–807, July 1968.

[48] E. H. Niewood. *A Two Dimensional Numerical Model of an MPD Thruster*. Ph. D. Thesis, Deparment of Aeronautics and Astronautics MIT, 1993.

[49] E.H. Niewood. The hall effect in a numerical model of mpd thrusters. *22nd International Electric Propulsion Conference*, (AIAA-91-099), October 14-17 1991.

[50] R.C. Oberth. *Anode Phenomenon in High-Current Discharges*. Ph.D. Thesis, Dept. of Aerospace and Mechanical Sciences, Princeton Univ., 1970.

[51] Friedberg P. *Class Notes: Plasma Laboratory.* MIT Press, Cambridge, MA, 1990.

[52] B. Palazweski. *Electric Propulsion Parameters for Manned Mars Exploration.* JANNAF Propulsion Meeting, Chemical Propulsion Information Agency, *May 1989.*

[53] *E.W. Peterson and L. Talbot. Collisionless electrostatic single-probe parameters by means of triple probe.* AIAA Journal, *Vol. 8(No. 12), 1970.*

[54] *D. Pivirotto, T. King and W. Deininger. The design and operating characteristics of a 30 kw thermal arcjet engine for space propulsion.* 22nd Joint Propulsion Conference, *(AIAA-86-1508), June 16-18 1986.*

[55] *D.Q. Pivirotto, T.J. King and W.D. Deininger. Long duration test of a 30 kw class thermal arcjet engine.* AIAA/SAE/ASME/ASEE 23rd Joint Propulsion Conference, *(AIAA-87-1947), June-July 1987.*

[56] *J. Preble.* Onset in Magnetoplasmadynamic Thrusters: A Model of an Electrothermal Instability. *MIT Dept. of Aeronautics and Astronautics, May 1990.*

[57] *D. Robinson and P. D. Lenn. Plasma diagnostics by spectroscopic methods.* Applied Optics, *Vol. 6(No. 6), June 1967.*

[58] *L.K. Rudolph and D.Q. King. Electromagnetic thrusters for spacecraft prime propulsion.* AIAA/SAE/ASME 20th Joint Propulsion Conference, *(AIAA-84-1446), June 11-13 1984.*

[59] *L. Schott.* Plasma Diagnostics. *John Wiley and Sons, Inc., New York, NY, 1968.*

[60] *K.T. Shih. Anode current and heat flux distributions in an mpd engine.* AIAA 7th Electric Propulsion Conference, *(AIAA-69-244), March 3-5 1969.*

[61] *K.T. Shih and E. Pfender. Electrode energy transfer mechanisms in a mpd arc.* AIAA Journal, *Vol. 8(No. 2):pp. 211-215, Feb. 1970.*

[62] A.P. Shubin. *Dynamic nature of critical regimes in steady-state high current plasma accelerators.* Sov. J. Plasma Phys., *Vol. 2(No. 1):pp. 18–21, Jan-Feb 1976.*

[63] J.S. Sovey and M. M. Mantenieks. *Performance and lifetime assessment of magnetoplasmadynamic arc thruster technology.* J. Propulsion, *Vol. 7(No. 1):pp 71–83, Jan-Feb 1991.*

[64] D. Tilley. *The application of the triple probe method to mpd thruster plumes.* 21st International Electric Propulsion Conference, *(AIAA-90-2667), July 18-20 1990.*

[65] P.J. Turchi and R.G. Jahn. *The cathode region of a quasi-steady mpd arcjet.* AIAA 8th Electric Propulsion Conference, *(AIAA-70-1094), Aug-Sept 1970.*

[66] G.A. Vainberg, L.I. Lyubimov and G.G. Smolin. *High current discharge effects and anode damage in an end-fire plasma accelerator.* Sov. Phys. Tech. Phys., *Vol. 23(No. 4):pp 439–443, April 1978.*

[67] Subramaniam V.V. *Onset and erosion in self-field mpd thrusters.* AIDAA/AIAA/DGLR/JSASS 22nd International Electric Propulsion Conference, *(IEPC-91-021), October 14-17 1991.*

[68] Ed. Lochte-Holtgreven W. Plasma Diagnostics. *North Holland Publishing Company, Amsterdam, Holland, 1968.*

[69] D. M. Zube and R. M. Myers. *Techniques for spectroscopic measurements in an arcjet nozzle.* Journal of Propulsion and Power, *Vol. 8(No. 1), January-February 1992.*